Electronic and Geometric Structure of Biological Spin Centers Investigated with EPR Spectroscopy

Ellen C. Hayes

A dissertation submitted in partial fulfillment of the requirements for the degree of

Doctor of Philosophy

University of Washington

2017

Reading Committee:

Stefan Stoll, Chair

Niels H. Andersen

Gary P. Drobny

Program Authorized to Offer Degree:

Chemistry

University of Washington

Abstract

Electronic and Geometric Structure of Biological Spin Centers Investigated with EPR Spectroscopy

Ellen C. Hayes

Chair of Supervisory Committee:

Professor Stefan Stoll

Department of Chemistry

In this dissertation, the fundamental concepts and techniques of electron paramagnetic resonance (EPR) spectroscopy, which are important for understanding electronic structure and relating it to geometric structure, are presented in Chapter 1. Following this are five chapters each dedicated to a separate topic where EPR spectroscopy was a central tool in studying the properties of biologically relevant systems. Chapter 2 focuses on the study of tryptophan radicals in small peptide systems. The studies aim to understand how microenvironment influences the electronic structure (through measuring magnetic and electrochemical properties) of these radicals. In Chapter 3, the identity of an unknown organic radical in the active site of the enzyme spore photoproduct lyase (SPL) is investigated. This radical is believed to be a part of a radical transfer chain involved in the repair of photodamaged DNA by the enzyme SPL. In Chapter 4, closely related to the topics of Chapter 3, the pathway of DNA photodamage by ultraviolet light is investigated. The damaged DNA is believed to form through a radical recombination process amenable to study with EPR spectroscopy. Chapter 5 discusses the magnetic properties of an intermediate formed during O-O bond activation and cleavage by a small molecule Mn^{II} compound. Results of EPR spectroscopy suggest the intermediate is a $Mn^{III}Mn^{IV}$ dimer and aim to characterize the bridging motif and protonation state of the $Mn^{III}Mn^{IV}$ dimer. Finally, Chapter 6 presents a study of a small molecule Cu^{II}-alkoxide compound relevant for understanding Cu^{II} mediated alcohol oxidations (which occur in enzymes such as galactose oxidase). A detailed electronic structure characterization was carried out by using single-crystal EPR spectroscopy in tandem with magnetic circular dichroism spectroscopy, resonance Raman spectroscopy, and density functional theory calculations.

Table of Contents

List of Figures and Schemes

List of Tables

Acknowledgements

My time in graduate school has been extremely rewarding and much of that positive experience is due to the support I have received both academically and non-academically. First, I must thank my adviser Stefan Stoll. Stefan and I both arrived at UW in the fall of 2011 and shortly after I became Stefan's first mentee. When I joined his research group I knew almost nothing about the spectroscopy I would soon be studying. I owe so much of my academic success to Stefan's patient teaching and long hours spent in the spectroscopy lab with me. Just as important as the scientific training, he relentlessly pursues excellence in publication and presentation quality and passes on those qualities to his students. I am so grateful for all that I have learned.

The members of the Stoll research group (more generally known as the Stoll Patrol) have enriched my graduate studies. Our group is full of diverse scientists and thinkers and I owe at least one aspect of my success to each of the members including the post-docs (Hannah Deberg, Claudia Tait, Eric Evans, and Joscha Nehrkorn), the graduate students (Thomas Edwards, Jeremey Lehner, Donald Mannikko, Saralyn Ogden, Jessica Dottl, Lizzy Canarie, and Sam Jahn), and the undergraduate researchers I have had the opportunity to mentor (Thao Nguyen and Timothy Welsh). It doesn't hurt either that this is a great crowd to enjoy drinks and pizza with at Big Time or to dominate the foosball table with at the annual EPR conference.

Many of my studies would not have been possible without the support of other research groups both outside of UW and in the UW Chemistry Department. Outside of UW, I was in a collaboration with the Li group at IUPUI. The studies in Chapters 3 and 4 would not have been possible without Lei Li's, Yajun Jian's, and Linlin Yang's willingness to prepare samples. I was also very fortunate to get to spend two weeks in Germany at the Max Planck Institute (CEC) in Mülheim. I want to thank Dr. Wolfgang Lubitz for inviting me to present my research to his group. In particular, Dr. Nicholas Cox spent a significant amount of time while I was visiting teaching me the intricacies of EPR spectroscopy on systems containing manganese.

The UW Chemistry Department fosters an extremely collaborative environment which allowed me to work with many of my peers on research projects. The project described in Chapter 6 included contributions from Tom Porter (a fantastic synthetic chemist), Charlie Barrows (an excellent MCD spectroscopist), and George Blouin (an incredibly helpful post-doc). In addition, I am humbled that I got to work with and discuss results with their advisers Jim Mayer, Daniel Gamelin, and Tom Spiro all of whom are widely well-respected in their fields. The studies in Chapter 2 would not have been possible without Niels Andersen and his group members (UW). Aimee Byrne, Brandon Kier, Jordan Anderson, and Kalkena Sivanesam were incredible sources of knowledge on peptide synthesis and characterization. Jordan, also one of my best friends, very patiently taught me how to use the NMR instruments and analyze the data. From Julie Kovacs's group, I was very fortunate to work with talented synthetic chemists, including Audra Johansen, Ben Leipzig, and Julian Rees, who have also been amazing friends. Audra has been a fantastic friend to decorate cookies with and is always ready for a dance party. Ben and I both knew Tom Brady would end up with 5 (at the time of this writing) super bowl rings. Julian has

been a constantly supportive boyfriend and I am so happy we could learn from each other, both in and out of grad school.

Finally, I want to thank my family, especially my mom, dad, and brother Steven for their constant love. To my brother, I am so proud of you for recently finishing your M.S. in Geology. To my parents, you have always been a source of love and guidance and I know that without your influence, I may not have attended graduate school. To all three of you, thank you for always making the effort to visit me here in Seattle, all the way from Texas.

Chapter 1

Spin centers in biology and their study with electron paramagnetic resonance spectroscopy

Abstract

This chapter gives a brief overview of spin centers in biology and discusses the essentials of continuous-wave (CW) and pulse electron paramagnetic resonance (EPR) spectroscopy, the primary tool I have used in the experimental work for this thesis. I provide pictorial descriptions of the magnetic properties, including *g* shifts and hyperfine coupling, probed with EPR spectroscopy especially as these properties pertain to the systems I have studied. In addition, I provide illustrations of the pulse sequences I use regularly in my experiments to provide a general understanding of the origin of the measured signals. With these descriptions, one should have a qualitative understanding of all the analysis of EPR data.

1.1 Spin centers in biology

The common theme of the systems studied in this thesis is their involvement in single-electron redox reactivity. Scientists continually find more and more instances of single-electron reduction and oxidation (or redox) reactions in Nature, mediated by paramagnetic organic radicals and metal ions. Interestingly, some fifty years ago, scientists believed Nature would avoid single-electron reactions in favor of two-electron processes to avoid the formation of highly reactive organic radicals. These mediating systems can consist of isolated organic radicals, single metal ions, clusters of metal ions, and coupled organic radicals and metal centers. These systems perform some of the most fundamental and complicated chemical transformations we know of, and often at ambient temperatures and pressures.

The simplest instances of single-electron processes that results in unpaired electrons are organic radicals that form due to damage of biological materials by ultraviolet (UV) radiation. For instance, DNA exposed

to UV radiation will often form dimers between adjacent DNA bases, leading to kinks in the DNA strand and disrupted DNA replication. Many of these damage processes are believed to proceed through organic radical species (see Chapter 4).

However, UV light can also lead to the initiation of biological responses that rely on organic radical transfer chains. For instance, cryptochromes and DNA photolyases absorb blue light and are responsible for circadian rhythms and DNA repair. When the blue light receptors of these enzymes absorb a UV photon, the excited state of the chromophore becomes highly reactive and oxidizes a nearby amino acid residue. The reduced state of the chromophore is believed to induce conformational changes in the enzymes which result in a signal cascade and the biological response. The reduced state of the chromophore is maintained through a series of electron transfer reactions from other amino acids (see Chapter 2).

Although amino acid radicals play a key role in electron transfer processes, metal centers can also perform electron transfer. The $Cu^{II/I}$ center in blue copper proteins is characterized by a highly covalent Cu-thiolate bond that facilitates long-range electron transfer between enzymes and proteins. Copper also commonly performs redox reactions where, when coupled with an organic radical, their chemistry bridges the gap between one-electron and two-electron reactivity. For instance, in galactose oxidase a Cu^{II} ions is covalently bound to a modified tyrosyl radical. Together, the tyrosyl radical and Cu^{II} ion oxidize primary alcohols to aldehydes, a two-electron process (see Chapter 6).

Nature also makes use of other abundant first-row transition metals for catalytic activity, commonly utilizing paramagnetic iron and manganese ions. As components of clusters, these ions perform fundamental reactions necessary for life. In addition to many complicated reactions, iron clusters repair photodamaged DNA (see Chapter 3), thus protecting organisms from the damaging effects of radiation. A vital manganese cluster is located in the oxygen-evolving complex of photosystem II. As its name suggests, this complex splits water to ultimately form O_2. Manganese also activates and splits O-O bonds such as in manganese catalase, which decomposes destructive H_2O_2 and protects cells from oxidative damage (see Chapter 5).

All of the biological systems that have paramagnetic centers (or centers with unpaired electrons) can be studies with electron paramagnetic resonance (EPR) spectroscopy. Biological paramagnetic spin centers with one or more unpaired electrons can range from simple, S=1/2 organic radicals to the complex clusters of metal ions discussed above which magnetically couple to integer and half-integer spin states of S=1/2 and higher. With EPR spectroscopy, one can characterize both the electronic structure (spin density distribution in the ground state) and the geometric structure, including the location of protons. A major advantage of EPR for the study of spin centers is the selectivity of the technique for only the paramagnetic species.

In this chapter, I outline the ways in which EPR spectroscopy can be used to determine both electronic and geometric structure. I present visual representations of the magnetic interactions between electrons and nuclei that lead to the features in EPR spectra. Brief descriptions of both continuous-wave CW EPR and pulse EPR will be given along with a vector picture representation for understanding how electron spins behave in the applied magnetic fields.

1.2 Magnetic properties measured with EPR spectroscopy

1.2.1 Magnetic interactions expressed as tensors

In the EPR experiment, a sample of paramagnetic molecules is placed in an externally applied magnetic field, $\boldsymbol{B}_0$, which causes the magnetic moments of the unpaired electrons to align with the field. The interaction of the external magnetic field and the electron magnetic moment is called the Zeeman interaction. Within each molecule, the unpaired electron experiences additional magnetic fields due to interactions with magnetic nuclei and sometimes other unpaired electrons. The magnetic interaction between an electron and nucleus is called hyperfine coupling. Depicted in Figure 1.1 is how the presence of another magnetic field generated by the magnetic moment of a nucleus creates a field, $\boldsymbol{B}_{\mathrm{HF}}$ (hyperfine field), at the electron. The vector sum of these two fields leads to the effective field, $\boldsymbol{B}_{\mathrm{eff}}$, which the electron experiences.

While the Zeeman interaction and hyperfine interactions are used most extensively in this thesis to study paramagnetic systems, there are several other key EPR-observable interactions in biological spin centers that make up the effective field experienced by an electron. These interactions are summed up in the spin Hamiltonian. For the simple case of one unpaired electron and one nucleus in an externally applied magnetic field, there is the Zeeman term, the nuclear Zeeman term, the hyperfine coupling term, and the quadrupole term (if the nucleus is of spin, *I*, greater than 1/2)

$$\hat{H} = \mu_{\mathrm{B}} \boldsymbol{B}^{\mathrm{T}} \boldsymbol{g} \hat{\boldsymbol{S}} - g_{\mathrm{N}} \mu_{\mathrm{B}} \boldsymbol{B}^{\mathrm{T}} \hat{\boldsymbol{I}} + \hat{\boldsymbol{S}}^{\mathrm{T}} \boldsymbol{A} \hat{\boldsymbol{I}} + \hat{\boldsymbol{I}}^{\mathrm{T}} \boldsymbol{Q} \hat{\boldsymbol{I}} \qquad \text{Eq. 1.1}$$

For multiple unpaired electrons, the spin Hamiltonian will include an additional zero-field splitting term

$$\hat{H} = \mu_{\mathrm{B}} \boldsymbol{B}^{\mathrm{T}} \boldsymbol{g} \hat{\boldsymbol{S}} - g_{\mathrm{N}} \mu_{\mathrm{B}} \boldsymbol{B}^{\mathrm{T}} \hat{\boldsymbol{I}} + \hat{\boldsymbol{S}}^{\mathrm{T}} \boldsymbol{A} \hat{\boldsymbol{I}} + \hat{\boldsymbol{I}}^{\mathrm{T}} \boldsymbol{Q} \hat{\boldsymbol{I}} + \hat{\boldsymbol{S}}^{\mathrm{T}} \boldsymbol{D} \hat{\boldsymbol{S}} \qquad \text{Eq. 1.2}$$

Both the spin operator, $\hat{\boldsymbol{S}}$, and the magnetic field, $\boldsymbol{B}$, are vectors and the term that describes their interaction, $\boldsymbol{g}$, takes the form of a 3x3 matrix or tensor. Similarly, the 3x3 hyperfine matrix/tensor, $\boldsymbol{A}$, describes the interaction between the electron spin and nuclear spin operators. Generally, if the tensor is symmetric across the diagonal, it can be diagonalized such that

$$\boldsymbol{R} \cdot \begin{bmatrix} g_{xx} & g_{yx} & g_{zx} \\ g_{xy} & g_{yy} & g_{zy} \\ g_{xz} & g_{xz} & g_{zz} \end{bmatrix} \cdot \boldsymbol{R}^{\mathrm{T}} = \begin{bmatrix} g_{xx} & 0 & 0 \\ 0 & g_{yy} & 0 \\ 0 & 0 & g_{zz} \end{bmatrix} \qquad \text{Eq. 1.3}$$

Here, the values g_{xx}, g_{yy}, and g_{zz} are the principal values of the *g* tensor and $\boldsymbol{R}$ is a rotation matrix. An analogous procedure can produce the principal values (A_{xx}, A_{yy}, and A_{zz}) of a hyperfine tensor. These diagonalized tensors can be isotropic, where the three principal values are equal (i.e. xx = yy = zz), or anisotropic with two identical principal values (i.e. xx = yy ≠ zz; an axial tensor), or three different principal values (i.e. xx ≠ yy ≠ zz; a rhombic tensor). The strength of an isotropic interaction does not depend on the orientation of the externally applied magnetic field in the paramagnetic molecule under study. The strength of an anisotropic interaction, however, does change as the orientation of the molecule in the external field is varied. The physical origins of this are discussed in 1.2.2 and 1.2.3.

Immediately below is how these interactions manifest mathematically in the principal values of the diagonalized tensors for axial (*T*), isotropic (*I*), and rhombic (ε) components.

a. Axial components

$$\begin{bmatrix} -T & 0 & 0 \\ 0 & -T & 0 \\ 0 & 0 & 2T \end{bmatrix} = T \begin{bmatrix} -1 & 0 & 0 \\ 0 & -1 & 0 \\ 0 & 0 & 2 \end{bmatrix}$$

If the principal values of a tensor sum to zero (i.e. the tensor is traceless as shown above) then the interaction is a purely dipolar or through-space magnetic interaction. This type of interaction occurs between electrons and nuclei and between electrons. This interaction is always present between magnetic particles but decreases rapidly with distance. As the interaction is inversely proportional to the cube of the distance between particles, it can be used to gain insight into geometric structure.

b. Isotropic components

$$\begin{bmatrix} -T+I & 0 & 0 \\ 0 & -T+I & 0 \\ 0 & 0 & 2T+I \end{bmatrix} = I + T \begin{bmatrix} -1 & 0 & 0 \\ 0 & -1 & 0 \\ 0 & 0 & 2 \end{bmatrix}$$

An isotropic component adds as a constant to the principal values of the diagonalized interaction tensor. In this way, the average of the principal values always equals the isotropic component. The dipolar term, *T*, can be extracted from the principal values by subtracting the average (*I*) and dividing the largest-magnitude term by two.

c. Rhombic components

$$\begin{bmatrix} -T(1-\varepsilon)+I & 0 & 0 \\ 0 & -T(1+\varepsilon)+I & 0 \\ 0 & 0 & 2T+I \end{bmatrix} = I + T \begin{bmatrix} -(1-\varepsilon) & 0 & 0 \\ 0 & -(1+\varepsilon) & 0 \\ 0 & 0 & 2 \end{bmatrix}$$

A rhombic interaction, ε, enters the matrix for two of the principal values as shown above. The average of the diagonal equals the isotropic interaction. The dipolar term, *T*, can be extracted from the principal values by subtracting the average (*I*) and dividing the largest term by two. The rhombic term is half the difference between the two smaller terms.

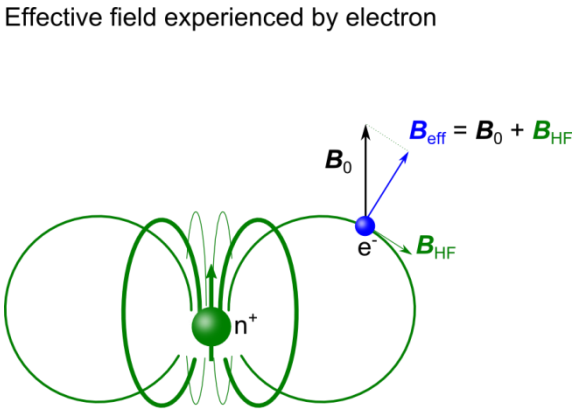

Figure 1.1. The vector sum of externally applied ($\boldsymbol{B}_0$) and internal (due to the hyperfine interaction, $\boldsymbol{B}_{HF}$) fields makes up the effective magnetic field, $\boldsymbol{B}_{eff}$, experienced by an electron (blue sphere) during the EPR experiment. The field lines due to the magnetic nucleus (green sphere) are shown in green.

As an experimental EPR spectroscopist, the goal is to measure the principal values and orientations of the ***g***, ***A***, and, if applicable, ***Q*** and ***D*** tensors using the wide range of CW and pulse EPR techniques available. These parameters can provide valuable information on the structure of the spin center and thereby oftentimes insight into their mechanisms of reactivity.

In a biological spin center, anisotropy occurs because the unpaired electron moves in a molecular orbital, the shape of which is affected by the nuclei and bonds. It should be familiar that molecules and orbitals can be described in a coordinate xyz frame. These molecular and orbital axes and orientations can be directly correlated with the directional anisotropy of the ***g*** and ***A*** tensors. This naturally leads to information about the geometric and electronic structure of a spin center. Below I describe the most frequently encountered mechanisms that lead to ***g*** and ***A*** anisotropy in biological spin centers. Using pictorial representations, I will show how these ***g*** and ***A*** values are related to structure and how a chemist can picture this information. Nearly all the physical interactions measurable with EPR can be rationalized by picturing the magnetic field lines induced by the motion of electrons and the presence of nuclei when placed in an external magnetic field.

1.2.2 Chemical shifts in the g tensor

Spin-orbit coupling. The *g* value describes the magnetic interaction between an electron and an externally applied magnetic field, $\boldsymbol{B}_0$, and for a free electron the value, g_e, is a known constant

approximately equal to 2.0023. The electron has intrinsic angular momentum (or spin). In a molecule, the electron possesses additional orbital angular momentum due to its motion in an orbital. Spin-orbit coupling is the interaction between spin and orbital angular momentum and it induces chemical shifts in the value g_e. These shifts can be related to both electronic and geometric structure.

The magnitude of these shifts depends on the charge of the nucleus and excited-state mixing into the ground state. When spin-orbit coupling is treated with perturbation theory, shifts in *g* value take on the form

$$g = g_e + \frac{C}{E_{es} - E_{gs}} \qquad \text{Eq. 1.4}$$

where nuclear charge and excited-state mixing are taken into account in the numerator *C* and scaled by the denominator $E_{es}-E_{gs}$, the difference in energy between the excited state (E_{es}) and the ground state (E_{gs}).

To first understand how these chemical shifts occur, one must recognize that placing a molecule in an external magnetic field will induce rotation of the electron density around the field vector in a counter-clockwise manner (following the right-hand rule). When considering the influence of nuclear charge, one must switch the frame of reference to a stationary electron with an orbiting nucleus. The orbiting positively charged nucleus represents a current, which induces a magnetic field that the electron experiences in addition to the externally applied magnetic field (see Figure 1.2). The larger the nucleus, the more rotating charge, the larger the current, and the larger the additional field experienced by the electron. It is this additional field which results in shifts away from the free-electron *g* value, g_e. Larger shifts in the *g* values are expected in moving from spin centers on the lighter atoms (organic radicals) to spin centers on first-row transition metals.

Excited-state mixing through spin-orbit coupling can lead to *g* anisotropy because the denominator in Equation 1.4 (and which excited state mixes with the ground state) depends on the orientation of the molecule in the external magnetic field. The mixing of ground and excited states can be visualized by

imagining the movement of an electron through orbitals around a nucleus once an external field is applied.

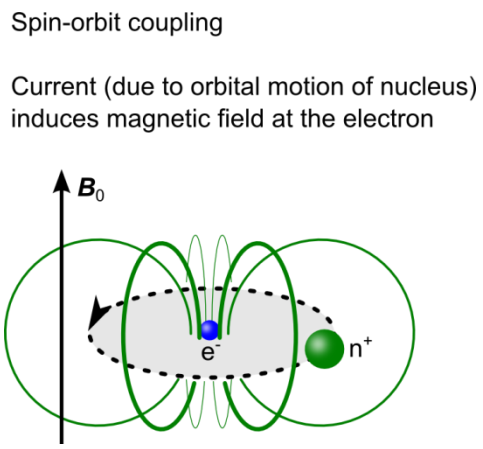

Figure 1.2. Spin orbit coupling. From the electron's perspective, the moving nucleus forms a current loop perpendicular to the external field around the electron and induces a magnetic field (field lines due to the moving nucleus are shown in green).

Excited-state mixing in organic aromatic π-type radicals. The singly occupied molecular orbital (SOMO) in an aromatic ring molecule is a conjugated π system of p_z orbitals spatially located above and below the plane of the ring (see Figure 1.3). Placing the molecule in a field oriented perpendicular to the plane of the ring will cause the electrons to circulate in the π conjugated MO. Efficient orbiting motion is achieved without the electron passing through other orbitals (or equivalently without excited state mixing). This makes the numerator *C* in Equation 1.4 very small, so *g* shifts when the field $\boldsymbol{B}_0$ is parallel to the orbital z axis (by convention parallel to the g_{zz} axis for aromatic π-type radicals) are very small. If instead the field lies in the plane, orbital motion of the electrons involves passing out of the SOMO. This motion is efficient if there is excited-state mixing, which can be thought of as the electron passing out of the SOMO and into either p_x or p_y orbitals (such as bonding orbitals or in-plane lone-pair orbitals). See Chapter 2 for details on this effect in tryptophan radicals.

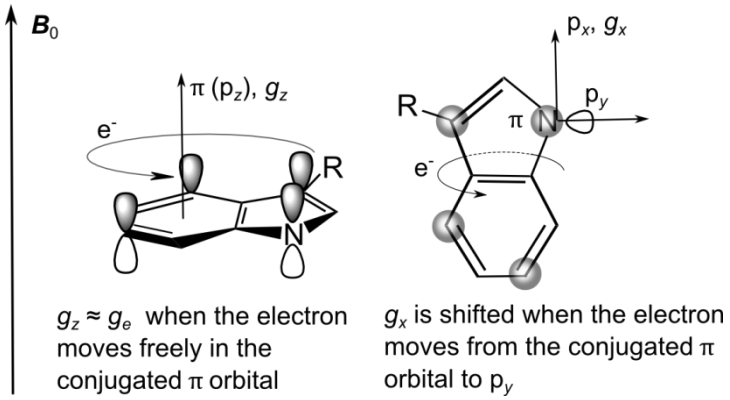

Figure 1.3. Mixing of the ground state (singly occupied conjugated π bond) with an excited state (singly occupied nitrogen p_y orbital) leads to shifts in *g* values in aromatic π-type radicals. It can be understood as the induced rotation of the electron around the applied field $\boldsymbol{B}_0$.

Excited-state mixing in transition metal complexes. In transition metal compounds, this orbital motion of unpaired electrons occurs in molecular orbitals with substantial metal-ion d character. By considering the magnitude of chemical shifts in *g* value, one can make a good guess about the ground state of the transition metal and therefore (some of) the d orbital splitting pattern. If one already knows the structure of the molecule from a crystal structure, one can make a much better conjecture about the d orbital splitting pattern and the orientation of the d orbitals in the molecule. Understanding how this is so is easiest by considering a common structural distortion of axial elongation or compression along the *z* axis in an octahedral ligand field (see Figure 1.4). Axial elongation will lower the dz^2 orbital energy whereas compression will raise its energy. For a d^9, S = ½ system in these situations, the unpaired electron will reside in the dx^2-y^2 or the dz^2 orbital, respectively.

In the first case of the unpaired electron in the dx^2-y^2 orbital, an externally applied magnetic field along the *z* axis will cause the electrons to rotate (which appears like the hole rotating in the opposite direction) from the dx^2-y^2 into the dxy orbital. The closer in energy these two orbitals are (smaller denominator in Equation 1.4), the more efficient the excited-state mixing. Thus, large shifts for one *g* value away from g_e are often indicative of a dx^2-y^2 ground state. In this situation, similar arguments can be made for the g_{xx} and g_{yy} values where excited mixing occurs between the dx^2-y^2 orbital and the dxz and dyz orbitals, respectively (see Chapter 6 for an application of these ideas in Cu^{II} molecules).

In the second scenario, the unpaired electron is in the dz^2 orbital. When the magnetic field applied parallel to the z axis, the orbital motion of the electron is contained within the dz^2 orbital, or equivalently, there is no excited-state mixing. When transition metal compounds have one *g* value that is close to the free value g_e, this is indicative of the unpaired electron in the dz^2 orbital.

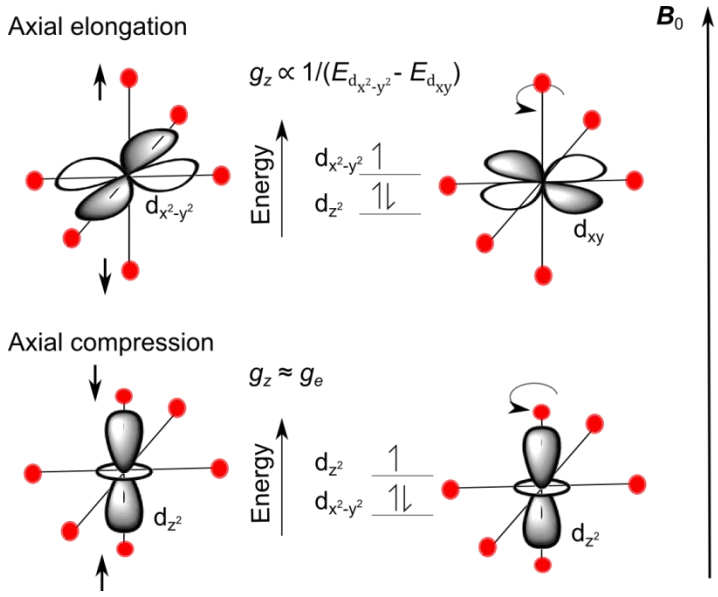

Figure 1.4. Excited-state mixing in transition metal compounds can be understood as the induced rotation of the electron around the applied field $\boldsymbol{B}_0$. Mixing of the ground state (half-occupied dx^2-y^2 orbital) with an excited state (half-occupied dxy orbital) leads to large shifts in g_{zz} values for transition metal compounds. In contrast, if the ground state is a half-occupied dz^2 orbital, no excited-state mixing occurs and shifts in g_{zz} are very small.

1.2.3 Hyperfine coupling

The hyperfine coupling interaction can also offer valuable information on electronic and geometric structure. Common magnetic nuclei found naturally in biological spin centers are ^{1}H, ^{14}N, ^{63,65}Cu, ^{55}Mn, ^{59}Co, and ^{51}V. In addition, some isotopes of common biologically relevant elements such as ^{2}H, ^{13}C, ^{15}N, ^{17}O, and ^{33}S are also magnetic and can be incorporated into biological materials through synthesis or mutagenesis. Their vastly different magnetic properties (compare gyromagnetic ratios $^{1H}\gamma/^{2H}\gamma \approx 6.5$ and spins $^{1H}I = ½$, $^{2H}I = 1$ for isotopes of hydrogen) will change their EPR spectra compared to the natural-abundance isotopes, making isotopic labeling a useful way of identifying spin centers.

Hydrogen and nitrogen occur frequently in organic radicals and in the ligands of paramagnetic transition metal ions. Because of this frequency, the mechanisms that lead to hyperfine coupling between unpaired electrons and these nuclei are discussed below.

Point-dipole coupling. Point-dipole coupling is a through-space interaction characterized by a traceless axial tensor making this interaction a source of anisotropy (tensor shown in 1.2.1). The through-space interaction can be computed using the equation $T_{\mathrm{dip,en}} = \frac{\mu_0}{4\pi}\mu_{\mathrm{B}}\mu_{\mathrm{n}}g_{\mathrm{n}}g_{\mathrm{e}}\frac{1}{r_{\mathrm{en}}^3}\left[\left(\frac{3\boldsymbol{r}_{\mathrm{en}}\boldsymbol{r}_{\mathrm{en}}^{\mathrm{T}}}{r_{\mathrm{en}}^2} - \mathrm{I}\right)\right]$, where the strength of the dipole coupling between an electron and nucleus, $T_{\mathrm{dip,en}}$, weakens as the distance r between the electron, e, and nucleus, n, increases (with $1/r^3$) and depends on the nuclear g value g_{N}, the electron g value g_{e}, the nuclear magneton μ_{N}, the Bohr magneton μ_{B}, and the vacuum permeability constant μ_0.

The through-space interaction is always present (although sometimes it is too weak to measure) and is always an anisotropic interaction. In some cases, the through-space interaction is the only source of anisotropy, especially for hyperfine coupling to ^{1}H nuclei where spin population is in a spherically symmetric s orbital (see below for the s and p orbital spin population). In these cases, the anisotropic component of the hyperfine tensor can be separated from the isotropic component and used to determine distances between ^{1}H nuclei and spin population distributed in a molecule (see the distributed point-dipole approximation used in Chapter 6).

Hydrogen and nitrogen s orbital spin density leads to isotropic hyperfine coupling. Hydrogen and nitrogen are present in organic radicals and in the ligands of transition metal compounds. In paramagnetic transition metal compounds with a delocalized SOMO, the spin density can be distributed onto the ligands resulting in measureable hyperfine coupling to these nuclei. The isotropic component of the hyperfine coupling is typically due to nitrogen 2s and hydrogen 1s orbital character in the SOMO. The hyperfine coupling strength if 100 % spin population is in a nitrogen 2s or hydrogen 1s orbital (an unpaired electron fully localized in this orbital) has been calculated based on the shape of the s orbitals.[1] By simply taking the ratio of the isotropic component of the measured hyperfine coupling and this

calculated hyperfine coupling and one can estimate the spin population in the nitrogen 2s or hydrogen 1s orbital. This technique is used in Chapter 6 for predicting spin populations on nitrogen ligated to a Cu^{II} ion.

Nitrogen p orbital spin density leads to anisotropic hyperfine coupling. Anisotropic coupling to nitrogen nuclei can occur due to spin population in a nitrogen p orbital. Ultimately, this interaction is a through-space dipolar interaction, but it is averaged over the shape of the p orbital. Similar to the case of spin population in a nitrogen 2s orbital, the hyperfine coupling strength if 100 % spin population is in a nitrogen 2p orbital has been calculated based on the shape of the 2p orbital. Once again, by simply taking the ratio of the anisotropic component of the measured hyperfine coupling and this calculated hyperfine coupling, one can estimate the spin population in the nitrogen p orbital. This technique is used in Chapter 6 for predicting spin populations on nitrogen ligated to a Cu^{II} ion.

By visualizing the shape of a p orbital, one can easily understand why nitrogen hyperfine coupling is often strongly anisotropic, especially when there is substantial spin density around a nitrogen nucleus such as in an organic radical (see Figure 1.5 top). For instance, if the external magnetic field $\boldsymbol{B}_0$ is aligned along the z axis of a p_z orbital, the unpaired electron sits in the densest field lines due to the magnetic nitrogen nucleus, resulting in large hyperfine coupling. When $\boldsymbol{B}_0$ is perpendicular to the p_z orbital z axis, the electron sits in less dense field lines due to the nitrogen nucleus. This results in a smaller hyperfine coupling.

In a similar way, one can envision why anisotropic hyperfine tensors in transition metal complexes have certain orientations. Generally, the majority of spin density in metal complexes resides on the metal ion, with some spin density delocalized on to directly coordinated atoms such as nitrogen. The delocalization occurs through the bonding orbital which connects the metal and bound atom. When the magnetic field $\boldsymbol{B}_0$ is applied along the bond axis, the unpaired electron lies in the strongest field lines due to the nucleus as depicted in Figure 1.5, bottom. This is why the largest component of an axial hyperfine tensor in transition metal complexes generally points along the bond axis toward the metal center.

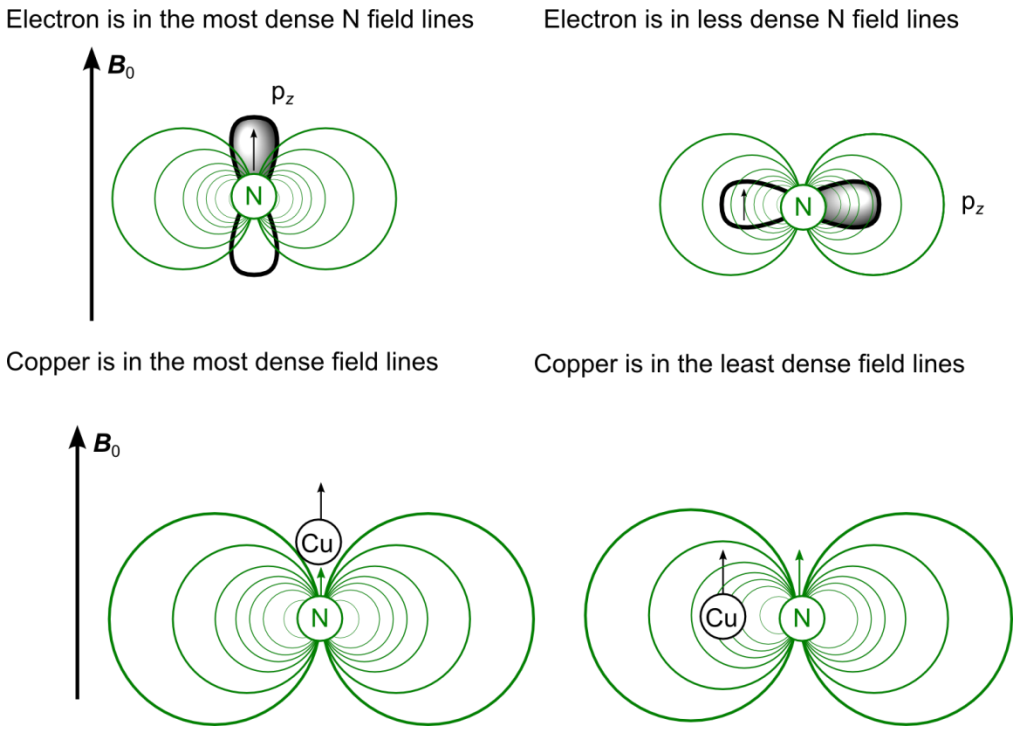

Figure 1.5. Pictorial representation of how anisotropy arises in nitrogen hyperfine coupling. *Top*: When the unpaired electron resides in a p orbital and the external field $\boldsymbol{B}_0$ is aligned along the p orbital axis, the hyperfine coupling interaction is strongest. This is because the field lines due to the magnetic nucleus are the densest in this orientation. When rotated by 90°, the electron, still in the same orbital, sits in less dense field lines and the hyperfine interaction is weaker. *Bottom*: In a similar way, in transition metal complexes the hyperfine interaction between a ligand (in this case nitrogen) and unpaired electron density on the metal ion is strongest along the bonding axis.

Hyperfine coupling of hydrogens in conjugated π-radicals. The resonance structures of aromatic and π-conjugated organic molecules stabilize radicals of these species. In these radicals, the SOMO consists of overlapping p orbitals so that the unpaired electron is delocalized across all the p orbitals and nuclei involved in the MO (i.e. allylic and benzylic radicals). These types of radicals typically have two distinct types of protons which exhibit hyperfine coupling; the α-hydrogens and β-hydrogens. By convention, α-hydrogens indicate hydrogens covalently bound to the carbon atoms which contribute to the SOMO, so they are nearest to the π-conjugated orbital. The β-hydrogens are those on carbons one bond away from the π-conjugated orbital (e.g. a methyl or methylene group on an aromatic ring). (This is described in more detail in Chapter 2 and visualized in Figure 2.1).

α-Hydrogen hyperfine coupling of planar conjugated and aromatic π organic radicals. α-Hydrogens lie in the plane of the p orbital nodes and they display significant hyperfine coupling when the adjacent atom (i.e. C, N, or O) has substantial unpaired spin population. Their hyperfine couplings contain both isotropic and anisotropic components. The anisotropic component arises from the through-space dipole coupling of the hydrogen to the spin population delocalized throughout the π orbital.

The isotropic hyperfine coupling depends on the spin population, ρ, at the adjacent atom (X) according to the McConnell relationship $A_{\text{iso}}^{\text{H}(X)} = Q\rho(X)$. Here, Q is a semiempirical constant that depends on the species of planar aromatic radical and has been calculated and measured for certain classes of radicals (including tyrosyl,[2] benzosemiquinone,[3] and allylic[4] radicals). The isotropic coupling arises through spin polarization (described in Figure 1.6). This creates an excess of m_s = -1/2 electron spin population in close proximity to the nucleus, in the 1s orbital, leading to an isotropic contribution to the hyperfine coupling.

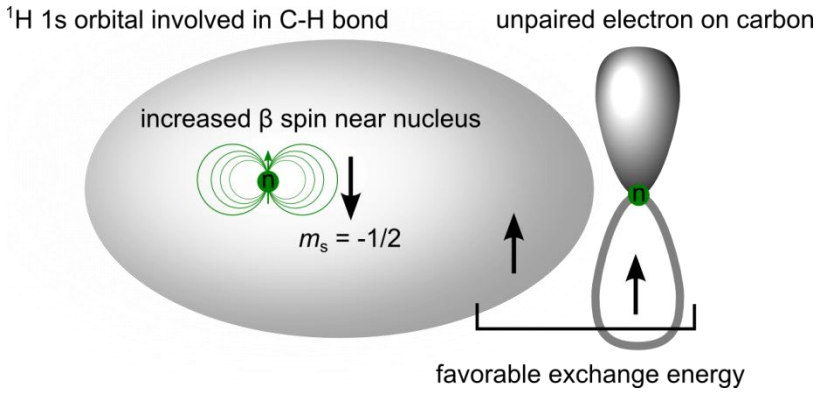

Figure 1.6. Spin polarization for α hydrogens occurs when the unpaired electron (represented by black arrows) in the π orbital forces one of the nearby electrons in a C-H bond (i.e. an electron in a different spatial orbital) to align parallel (Hund's rule). This in turn causes the other electron in the bond, which is further from the unpaired electron and closer to the ^{1}H nucleus, to align antiparallel (Pauli exclusion principle). This creates a small increase in the population of spin-down electrons in a bonding orbital with ^{1}H s orbital character close the nucleus.

β-Hydrogens. β-Hydrogens typically have large isotropic hyperfine coupling values indicating spin population in the 1s orbital of the hydrogen. This is a type of Fermi contact interaction and unlike spin polarization which leads to the isotropic interaction in α-hydrogens, the physical origin of the Fermi contact interaction in β-hydrogens is due to hyperconjugation, which is less easily visualized. Empirically,

it is known to depend on the angle between the z axis of the conjugated π orbital (perpendicular to the plane of an aromatic molecule) and the projection of the H_β-C_β bond axis onto the z axis (see Chapter 2, Figure 2.1, for details). As this angle gets smaller and the p_z axis and H_β-C_β bond axis become collinear, the hyperfine interaction grows larger. One can imagine this as the proton coming in to contact with the SOMO. This relationship is summarized in the semiempirical formula $A_{\mathrm{iso,H}\beta} = \rho_{\mathrm{C}\alpha 1} B \cos^2\theta_{1,2}$ where ρ is the spin population at $C_{\alpha 1}$, B is an empirical constant that depends on the species of radical, and θ is the angle between the p_z axis and the projected $C_\beta H_\beta$ bond.

Quadrupole interaction in *I*>1/2 nuclei. The quadrupole interaction, though not a major component of the analysis of data presented in this thesis, deserves mention as it is present for $I > ½$ nuclei such as ^{2}H, ^{14}N, and ^{55}Mn. The quadrupole interaction is an interaction between the electric quadrupole moment of a nucleus and a local electric field gradient. The quadrupole moment arises from non-spherical charge distribution within the nucleus. The local electric field gradient arises from the distribution of electrons around the nucleus, which is of course dependent on the geometry of the molecule. When the charge distribution at the nucleus is not spherically symmetric, there is a lowest-energy orientation of the quadrupole moment in the inhomogeneous electric field. This causes shifts, splittings or broadening in the resonance frequencies measured in hyperfine spectroscopy. In addition, the quadrupole interaction for ^{14}N nuclei often leads to strong state mixing observable with ESEEM and HYSCORE spectroscopy (described in Section 1.4.5).

1.3 Experimental EPR spectroscopy

1.3.1 Probing magnetic interactions with an applied B_1 field

So far the effects of an externally applied magnetic field $\boldsymbol{B}_0$ and the local magnetic fields due to magnetic nuclei on an unpaired electron have been considered. To probe these interactions, transitions between the ground $m_s = -1/2$ and excited $m_s = +1/2$ states are induced with microwave radiation. In traditional perpendicular-mode EPR (used throughout the experiments presented in this thesis), the microwave radiation is applied perpendicular to the external field $\boldsymbol{B}_0$. The magnetic component of the radiation, $\boldsymbol{B}_1$, exerts a torque on the magnetic dipole of the electron which tilts it off of the $\boldsymbol{B}_0$ axis. In different

experiments, this tilt can be large or small (see Figure 1.7) but in all cases if the $\boldsymbol{B}_1$ field is turned off, the spin vector of the electron will undergo gyroscopic precession in a cone around $\boldsymbol{B}_0$ (or the z axis in Figure 1.7). The tilting of the electron's magnetic moment off of the $\boldsymbol{B}_0$ axis is measured differently in CW and pulse EPR experiments but is ultimately what results in the measured EPR spectra. In section 1.4 I will discuss the mechanics of EPR experiments, but immediately below I will discuss EPR samples and the two types of spectra presented in this thesis. These spectra are distinguished by either a magnetic field x axis in millitesla (mT, measured with CW or pulse EPR) or a frequency x axis in megahertz (MHz, measured with pulse hyperfine spectroscopy).

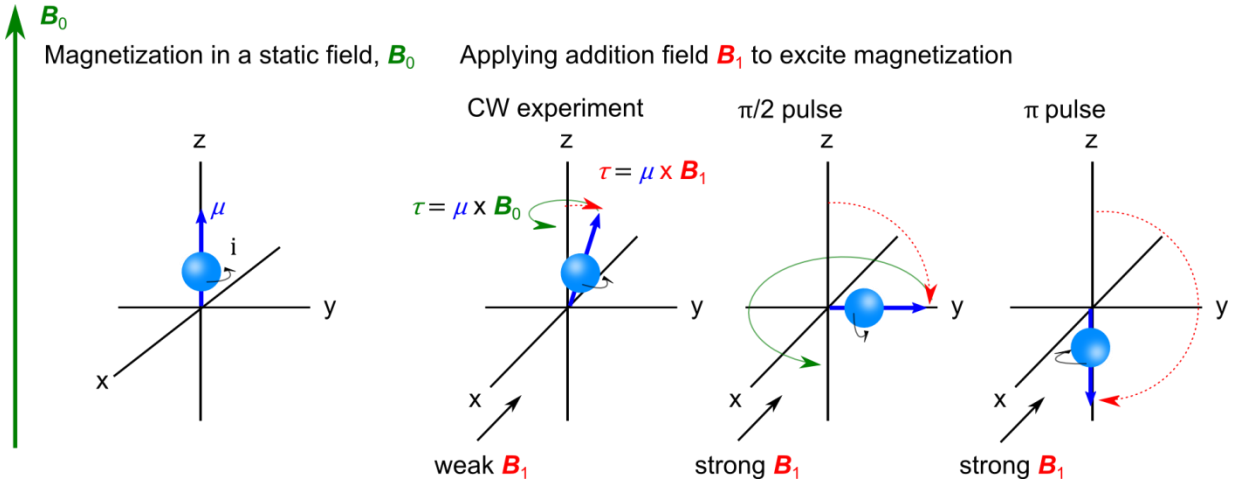

Figure 1.7. In an externally applied magnetic field $\boldsymbol{B}_0$, the magnetic moment, $\boldsymbol{\mu}$, of the spinning electron aligns parallel to the field. In the CW EPR experiment, a $\boldsymbol{B}_1$ microwave field applied along the x direction induces a torque, τ, on the electron tilting the magnetic moment toward the y axis (red dashed arrows). In the pulse EPR experiments, the $\boldsymbol{B}_1$ field is much stronger and can tilt the magnetic moment 90° on to the y axis (image labeled π/2 pulse), or 180° on to the –z axis (image labeled π pulse). If the magnetic moment is not parallel or antiparallel to the field $\boldsymbol{B}_0$ (CW or π/2 pulse images), the magnetic moment will undergo gyroscopic precession around the z axis due to the electron spin (green dashed arrows).

1.3.2 The EPR sample

Before considering how the experiments work, it is important to understand the conditions under which most EPR experiments are carried out. For biological spin centers, an EPR sample is typically a frozen solution of the analyte of interest and EPR experiments are carried out at liquid-nitrogen (boiling point ≈77 K) or liquid-helium (boiling point ≈ 4 K) temperatures. Samples are frozen for several reasons. The first reason for biological samples is to trap highly reactive paramagnetic intermediates that would

otherwise decay chemically into diamagnetic species (especially true for organic radicals or O_2 sensitive transition metal compounds). The second reason for using colder temperatures is to take advantage of increased thermal population (according to the Boltzmann distribution) of the lower energy $m_s = -1/2$ state. Third, pulse EPR experiments last hundreds of nanoseconds and up to tens of microseconds. However, at room temperature many spin centers will relax out of the excited state before the experiment is over. At low temperature, relaxation is slower, and the excited state lasts long enough to be measured (see Section 1.4.4 for measuring relaxation). Finally, low temperatures guarantee that the spin centers are immobilized and the anisotropic interactions, which contain structural information, are not averaged out (see 1.3.5 and Figure 1.10 for orientation selection).

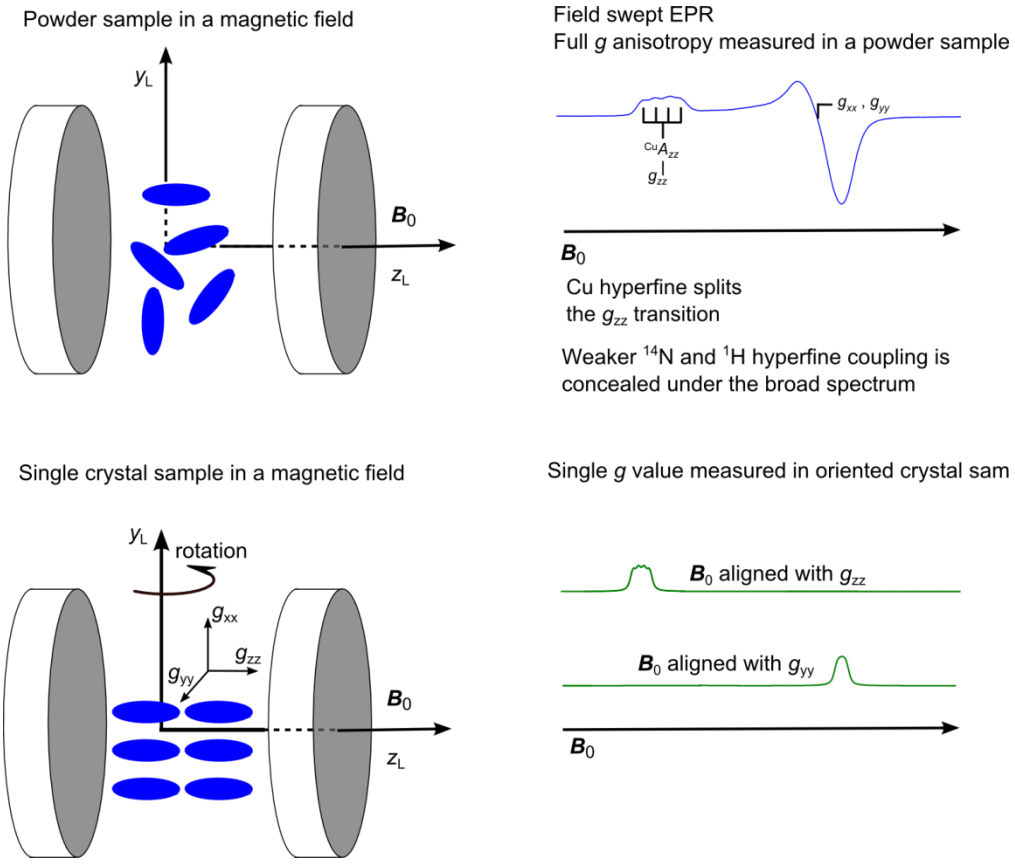

Figure 1.8. Powder vs single-crystal field-swept EPR spectra. *Top panel*: In a powder sample, all the molecules are randomly oriented in the applied field $\boldsymbol{B}_0$ and all components of the *g* and *A* tensors will be measured during a field-swept EPR experiment. This produces the blue spectrum. This spectrum is representative of a transition metal spectrum (Cu^{II}) where the *g* values are well-resolved and the strong copper hyperfine coupling at the g_{zz} resonance is also visible. *Bottom panel*: In a single-crystal sample, all molecules are aligned in one orientation (depicted here with g_{zz} and the external field $\boldsymbol{B}_0$ collinear).

When the EPR spectrum is collected, all the molecules will resonate at the same position (in this case at the field corresponding to g_{zz}). By rotating the crystal 90°, the g_{yy} value can be measured.

A frozen-solution sample is an example of a powder sample. In a powder sample, the molecules are oriented randomly with respect to the magnetic field, $\boldsymbol{B}_0$. During the experiment, signals from all of these orientations are measured and any anisotropy in the interactions (such as the Zeeman interaction or hyperfine interaction) appears in the spectrum.

Another less common but extremely useful sample is the single crystal. In this case, all paramagnets in the sample are oriented in the same direction (or set of discrete directions in the case of multiple molecules per unit cell). If an interaction is anisotropic, only one component of the tensor will be measured. However, by rotating the crystal in the magnetic field systematically, all components of the tensor can be sampled allowing measurement of the full interaction tensor (i.e. its principal values and its orientation, see Chapter 6). The different ways that EPR spectra manifest in powder vs. single crystal samples are shown in Figure 1.8.

1.3.3 Measuring *g* values and large hyperfine coupling with field-swept spectra

In field-swept EPR experiments, transitions occurs between the electron β and α states (or m_s = -1/2 and m_s = 1/2 states) as shown in Figure 1.9. The difference in energy between the β and α states gets larger as the magnetic field increases which is continuously swept in these experiment to create the x axis. When the applied microwave radiation, $\boldsymbol{B}_1$, matches the energy gap between the spin states, the sample absorbs microwave radiation and the EPR transition occurs. This is described by the most basic equation for the EPR experiment, $h\nu = \Delta E = g\mu_B B_0$, where ΔE is the difference in energy between the β and α states and B_0 is the strength of the applied magnetic field. If a hyperfine interaction is present, the difference in energy gains terms such as $\Delta E = g\mu_B B_0 + m_I A$. At what fields the signals occur therefore depends on the *g* shifts, a constant (the Bohr magneton μ_B), the hyperfine coupling, and the microwave frequency.

For transition metal compounds, shifts in *g* are often large and can be read directly from the field-swept EPR spectrum to reveal details about the electronic structure (see Chapter 6 Appendix 6.6). For organic

radicals, *g* shifts are typically small and undiscernible in the low field/frequency experiments presented in this thesis (X band ≈ 10 GHz and Q band ≈ 33 GHz).

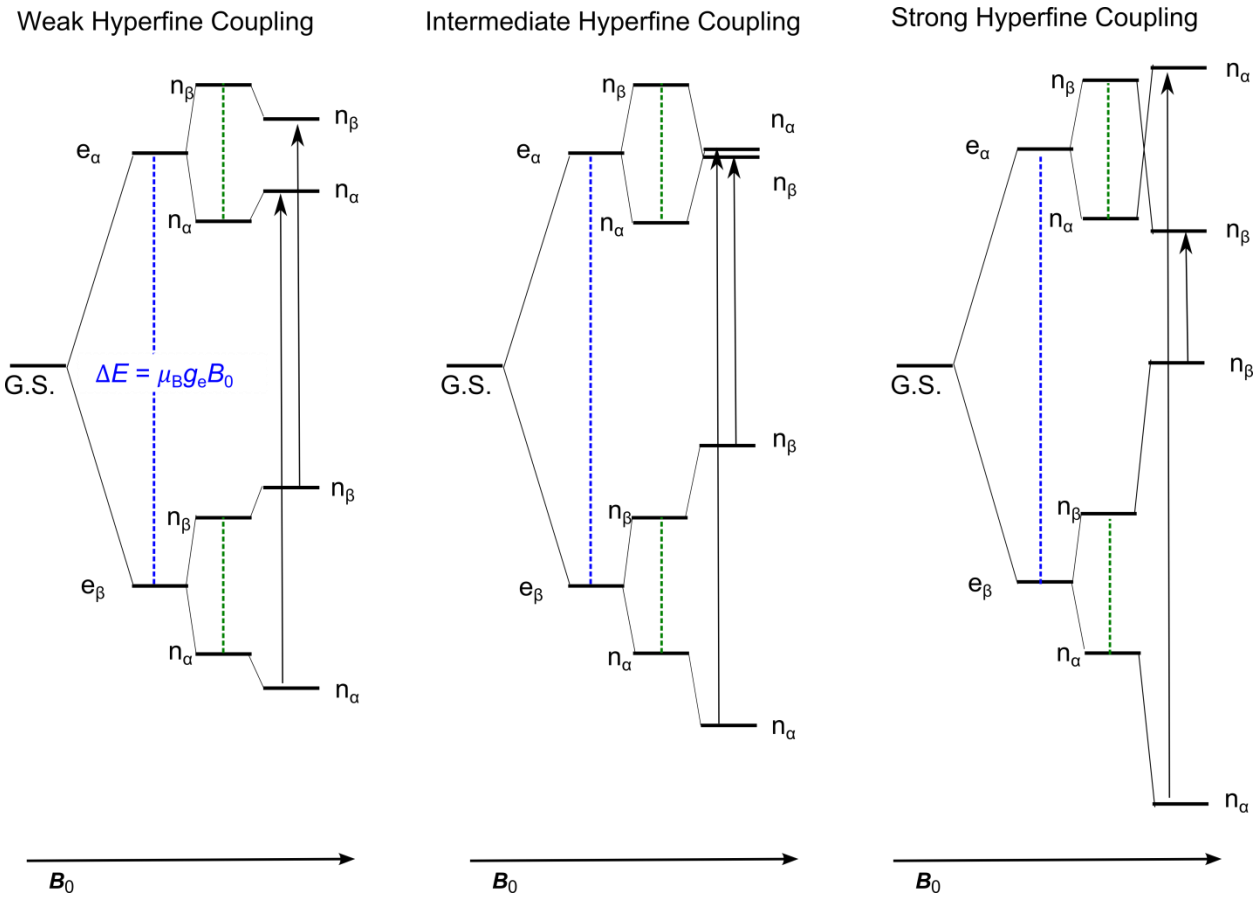

Figure 1.9. Energy level diagram depicting the weak, intermediate, and strong hyperfine coupling regimes. In each regime, the first set of levels represents the electron Zeeman splitting (blue dashed lines), the second set (green dashed lines) shows the effect of the nuclear Zeeman interaction, and the third (with solid arrows to represent transitions) the hyperfine interaction. The allowed EPR transitions occur between the spin-down (e_β) and spin-up (e_α) states where the spin states of an $I = 1/2$ nucleus do not change. In the weak-coupling regime, the features in hyperfine spectra appear centered at the nuclear Larmor frequency and split by the hyperfine coupling. In the strong-coupling regime, the features are centered at half the hyperfine coupling ($A/2$) and split by twice the Larmor frequency. In the intermediate-coupling regime, experiments that probe nuclear modulations (such as ESEEM and HYSCORE) are most efficient.

Strong hyperfine coupling values (larger than the spectral linewidth) can also be read directly from the field-swept EPR spectrum. As shown in Figure 1.9, a nuclear spin of $I = ½$ will split the electron Zeeman energy levels, resulting in four states. The microwave radiation will only induce EPR transitions ($\Delta m_s = \pm 1$) and not nuclear transitions, so that two resonances appear in the spectrum split by the hyperfine

coupling. The number of lines that appear in a spectrum depends on the nuclear spin following 2*I*+1. As hyperfine coupling can also be anisotropic, it may be possible to detect this anisotropy as well in the field-swept spectrum. This is especially apparent if the *g* shifts are large as in transition metal compounds (see Figure 1.8). An example of how well-resolved *g* values and hyperfine coupling will manifest in field-swept spectra are shown in Figure 1.8.

1.3.4 Measuring small hyperfine coupling with pulse EPR spectroscopy

In some cases, field-swept EPR experiments combined with isotopic labeling are enough to characterize the hyperfine coupling values in a system and to make interesting structural conclusions (see Chapters 3 and 4). However, in many instances, small hyperfine coupling values are not resolved due to broad experimental linewidths (see Chapter 2, tryptophan) in powder EPR samples. A significant source of broadening comes from structural heterogeneity which arises when each spin center has slightly different bond lengths and angles. Since *g* and hyperfine coupling values depend on structure, each spin center will have different values which leads to inhomogeneous broadening that can usually be modeled as Gaussian. Other times, the small hyperfine splittings due to ligand atoms are masked by the much larger and broadened hyperfine splitting due to transition metal ions (see Chapters 5 and 6). In these cases, pulse EPR experiments can be used to directly measure these smaller hyperfine coupling values hidden under the broadened EPR line shape.

Broad EPR spectra can have bandwidths from ≈ 250 MHz (or ≈ 9 mT) in organic radicals to ≈ 1700 MHz and larger (or ≈ 60 mT) in transition metals in the frequency domain. In pulse EPR, the applied rectangular pulses have bandwidths (BWs) which can be approximated with the relation BW = 1/(pulse length). The shortest pulses that can be applied (due to hardware limitations) are around 10 ns, corresponding to a bandwidth of 100 MHz. For organic radicals, a large portion of the spectrum (and therefore the electron spins in many orientations in the sample) can be excited during an experiment. However, for large-bandwidth spectra, only a small portion of the electrons (and therefore orientations of molecules in a powder sample) are excited with a given pulse.

1.3.5 Effects of finite-bandwidth pulses in hyperfine spectroscopy of narrow and broad EPR spectra

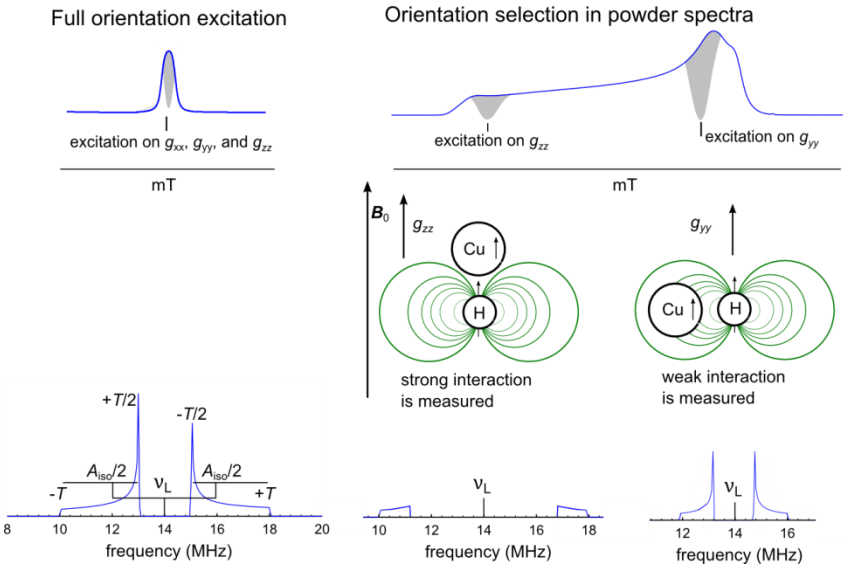

Figure 1.10. Measuring anisotropy in the *A* tensor with hyperfine spectroscopy. During hyperfine experiments with pulse EPR, the magnetic field is held constant and microwave pulses of a particular bandwidth (represented by the gray shaded regions on the spectra) are applied. *Left panel*: In narrow-bandwidth EPR spectra typical for organic radicals (left), a microwave pulse will excite a large portion of the spectrum. Typically molecules with all possible orientations of the *g* tensor with the applied field are excited. Because of this, a hyperfine spectrum such as the one shown in the bottom left will result from the experiment. As is typical for the weak coupling regime, the resonance positions of the hyperfine features are centered at the nuclear Larmor frequency and split by the isotropic component of the tensor (A_{iso}) and the dipolar component of the tensor, *T*. *Right panel*: In a broad-bandwidth spectrum, the finite bandwidth of the pulses means only a portion of the molecules are excited that have a certain orientation with respect to the applied field, $\boldsymbol{B}_0$. In this figure, a molecule where the g_{zz} axis is collinear with the strongest component of the ^{1}H hyperfine coupling tensor and the g_{yy} axis is collinear with the weakest component of the hyperfine coupling tensor is shown. If a hyperfine experiment such as ENDOR is performed with the field $\boldsymbol{B}_0$ held constant at the g_{zz} position, a stronger ^{1}H hyperfine coupling will be measured than if the experiment is performed at the g_{yy} field position. In this way, the orientation of tensors and orbitals can be established, leading to structural information.

Measuring the anisotropy of hyperfine interactions is important for structure determination. The ways anisotropy manifests in the hyperfine spectra of a typical narrow-BW organic radical and a wide-BW transition metal EPR spectra are shown in Figure 1.10. In a narrow-bandwidth EPR signal, when all orientations are excited, the anisotropic and isotropic components of the hyperfine coupling will all appear during one hyperfine experiment. Considering geometric structure, the anisotropic component can be used to determine the distance between the nucleus being studied and the unpaired electron.

However, if the orientation of the *g* tensor is not resolved, no relationship between the orientations of these two particles can be established.

However, in transition metal compounds with well separated *g* values, a relationship between the orientation of the *g* and *A* tensors can be established using narrow-bandwidth pulses that only excite a portion of the EPR spectrum. As shown in Figure 1.10, a pulse applied along the g_z resonance position is effectively exciting only molecules in the sample where the g_z axis is aligned with the magnetic field. If an ENDOR experiment is performed on a nearby ^{1}H nucleus, only the component of the hyperfine interaction that is parallel to g_z and the field $\boldsymbol{B}_0$ is probed. If the static magnetic field of the ENDOR experiment is changed to the g_x or g_y direction, then the component of the hyperfine coupling parallel to g_x or g_y is probed. Using the spectra in Figure 1.10 as an example, one can derive an understanding of the orientation of the *g* tensor relative to the hyperfine tensor. As an example, this might be useful in determining the approximate location of a proton relative to a metal center if the orientation of the *g* tensor is known.

1.4 Technical details of CW and pulse EPR spectroscopy

1.4.1 CW EPR spectroscopy

The CW EPR experiment is simply an absorption experiment where the transition occurs between the β and α states (or m_s = -1/2 and m_s = +1/2 states) as shown in Figure 1.9. The typical experiment takes place in a microwave resonator because the absorption coefficient for the EPR transition is very small. Also, instead of measuring change in transmitted power (like in a typical visible-light absorption experiment), change in power reflected from the resonator is measured. The CW EPR spectra presented in this thesis will appear as derivative line shapes. This is for technical reasons and is a result of using field modulation on B_0 to enhance the EPR signal.

1.4.2 Pulse EPR spectroscopy

Unlike in CW EPR where the excitation field ($\boldsymbol{B}_1$) is continuously applied while $\boldsymbol{B}_0$ is swept, in pulse EPR, $\boldsymbol{B}_1$ is applied for short periods of time on the tens to hundreds of nanoseconds time scale. While the

external field $\boldsymbol{B}_0$ is held constant, the response of the sample (in the form of an FID or echo as discussed below) is measured. The pulses are much more powerful than the $\boldsymbol{B}_1$ field used in CW EPR so that in a short period of time, a pulse can tilt the magnetic moment of the electron much farther such as 90° into the xy plane. A pulse with equal amount of power, but applied twice as long can tilt an electron's magnetic moment by 180° onto the -z axis (see Figure 1.7).

Once tilted into the *xy* plane, the electron spins precess and dephase around the z axis in this plane. The precession frequency of each spin varies slightly due to the small differences in microenvironment each electron experiences. This is usually due to the slight structural differences in each molecule containing the unpaired spin, or due to different states of the nearby magnetic nuclei. This leads to slightly different *g* values and hyperfine coupling values which alter the effective field experienced by the electron and therefore its precession frequency.

1.4.3 Generating a signal; FID, refocused echo, and stimulated echo

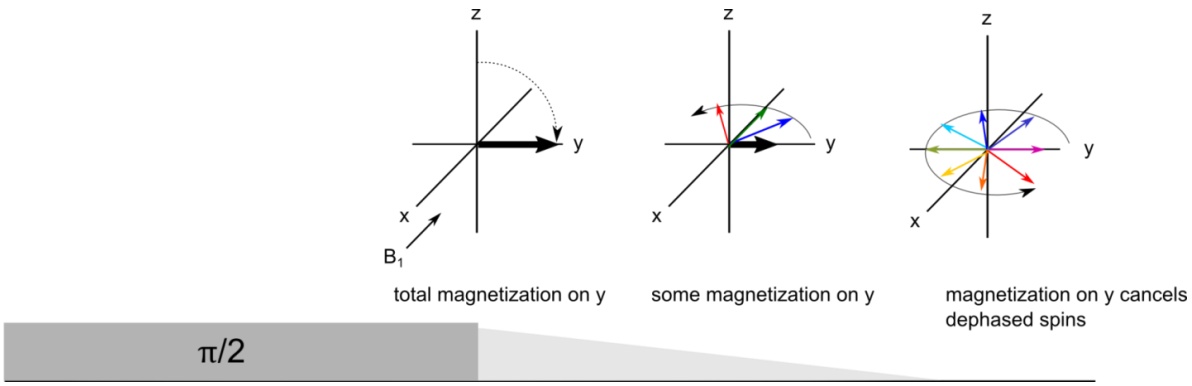

Figure 1.11. An FID is generated by a long π/2 pulse which drives the magnetization to the y axis. Over time, while detecting magnetization along y, the individual spins begin to undergo precession around z. However, the precession frequency of each spin is slightly different due to the slightly different magnetic environment (or effective magnetic field) around each spin. The spins spread out in the xy plane (or dephase). The FID (or decreasing magnetization along y) is detected as it decays and the area integrated to obtain an intensity (which forms the y axis of the pulse EPR experiments described herein).

A signal is detected when the spin magnetic moments precess in the xy plane and add up to a total non-zero magnetic moment. The first type of signal, called free-induction decay detection (FID detection), can be used when an FID is visible after a 90° pulse. As shown in Figure 1.11, after a 90° pulse applied

along x, the spin magnetization is tilted to the y axis. The different precession rates of the electron spins causes the total magnetic moment to steadily decrease in the y direction. This decrease is the FID.

For technical reasons, it is not always possible to detect the FID, usually because it has fully dephased before detection is possible. Because the applied pulses are so powerful in pulse EPR, for a period of time after the pulse ends, no detection can occur while the power fully dissipates. Otherwise the dissipating power would damage the sensitive detector. To remedy this detection problem, echo detection is often employed. This requires two pulses; a 90° pulse followed after a time τ by a 180° pulse as shown in Figure 1.12. The 180° pulse refocuses the dephased magnetic moments of the electrons which realigns the magnetization along –y. This realignment, called a primary echo which is two FIDs back to back, can be detected.

Finally, a second type of echo known as a stimulated echo can be generated with three 90° pulses. The first two pulses are separated by a time τ. The third pulse can be at any time T after the second which will cause an echo to form at a time τ after the third 90° pulse as depicted in Figure 1.12.

With these detection schemes, a typical pulse EPR experiment is collected as either integrated FID or integrated echo intensity as a function of some other experimental variable. In the most basic experiment, the independent variable is magnetic field $\boldsymbol{B}_0$. Detecting FID or echo intensity vs. magnetic field provides the same information as a CW EPR experiment.

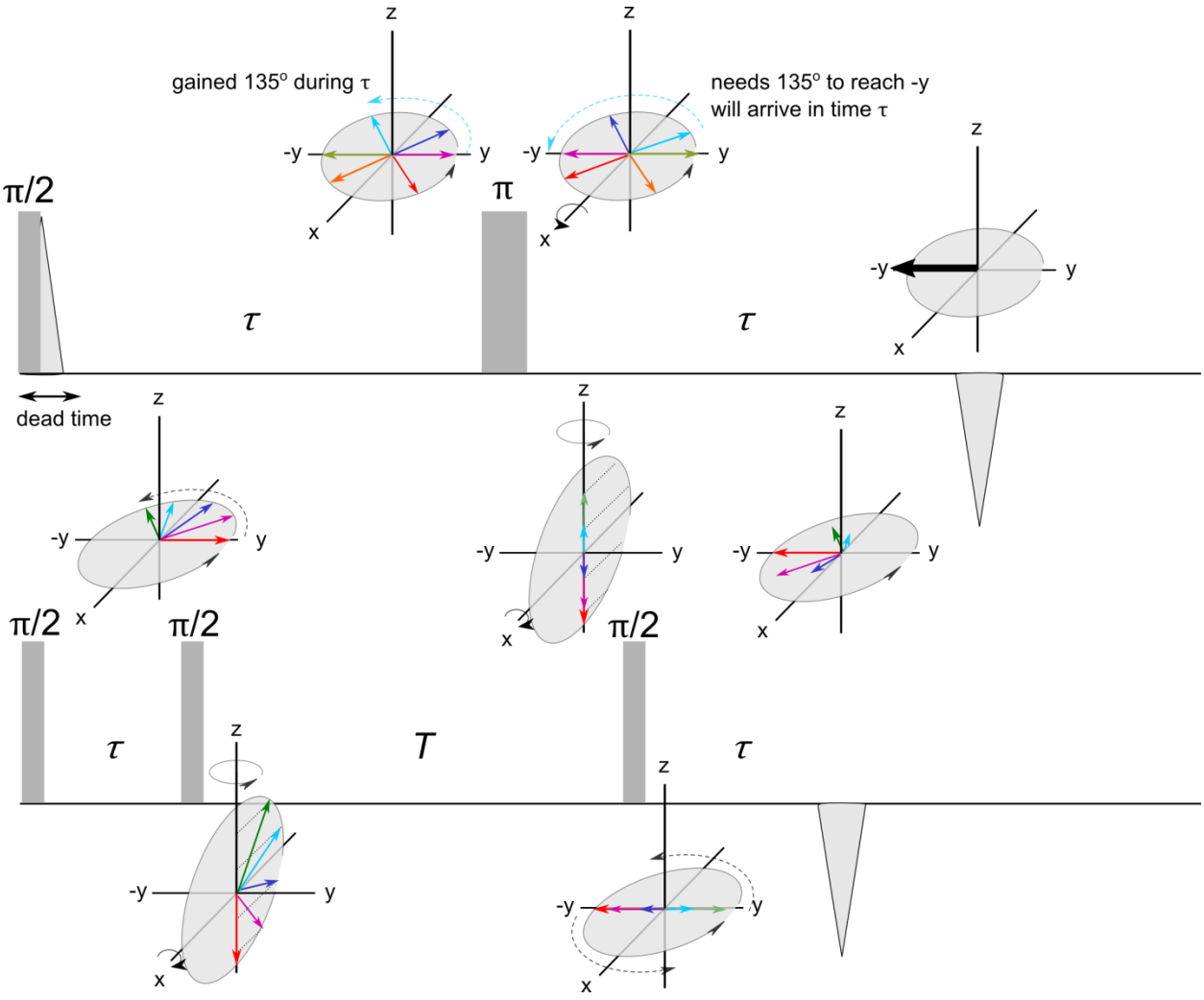

Figure 1.12. Two types of echoes can be generated using either a two-pulse sequence (top) or a three-pulse sequence (bottom). Echoes are used for detecting EPR signals when the FID decays during the dead time of the instrument. *Top*: The two-pulse sequence generates a primary echo. After the first π/2 pulse, the FID decays and the spins continue to precess during the time τ, with different precession frequencies represented by the colors of the arrows in the xy plane. At time τ, when a π pulse is applied, the spins nutate around the x axis by 180°, so that they are all in a mirror image position around x, in the xy plane. After another time τ, the colored spins all refocus along the –y axis where the magnetization is detected. *Bottom*: The three-pulse sequence generates a stimulated echo. In the figure, after the first π/2 pulse the different color spins dephase in the xy plane. At time τ another π/2 pulse nutates the spins 90° around the x axis into the xz plane. During the wait time T of an arbitrary length, the spins continue to precess around z. However, the z or –z component of each spin's magnetization remains constant. When the third π/2 pulse is applied, only the z component of the magnetization is rotated around the x axis such that it is transferred to the y or –y axis. The spins precess around z and after a time τ generate the stimulated echo. (Notice that after τ, the blue and green spin will gather enough phase to reach the second quadrant of the xy plane, the pink and purple spins will have reached the third quadrant, and the slowly precessing red spin will still be along –y).

1.4.4 Measuring relaxation

In other pulse EPR experiments, the magnetic field is held constant and other parameters can be measured. For two basic experiments used to measure relaxation rates, the independent variable is pulse timing. Two types of relaxation occur for electron spins; T_m relaxation, which is relaxation of the magnetization in the xy plane to zero, and T_1 relaxation which is a return of the magnetization to the initial positive z direction. In solid-state EPR, T_m relaxation is always a much faster process than T_1 relaxation. T_m can be measured with the pulse sequence shown in Figure 1.13, which is a two-pulse echo generating sequence where the time τ is varied incrementally. In this pulse sequence, T_m is measured because the spins only spend time in the xy plane.

T_1 is somewhat more difficult to measure accurately, but the pulse sequence shown in Figure 1.14 (used in the experiments described throughout this thesis) can provide a decent approximation. This sequence adds a 180° inversion pulse to the beginning of the detection pulses. The time of detection after the inversion pulse, labeled T, is varied incrementally. During this time, all the spins aligned along –z return to positive z. T typically needs to be incremented out to hundreds of microseconds and potentially milliseconds to capture the full return of the magnetization to positive z.

Relaxation measurements are an important first step in performing other pulse EPR experiments as they reveal the feasibility of performing other, longer experiments for measuring hyperfine coupling. Many experiments are available for measuring hyperfine coupling and the utility of each depends on the information desired from the spin system under study. For instance, as will be described below, during ENDOR experiments a long radio frequency (RF) pulse ($\approx$ 10-50 μs) is applied when electron spins are along the –z axis. If T_1 is fast, the electron spins may relax out of the excited state before the end of the pulse sequence.

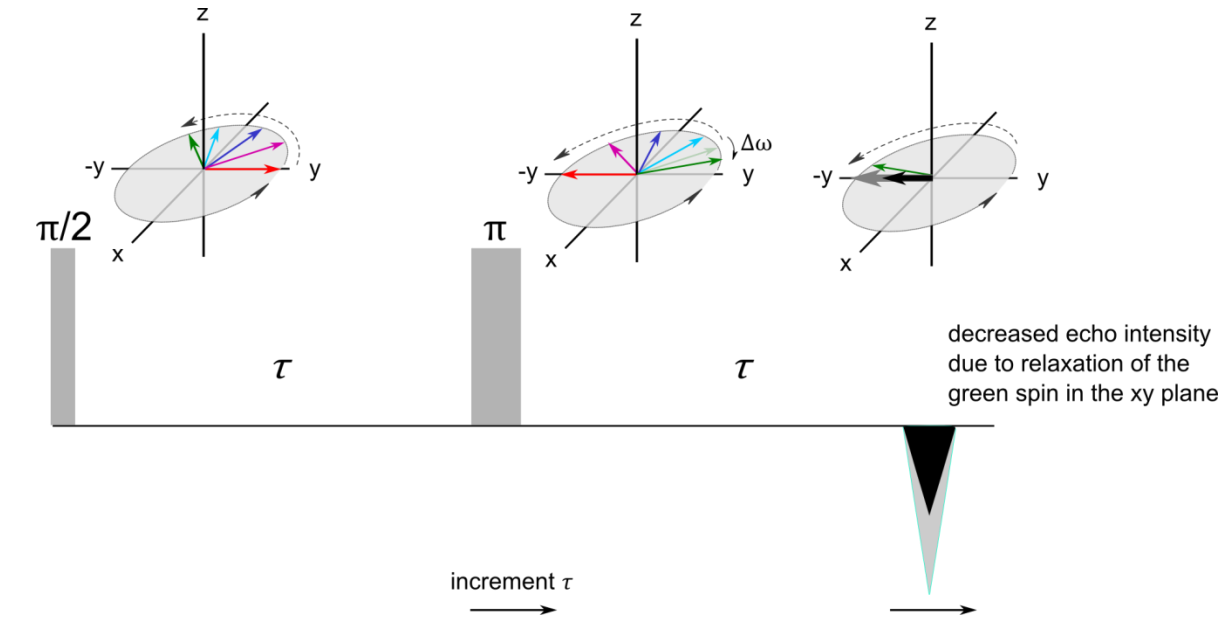

Figure 1.13. The two-pulse ESEEM sequence is the same as the two-pulse echo detection sequence. However, the time τ is incremented which creates an independent x axis, and the echo intensity is measured as a function of the incrementation. The longer the new spacing between pulse becomes the more spin will relax (or change their precession frequency) within the xy plane, as represented by the green arrow which does not fully realign with the total magnetization. This T_m relaxation cannot be refocused by additional π pulses.

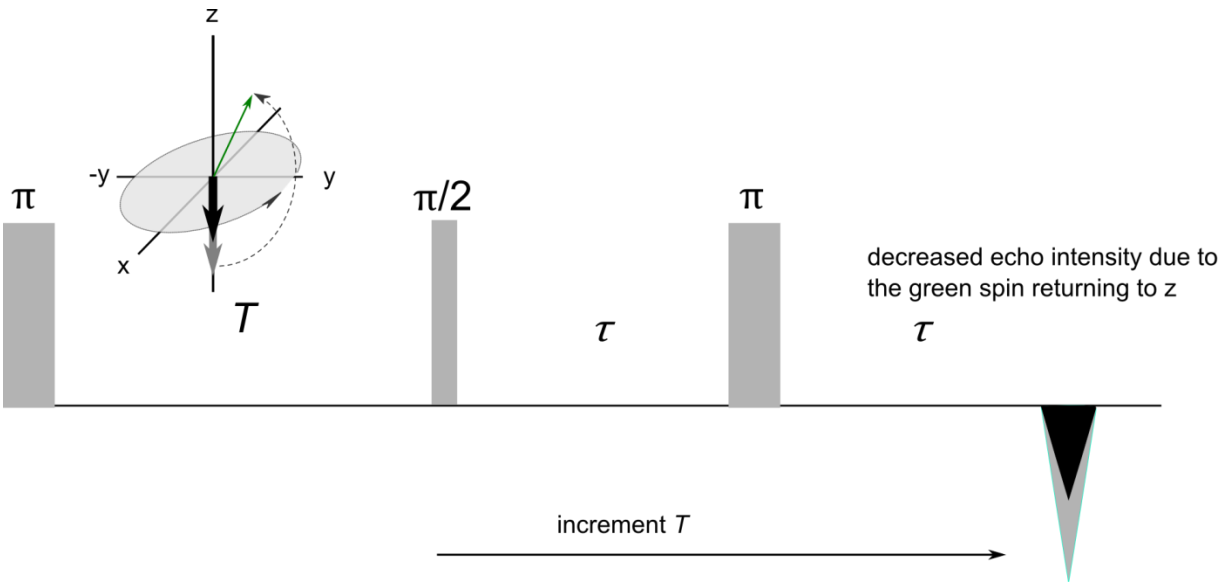

Figure 1.14. In the inversion recovery sequence, the last two pulses are simply a 2-pulse echo detection scheme as described in Figure 1.12 which is used to monitor echo intensity. The first pulse flips the magnetization to the –z axis, and the last two bring any of that magnetization into the xy plane for measurement, always keeping the spacing between these pulses constant. After the first π pulse, there is no precession around z. The time *T* after this pulse is incremented to create an independent x axis, and the echo intensity is measured as a function of the incrementation. However, for very long wait times *T*, some of the spins begin to return to positive z due to T_1 relaxation, and these spins do not contribute to the final echo.

1.4.5 Hyperfine spectroscopy

The pulse experiments used in the work described in this thesis to measure hyperfine coupling generally fall into two categories: those which detect modulation of FID or echo intensity as pulse positions are varied in time, and those which utilize RF radiation to more directly probe nuclear transitions. The former will be discussed first.

Before discussing the sequences used to obtain information about hyperfine couplings, some general expectations can be established. All hyperfine spectra are eventually plotted on a frequency axis in the MHz range. There are three regimes of hyperfine coupling with energy level splittings shown in Figure 1.9; the weak-coupling regime where $|A| < 2|\nu_{Larmor}|$, the intermediate-coupling regime where $|A| \approx 2|\nu_{Larmor}|$, and the strong-coupling regime where $|A| > 2|\nu_{Larmor}|$. In the weak-coupling regime, resonances appear centered around the Larmor frequency of the nucleus and split by the hyperfine coupling, $|A|$. In the strong-coupling regime, the resonances appear centered at $|A|/2$ and split by twice the Larmor frequency. Naturally, in the intermediate regime, the pattern is less easily predicted and intermediate between the two extremes.

ESEEM. Two-pulse and three-pulse electron-spin echo envelope modulation (2P ESEEM and 3P ESEEM, respectively) sequences are one-dimensional experiments where pulse positions are varied in time. 2P ESEEM utilizes the same pulse sequence as that for T_m measurements. As such, during the time incrementation in 2P ESEEM, the spins are always in the xy plane, thus the signal intensity of this experiment decays with T_m. The 3P ESEEM sequence is shown in Figure 1.15. During the time incrementation in 3P ESEEM the spins are in the –z direction so that the signal intensity decays with T_1.

If a nucleus is interacting with the electron through hyperfine coupling, the signal intensity will also oscillate with a frequency that corresponds to the interaction strength. This is called a nuclear modulation, and a vector picture of how this occurs is shown in Figure 1.16. Fourier transformation of this time trace produces a frequency spectrum with peaks from which the interaction strength can be deduced.

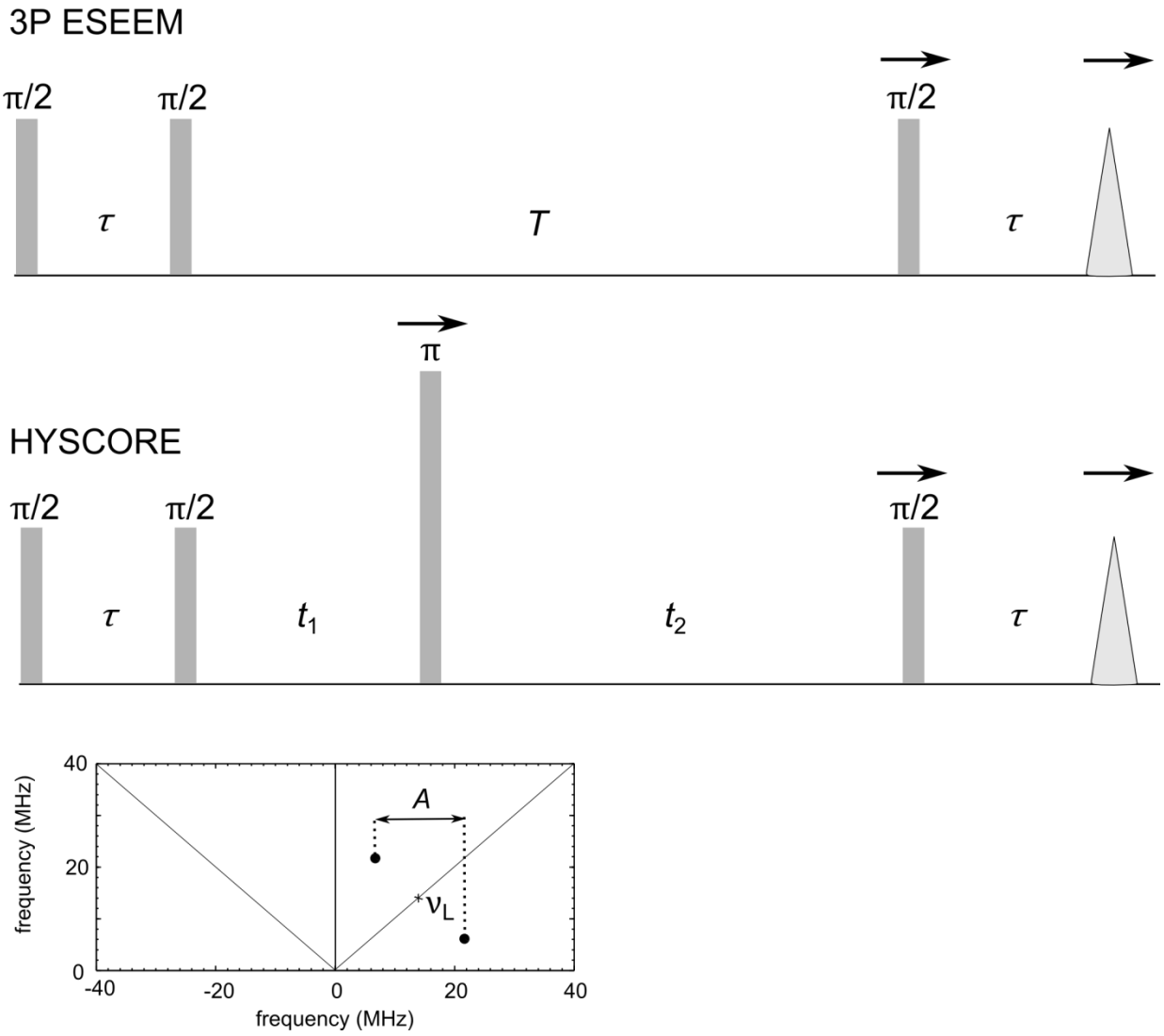

Figure 1.15. *Top*: The three-pulse ESEEM sequence generates a stimulated echo as described in Figure 1.12. However, the stimulated echo intensity is measured as a function of incrementing *T* which affects the last pulse position. During time *T*, the spins have –z magnetization and so relax slowly, according to T_1 relaxation, which decreases the echo intensity with *T* incrementation. In addition to the decrease in intensity, the echo might also be modulated by nuclear coherence which appears at a frequency corresponding to the internal interactions the nucleus experiences (such as hyperfine coupling or quadrupole coupling) and is visualized in Figure 1.16. *Bottom*: In the HYSCORE experiment, the three π/2 pulses generate a stimulated echo which has the same behavior as that generated by the three-pulse ESEEM experiment. However, part way through the wait time *T* (which is divided into t_1 and t_2), an additional π pulse is applied that changes the nuclear coherence (or modulation). In this way, a nucleus precesses during the experiment with the electron in both the α and β state. 2D Fourier transformation of this results in off diagonal elements of the 2D frequency spectrum that correlates nuclear frequencies from the two electron spin manifolds and reveals interactions such as hyperfine and quadrupole coupling. A representative HYSCORE spectrum is shown. In the first quadrant, along the diagonal will be the nuclear Larmor frequencies. Symmetrically about the Larmor frequency will be features due to hyperfine coupling, *A*.

HYSCORE. A disadvantage of the ESEEM experiments is that the Fourier transformed resonances appear in one dimension and sometimes overlap substantially, making identification as well as assignment of features in the spectrum difficult. By using a two-dimensional experiment where time incrementation occurs at two positions in the pulse sequence, a 2D Fourier transformation can be carried out along both dimensions. This spreads the resonances out in a predictable manner. Hyperfine sublevel correlation (HYSCORE) spectroscopy is commonly utilized for this purpose and the pulse sequence is shown in Figure 1.15. This sequence is the same as the 3P ESEEM sequence with an additional 180° pulse between the second and third pulse. This additional pulse transfers nuclear coherence between the electron spin-up and -down manifolds so that the 2D frequency domain spectrum has off-diagonal elements symmetrically split around the diagonal as shown in Figure 1.15. These correspond to hyperfine coupling of the nucleus. All of the hyperfine experiments that depend on nuclear modulation are most efficiently driven when the hyperfine coupling is in the intermediate-coupling regime.

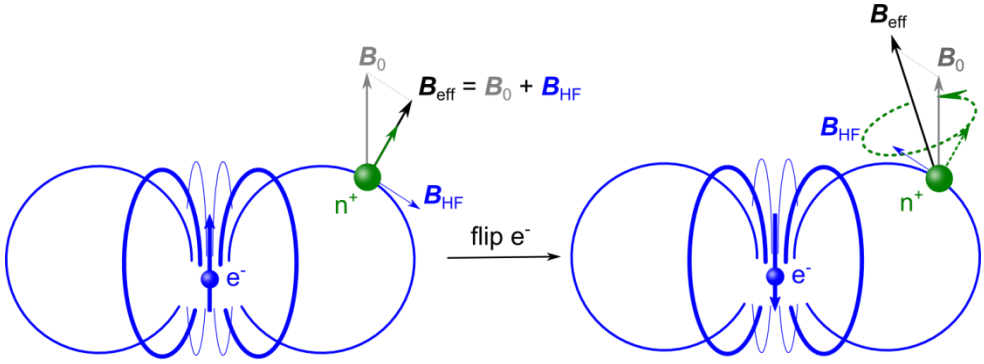

Figure 1.16. A vector picture description of nuclear modulations. A nucleus in an externally applied magnetic field ($\boldsymbol{B}_0$) interacting with an electron through hyperfine coupling ($\boldsymbol{B}_{HF}$) experiences a total effective field ($\boldsymbol{B}_{eff}$). The nuclear spin aligns with $\boldsymbol{B}_{eff}$. When the direction of the electron spin is suddenly changed (by a π pulse), the direction of $\boldsymbol{B}_{eff}$ is changed. The nucleus, because it is spinning, will undergo gyroscopic precession around the new $\boldsymbol{B}_{eff}$. From the electron's point of view, the nucleus is now a wiggling magnet which changes the local field at the electron. This affects the electron's precession frequency and therefore whether or not the full magnetization realigns along –y to produce the stimulated echo. An additional flip of the electron spin, such as during the HYSCORE experiment, once again changes the direction of $\boldsymbol{B}_{eff}$ and causes the nucleus to precess on a cone around the new $\boldsymbol{B}_{eff}$. The electron experiences the nucleus wiggling at two different frequencies, the difference of which corresponds to the hyperfine coupling.

ENDOR. In a second class of experiments used for measuring hyperfine coupling (known as electron nuclear double resonance or ENDOR), RF radiation in the MHz range is directly applied to the system to excite nuclear transitions. Two types of ENDOR sequences have been used for the experiments described in this thesis; Davies ENDOR and Mims ENDOR. The Davies ENDOR pulse sequence is shown and described in Figure 1.17, and the Mims ENDOR pulse sequence is shown and described in Figure 1.18. In these experiments, the independent variable is frequency of the RF pulse. The dependent variable is echo intensity, which is decreased when a nuclear transition is excited as depicted in Figure 1.17. Both of these experiments are constant in time and generally the echo is detected 15-50 μs after the initial excitation pulse. As such, these experiments are most efficient when T_1 is on the order of hundreds of microseconds.

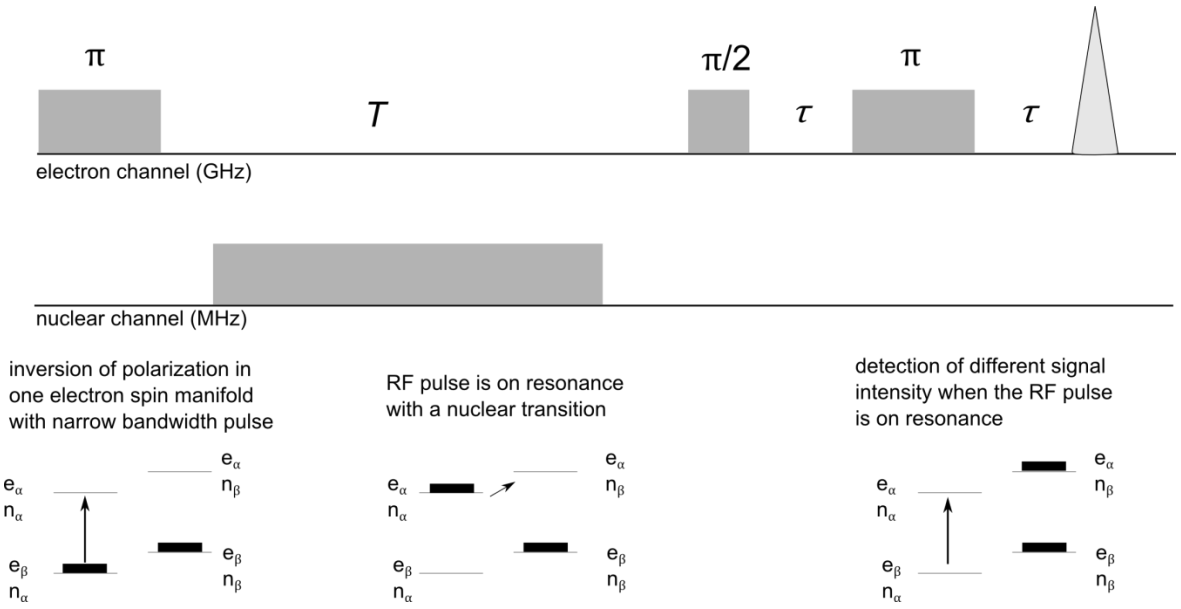

Figure 1.17. The Davies ENDOR pulse sequence shown above utilizes a primary echo detection scheme (the last two pulses). In addition, there is an initial inversion pulse which makes this sequence resemble the inversion recovery experiment. However, no timings in between pulses are changed in this experiment. Instead, a radio frequency pulse is applied during the time *T* which directly flips nuclear spins. The frequency of the RF pulse is changed to create the x axis in an ENDOR experiment. This experiment is best understood by following the population transfer diagram below the sequence. One electron manifold is excited by the first π pulse and population is transferred to this new state. If an RF pulse is on resonance with this newly filled e_α/n_α state, the population will again be moved over to the e_α/n_β state. When the final detection pulses are used to probe the initial spin manifold, there is a reduction in the echo intensity. It is important that only one electron spin manifold is excited in this experiment for the difference in echo intensity to be observed. This is why Davies ENDOR is performed with long, narrow-bandwidth pulses.

Figure 1.18. The Mims ENDOR experiment utilizes a stimulated echo for detection. Again, in this ENDOR experiment, no changes are made to the pulse timings. Instead, an RF pulse is applied to directly excite nuclear transitions. Flipping a nuclear spin changes the precession frequency of a coupled electron during the second time τ and prevents all the electron spins from completely rephasing for the stimulated echo. As a result, the echo intensity is reduced, depending on the frequency of the applied RF pulse.

EDNMR. A last experiment utilized here for hyperfine measurements is ELDOR (electron double resonance) detected nuclear magnetic resonance (EDNMR). The pulse sequence is shown in Figure 1.19 and utilizes a high turning angle (HTA) microwave pulse to drive forbidden transitions that involve both an electron spin and a nuclear spin flip (double-quantum or zero-quantum transition). The microwave frequency of the HTA pulse is swept symmetrically around the detection frequency and spectra are always plotted as function of the difference between HTA frequency and detection frequency. This creates a horizontal axis in MHz equivalent to an ENDOR experiment. This experiment is best for large hyperfine couplings or nuclei with large Larmor frequencies because when the HTA frequency equals the detection frequency, a broad blind spot appears, the width of which is usually around 40 MHz (depending on detection bandwidth). Any nuclei that resonate under this blind spot are not well-resolved. However, strongly coupled nuclei (such as ^{55}Mn) or nuclei with large Larmor frequencies (^{1}H at 33 GHz) will resonate outside of this signal.

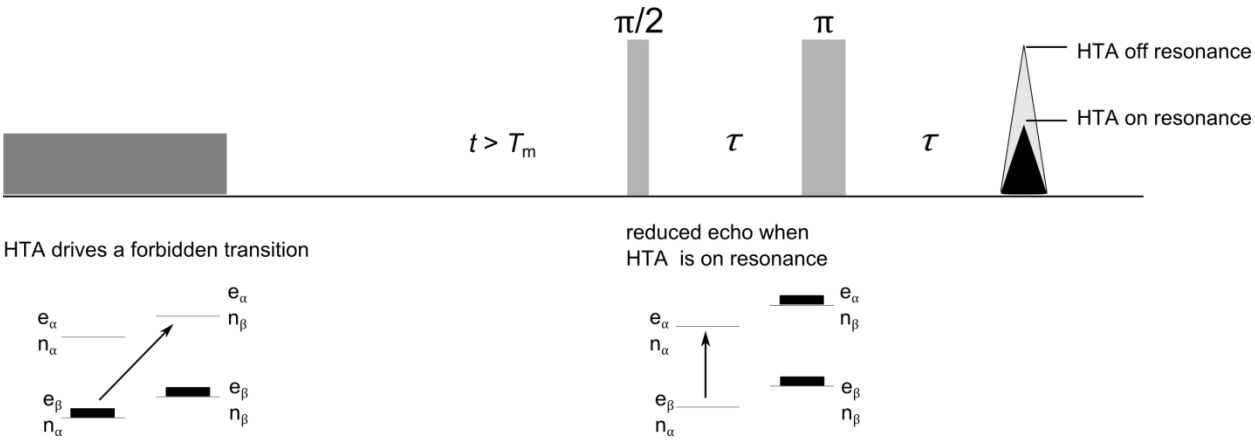

Figure 1.19. The EDNMR experiment utilizes two channels of microwave radiation. The detection scheme shown above utilizes a two-pulse primary echo. Before the detection, a long high turning angle (HTA) pulse is applied which drives forbidden transitions (i.e. both an electron spin and nuclear spin transition from $e_\beta/n_\alpha \rightarrow e_\alpha/n_\beta$). The frequency of this HTA pulse is varied to create the x axis in this experiment.

1.4.6 Tau blind spots

Pulse sequences that rely on generating stimulated echoes with three 90° pulses (3P ESEEM, HYSCORE, and Mims ENDOR) suffer from τ blind spots. In the frequency domain, these blind spots manifest as suppressions of the signal intensity at frequencies $n/(m_s\tau)$ where n = 0, 1, 2, ... Because of this, these experiments are usually recorded at multiple τ values and averaged together to eliminate these blind spots.

1.5 References

(1) Morton, J. R.; Preston, K. F. *J. Magn. Reson.* **1978**, *30*, 577.
(2) Bender, C. J.; Sahlin, M.; Babcock, G. T.; Barry, B. A.; Chandrashekar, T. K.; Salowe, S. P.; Stubbe, J.; Lindstrom, B.; Petersson, L.; Ehrenberg, A.; Sjöberg, B.-M. *J. Am. Chem. Soc.* **1989**, *111* (21), 8076.
(3) O'Malley, P. J.; Babcock, G. T. *J. Am. Chem. Soc.* **1986**, *108* (14), 3995.
(4) McConnell, H. M.; Chesnut, D. B. *J. Chem. Phys.* **1958**, *28* (1), 107.

Chapter 2

Redox properties of tryptophan

Abstract

Organic radicals, especially on amino acids, play import roles shuttling electrons and performing redox chemistry in enzymes. The microenvironment surrounding the organic radicals is believed to have a profound effect on their redox properties and therefore reactivity. Using a model peptide system, we have studied how making point mutations to the sequence affects the magnetic properties and the redox properties of the redox active amino acid tryptophan.

Contributions

The Andersen Group at the University of Washington has been instrumental in teaching our group peptide synthesis, purification, and the appropriate NMR experiments for characterizing these peptides' structures. In particular we would like to thank Jordan Anderson, Aimee Byrne, Brandon Kier, and Kalkena Sivanesam. In addition, there have been two very helpful undergraduates in the Stoll group working on this project. Thao H. Nguyen synthesized peptides, including some of the deuterated versions, and helped with NMR assignments. In addition, she helped design some of the *in situ* EPR electrochemistry experiments. Timothy Welsh synthesized peptides and performed the differential pulse voltammetry experiments.

Publications

This work is currently unpublished.

2.1 Background and Motivation

The existence of tryptophan radicals in the active sites of enzymes has been known for some time; however, the role of the protein environment in tuning the physical characteristics of these radicals

remains incompletely understood.[1] Elucidation of the mechanisms of electron transfer in proteins will depend on understanding the influence of the microenvironment in tuning redox chemistry of aromatic amino acids.[2]

Tryptophan radicals play mechanistic roles in the protein families of cryptochromes,[3,4] photolyases,[5] and peroxidases.[6] It is less well understood if tryptophan plays a mechanistic role, but the radical has also been observed in ribonucleotide reductase, an enzyme essential to DNA synthesis. In the cryptochromes and photolyases, tryptophan works as an electron shuttle. Cryptochrome proteins control the effects of blue light on plant development and the circadian rhythms of mammals while DNA photolyases repair DNA that has been damaged by UV radiation.[3,5,7] Both families are activated by UV light which excites a flavin cofactor (either FAD or $FADH^{-}$, respectively). The excited flavin is reduced by a nearby tryptophan residue. This produces a tryptophan radical with an electron hole that is rapidly shuttled away from the enzyme active site through the oxidation of two additional tryptophan residues.[4] The three tryptophan residues in this triad act as an electron transfer shuttle, however tryptophan residues can also directly participate in the chemical transformations such as in peroxidase enzymes, including versatile, lignin, manganese, and cytochrome c peroxidases. Generally, the peroxidase enzymes consist of an Fe^{III}(heme) active site and carry out oxidations of a wide range of substrates. The initial oxidation occurs when H_2O_2 reacts with the enzymes in a two electron oxidation. This produces an oxidized Fe^{IV}=O species and a porphyrin π-cation radical. However, in several classes of the enzyme including lignin, cytochrome c, and versatile peroxidases the π-cation radical is replaced with a tryptophan radical. These enzymes catalyze the oxidative breakdown of plant cell wall materials (lignin), oxidize other macromolecules (cytochrome c), and oxidize metals such as manganese, respectively, with the tryptophan radical playing a key role in the reactivity. Depending on the environment and the role of the tryptophan radical in the enzyme, it can be present as either the cation radical or the deprotonated neutral radical (shown in Scheme 2.1). For instance, in the electron transfer chain of the cryptochromes and photolyases, the first two tryptophan side chains are oxidized to the cation radical. Electron transfer is so rapid that it is not until the third, solvent exposed tryptophan residue in the triad that it deprotonates to the neutral radical.[8,9]

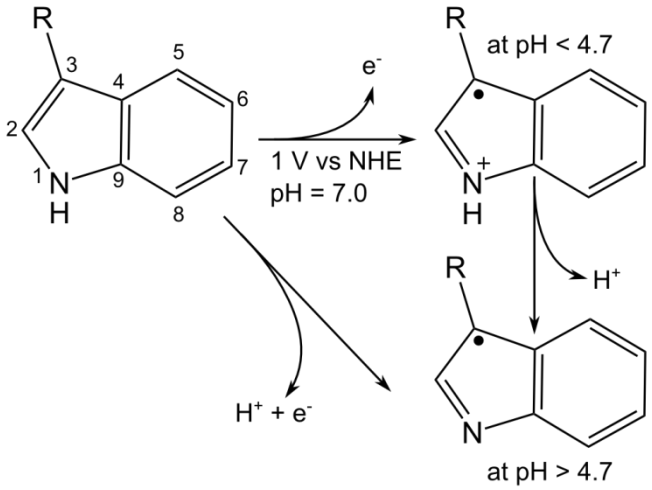

Scheme 2.1. Oxidation and deprotonation of L-tryptophan. The redox potential (1 V vs NHE) and pK_a (4.7) of the oxidized side chain have been suggested to depend on the microenvironment around the tryptophan residue.

As researchers' understanding of tryptophan and other redox active amino acids has increased, they have begun reengineering enzyme active sites that include tryptophan radicals to perform certain chemical reactions. For instance, incorporation of tryptophan residues into azurin has been observed to increase electron transfer rates.[10] Researchers have also redesigned a peroxidase enzyme to include tryptophan in a negatively charged microenvironment (which mimics the highly oxidizing lignin peroxidase active site). They found the microenvironment was important for tuning the reduction potential of tryptophan up to 1.4 V at pH ≈ 3-4, well above 1.15 V reported for L-tryptophan in solution at pH ≈ 2 (vs. NHE).[11,12]

Currently, tryptophan radicals are being studied by a number of methods, including UV and visible resonance Raman spectroscopy,[13–15] picosecond transient absorption,[10] fluorescence,[16] and electron paramagnetic resonance spectroscopies.[6,17–19] However, current literature lacks a systematic and controlled comparison of the spectroscopic and physical characteristics of structurally similar, yet environmentally unique tryptophan radicals, which the work reported here aims to provide. Control of the protein environment is accomplished using model peptide systems. Continuous-wave and pulse EPR spectroscopy as well as electrochemistry are used as central tools in understanding the redox properties of tryptophan. In this study, there are two goals:

1. The first goal is to map the changes in spin density on the tryptophan indole ring as the microenvironment changes. This is probed by measuring hyperfine couplings with various EPR techniques. The measured hyperfine couplings can then be related to spin density on the indole ring through some well-understood relationships described below.
2. Second, it is interesting to determine the redox activity of tryptophan in the different microenvironments as well as determine if certain microenvironments promote different pK_as for oxidized tryptophan, therefore stabilizing the cation radical at different pHs. This goal is readily explored with electrochemistry, whereby measuring the redox potential of tryptophan in the various peptides at different pHs, a Pourbaix diagram that reveals the pK_a of oxidized tryptophan can be constructed.

While the model peptide systems are not inherently involved in the redox chemistry of an enzyme active site, studying tryptophan radicals in a controlled environment has several benefits. In an enzyme, organic radicals are often seen in an EPR spectrum but identifying their origin can be difficult when many redox-active residues (including multiple tryptophan or tyrosine residues) are known to be present. Controlled studies may help in radical identification in more complicated systems. Once a radical is identified in an enzyme active site, researchers often want to understand what microenvironment the radical experiences and correlate this with the observed reactivity. Understanding the influence of the microenvironment on EPR properties before trying to identify these properties in a complicated system may lead to more quantitative and robust conclusions. In a small model system, the limits of microenvironment influence may be tested and aid in the design of better artificial electron transfer and redox active enzymes based on intelligent design of the active site.

2.2 EPR theory for the neutral, H-bonded, and cation tryptophan radical

In this section, the relationship between properties measured with EPR spectroscopy, such as the *g* tensor and hyperfine coupling, and electronic and geometric structure of tryptophan cation and neutral radicals will be described. Examples of measured EPR properties from the literature are given in Table 2.1.

Table 2.1. ^{1}H and ^{14}N hyperfine coupling in mT (xx, yy, zz, iso), *g* values, and carbon spin populations (ρ) in trp radicals [a,b,c]

		Hβ(proS)	Hβ(proR)	H5	H7	N	H2	H-bond to N	*g*
versatile peroxidase[6] neutral radical	xx	2.35	1.13	-0.64	<0.15	<0.15	0.28	-0.1	2.00352
	yy	2.75	1.13	<0.15	-0.62	<0.15	-0.04	0.19	2.00255
	zz	2.7	1.18	-0.49	-0.46	1	-0.11	-0.07	2.0022
	ρ	0.52		0.17	0.15	0.2	<0.05		
versatile peroxidase[19] neutral radical	xx	2.15	1.75	-0.64	<0.15	<0.15			2.0035
	yy	2.3	1.95	<0.15	-0.62	<0.15			2.0025
	zz	2.3	1.95	-0.49	-0.46	1.05			2.0022
E.coli RNR trp 111[17] neutral radical	xx	2.7	1.38	-0.68	<0.1	<0.15		-0.1	
	yy	2.75	1.38	<0.1	-0.61	<0.15		0.19	
	zz	2.83	1.38	-0.5	-0.51	1.05		-0.07	
azurin trp 108[14] neutral radical	xx	1.15	0.21	-0.6	<0.1	<0.1		-0.12	2.00355
	yy	1.43	0.15	-0.21	-0.79	<0.1		0.19	2.00271
	zz	1.19	0.23	-0.48	-0.42	1.04		-0.08	2.00221
	ρ	0.45		0.17	0.17	0.19			
azurin trp 48[14] neutral radical	xx	0.9	0.66	-0.71	-0.18	<0.1			2.00355
	yy	0.87	0.73	-0.18	-0.39	<0.1			2.00271
	zz	0.74	0.5	-0.29	-0.49	1.18			2.00221
	ρ	0.5		0.16	0.14	0.22			
[6]cytrochrome *c* peroxidase[20] cation radical	iso	0.46	0.75				0.53	0.57	
	ρ	0.41				0.14	0.35		

[a] The ^{1}H hyperfine coupling principle values (xx, yy, and zz) or the isotropic (iso) component are provided
[b] The ^{1}H numbering follows the carbon numbering in Scheme 2.1
[c] Spin population is provided for carbons 2, 5, and 7 based on α proton hyperfine coupling, for carbon 3 based on β proton coupling, or for nitrogen following the equations in section 2.2.2

2.2.1 Changes to the *g* tensor

Based on experimental and calculated EPR properties of the tryptophan cation radical ($TrpH^{\bullet+}$), the hydrogen-bonded neutral tryptophan radical ($TrpN^{\bullet}$---H), and the neutral tryptophan radical ($Trp^{\bullet}$) in the

literature there are several trends expected for the magnetic properties as the tryptophan indole ring nitrogen becomes protonated.

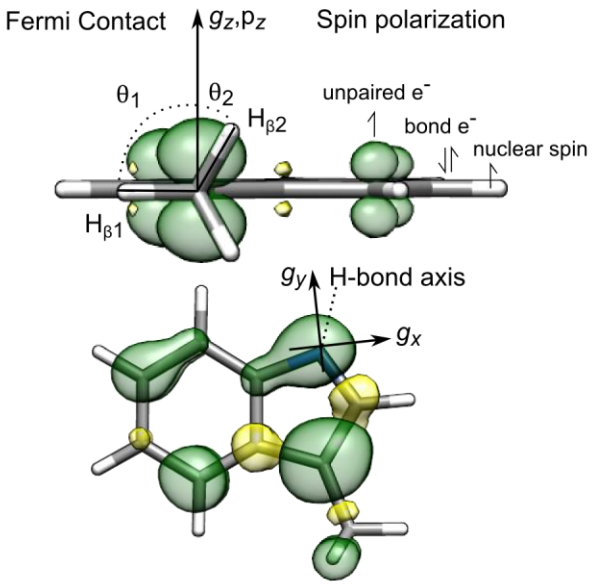

Figure 2.1. The Fermi contact and spin polarization mechanisms which lead to hyperfine coupling of the C_β protons and indole ring protons of tryptophan, respectively. *Top:* A strong Fermi contact interaction occurs if a β proton can contact the molecular orbital in which the unpaired electron sits ($H_{\beta 2}$) and a weak interaction occurs when the proton is in the same plane as the node of the orbital ($H_{\beta 1}$). Spin polarization occurs when the unpaired electron forces one of the nearby electrons in a C-H bond (i.e. an electron in a different spatial orbital) to align parallel (Hund's rule). This in turn causes the other electron in the bond, which is further from the unpaired electron and closer to the ^{1}H nucleus, to align antiparallel (Pauli exclusion principle). This creates a small increase in the population of spin down electrons in a bonding orbital with ^{1}H s character close the nucleus. *Bottom:* A depiction of the direction of *g* tensor axes in tryptophan. The g_x value, with axis perpendicular to an H-bonding interaction or covalent N-H bond, will depend most significantly on the protonation state of the indole nitrogen.

First are shifts in the g_x component of the *g* tensor. As shown in Figure 2.1, the g_z component of the tensor lies perpendicular to the plane of the indole ring, g_y lies approximately along the NH bond, and g_x lies perpendicular to g_y. Simply looking at the structure, it is apparent that the N of the indole ring will have axial symmetry when the NH bond is present resulting in a more axial *g* tensor and similar values for g_x and g_y. Removal of the covalent bond (and therefore the axial symmetry) is expected to make the principal components of the *g* tensor more rhombic and high-field EPR experiments have shown the g_x value to increase upon removal of hydrogen bonding to the indole nitrogen.[21] This can also be understood based on the spin-orbital contributions to the *g* shifts as was discussed in Chapter 1. The g_x

value will be shifted by H-bonding interactions because these will occur in the plane approximately perpendicular to g_x. The *g* shift is inversely proportional to the energy difference between the ground state and the excited state within this perpendicular plane.[22] In the case of the tryptophan radical with the ground state approximated as the nitrogen p_z orbital, the excited state occurs when the nitrogen p_y orbital is half-occupied. The ground state non-bonding p_y orbital is stabilized in energy (lowered in energy) by a bonding interaction. This makes the transition energy into the half-occupied p_y state larger (increase in $\Delta E = E_{G.S.}\text{-}E_{E.S.}$) and the inversely proportional g_x shift smaller.

2.2.2 Changes in hyperfine coupling values reflect changes in spin density distribution

In addition to the *g* tensor, the nuclear hyperfine coupling constants are expected to change with the protonation state of the indole nitrogen. This occurs because protonation or deprotonation of the indole ring N changes the spin density distribution of the unpaired electron on different carbons in the indole ring. Generally, the more concentrated the spin density at a particular carbon or nitrogen, the stronger the hyperfine coupling of the proton which is covalently bound. One expects spin density to be largest on N1 and C3 with C5 and C7 having smaller spin density based on the resonance structures that can be drawn for $Trp^{\bullet}$. As the N1 becomes protonated, going from $Trp^{\bullet}$ to $TrpH^{\bullet+}$ it has been shown that spin density generally decreases on N1 and C3, while increasing on C2. In addition, the spin density tends to move away from the five-membered ring and spread more evenly onto the whole indole side chain. [23–25]

Changes to the N hyperfine coupling. The nitrogen will follow the simple trend of decreased hyperfine coupling strength as the spin density on the nitrogen decreases (i.e. if the tryptophan radical is protonated). This should lead to an observable change in the hyperfine coupling of the nitrogen which can be probed with techniques such as ^{14}N ESEEM and HYSCORE using X-band pulse EPR and CW EPR if the linewidth is sufficiently narrow.

As discussed in Chapter 1, the isotropic and anisotropic components of the hyperfine coupling can be used to determine the spin density at the 2s and 2p orbitals of the nitrogen, respectively. Spin population is expected to change from ≈ 0.14 to ≈ 0.2 upon deprotonation of the indole ring.

Changes to α and β proton coupling. The hyperfine coupling strength is known to depend on spin density through two simple relationships. First, the hyperfine coupling of the ring protons (at C2, C5, C6, C7, and C8) will follow equation 2.1.

$$A_{\mathrm{iso}} = Q\rho \qquad \text{Eq. 2.1}$$

Here *A* is the hyperfine coupling, *ρ* is the spin population, and *Q* is an empirical constant equal to -2.48 mT.[17,26] The ring proton couples to spin density on a covalently bound carbon through spin polarization (shown and explained in Figure 2.1).

Second, the hyperfine coupling strength of the Cβ protons ($H_{\beta1}$and $H_{\beta2}$) will depend on the spin population at C3 and the dihedral angles $C_2{-}C_3{-}C_\beta{-}H_{(\beta1\text{ or }\beta2)}$ through equation 2.2.

$$A_{\mathrm{iso,H1,H2}} = \rho_{\mathrm{C3}} B \cos^2\theta_{1,2} \qquad \text{Eq. 2.2}$$

Here *A* is the isotropic hyperfine coupling, *ρ* is the spin population at C3, *B* is an empirical constant (5 mT = 140 MHz for the neutral radical and X mT for cation), and θ is the angle from the z axis of the molecule (perpendicular to the ring plane) and the projected $C_\beta{-}H_\beta$ bond (Figure 2.1).[27,28] The β-protons couple to spin density on C3 through Fermi contact coupling. This contact term increases as the protons are brought into close proximity to the molecular orbital which holds the unpaired electron. The highest-energy occupied molecular orbital in the tryptophan radical is a π system with spatial components above and below the ring. As the dihedral angle C_2-C_3-C_β-$H_{(\beta1\text{ or }\beta2)}$ approaches 90° (and θ approaches 0°) the hyperfine coupling of the β-protons grows larger.

Using equation 2.2, an approximate spin population ρ_{C3} of 0.55, and the angles θ of 43° and 75° from the NMR structure of TC16bP12W (pdb 2M7D), the expected isotropic hyperfine couplings of the C_β protons in the trp-cage peptides are 40 MHz and 5 MHz, respectively.

Coupling of proton associated with indole nitrogen. If a hydrogen bond donor is interacting with the indole nitrogen, the proton will be weakly coupled and the hyperfine coupling can be approximated with the point-dipole approximation as in equation 2.3[17]

$$A^H(\theta) = \frac{\mu_0}{4\pi}\mu_B\mu_N g_e g_N \sum_i \frac{1}{r_i^3}\rho_i(3\cos^2\theta_i - 1) \qquad \text{Eq. 2.3}$$

where *i* is the index over all nuclei which have substantial spin population (ρ), r_i is the distance between the coupled proton and nucleus *i* in meters, and θ_i is the angle between the applied magnetic field and the vector connecting the electron and proton. The constants take their usual values for the permeability of free space, the Bohr magneton, the nuclear magneton, the electron *g* value, and the nuclear *g* value to give the coupling strength in Joules. For this calculation the spin population ρ is typically assumed to be mainly on the nitrogen and C_3.

For the cation radical, an isotropic coupling due to spin polarization through the covalent N—H bond will also be present, similar to the mechanism discussed above. However, when protonation of the nitrogen increases the spin population on C2, the through-space dipole interaction between the proton and the spin population on C2 and C3 is significant enough to contribute to the measured hyperfine coupling.[20,29] This effect will become even stronger for the fully protonated $TrpH^{\bullet+}$. Typical spin population and hyperfine coupling values are summarized in Table 2.1.

2.2.3 Motivation for electrochemistry experiments

The protein microenvironment has been reported to exhibit profound effects on pK_a and reduction potentials of tryptophan radicals resulting in the variety of electron transfer and catalytic roles they can play in biology. An estimation of the pK_a can be made with Pourbaix diagrams; a plot of redox potential vs. pH. In these plots, at pHs above the pK_a of oxidized tryptophan, the redox potential should decrease linearly with increasing pH as the oxidized tryptophan side chain deprotonates. At the pK_a and lower pHs, the redox potential will become independent of solution pH, indicating formation of the cation radical. Previous reports have found the pK_a of $TrpH^{\bullet+}$ to be 4.7, within the range of biologically relevant pHs.[11] Interestingly, tryptophan pK_a values lower than 4 have been reported in the blue copper protein

azurin[13] and in lysozyme[30] which are attributed to protein microenvironment. Obviously, these measurements will also provide a direct measure of the redox potential of tryptophan in different microenvironments.

2.3 The trp-cage peptide model system

Systematic control of the protein microenvironment is accomplished using trp-cages and β-hairpins, two tryptophan-containing model peptide systems that have been previously characterized for structure and folding stability by the Andersen group at the University of Washington Chemistry Department. Motivation for using model peptides stems from the achievable level of control over the microenvironment. Studying the oxidation of tryptophan in a distinct microenvironment using either EPR spectroscopy or electrochemistry requires a similar set of prerequisites which can be found in either of these systems. These prerequisites include:

1. fold stability upon point mutations that significantly alter the tryptophan microenvironment without disrupting the backbone geometry
2. similar fold stability across a wide range of pH values
3. lack of other redox active side chains (especially tyrosine, methionine, and cysteine)

The trp-cage and β-hairpin systems (Figure 2.2 and A2.1) offer such properties, making them good candidates for these studies. Below I outline the design of these systems (performed by many members of the Andersen group), including the milestones which led to understanding the important structural features for fast and stable folding. I will discuss how I have used the previous data to make and characterize several new peptide constructs which fit the prerequisites for my studies outlined above. The results of subsequent EPR and electrochemical measurements on trp-cage peptides are presented in the main text that follows. Similar information is given in the Appendix Section A2.1 for the β-hairpin peptides.

2.3.1 Chemical shift deviations measured by 2D NMR for structure determination

The structure and the folding percentage of the peptides is determined by 2-dimensional NMR spectroscopy. With the TOCSY and NOESY pulse sequences, the resonances of nearly all protons in the system can be assigned relative to an internal standard 4,4-dimethyl-4-silapentane-1-sulfonic acid (DSS, resonance set to 0 ppm) (see 2.3.2 Methods for experimental details). Large chemical shifts occur when the electron density near a magnetic nucleus (^{1}H in all cases in these studies) is reduced. The magnetic field induced in the electron density opposes the externally applied magnetic field so that in a lower electron density environment the nucleus feels an overall larger field and resonates at higher frequencies. Therefore, all amino acids have distinct chemical shifts when they are in an unfolded or random-coil structure (δ_{rc}). The residues in a completely unfolded peptide (0 % folded) will have chemical shifts equal to the random coil values which have been established.[31–33]

When a peptide folds, the electron density in the peptide is shifted due to features such as H-bonding or when ^{1}H nuclei come into proximity of the ring currents induced in aromatic amino acids. This leads to deviations away from random-coil chemical shifts or chemical shift deviations (CSDs) defined as CSD = δ_{obs} - δ_{rc}. The largest deviations will occur when the peptide is 100 % folded. However, determining when a peptide is 100 % folded is not obvious and the CSDs for a 100 % folded construct can evolve as more stable constructs are designed. This is because when a peptide folds fast on the NMR time scale, a two-state model of folding (folded ⇌ unfolded) is valid. In this case, the measured chemical shifts are a weighted average of the folded and unfolded proton resonances. In the case of the trp-cage, fold melting experiments performed with NMR, circular dichroism, and temperature-jump fluorescence monitoring showed the original trp-cage folds in about 4 μs.[34,35] Since then, many different trp-cage constructs have been shown to begin folding in the N-terminus helix with simultaneous or subsequent cage formation followed by H-bond and salt-bridge formation in the 0.9 – 7.5 μs range validating the two-state model.[36] In the case of the trp-cages used in these studies, the CSDs for 100 % folding are assigned from a cyclized trp-cage covalently pinned at the N and C termini.[37]

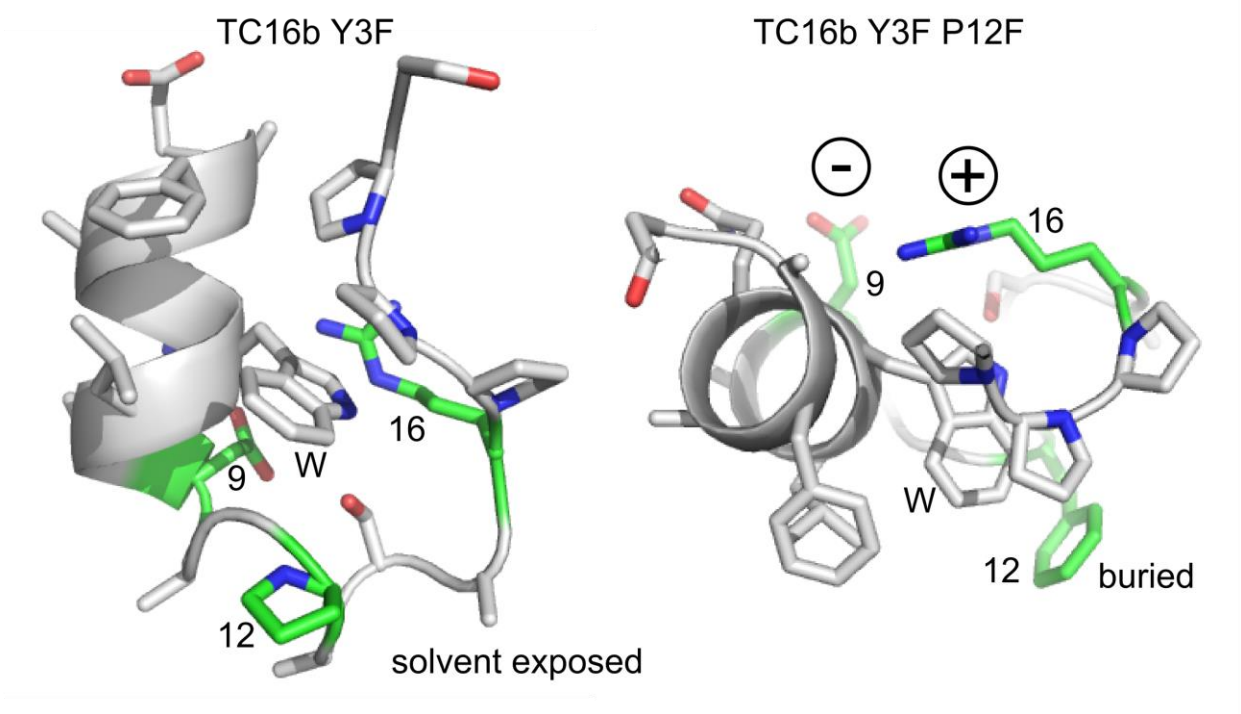

Figure 2.2. Structure of the trp-cage peptide motif developed by the Andersen group with the 9th, 12th, and 16th residues, which were mutated for the studies herein, highlighted in green. *Left:* Side view showing a charged solvent-exposed environment around tryptophan. *Right:* Top down view showing the burial of the tryptophan side chain by the salt-bridge D9/R16 and the phenylalanine P12F. Images were generated from the pdb file 2M7D of the stable TC16b P12W construct. The mutations Y3F, W12P, and W12F to the NMR structure were done with the mutate function in Pymol. Hydrogens are omitted for clarity. The numbers correspond to the residues that were mutated in these studies and W labels the tryptophan residue.

The trp-cage is a structural motif originally characterized in the poorly folded 39-residue peptide exendin-4 (isolated from saliva of the *Heloderma suspectum* lizard).[38] By truncation and mutation of the sequence, the Andersen group developed the significantly more stable 20 amino acid trp-cage miniprotein TC5b (NLYIQWLKDGGPSSGRPPPS), now generally recognized as one of the smallest peptides to display characteristics of protein folding.[34] The trp-cage consists of an α-helix in residues 2-8, a 3_{10}-helix in residues 11-14, and hydrophobic collapse around the W6 tryptophan indole ring.

The original well-folded trp-cage reported in 2002 has several structural features that lead to its stable and fast folding. These features have since been optimized and characterized extensively and include the following:

1. In the TC10b variant, mutations of long chain residues in the helix to alanine (2LA and 4IA) increase the melting temperature of the trp-cage from 42°C to 64°C due to decreased entropic favorability of unfolding.[39] The further addition of L-Ala at K8 and S13 and D-Ala at G10 and G15 resulted in the ultra-stable TC16b construct with a melting temperature above 70°C (DAYAQWLADaGPASaRPPPS).[40]
2. The hydrophobic interaction of tryptophan 6 with tyrosine 3 and prolines 17-19 is essential for folding. Mutations of tryptophan to other aromatic amino acids such as W6H or W6F were found to be destabilizing in early trp-cage constructs.[39] Increasing the hydrophobicity around W6 was also shown to be highly stabilizing in a P12W mutation in the very stable TC16b construct.[36,41] The hydrophobic interaction between Y3 and P19 (known as a C-terminus and N-terminus staple) was shown to be highly stabilizing through Y3A and P19A mutations which were both unfavorable. In addition, it was shown the structure could be circularly permuted so long as a hydrophobic C-terminus N-terminus staple was introduced.[41] However, the mutation Y3F to TC16b was shown to maintain the stabilizing hydrophobic interaction while removing the redox active tyrosine residue.[16]
3. Early $^{1}H/^{2}H$ exchange studies revealed that 10 backbone NH groups are well-protected in H-bonding interactions in the trp-cage. Especially interesting for studying the tryptophan cation or H-bonded neutral radical is the H-bond from W6NH to the i+10 backbone carboxyl group (or the 16th position since tryptophan is at position 6). Burial of S14 also results in a stabilizing hydrogen bond and mutations to this residue are poorly tolerated.[39]
4. The electrostatic interaction between negatively charged aspartate 9 and positively charged arginine 16 creates a stabilizing salt-bridge. This was observed in early constructs when the protection factor of the W6ε1NH decreased at lower pH values. This was attributed to protonation and neutralization of the charge on D9. Subsequent studies including D9E and D9R/R16D mutations have shown the original combination of D9/R16 to be the most stable salt bridge.[42]
5. Although the D9/R16 salt bridge creates a stabilizing effect in the TC16b construct, mutations of these residues to hydrophobic amino acids were previously shown to be only slightly destabilizing. In addition, these hydrophobic mutations are more stabilizing at low pH values.[43]

There are several distinct CSDs that indicate folding in the trp-cage. α-helix formation in residues 2-8 in the trp-cage is indicated by deviations in α-carbon proton resonances at Y3, Q5, W6, and K8.[34,39] Formation of the cage is monitored by large shifts in L7α, G11α2, P18αH, P18β3H, P19δ2H, and P19δ3H. The NMR structure shows stacking of prolines both above and below the plane of the W6 indole ring. This structure leads to large CSDs in these protons due to the ring currents of the aromatic tryptophan residue.

Tables 2.2 a, b, c, and d list the trp-cage constructs utilized in this study along with their CSDs and percent fold. Some of the constructs have been previously structurally characterized and used for other studies.[16,43] However, some of the constructs are newly reported herein including 16bY3FR16I, 16bY3FP12F, 16bY3FD9AP12F, 16bY3FP12FR16I, and 16bY3FD9LP12FR16Nle. The P12F mutation is new; however, a P12W mutation had been previously made and reported as a highly stabilized construct (NMR structure used for Figure 2.2). The ring current of P12W causes a strong CSD in the W6η2 proton (or C7 proton). The magnitude of this CSD in trp-cages with the P12F mutation has been used to monitor whether the phenylalanine is interacting with tryptophan and protecting it from solvent exposure.

In parallel to studies on the trp-cage peptides, EPR properties and electrochemical studies were performed on a β-hairpin system also developed in the Andersen group (HP8). The results of these studies are summarized in Appendix A2.1.

Table 2.2a. NMR fold populations and CSDs of various trp-cage constructs at 280 K and pH=7.5

pH 7.5, 280K	L7 Ha	P18 Ha	P18 Hb3	P19 Hd2	P19 Hd3	G11 Ha2	W6 Hh	Σ CSD's	Fraction Folded
16b cyclo[a]	-0.973	-2.722	-2.644	-0.799	-0.508	-3.638		-11.28	0.995
16b P12W[a]	-1.015	-2.671	-2.701	-0.727	-0.643	-3.62	-1.04	-11.38	1.0032
16b Y3F	-0.94	-2.351	-2.14	-0.676	-0.601	-3.614	0.031	-10.32	0.9102
16b Y3F D9L[a]	-0.966	-2.265	-1.856	-0.685	-0.699	-3.491	0.021	-9.962	0.8784
16b Y3F R16I									
16b Y3F D9L R16I[a]	-0.996	-2.291	-1.974	-0.776	-0.724	-3.46	-0.093	-10.22	0.9013
16b Y3F P12F	-1.021	-2.485	-2.335	-0.721	-0.632	-3.585	-1.211	-10.78	0.950
16b Y3F P12F, 30% MeCN	-1.055	-2.521	-2.396	-0.786	-0.686	-3.648	-1.274	-11.09	0.9781
16b Y3F D9A P12F									
16b Y3F P12F R16I									
16b Y3F D9L P12F R16Nle	-1.056	-2.338	-2.009	-0.762	-0.736	-3.51	-1.441	-10.41	0.918
16b W6F[a]	-0.448	-0.859	-0.079	-0.244	-0.244	-1.378		-3.252	0.2868
Ru-16b Y3F[b]	-0.904	-2.022	-1.802	-0.69	-0.54	-3.268	-0.093	-9.226	0.814

[a] pH=7.0

[b] pH = 6.4

Table 2.2b. NMR fold populations and CSDs of various trp-cage constructs at 300 K and pH=7.5

pH 7, 300K	L7 Ha	P18 Ha	P18 Hb3	P19 Hd2	P19 Hd3	G11 Ha2	W6 Hh	Σ CSD's	Fraction Folded
16b	-0.928	-2.295	-2.066	-0.69	-0.621	-3.518		-10.12	0.892
16b P12W	-1.013	-2.607	-2.604	-0.517	-0.901	-3.56	-1.073	-11.2	0.988
16b Y3F									
16b Y3F D9L	-0.921	-2.126	-1.74	-0.699	-0.709	-3.316	0.008	-9.511	0.839
16b Y3F R16I									
16b Y3F D9L R16I	-0.951	-2.171	-1.847	-0.801	-0.752	-3.292	-0.107	-9.814	0.865
16b Y3F P12F									
16b Y3F D9A P12F									
16b Y3F P12F R16I									
16b Y3F D9L P12F R16Nle									

Table 2.2c. NMR fold populations and CSDs of various trp-cage constructs at 280 K and pH=2.5

pH 2.5, 280K	L7 Ha	P18 Ha	P18 Hb3	P19 Hd2	P19 Hd3	G11 Ha2	W6 Hh	Σ CSD's	Fraction Folded
16b	-0.97	-2.288	-1.997	-0.671	-0.569	-3.498		-9.993	0.881
16b Y3F									
16b Y3F D9L	-0.949	-2.201	-1.828	-0.684	-0.649	-3.415	0.021	-9.726	0.858
16b Y3F R16I									
16b Y3F D9L R16I	-0.984	-2.239	-1.93	-0.788	-0.696	-3.406	-0.096	-10.04	0.886
16b Y3F P12F									
16b Y3F D9A P12F									
16b Y3F P12F R16I									
16b Y3F D9L P12F R16Nle									

Table 2.2d. NMR fold populations and CSDs of various trp-cage constructs at 300 K and pH=2.5

pH 2.5, 300K	L7 Ha	P18 Ha	P18 Hb3	P19 Hd2	P19 Hd3	G11 Ha2	W6 Hh	Σ CSD's	Fraction Folded
16b	-0.947	-2.13	-1.839	-0.442	-0.82	-3.274		-9.452	0.833
16b Y3F									
16b Y3F D9L	-0.881	-1.998	-1.659	-0.67	-0.641	-3.143	0.012	-8.992	0.793
16b Y3F R16I									
16b Y3F D9L R16I	-0.922	-2.08	-1.775	-0.796	-0.717	-3.188	-0.11	-9.478	0.836
16b Y3F P12F									
16b Y3F D9A P12F									
16b Y3F P12F R16I									
16b Y3F D9L P12F R16Nle									

Full NMR characterization of the peptides is on-going at the time of this writing. The CSDs are (or will be) available online at http://andersenlab.chem.washington.edu/CSDb/.

2.3.2 Methods

NMR samples were prepared by dissolving peptide to 1 mM in 20 mM phosphate buffer prepared at pH values of either 2.5 or 7.5. 450 µL of this solution was combined with 50 µL of 1 mM DSS in D_2O and transferred to an NMR sample tube. TOCSY and NOESY 2D NMR were carried out at 280 K and 300 K on

Bruker DRX-499 MHz, AV-500 MHz, or AV-700 MHz instruments. These techniques are complementary for assigning resonances in peptides. TOCSY provides correlations through bonds between ^{1}H nuclei within a spin system, such as the side chain, and can be used to identify individual amino acids. NOESY provides correlations through space when two nuclei interact via the nuclear Overhauser effect and aids in determining and confirming the peptide sequence. In both cases the ^{1}H peak from water dominated the spectra. This peak was suppressed with the WATERGATE technique.[44]

2.3.3 Peptide synthesis

Peptides were synthesized using standard solid-state peptide synthesis either on a Liberty Blue microwave peptide synthesizer (CEM) or by hand. In both cases, typically 100 μmol preparations were started by weighing out Wang resin preloaded with Fmoc protected serine (resins come with a unique loading numbering in units of moles/gram). This was placed in the reaction vessel.

On the CEM synthesizer, the procedure consisted of a deprotection step, rinse, coupling step, and rinse until the final deprotection and completion of the sequence. Generally solutions of 0.2 M amino acids, 20% piperidine in DMF (deprotection), and 7.7% DIC (N,N'-Diisopropylcarbodiimide) in DMF with ≈ 800 mM oxyma and 1.7% DIEA in DMF (coupling). Setting the synthesis to run at 70°C typically resulted in the best yield of peptide. In the case of arginine, a double coupling was performed.

When performed by hand, the procedure below was followed:

1. Place resin in ≈ 12 mL fritted and cappable reaction vessel.
2. Swell resin in ≈ 7 mL of NMP (N-methyl-2-pyrrolidone) by shaking vessel (with 180 degree inversion) for 30 minutes. Note the resin will not dissolve.
3. Drain NMP with an aspirator and rinse thoroughly with DCM (dichloromethane).
4. Add ≈ 7 mL of deprotection reagent (20% v/v piperidine (Sigma-Aldrich 411027) in NMP) to reaction vessel. Shake for 25 minutes.
5. Drain. Rinse with DCM.
6. Add ≈7 mL deprotection reagent to reaction vessel. Shake for 5 minutes.
7. Drain. Rinse with DCM.
8. Check for deprotection with ninhydrin test (described below) looking for all of the beads to show an equally dark purple color. If necessary, repeat steps 4-7 for up to 1.5 hours total deprotection time,

then move on to step 9. If each deprotection step yields an improved ninhydrin test (more beads are purple) continue with steps 4-7 until no more improvement is seen, then proceed to step 9.

9. Add the coupling reagents for the next amino acid in the following order to the resin reaction vessel:
    a. 1 mL of 20% 6-Cl-HOBt/HBTU (Hydroxybenzotriazole/N,N,N',N'-Tetramethyl-O-(1H-benzotriazol-1-yl)uronium hexafluorophosphate) in DMF
    b. 1 mL of 0.5 M Fmoc-amino acid in NMP
    c. 0.6 mL of 40% DIEA ((N,N-diisopropylethylamine) in NMP
10. Shake for 30 minutes.
11. Drain. Rinse with DCM.
12. Check for coupling with a ninhydrin test. Look for the beads to remain clear. If any beads are purple, repeat steps 9-11 until the ninhydrin test shows all beads are clear.
13. Repeat steps 4-12 until all amino acids in the sequence have been coupled and final deprotection has been performed on the N-terminus.

At the end of either a synthesizer or by-hand peptide preparation, the peptide must be cleaved from the resin and the side chain protecting groups removed. Transfer the peptide to a glass fritted and cappable reaction vessel with ground glass joint and perform the following:

1. Add cleaving cocktail to reaction vessel in the following order:
    a) 0.25 mL nanopure water
    b) 0.25 mL TIPS (triisopropylsilane)
    c) 9.5 mL TFA (trifluoroacetic acid)
2. Shake for 1.5 hours.
3. Drain the solution into a clean flask. The peptide is in the flow through.
4. Rinse the reaction vessel with DCM allowing it to flow into pear shaped flask.
5. Pump off the excess DCM from the flask either on a vacuum manifold or on an aspirator down to a volume of ≈ 2 mL. In either case, a cold trap should be used to capture the TFA and DCM which should then be disposed of properly. A heating mantle can be used to speed up the process but the peptide should not be allowed to burn.
6. Transfer the ≈2 mL peptide solution to a 50 mL falcon tube. Rinse the flask with 5 mL aliquots of cold diethyl ether, scraping the side walls to remove all peptide (the peptide will fall out of solution when diethyl ether is added). Add each aliquot to the 50 mL falcon tube until a volume of 30 mL has been reached.
7. Vortex the falcon tube to help lift the TFA off of the peptide.
8. Centrifuge the 50 mL falcon tube at 4°C and 3000 rpm for 5 minutes to pack the now solid peptide at the bottom of the falcon tube. *Caution: use a counter weight in the centrifuge.
9. Decant the ether into an appropriate waste container being careful not to dump out the solid peptide. *Caution: ether is a peroxide former. Do not keep waste containers around for a long time. Do not mix with aqueous or organic waste.
10. Add another 30 mL of cold ether to the peptide.
11. Vortex.
12. Repeat steps 7-8.
13. Repeat steps 9-11 for a total of 3 ether rinses and centrifuge cycles.
14. Dry the peptide in the falcon tube under nitrogen gas and store until purification.

Coupling reagent: HOBt/HBTU:

Make in 10 mL batch in glass vial. Small batches are necessary as the reagent will go bad over 7-10 days. It will turn a dark yellow color when it is no longer viable. Add each to 5% (mol/mol) of DMF.

1.89 g HBTU (CAS 94790-37-1)

0.84 g 6-Cl-HOBt (CAS 26198-19-6)

10 mL DMF (dimethylformamide)

DIEA: Prepare 40% (v/v) DIEA to NMP in 10 mL batches in a glass vial.

Amino acid: Make 2 mL batches of 0.5 M N-Fmoc-AA in NMP.

Ninhydrin test

During the ninhydrin test, ninhydrin reacts with primary amines to form an intense purple color. Therefore, it cannot be reliably used to check the coupling of proline, which has a terminal secondary amine. To perform the test, take ≈15 beads from the reaction vessel and transfer to a test tube. Add 2-3 drops of reagent A, 2-3 drops of reagent B, and 2-3 drops of reagent C to the beads and heat to 110°C for 5 minutes. Check the color.

Reagent A: Dissolve 13 mg of KCN in 20 mL of nanopure H2O, dilute 20 µL of this in to 980 µL of pyridine.

Reagent B: Dissolve 250 mg of ninhydrin in 10 mL of ethanol.

Reagent C: Dissolve 15 g of phenol in 4.5 mL of ethanol.

Coupling Fmoc-tryptophan-d_5 into either the trp-cage or hairpin system was always done by hand using the sequence leading up to tryptophan synthesized either by hand or on the CEM synthesizer. Typically, this was prepared in small batches, using 20 µmol of resin with pre-synthesized peptide leading up to tryptophan, 20 mg of d_5-N-Fmoc-trp, 200 µL of HOBt/HBTU, 120 µL of DIEA, and 120 µL of NMP. This was allowed to react for roughly 5 hours. If necessary, the remaining amino acids can be coupled by hand or on the synthesizer.

Cleavage from the resin of peptides containing d_5-tryptophan has special considerations. First, it was observed that if the cleavage reaction ran for extended periods of time (2.5 hours), the deuterium would begin to partially exchange with protium. This can be avoided by performing shorter cleavage reactions (around 1 hour, however this may result in incomplete side-chain protecting group removal). In addition, commercially available d_5-N-Fmoc-Trp is not protected on the tryptophan side chain (typically N-Fmoc-Trp(Boc)-OH is used). This was not found to be a problem during synthesis of these peptides, however, during cleavage the Pbf protecting group of arginine can sometimes oxidize the trp

side chain. This can be mitigated with the addition of thioanisole to the cleavage cocktail making the final composition 2.5 % H_2O, 2.5% TIPS, 5% thioanisole, and 90% TFA.

2.3.4 Peptide purification

Peptides are purified using reverse-phase HPLC typically on an Agilent C18 column with buffer A composed of 0.1% TFA in H_2O and buffer B composed of 0.085% TFA in acetonitrile. To prepare the peptide for purification, it was dissolved in roughly 5-7 mL of an aqueous solution by adding small aliquots of water until the peptide began to dissolve. Highly charged peptides will dissolve readily. However, if solvation is a problem, the solution can be made more acidic with HCl or more basic with NaOH to protonate or deprotonate the side chains and create charged species. In addition, very small amounts of MeCN can be added to aid solvation of hydrophobic peptides (while being aware this may disrupt the mobile phase once loaded on to the HPLC column). Separation was performed at 10 mL/min flow rate with typical gradients of 10-50% buffer B in 20 to 30 minutes. Generally, peptides eluted between 30-40 % buffer B. Eluting peptide was detected with the 280 nm UV-Vis absorption of tryptophan and collected in fractions. The presence of desired peptide in active fractions was determined with ESI-MS on a Bruker Esquire ion-trap mass spectrometer. Fractions containing the desired peptide were combined and reduced to a volume of ≈ 5 mL using rotary evaporation. The remaining solution was frozen slowly on dry ice and lyophilized.

2.4 EPR Results: Oxidation of tryptophan with Ce^{IV}

2.4.1 Results

Tryptophan radicals in the trp-cage land β-hairpin peptides can be generated in high yield with Ce^{IV} ammonium nitrate (CAN) which has been shown previously to be an effective tryptophan oxidant.[15,45] Their solid-state CW X-band EPR spectra (Figure 2.3) show a somewhat featureless resonance at $g \approx 2$ of about 2 mT peak-to-peak width. The pulse field-swept Q-band spectra (Figure 2.3) show a distinct splitting of 2 mT attributed to hyperfine coupling to the C_β protons. The resolution of this splitting increases for the deuterated trp-cage TC16bY3FW6(d_5-W)D9LP12FR16Nle (abbreviated d_5-TC).

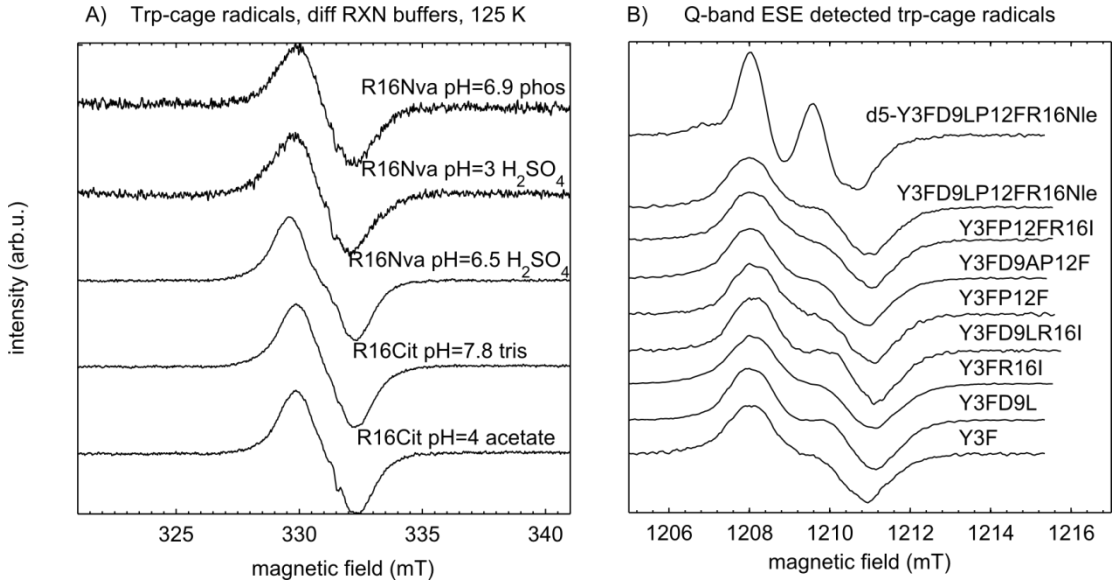

Figure 2.3. A) 9.29 GHz CW EPR spectra of trp-cage radicals generated with Ce^{IV} ammonium nitrate (CAN). Spectra were recorded at 125 K with 13 μW microwave power, 2 G modulation amplitude, and 0.5 mT/s sweep rate. Spectra are scaled by power, gain, and number of scans. Radicals were generated in different starting reaction buffers (indicated in the figure). Note, the final pH of the reaction is always approximately 2 due to acidification of the solution when Ce^{IV} oxidizes H_2O. B) 33GHz ESE-detected pulse field swept EPR spectra of trp-cage radicals collected at 40 K. Samples were prepared to 1 mM peptide in 100 mM tris at pH=7.2 and oxidized with a 10-fold excess of CAN in MeCN to a final v/v ratio of 1:2 MeCN:H_2O. Spectra were acquired with the pulse sequence $\pi/2$(30 ns) – τ(220 ns) – π(60 ns) – τ(220 ns) – echo using repetition times of 3-5 ms. Spectra are normalized and are shifted along the x axis so that the peak maximum of each spectrum is aligned at 1206 mT allowing the widths and shapes to be more easily compared.

ENDOR data of trp-cage radicals are shown in Figure 2.4. The ENDOR spectra show two dominant splittings, one of about 14 MHz and one of about 3.6 MHz, centered around the ^{1}H Larmor frequency. Also in Figure 2.4 is the spectrum of d_5-TC deuterated on the tryptophan indole ring. The Larmor frequency of deuterium is 6.5 times smaller than for hydrogen, so the peaks due to ring proton hyperfine couplings are expected to shift out of the frequency range of the experiment. Indeed, many of the ^{1}H features are drastically decreased in d_5-TC. The incomplete loss of the ^{1}H features is due to incomplete deuteration of the indole ring, as confirmed by some residual ^{1}H features in the 2D NMR spectrum of d_5-TC. This incomplete deuteration likely occurs due to ^{2}H/^{1}H exchange during the cleavage of the peptide from the solid-state resin at the end of synthesis. We have shown that in a β-hairpin construct, where full deuteration of the indole ring was maintained (as confirmed by NMR), that the ^{1}H ENDOR spectrum shows no features (Figure A2.3). These results confirm that the radicals in the EPR

spectra are due to tryptophan and allow assignment of the dominant peaks in the ENDOR spectrum to the ring protons. The inset in Figure 2.4 shows the ^{2}H ENDOR spectrum of d_5-TC centered at the ^{2}H Larmor frequency. As expected, the ^{2}H hyperfine splittings decrease by a factor of about 6.5 (to 2 MHz and 0.6 MHz) compared to the ^{1}H hyperfine splittings.

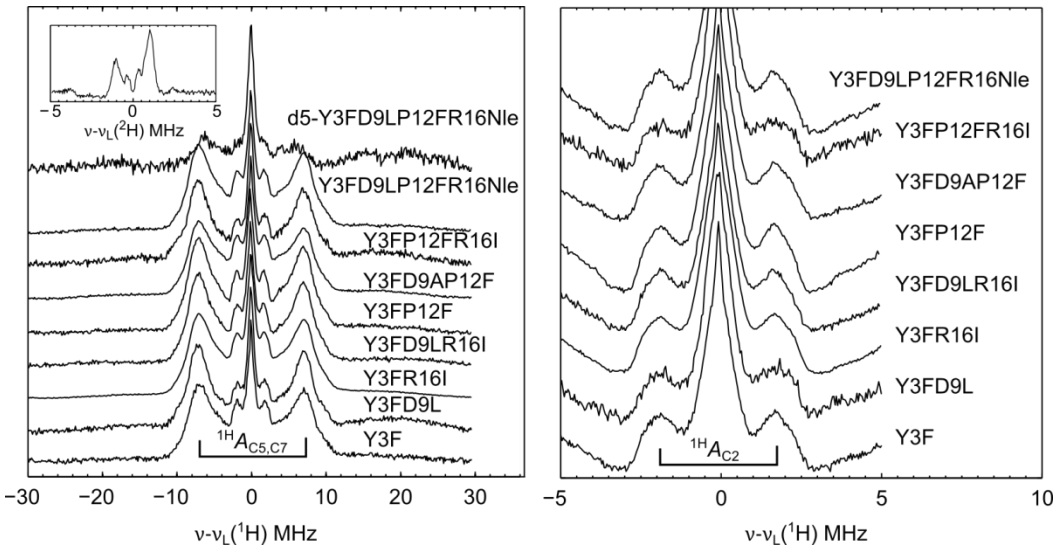

Figure 2.4. 33 GHz Davies ENDOR spectra of trp-cage peptides oxidized with Ce^{IV} ammonium nitrate. Samples were prepared to 1 mM peptide in 100 mM tris at pH=7.2 and oxidized with a 10-fold excess of CAN in MeCN to a final v/v ratio of 1:2 MeCN:H_2O. Spectra were acquired with the pulse sequence π(100 ns) – RF(8 μs) –π/2(50 ns) – τ(460 ns) – π(100 ns) – τ(460 ns) – echo using repetition times of 3-5 ms (except for Y3FD9L and Y3FP12FR16I which were collected with a 15 μs RF pulse and a τ of 300 ns). Spectra are normalized and are shifted along the x axis so that they are centered at the ^{1}H Larmor frequency (except for the inset in the left figure which is centered at the ^{2}H Larmor frequency). *Right*: Wide ENDOR sweeps showing the larger hyperfine splittings. The inset figure shows ^{2}H ENDOR on d_5-Y3FD9LP12FR16Nle. *Left*: Narrow ENDOR sweeps of the hyperfine coupling currently assigned to the C2 proton.

Based on the literature values in Table 2.1, the smaller splitting of 3.6 MHz is most likely due to H_{C2}. This coupling strength should be sensitive to the protonation state of the indole nitrogen on Trp• (section 2.2), the charged environment, and the dielectric constant around Trp• or $TrpH^{+}$• (section 2.6). However, the changes are expected to be small according to DFT calculations presented in section 2.6 (≈ 3 MHz going from a dielectric constant of 1 to 100, Figure 2.10, and ≈ 1.5 MHz in changing from a neutral to positively charged environment, Figure 2.11). As such, ENDOR spectra of the H_{C2} splitting were collected with increased resolution along the x axis and are shown in Figure 2.4. However, these spectra are all nearly identical.

For one trp-cage (Y3FP12F), the effects on the ENDOR spectrum due to varying the concentration of oxidant (Ce^{IV}), buffer, starting pH, and solvent were also studied and the results shown in Figure 2.5. In general, when a lower concentration of Ce^{IV} is used for oxidation, the signal-to-noise ratios of the ENDOR spectra decrease drastically, indicating less efficient oxidation of tryptophan. Also, using a solvent mixture of 9:1 MeCN:H_2O (which should have a significantly decreased dielectric constant compared to the typical mixture of 1:2 MeCN:H_2O) seems to have no effect (see 2.4.2 Experimental Considerations for a rationalization for this solvent mixture).

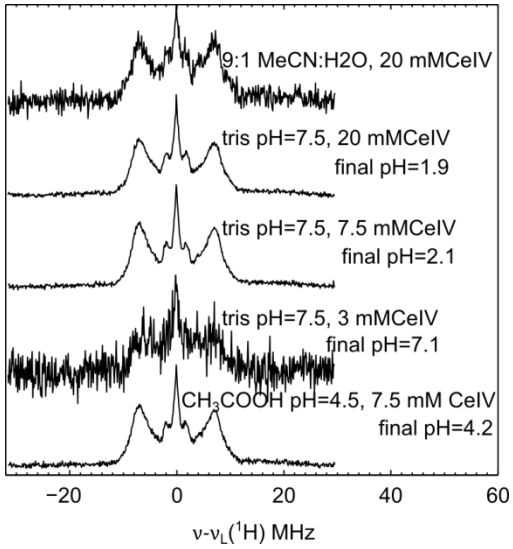

Figure 2.5. Solvent and Ce^{IV} concentration effects on Y3FP12F ENDOR. 33 GHz Davies ENDOR spectra of trp-cage peptides oxidized with Ce^{IV} ammonium nitrate. Samples were prepared to 1 mM peptide in 100 mM tris or acetate buffers at the pHs indicated in the figure (except for the sample labeled 9:1 MeCN:H_2O which was prepared in this solvent mixture). Peptides were oxidized with the concentration of CAN in MeCN indicated in the figure. Spectra were acquired with the pulse sequence π(100 ns) – RF(8 μs) –π/2(50 ns) – τ(460 ns) – π(100 ns) – τ(460 ns) – echo using repetition times of 3-6 ms. Spectra are normalized and are shifted along the x axis so that they are centered at the ^1H Larmor frequency.

In addition to probing the ^1H hyperfine coupling, the region where ^{14}N hyperfine coupling is expected to appear (between 1 and 25 MHz) was also explored. However, no ^{14}N resonances were detected using Q-band ENDOR. Instead, X-band and Q-band 3-pulse ESEEM and HYSCORE spectra were collected to probe the ^{14}N coupling and the spectra are shown in Figure 2.6. X-band ESEEM was collected for two constructs which differ in their degree of solvent exposure due to either P or F in the 12th position. There are no distinct differences between these spectra. In addition, there are no resonances indicative of the

strong axial component of the nitrogen hyperfine tensor (expected around 30 MHz). Q-band ESEEM was carried out for all trp-cage constructs. There are some differences in the spectra at lower frequencies especially for the construct Y3FP12FR16I.

To gain better resolution of these features by spreading them over two dimensions, HYSCORE spectroscopy was performed. The X-band HYSCORE spectra reveal some of the same proton couplings seen in the Q-band ENDOR spectra, especially the ≈ 14 MHz coupling. In addition, there is a faint 25 MHz coupling around the ^{1}H Larmor frequency in the first quadrant of the HYSCORE spectrum, and a faint splitting of 28.5 MHz around (-14.6, 14.6) in the second quadrant potentially due to a proton in the strong coupling regime. These are most likely due to the C_{β} protons.

Although there are features in the second quadrant at low frequencies where ^{14}N is expected to resonate, it is currently unclear if these features are due to hyperfine coupling or nuclear quadrupole coupling. Simulations of the data may be useful in this determination but have not been performed at this time. Most importantly, there are no obvious differences in the ESEEM or HYSCORE spectra collected for the different trp-cage constructs suggesting these spectral features are not overly sensitive to the microenvironment.

Although using Ce^{IV} as an oxidant results in excellent signal-to-noise ratios of the collected data, there are two sub-optimal aspects of this oxidation technique. First, the final pH of the Ce^{IV} reaction is roughly 4 or less to achieve good signal to noise. The decrease in pH is assumed to occur through acidification of the reaction as Ce^{IV} oxidizes water. This means that acidic side chains are potentially protonated and the effects of negative charges, such as from aspartate, cannot be reliably studied. Second, the final concentration ratio of Ce^{IV} to peptide is 10:1, making Ce^{III}/Ce^{IV} a large part of the environment around tryptophan. The second problem may be overcome by using more thorough and rapid mixing and freezing techniques such as a rapid-freeze-quench instrument. More thorough mixing may allow a stoichiometry closer to 1:1 Ce^{IV}:peptide to be used. However, the first problem cannot be overcome when using Ce^{IV} as an oxidant as it is known that Ce^{IV} is only more oxidizing than $Trp^{\bullet}$ at low pHs. Attempts to address this issue were made by using phototriggered oxidation and continuous flow

electrochemical and chemical oxidation as described in Appendix Sections A2.3, A2.4, A2.5, and A2.6. Supplementary EPR and ENDOR spectroscopy of β-hairpin peptides are shown and discussed in Appendix Section A2.1.

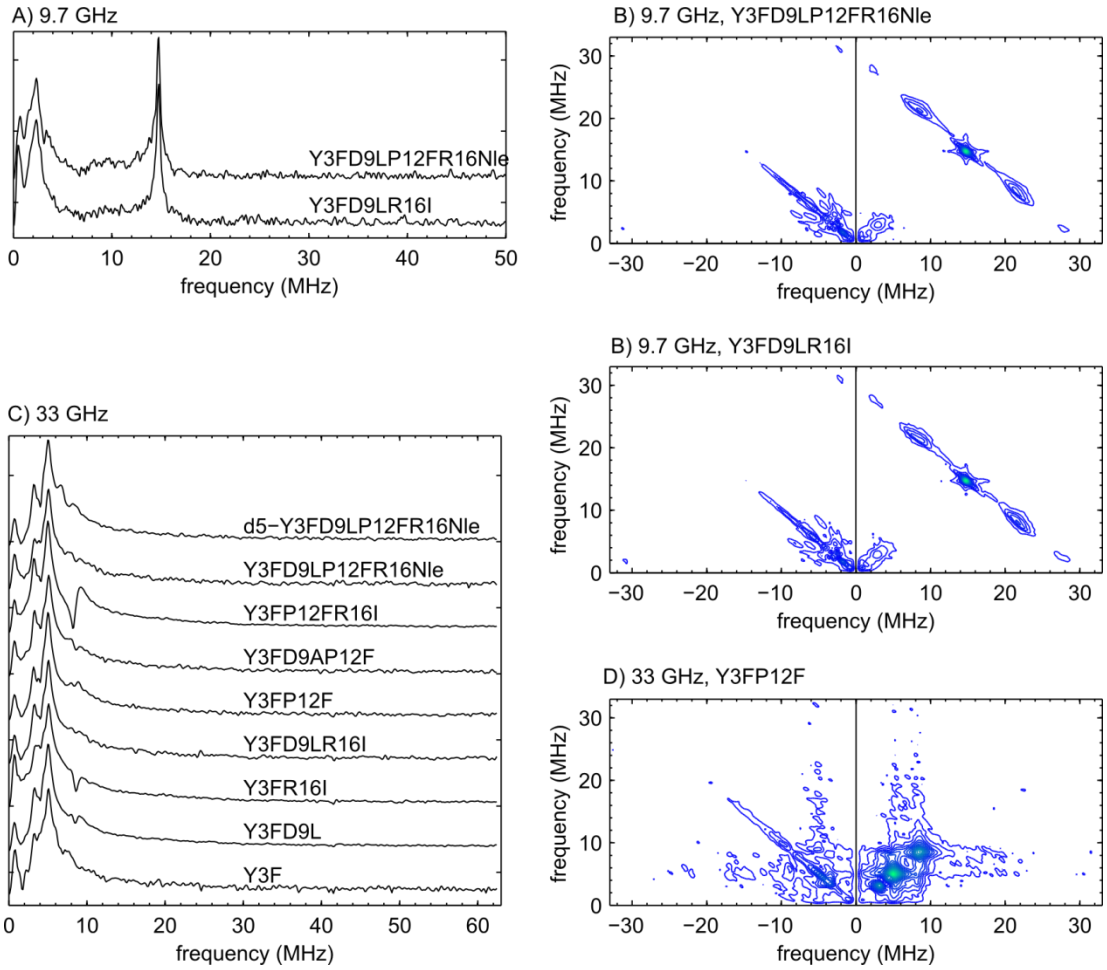

Figure 2.6. 3-pulse ESEEM and HYSCORE of Ce^{IV}-oxidizied trp-cages.

A) 9.69 GHz 3-pulse ESEEM: Time traces were collected at 40 K with the sequence π/2(8 ns) – τ(average) – π/2(8 ns) – (T_0 = 40 ns) – π/2(8 ns) – τ(average) – echo where T was stepped in 4 ns increments. τ was averaged over eight values incremented by 12 ns starting at 150 ns. The time traces were summed over τ for each peptide, the sum fit to a second order polynomial which was subsequently subtracted, zero-filled and multiplied by the positive half of a cosine apodization window. This was then Fourier transformed to the spectra above. Spectra were collected at the central field maximum using a 1.5 ms repetition time.

B) 9.69 GHz HYSCORE: Time traces were collected at 40 K with the sequence π/2(16 ns) – τ(average) – π/2(16) – ($t_{1,0}$ = 30 ns) – π (16 ns) – ($t_{2,0}$ = 30ns) – π/2(16 ns) – τ(average) – echo where t_1 and t_2 were stepped in 6 ns increments. The π pulse was applied with twice the power of the π/2 pulses. τ was averaged over three values (160 ns, 180 ns, and 200 ns). After summing the 2D time traces over τ, they were fit with second order polynomials which were subsequently subtracted, zero-filled and multiplied by the positive half of a cosine apodization window. These were then 2D Fourier

transformed to the spectra above. Spectra were collected at the central field maximum using a 1.5 ms repetition time.

C) 33.8 GHz 3-pulse ESEEM: Time traces were collected at 40 K with the sequence π/2(30 ns) – τ(average) – π/2(30 ns) – (T_0 = 50 ns) – π/2(30 ns) – τ(average) – echo where T was stepped in 8 ns increments. τ was averaged over eight values incremented by 12 ns starting at 170 ns. The time traces were summed over τ for each peptide, the sum fit to a second order polynomial which was subsequently subtracted, zero-filled and multiplied by the positive half of a cosine apodization window. This was then Fourier transformed to the spectra above. Spectra were collected at the central field maximum using a 5 ms repetition time.

D) 33.8 GHz HYSCORE: Time traces were collected at 40 K with the sequence π/2(32 ns) – τ(200 ns) – π/2(32 ns) – ($t_{1,0}$ = 50 ns) – π (32 ns) – ($t_{2,0}$ = 50 ns) – π/2(32 ns) – τ(200 ns) – echo where t_1 and t_2 were stepped in 10 ns increments. The π pulse was applied with twice the power of the π/2 pulses. Traces were collected at a single τ value. In both dimensions, the 2D time traces were fit to second order polynomials which were subsequently subtracted, zero-filled and multiplied by the positive half of a cosine apodization window. These were then 2D Fourier transformed to the spectra above. Spectra were collected at the central field maximum using a 5 ms repetition time.

2.4.2 Experimental considerations

Samples are prepared by dissolving peptide to a concentration of 1 mM in 100 mM tris buffer at pH = 7.5 with 10 % glycerol v/v. To prepare Q-band samples, 10 µL of this solution was deposited in a 1.1 mm inner diameter quartz EPR tube and oxygen removed from the sample by 3 cycles of freeze-pump-thaw on a Schlenk line. At the same time, a solution of 30 mM CAN (bright yellow solution) in acetonitrile was deoxygenated by freeze-pump-thaw on the Schlenk line. 5 µL of the CAN solution was deposited in the EPR tube and the yellow color of the CAN solution would quickly fade to clear presumably as Ce^{IV} was converted to Ce^{III}. The reaction was quenched by immediately freezing in liquid nitrogen. The final pH of the solution was shifted by the addition of CAN and an approximation of the pH is given by the titration curve in Appendix Figure A2.5. X-band samples were prepared by transferring 50 µL of peptide into a 4mm OD quartz EPR tube and subsequently oxidizing the solution with a final volume of 50 µL CAN in acetonitrile (for a final H_2O to MeCN ratio of 1:1 by volume).

Although past reports have suggested using Ce^{IV} sulfate to generate tryptophan radicals,[45] in my hands I found the yield of radicals to be low when using hand-quenched freezing to prepare samples. CAN, with a larger reduction potential (1.2 V vs 1.4 vs NHE), was better suited for these experiments. Reactions for EPR experiments were carried out in tris buffer despite NMR measurements and electrochemical measurements being performed in 20 mM phosphate buffers. Addition of CAN to a solution of

phosphate (without L-tryptophan or peptide present) was found to produce a large volume of precipitate. Tris however did not show precipitation upon addition of CAN. Finally, CAN was dissolved in acetonitrile for addition to the peptide solutions instead of an acidic buffer. This was due to the rapid reduction of Ce^{IV} to Ce^{III} (monitored as color bleaching) presumably through the oxidation of water. The EPR samples as a result are ≈ 30 % v/v acetonitrile. This solvent mixture was found to stabilize the fold of at least one of the trp-cage peptides at pH 7.5 as determined by NMR CSDs in H_2O and MeCN-d_3 (Table 2.1a).

2.5 Redox potentials of tryptophan in peptides

Electrochemical measurements are a natural complement to the EPR measurements on tryptophan radicals. Electrochemistry measures the energy required to remove one electron from tryptophan. With the EPR experiments, one can map out the molecular orbital occupied by the single electron after oxidation has occurred. As outlined above, both of these properties are expected to depend on the microenvironment of the tryptophan residue. Here I describe the results of differential pulse voltammetry for measuring the potential required to oxidize the tryptophan side chain in the trp-cage peptides.

2.5.1 Results

Differential pulse voltammetry (DPV) is a technique commonly used to measure solutions with a low concentration of analyte. As shown in Figure 2.7, an external voltage is applied as a constant pulse for a length “pulse width” (forward voltage), then the current response is recorded (forward current). The voltage is then dropped back down to the previous voltage plus the step size (reverse voltage). After a delay which is usually 5x longer than the pulse width the current response is again measured (reverse current). The current response plotted on the y axis of a DPV voltammogram is the difference of the forward current response and the reverse current response. In the voltammograms analyzed here, the reverse voltage is plotted on the horizontal axis.

Recording the current response over short times inherently suppresses the charging current (a current due to the response of the working electrode to the applied potential). This makes the technique more sensitive to small-amplitude currents unlike the more familiar electrochemical technique cyclic voltammetry. Examples of raw DPV voltammograms showing the anodic peak which forms as tryptophan is oxidized are given in Appendix Figure A2.6 for the trp-cage peptides.

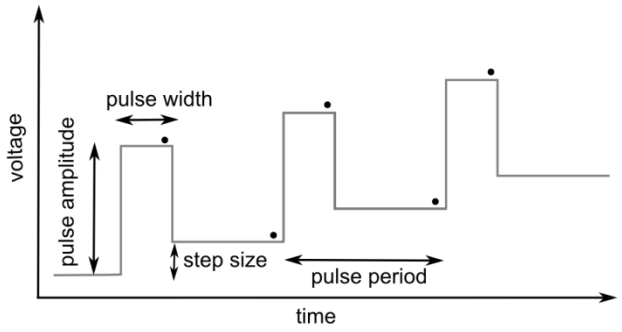

Figure 2.7. The DPV pulse sequence depicted as voltage vs. time and indicating the experimental parameters of pulse amplitude, width, and period. The points where the current response is measured are indicated by dots. The DPV voltammogram is plotted as the difference between the forward current (dot at the end of the pulse width) and reverse current (dot at the end of the pulse period).

The anodic peak potential (E_{ap}) measured using DPV can be plotted versus solution pH for trp-cage peptides to produce a Pourbaix diagram. For each peptide, a Pourbaix diagram was measured and confirmed by repeating the DPV experiments in triplicate. The raw Pourbaix plots are shown in Appendix Figure A2.7 along with a fit produced using equation 2.4. For simplicity, the fitted Pourbaix plots are shown together in Figure 2.7.

At pH values higher than the pK_a of oxidized tryptophan ($TrpH^{+\bullet}$), the indole nitrogen will deprotonate to form the neutral radical $Trp^{\bullet}$. This coupled deprotonation makes the anodic peak potential sensitive to the solution pH according to equation 2.4.[46,47]

$$E_{\mathrm{ap}} = E_{\mathrm{ap}}(\mathrm{pH}_0) + \; b \log\frac{\mathrm{RT}}{n\mathrm{F}} \log\frac{10^{-\mathrm{pH}}}{10^{-\mathrm{pH}}+10^{-\mathrm{p}Ka(\mathrm{WH}^{\bullet+})}} \qquad \text{Eq. 2.4}$$

Here E_{ap} is the measured anodic peak potential, $E_{ap}(pH_0)$ is the anodic peak potential at pH = 0, R is the gas constant, T is the temperature, F is the Faraday constant, n is the number of electrons transferred during the experiment, pH is the solution pH, and pK_a(WH•+) is the pK_a of oxidized tryptophan. $E_{ap}(pH_0)$,

b, and pK_a(WH$^{\bullet+}$) are all parameters that depend on the peptide being measured. The values used for the fits are summarized in the graphic of Figure 2.8.

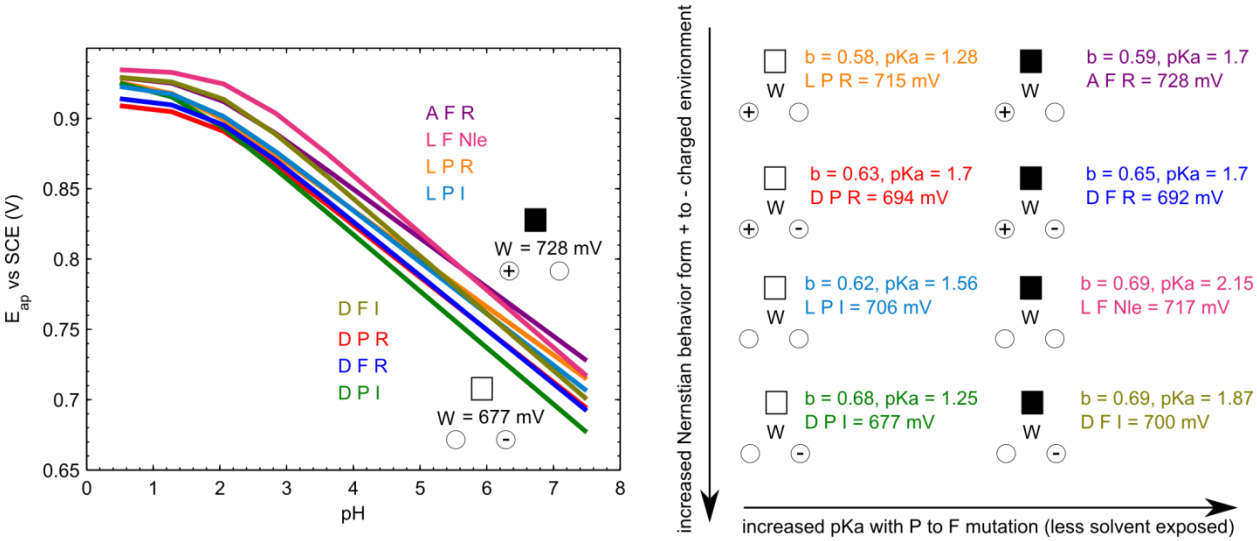

Figure 2.8. *Left*: Fits to the Nernstian equation (Eq. 2.4) of applied potential at current maximum vs. solvent pH measured with DPV on trp-cage peptides. The three letter labels correspond to the residues at the 9th, 12th, and 16th positions. The two redox potentials listed are for the the green fit (peptide D P I) and the purple fit (peptide A F R). DPV was collected with a 50 mV pulse amplitude, 20 ms pulse width, 100 ms period, and 2 mV step size. *Right*: A summary of the fitted parameters *b* and pK_a and the redox potential at pH 7.5 for the trp-cage peptides. The shapes around the W (tryptophan) indicate the microenviornment of the peptide. The bottom left circle (16th residue) has a plus sign for arginine or is empty for I or Nle mutations, the top square is (12th residue) is white for proline or solid for phenylalanine, and the bottom right circle (9th residue) has a negative sign for aspartate or is empty for L or A mutations.

b is an additional constant which we call the degree of Nernstian behavior. When the sample follows Nernstian behavior, the redox potential will increase by ≈ 59 mV for a decrease of one pH unit. However, we measured shallower slopes of between 30 and 40 mV per pH unit. This can be indicative of a multi-electron transfer (i.e. *n* is 2 in equation 2.4), which has been observed for tryptophan and other indole compounds previously.[48,49] Previously, these reactions tend to show two overlapping peaks in the voltammograms and the extent of overlap varies with pH. As shown by representative raw DPV traces of Figure A2.6, there is no obvious overlap of multiple peaks in the voltammograms of trp-cage peptides. In addition, we have shown with ENDOR spectroscopy of a d_5-W6 trp-cage peptide that only tryptophan-

based radicals are formed when the sample is oxidized with Ce^{IV}. Based on this, we will interpret the results assuming only a single electron transfer occurs.

In all cases, tryptophan has an E_{ap} around 115 mV higher compared to free tryptophan in solution (measured as ≈ 585 mV vs. a saturated calomel electrode (SCE) at pH 7.5 using our DPV set-up, data shown in Figure A2.4). This drastic increase in the potential required to oxidize tryptophan in a peptide environment has been observed previously.[50] There are additional smaller differences in the redox potential of tryptophan in the various mutants which seem to follow an easily understandable trend depending on the mutation, as illustrated in Figure 2.8. P12F mutations increases the shielding from solvent of the tryptophan residue, D9X mutations remove a negative charge (at pHs above the aspartic acid pK_a of 3.9), and R16X mutations remove a positive charge. The easiest peptide to oxidize is TC16bY3FR16I (labeled D P I in Figure 2.8, negative charge only) and the hardest peptide to oxidize is TC16bY3FD9AP12F (labeled A F R, positive charge only) at pH = 7.5. There is a difference of 50 mV in their redox potentials. This trend should be expected if one considers that oxidizing tryptophan creates a positively charged species, which should form more favorably in a negative environment than in a positive environment.

The graphic in Figure 2.8 highlights some of the other observed trends in the fitted values *b* and pK_a($WH^{\bullet+}$). First, the Nernstian behavior of the peptides seems to increase in going from a positively charged to negatively charged or neutral environment (moving down the graphic). However, in samples with equivalent charges (i.e. the same residue at the 9^{th} and 16^{th} positions), the degree of solvent exposure controlled with the P12F mutation (moving left to right in the graphic) does not have a large effect on the degree of Nernstian behavior. Second, the degree of solvent exposure in peptides with equivalent charges does seem to effect pK_a($WH^{\bullet+}$). Generally, decreased solvent exposure raises the pK_a by up to 0.5 pH units. However, in all cases pK_a($WH^{\bullet+}$) is substantially lower than the values reported for L-tryptophan (4.7) and *N*-acetyl-L-tryptophanamide (3.7).[11,50]

Finally, the DPV response can be simulated using equations 2.5[47] for a reversible electron transfer at a disk electrode

$$I = FADc\left(\frac{1}{1+e^{\eta 1}}f(t12) + \left(\frac{1}{1+e^{\eta 2}} - \frac{1}{1+e^{\eta 1}}\right)f(t2) - \frac{1}{1+e^{\eta 1}}f(t1)\right)$$

$$\eta 1 = \frac{F}{RT}\left(E(\text{reverse}) - E_{ap}\right) \qquad \eta 2 = \frac{F}{RT}\left(E(\text{forward}) - E_{ap}\right) \qquad \text{Eq. 2.5}$$

$$f(t) = \frac{4}{\pi}\frac{1}{r}\left(0.7854 + \frac{0.44315r}{\sqrt{Dt}} + 0.2146e^{-\frac{0.391158r}{\sqrt{Dt}}}\right)$$

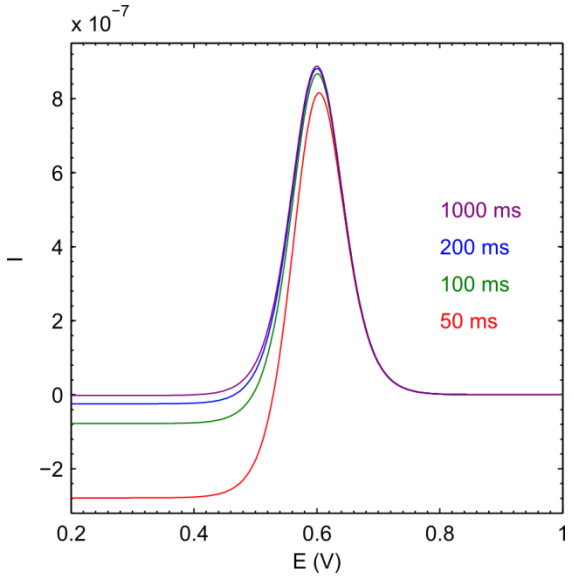

Figure 2.9. Simulated dependence of the current response on the pulse period of a redox process at 600 mV measured with differential pulse voltammetry (the pulse sequence shown in Figure 2.7). The simulation parameters match those used to collect the experimental data (pulse amplitude = 50 mV and pulse width = 20 ms). The simulation used equation 2.5, which is described in detail in the main text.

Here the current, *I*, depends on the Faraday constant *F*, the gas constant R, the temperature *T*, the area of the disk electrode *A*, the diffusion rate of the electroactive species *D*, the concentration *c*, and the radius of the disk electrode *r*. The function *f* depends on the variables t1, t2, and t12 which are the length of time between pulses, the pulse width, and the sum of the pulse width and time between pulses (or pulse period), respectively. This equation can be used to simulate the expected peak shape for the experimental parameters used in our data collection. Using a 50 mV pulse amplitude, 20 ms pulse width, and variable pulse period times between 50 and 1000 ms produces the simulated traces in Figure 2.9 for an anodic response at 600 mV. This shows that the peak center (in mV) is relatively insensitive to the pulse period. However, longer periods must be used to create a flat baseline. In addition, this shows

that for a reversible oxidation event, the peak width should be 100 mV. The full-width at half-maximum (FWHM) of each of our Gaussian fitted anodic peaks are also plotted in Appendix Figure A2.7. Generally, the FWHM are near 100 mV, indicating similar reversibility of all the peptides across the pH range utilized. As irreversibility is also known to shift the position of the anodic current response maximum to more positive values, it is important that similar irreversibility/reversibility is seen for each peptide.

2.5.2 Experimental Considerations

Choice of DPV over CV or SWV. Pulse voltammetry is widely preferred over cyclic voltammetry for measuring analytes of low concentration. The short measurement time period and sampling scheme reduces background currents and produces a higher-intensity faradaic response due to the analyte of interest. Along with DPV, square wave voltammetry (SWV), another pulse voltammetry method, also allows for measurement of samples with a low analyte concentrations. In addition, because of the fast time scales in which forward and reverse potentials are applied, redox reactions otherwise irreversible on the electrochemical time scale (i.e. tens of milliseconds) can be measured in the reversible regime. This has been demonstrated in the Tommos group on tyrosine containing peptides.[51] However, in our hands, at pulse frequencies higher than 30 Hz using SWV, the voltammogram produced unintelligible results. The Tommos lab utilizes a pyrolytic graphite edge electrode to achieve good-quality square wave voltammograms, and our poor SWV results with a glassy carbon working electrode corroborate these observations.

Sample preparations. Measurements were carried out with a glassy carbon working electrode, platinum wire counter electrode, and saturated calomel reference electrode. For pH values 0.5-2.5 and 6-7.5, 20 mM phosphate was used as buffering agent. For pH values between 3 and 4.5, 20 mM acetate was used as the buffering agent. In both cases 200 mM KCl was used as electrolyte. The final pH values were obtained by adjusting the solutions with KOH or HCl. Samples for a single Pourbaix diagram were prepared from a stock solution of peptide of 0.5-3 mM in water (depending on solubility of different constructs). The concentration of peptide stock solution was determined by tryptophan absorption at 280 nm (ε = 5500 M^{-1} cm^{-1}). The stock solution was diluted into sample vials to a final volume of 6 mL

and concentration of 20 μM peptide. The pH of the solution with peptide was recorded before electrochemical and after electrochemical experiments and found to vary less than 0.05 pH units. The temperature of each solution was recorded immediately before each experiment and all measurements were carried out between 20-24°C.

For each sample vial, three DPV experiments were carried out. As indicated by the color coding in the Pourbaix plots of Appendix Figure A2.7, the measurements were repeated on sample vials prepared from different stock solutions of each peptide as well. Experiments were performed with a DPV pulse period of 50 ms, 100 ms, or 200 ms. All other experimental parameters were held constant as follows: 50 mV pulse amplitude, 20 ms pulse width, 2 mV step size. In between each measurement, the working electrode was rinsed with nanopure water and isopropanol and polished with 0.05 micron alumina in two cycles. After the final rinse with water the electrode surface was dried quickly under a heavy stream of dry nitrogen. Refreshing and drying the electrode surface was necessary to achieve reproducible results for each sample cell.

Concentration dependence. The dependence of E_{ap} on concentration of analyte was determined for the parent trp-cage construct TC16bY3F and the results are plotted in Appendix Figure A2.9. It has been observed previously that E_{ap} is less dependent on tryptophan concentration when the concentration is in the tens of micromoles range.[52] Due to this dependence and for the sake of peptide conservation low concentrations of 20 μM were chosen for DPV measurements.

Background correction. The DPV voltammograms show the faradaic response of tryptophan oxidation on top of the strong background response due to water oxidation that begins to occur between 500 mV to 1000 mV vs. SCE depending on pH. In order to remove this background a cubic spline was fit to the voltammograms at the points indicated in Figure A2.6 and interpolated back on to the x axis values to create a background voltammogram. This background was subtracted from the data which created the Gaussian peaks shown in Figures A2.6. The boundary points around the tryptophan peak for the spline fit were chosen by eye to minimize dips below zero current in the peaks produced after background subtraction. The background subtracted voltammograms were fit to a Gaussian using a minimization of

least-squares errors and the "fminsearch" function in Matlab. The Gaussian center (voltage at maximum current), full width at half maximum, and area of the Gaussian were determined in the fit and the averages per sample vial of the first two of these values are plotted in Appendix Figure A2.6. Vertical error bars equal to one standard deviation from the average are plotted above and below the averages. Horizontal error is based on the pH measurements of the solution before and after the DPV experiments as $\pm$0.04.

DPV of TC16bY3FD9LW6FR16Nle and solvent blank. To confirm that the current response being measured was due to tryptophan, a trp-less W6F trp-cage TC16bY3FW6FD9LP12FR16Nle was synthesized and DPV experiments performed on a 20 μM solution at pH = 2.50 and 7.45. In addition, DPV experiments were carried out on blank solutions of phosphate buffer at pH = 2.50 and 7.45 and acetate buffer at pH = 4.54 (see Appendix Figures A2.10 and A2.11). Together, these control experiments confirm that the peak of interest is due to tryptophan oxidation and that the peptide backbone and other side chains do not show redox activity within the window of applied potentials.

2.6 Quantum chemical calculations on free tryptophan and truncated peptides

To predict the dependence of the EPR parameters of Trp radicals on their microenvironment, density functional theory (DFT) calculations were performed. A combination of DFT and QM/MM calculations have been successfully used previously to probe shifts in spin density on tryptophan radicals in different environments. In one such study, it was found that increasing the positive charge density around $Trp^{\bullet}$ moved the spin density from the five-membered ring to the six-membered ring of the indole compared to more negatively charged environments. $TrpH^{\bullet+}$ in the same variable microenvironments exhibited less changes to spin density distribution.[25] In our studies, since the peptides are small and tryptophan is likely somewhat solvent exposed, we looked at the effects of solvent dielectric and single nearby charges on $Trp^{\bullet}$ spin density.

2.6.1 Properties of Trp$^{\bullet}$ vs solvent dielectric

Results. First, the EPR properties of the monomer neutral tryptophan radical were calculated for a range of dielectric constants. The interior of a protein has dielectric constants on the order of 4, while it is 80 in water. Depending on whether a tryptophan side chain is buried in a protein interior or solvent exposed on the surface, it could experience a wide range of dielectric environments. As shown in Figure 2.10, the spin population of N and C2 decrease as the solvent dielectric increases.

Methods. The geometry of the neutral 3-methyl indole radical was optimized using the Gaussian09 software with unrestricted orbitals, the B3LYP functional, and the 6-311G basis set. The optimized geometry was then used in the Orca 3.0.2 software for EPR property calculations with unrestricted orbitals, the B3LYP functional, and the EPR-II basis set. The solvent dielectric was modeled using the COSMO keyword which models solvent as a continuum. Solvent dielectrics of 1, 2, 4, 10 and 100 were used.

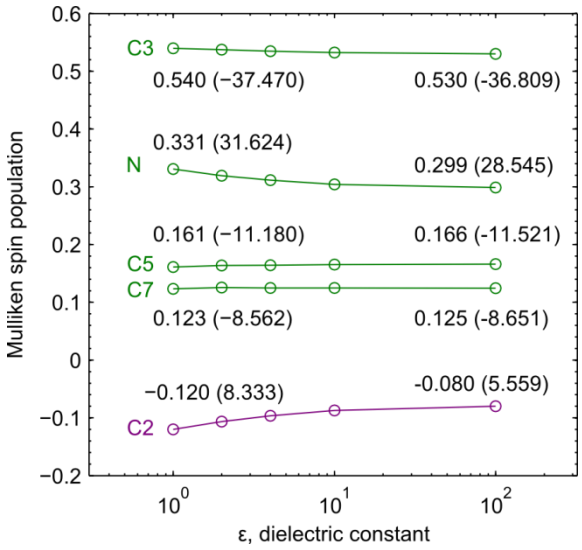

Figure 2.10. Calculated Mulliken spin populations of a neutral 1-methyl-indole radical at the nitrogen and carbons 2, 3, 5, and 7 as a function of solvent dielectric constant. In parentheses, the isotropic hyperfine copuling of the α protons covalently bound to the carbon, in MHz. In the case of nitrogen, in parentheses is the largest component of the hyperfine coupling due to spin population in the p orbital ($^{14N}A_{zz}$).

2.6.2 Properties of Trp• vs charged residues: Truncated β-hairpin peptides

Results. DFT was also used to predict if the presence of nearby charged amino acids would affect the EPR properties of tryptophan radicals. As shown in Figure 2.11, the presence of a positive charge (either on histidine or arginine) increases the calculated Mulliken spin populations on N and C2.

Methods. Input geometries were created from the NMR structure of the β-hairpin peptide HP8H. Structures were created for different residues (Asp, Arg, and Phe) in the 8th position using the mutate function in Pymol. Then, to simplify and speed up the calculations, the backbone and all residues except W1 and X8 were removed from the structure. Without geometry optimization, these coordinates were used for EPR property calculations.

The proton at indole nitrogen of the tryptophan residue was removed and the spin state set to a doublet to model the tryptophan neutral radical. The EPR properties were calculated with unrestricted orbitals, the B3LYP functional, and the EPR-II basis set with a dielectric constant of 4 modeled with COSMO.

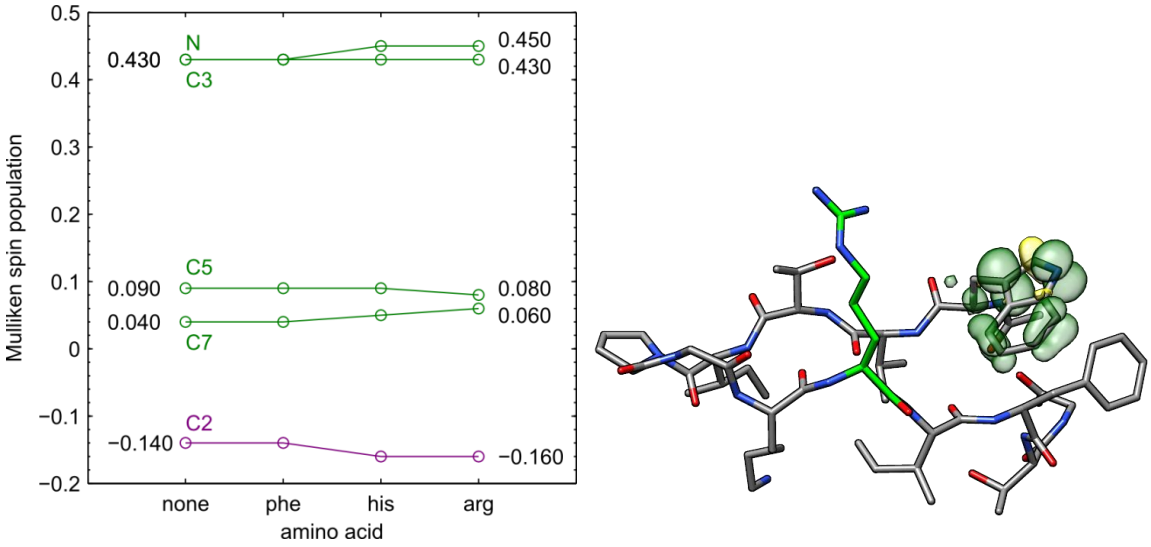

Figure 2.11. Calculated Mulliken spin populations on the tryptophan indole ring of the β-hairpin peptide at the nitrogen and carbons 2, 3, 5, and 7 as a function of the 8th amino acid (further details are given in the main text). The solvent dielectric was set to 4 and the pH of the "solution" was assumed to be neutral so that the Trp• radical is deprotonated and the histidine and arginine are positively charged. On the right is the NMR strucutre of the HP8X peptide where the 8th residue was mutated to arginine using pymol. Overlaid on the tryptophan residue is an example of the calculated Mulliken spin population with the isosurface contoured at $\pm 0.0025\ a_0^{-3}$.

2.7 Conclusions

We have shown that the trp-cage peptides can be utilized for studies of the redox properties of tryptophan. Despite their small size and minimal fold, results from DPV have shown rational trends in the redox potentials and pK_as of tryptophan and the tryptophan radical as a function of its microenvironment. In contrast, the magnetic properties, at least from the experiments conducted here, do not seem to strongly depend on the microenvironment.

2.8 References

(1) Stubbe, J.; Donk, W. A. Van Der. *Chem. Rev.* **1998**, *98*, 705.
(2) Stubbe, J.; Nocera, D. G.; Yee, C. S.; Chang, M. C. Y. *Chem. Rev.* **2003**, *103*, 2167.
(3) Giovani, B.; Byrdin, M.; Ahmad, M.; Brettel, K. *Nat. Struct. Biol.* **2003**, *10* (6), 489.
(4) Brettel, K.; Byrdin, M. *Curr. Opin. Struct. Biol.* **2010**, *20* (6), 693.
(5) Gindt, Y. M.; Vollenbroek, E.; Westphal, K.; Sackett, H.; Sancar, A.; Babcock, G. T. *Biochemistry* **1999**, *38* (13), 3857.
(6) Pogni, R.; Baratto, M. C.; Teutloff, C.; Giansanti, S.; Ruiz-Dueñas, F. J.; Choinowski, T.; Piontek, K.; Martínez, A. T.; Lendzian, F.; Basosi, R. *J. Biol. Chem.* **2006**, *281* (14), 9517.
(7) Sancar, A. *Biochemistry* **1994**, *33* (1), 2.
(8) Aubert, C.; Vos, M. H.; Mathis, P.; Eker, a P.; Brettel, K. *Nature* **2000**, *405* (6786), 586.
(9) Byrdin, M.; Lukacs, A.; Thiagarajan, V.; Eker, A. P. M.; Brettel, K.; Vos, M. H. *J. Phys. Chem. A* **2010**, *114* (9), 3207.
(10) Shih, C.; Museth, A. K.; Abrahamsson, M.; Blanco-Rodriguez, A. M.; Di Bilio, A. J.; Sudhamsu, J.; Crane, B. R.; Ronayne, K. L.; Towrie, M.; Vlcek, A.; Richards, J. H.; Winkler, J. R.; Gray, H. B. *Science* **2008**, *320* (5884), 1760.
(11) Harriman, A. *J. Phys. Chem.* **1987**, *91* (3), 6102.
(12) Smith, A. T.; Doyle, W. a; Dorlet, P.; Ivancich, A. *Proc. Natl. Acad. Sci. U. S. A.* **2009**, *106* (38), 16084.
(13) Shafaat, H. S.; Leigh, B. S.; Tauber, M. J.; Kim, J. E. *J. Phys. Chem. B* **2009**, *113* (1), 382.
(14) Shafaat, H. S.; Leigh, B. S.; Tauber, M. J.; Kim, J. E. *J. Am. Chem. Soc.* **2010**, *132* (26), 9030.
(15) Shafaat, H. S.; Kim, J. E. *J. Phys. Chem. Lett.* **2014**, *5*, 3009.
(16) Mcmillan, A. W.; Kier, B. L.; Shu, I.; Byrne, A.; Andersen, N. H.; Parson, W. W. *J. Phys. Chem. B* **2013**, *117*, 1790.
(17) Lendzian, F.; Sahlin, M.; Macmillan, F.; Bittl, R.; Fiege, R.; Po, S.; Sjo, B.; Gra, A.; Lubitz, W. **1996**, *7863* (9), 8111.
(18) Svistunenko, D. a; Wilson, M. T.; Cooper, C. E. *Biochim. Biophys. Acta* **2004**, *1655* (1–3), 372.
(19) Pogni, R.; Baratto, M. C.; Giansanti, S.; Teutloff, C.; Verdin, J.; Valderrama, B.; Lendzian, F.; Lubitz, W.; Vazquez-duhalt, R.; Basosi, R. *Biochemistry* **2005**, *44* (18), 4267.
(20) Huyett, J. E.; Doan, P. E.; Gurbiel, R.; Houseman, A. L. P.; Sivaraja, M.; Goodin, D. B.; Hoffman, B. M. *J. Am. Chem. Soc.* **1995**, *117* (35), 9033.
(21) Stoll, S.; Shafaat, H. S.; Krzystek, J.; Ozarowski, A.; Tauber, M. J.; Kim, J. E.; Britt, R. D. *J. Am. Chem. Soc.* **2011**, *133* (45), 18098.
(22) Stoll, S. In *Electron Paramagnetic Resonance*; Gilbert, B. C., Chechik, V., Murphy, D. M., Eds.; The Royal Society of Chemistry: Cambridge, U.K., 2011; pp 107–154.

(23) Un, S. *Magn. Reson. Chem.* **2005**, *43* (S1), 229.
(24) Bernini, C.; Pogni, R.; Ruiz-duen, F. J.; Martínez, A. T.; Basosi, R.; Sinicropi, A. *Phys. Chem. Chem. Phys.* **2011**, *13*, 5078.
(25) Bernini, C.; Pogni, R.; Basosi, R.; Sinicropi, A. *Proteins* **2012**, *80*, 1476.
(26) Bender, C. J.; Sahlin, M.; Babcock, G. T.; Barry, B. A.; Chandrashekar, T. K.; Salowe, S. P.; Stubbe, J.; Lindstrom, B.; Petersson, L.; Ehrenberg, A.; Sjöberg, B.-M. *J. Am. Chem. Soc.* **1989**, *111* (21), 8076.
(27) Stone, E. W.; Maki, A. H. *J. Chem. Phys.* **1962**, *37* (6), 1326.
(28) Sahlin, M.; Lassmann, G.; Potsch, S.; Sjöberg, B.-M.; Gräslund, A. *J. Biol. Chem.* **1995**, *270* (21), 12361.
(29) O'Malley, P. J.; Babcock, G. T. *J. Am. Chem. Soc.* **1986**, *108* (14), 3995.
(30) Furuta, K.; Tanizawa, Y.; Horiuchi, H.; Hiratsuka, H.; Okutsu, T. *Chem. Lett.* **2008**, *37* (4), 458.
(31) Wishart, D. S.; Sykes, B. D. *Methods Enzymol.* **1994**, *239*, 363.
(32) Andersen, N. H.; Neidigh, J. W.; Harris, S. M.; Lee, G. M.; Liu, Z.; Tong, H. *J. Am. Chem. Soc.* **1997**, *119* (36), 8547.
(33) Fesinmeyer, R. M.; Hudson, F. M.; Andersen, N. H. *J. Am. Chem. Soc.* **2004**, *126* (23), 7238.
(34) Neidigh, J. W.; Fesinmeyer, R. M.; Andersen, N. H. *Nat. Struct. Biol.* **2002**, *9* (6), 425.
(35) Qiu, L.; Pabit, S. a; Roitberg, A. E.; Hagen, S. J. *J. Am. Chem. Soc.* **2002**, *124* (44), 12952.
(36) Byrne, A.; Williams, D. V.; Barua, B.; Hagen, S. J.; Kier, B. L.; Andersen, N. H. *Biochemistry* **2014**, *53*, 6011.
(37) Scian, M.; Lin, J. C.; Le Trong, I.; Makhatadze, G. I.; Stenkamp, R. E.; Andersen, N. H. *Proc. Natl. Acad. Sci.* **2012**, *109* (31), 12521.
(38) Neidigh, J. W.; Fesinmeyer, R. M.; Prickett, K. S.; Andersen, N. H. *Biochemistry* **2001**, *40* (44), 13188.
(39) Barua, B.; Lin, J. C.; Williams, V. D.; Kummler, P.; Neidigh, J. W.; Andersen, N. H. *Protein Eng. Des. Sel.* **2008**, *21* (3), 171.
(40) Williams, D. V.; Barua, B.; Andersen, N. H. *Org. Biomol. Chem.* **2008**, *6* (23), 4287.
(41) Byrne, A.; Kier, B. L.; Williams, V. D.; Scian, M.; Andersen, N. H. *RSC Adv.* **2013**, *43*, 19824.
(42) Williams, D. V.; Byrne, A.; Stewart, J.; Andersen, N. H. *Biochemistry* **2011**, *50* (7), 1143.
(43) Byrne, A. NMR Studies of Polypeptide Structuring and Aggregation, University of Washington, 2013.
(44) Piotto, M.; Saudek, V.; Sklenar, V. *J. Biomol. NMR* **1992**, *2*, 661.
(45) Connor, H. D.; Sturgeon, B. E.; Mottley, C.; Sipe, H. J.; Mason, R. P. *J. Am. Chem. Soc.* **2008**, *130* (20), 6381.
(46) Clark, W. M. *Oxidation-Reduction Potentials of Organic Systems*; The Williams & Wilkins Co, Waverly Press Inc.: Baltimore, 1960.
(47) Molina, Á.; González, J. *Pulse Voltammetry in Physical Electrochemistry and Electroanalysis*; Springer International Publishing, 2016.
(48) Nguyen, N. T.; Wrona, M. Z.; Dryhurst, G. *J. Electroanal. Chem.* **1986**, *199*, 101.
(49) Tucker, D. J.; Bond, A. M.; Qing, Z.; Rivett, D. E. *J. Electroanal. Chem. Interfacial Electrochem.* **1989**, *261* (1), 127.
(50) Tommos, C.; Skalicky, J. J.; Pilloud, D. L.; Wand, A. J.; Dutton, P. L. *Biochemistry* **1999**, *38* (29), 9495.
(51) Berry, B. W.; Martínez-Rivera, M. C.; Tommos, C. *Proc. Natl. Acad. Sci. U. S. A.* **2012**, *109* (25), 9739.
(52) Mahmoudi, L.; Kissner, R.; Nauser, T.; Koppenol, W. H. *Biochemistry* **2016**, *55*, 2849.

Chapter 2 Appendix

Redox properties of tryptophan

A2.1 β-hairpin peptide studies

The β-hairpin peptides were synthesized in a manner similar to the trp-cages as reported in the main text Section 2.3.4. In this case, peptides were synthesized on a rink amide resin. In addition, after the final coupling and deprotection step, the N-terminus was acetylated by adding 3 mL of DMF, 140 µL of trimethylamine and 95 µL of acetic anhydride to the reaction vessel and allowing it to shake for ≈ 1.5 hours. The typical resin cleavage steps followed.

In the case of the β-hairpin system HP8, the sequence Ac-WVTIpGKKIWTG-NH_2 (where Ac– and –NH_2 indicate acetylation and amidation of the termini and "p" indicates D-Pro) has been established as the nearly 100 % folded construct based on NMR $^1H/^2H$ exchange studies.[1,2] The 100 % folded hairpin construct is stabilized by threonine 11 side chain –OH and the backbone NH H-bonding interactions with the N-terminal acetyl carbonyl. This is facilitated by the W/WTG cap and has been observed to be a stabilizing feature in many small β-hairpin constructs. The sequence –IpGK– forms the tight turn of the hairpin. Removal of one tryptophan is necessary for the studies herein and the mutation W10F was shown to have little effect on the folding stability. In addition, the 8th residue can be mutated to a variety of amino acids with little destabilization of the fold.[3] It has been established that β-sheet formation can be monitored using the backbone NH CSDs when they correlate with the NH chemical shift temperature gradient.[4] For the HP8 peptide Ac-WVTIpGK**X**IFTG-NH_2 used in these studies, the CSDs of T3α, X8α, V2NH, I4NH, and I9NH are used as the indicators of percentage folded. A hairpin structure is shown in Figure A2.1.

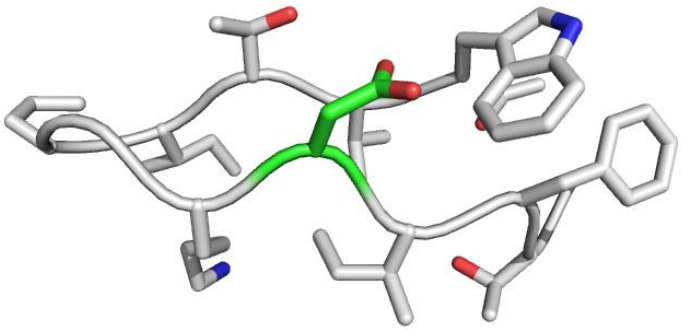

Figure A2.1. Structure of the hairpin peptide characterized by the Andersen group with the 8th residue highlighted in green. Image was generated from an unpublished ensemble of NMR structures for HP8a. The mutation to the 8th residue was done with the mutate function in Pymol. Hydrogens are omitted for clarity.

Table A2.1. β-hairpin fold populations based on indicated CSDs at pH=7.5 and 280 K

	T3 Ha	X8 Ha	V2 NH	I4 NH	I9 NH	Percent Folded
ref[a]	0.975	0.759	1.492	0.935	1.462	0.99
HP8F	0.987	0.757	1.224	0.733	1.193	0.88
HP8H	1.08	0.817	1.272	0.759	1.186	0.92
HP8R	0.991	0.799	1.342	0.853	1.233	0.94
HP8D	NA	NA	1.123	0.862	1.122	

[a] 99% folded sequence Ac-WVTIpGKKIWTG-NH_2

Table A2.2. β-hairpin fold populations based on indicated CSDs at pH=2.5 and 300 K

	T3 Ha	X8 Ha	V2 NH	I4 NH	I9 NH	Percent Folded
ref[a]	0.975	0.759	1.492	0.935	1.462	0.99
HP8F						
HP8H	1.051	0.698	1.409	0.766	1.164	0.90
HP8R						
HP8D	0.99	0.565	1.431	0.9	1.379	0.92

[a] 99% folded sequence Ac-WVTIpGKKIWTG-NH_2

Using a similar method of oxidizing the peptide with Ce^{IV} as described in the main text, the hairpin peptides can be oxidized for EPR studies. Shown in Figure A2.2 are the CW-EPR spectra of oxidized β-hairpin constructs. Figure A2.3 shows the ENDOR spectra of oxidized β-hairpins. ENDOR of a β-hairpin deuterated at tryptophan (labeled HP8D-d_5) shows that the paramagnetic signal is due to a tryptophan radical.

Generally, the spectra are similar to those presented for the trp-cage peptides in the main text. They show both a small splitting of ≈ 3.6 MHz and a larger splitting of ≈ 15 MHz. In addition, there are

noticeable broad features corresponding to a splitting of 30 MHz which are likely due to the C_β protons. Following equation 2.2 and using the angles θ of 71° and 47° from the NMR structure of HP8 (shown in Figure A2.1), the expected isotropic hyperfine couplings of the β protons in the hairpin peptides are 8 MHz and 36 MHz, respectively.

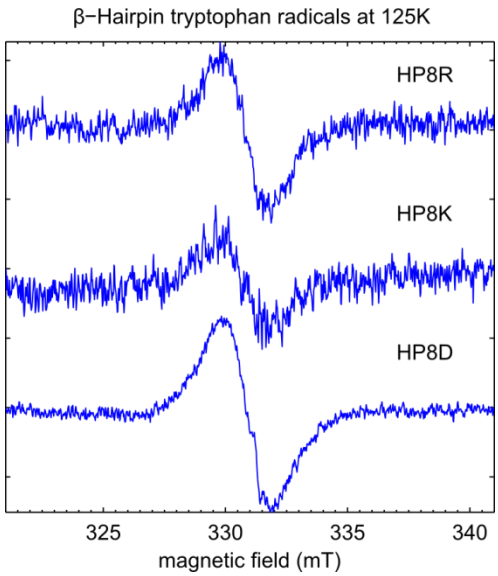

Figure A2.2. 9.29 GHz EPR spectra of β-hairpin radicals generated with Ce^{IV} ammonium nitrate. Spectra were recorded at 125 K with 13 μW of microwave power, a 2 G modulation amplitude, at 0.5 mT/s. Spectra are scaled by power, gain, and number of scans. β-hairpin radicals were generated by the addition of CAN in MeCN to peptides in tris buffer.

Some DPV experiments were also performed on the β-hairpin peptides. Generally, the redox potentials at pH 7.5 are all lower than for the trp-cage peptides. This is expected as the tryptophan side chain is more solvent exposed in the hairpin and burial of tryptophan in a peptide should increase the redox potential.[5] The β-hairpin peptides also follow the same trend of lower redox potentials found in more negative environments (i.e. when aspartate, D^-, is present vs. arginine, R^+). However, the difference is much smaller (within the error found for redox potentials of the trp-cage peptides) and further experiments would be necessary to determine if the difference is significant.

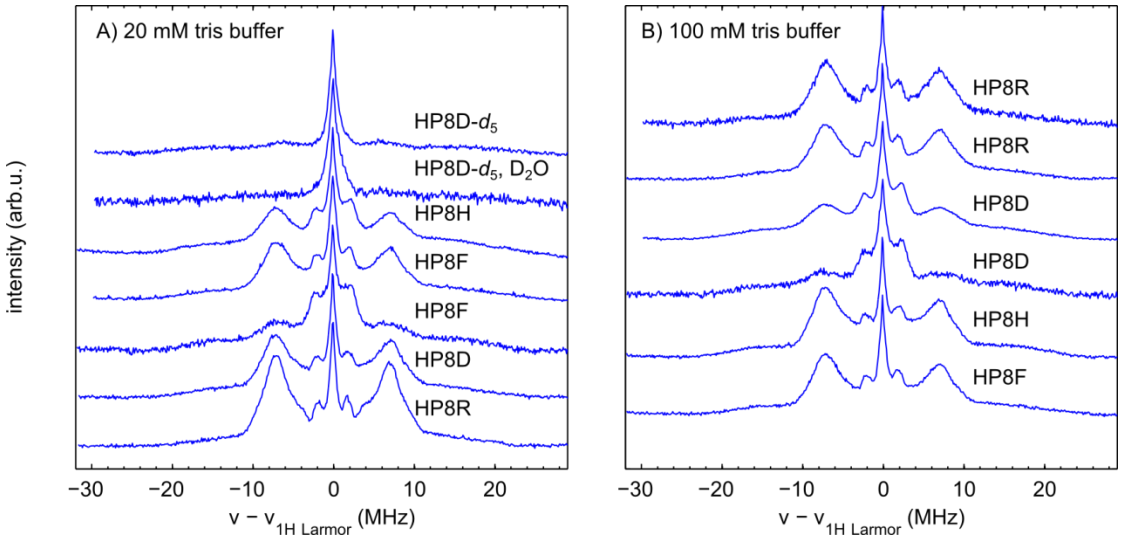

Figure A2.3. Davies ENDOR spectra near 34 GHz of β-hairpin peptides oxidized with Ce^{IV} ammonium nitrate. Spectra were collected at 40 K with $\pi(\pi/2)$ pulses of 100(50) ns and τ values between 230 and 400 ns. RF pulses ranging from 12.6 to 14 μs were applied to excite nuclear transitions. Data were collected with a 2 ms or longer repetition rate. A) Peptides were prepared in 20 mM tris buffer at pH = 7.5 before addition of Ce^{IV}. B) Peptides were prepared in 100 mM tris buffer at pH = 7.5 before addition of Ce^{IV}. However, both buffer systems shift to pH ≈ 2 upon addition of Ce^{IV}.

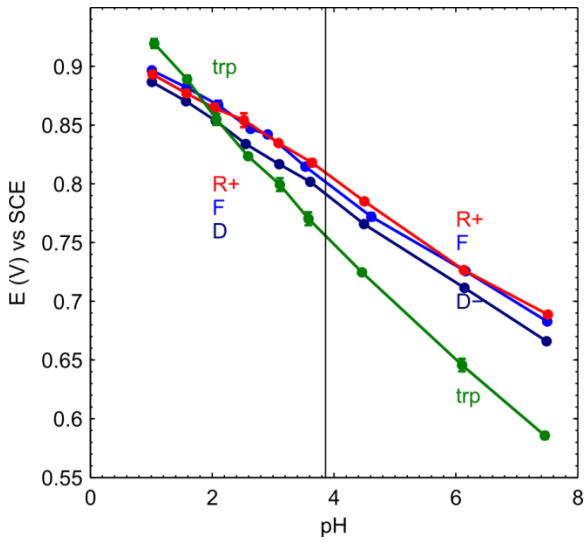

Figure A2.4. Applied potential at current maximum vs. solvent pH for differential pulse voltammograms of hairpin peptides. The 8th residue was systematically mutated in the peptides and is indicated in the figure. The fold populations are also indicated in percent. The vertical line marks the pK_a of the aspartate side chain. DPV was collected with a 50 mV pulse amplitude, 20 ms pulse width, and 100 ms period.

A2.2 Additional trp-cage data

A2.2.1 Cerium titration

Although oxidation of tryptophan containing peptides is efficient with Ce^{IV} and results in excellent signal-to-noise ratios for the EPR and ENDOR experiments, Ce^{IV} dramatically changes the pH of aqueous solutions. Shown in Figure A2.5 are curves produced by titrating in small aliquots of Ce^{IV} to a buffered solution. With the final Ce^{IV} concentration used to oxidize the peptides (≈ 10 mM), the final solution pH is always near 2.

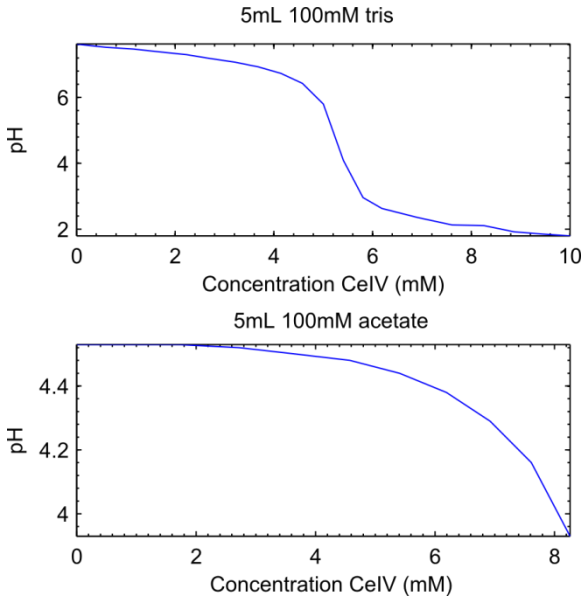

Figure A2.5. The dependence of pH on a solution of 100 mM tris or 100 mM acetate as 30 mM ceric ammonium nitrate in acetonitrile is titrated in to the solution in 100-200 µL increments. To prepare typical samples for ENDOR experiments on tryptophan containing peptides, the peptides were prepared in 100 mM tris at pH ≈ 7.2 Ce^{IV} was added to a final concentration of ≈ 10 mM making all of the ENDOR samples pH ≈ 2.

A2.2.2 Supplemental DPV data

The raw DPV voltammograms for selected trp-cage peptides are shown in Figure A2.6. These figures show the tryptophan oxidation peak as well as the background due to water oxidation. The background is removed from the tryptophan response by fitting it with a cubic spline and the subtracting it. This produces peaks which are fit with a Gaussian function to obtain the redox potential and FWHM which are plotted in Figure A2.7.

TC16bY3FD9AP12F 100 ms

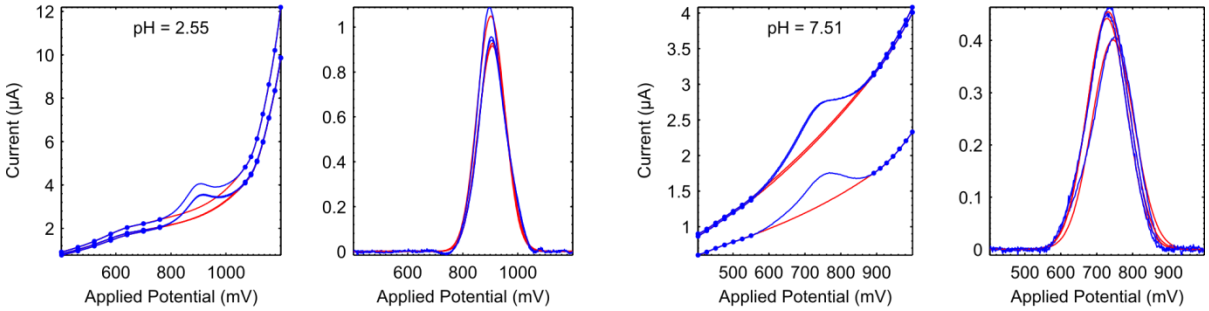

TC16bY3FD9LR16I 100 ms

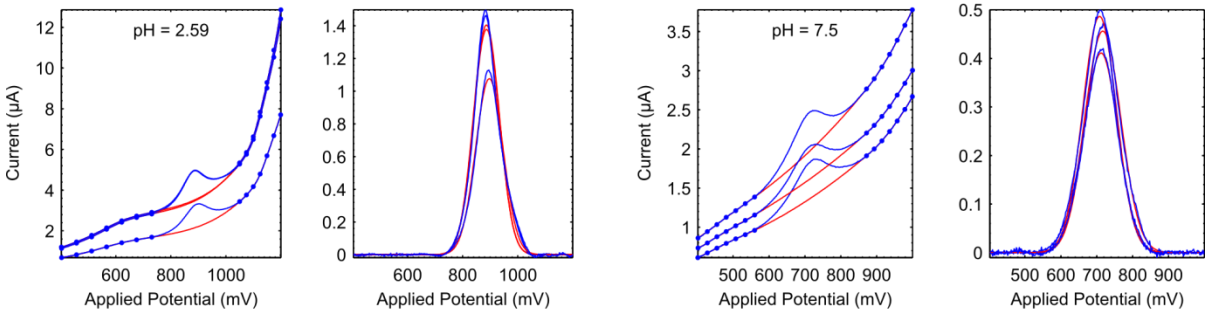

TC16bY3FP12F 100 ms

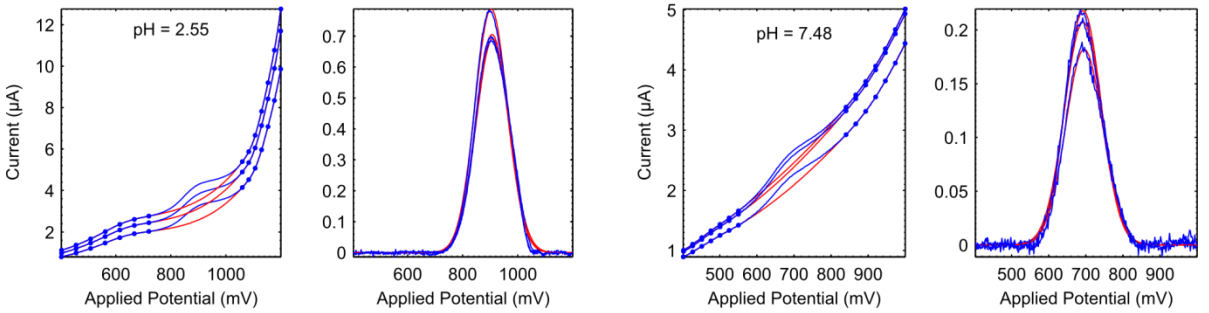

TC16bY3F 100 ms

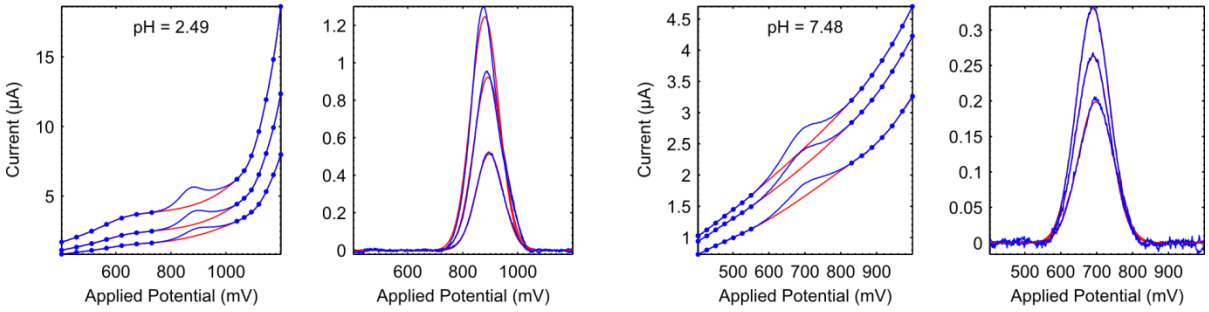

TC16bY3FR16I 100 ms

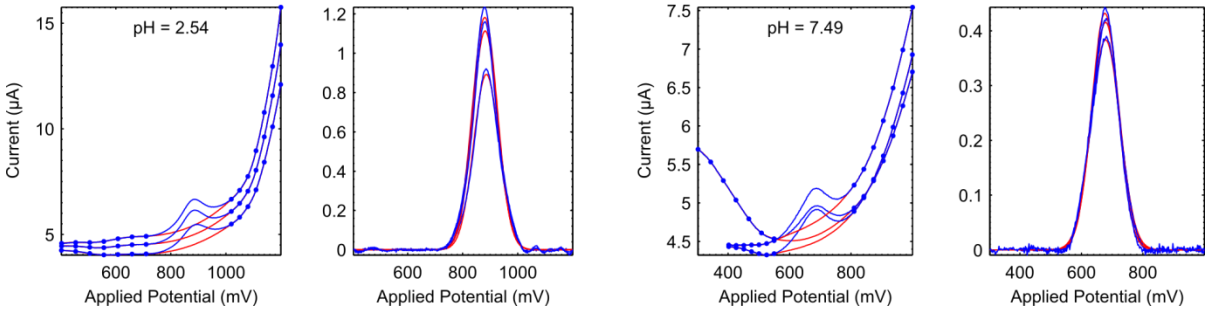

Figure A2.6. Representative differential pulse voltammograms of selected trp-cage peptides. Each panel contains an example of a triplicate data set taken on one sample vial. Raw voltammograms are shown in blue in the first column (at pH ≈ 2.5) and in the third column (at pH ≈ 7.5) from the left. Also shown in these columns are the fitted splines in red. The points indicate where the spline was fit. In the second and fourth columns in blue are the Gaussian peaks produced by subtracting the spline from the raw data. In red in these columns are the fitted Gaussian peaks. The average voltage at maximum current and average FWHM of the three Gaussians for each sample are used to create the points with standard deviation bars in Figure A2.7.

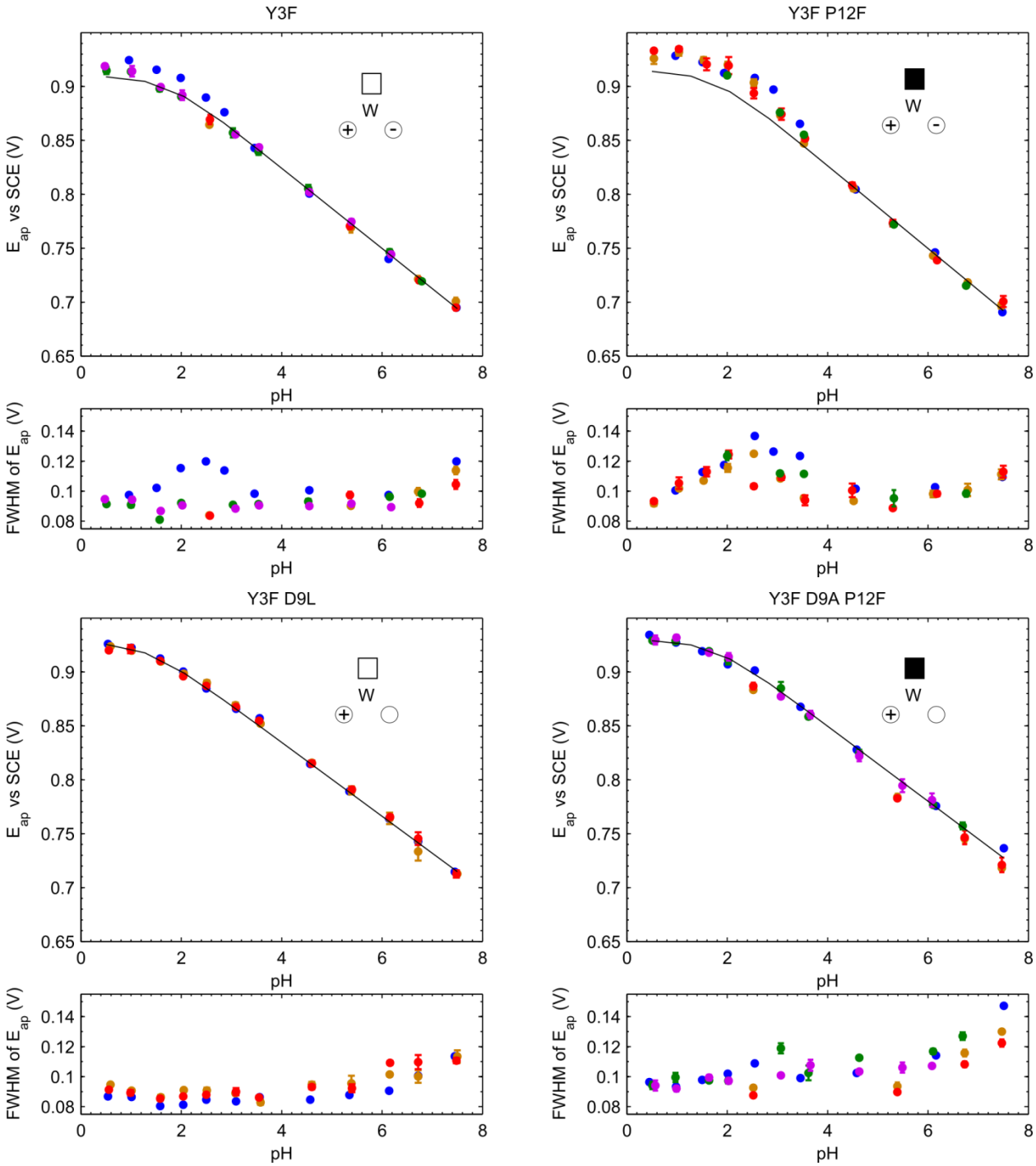

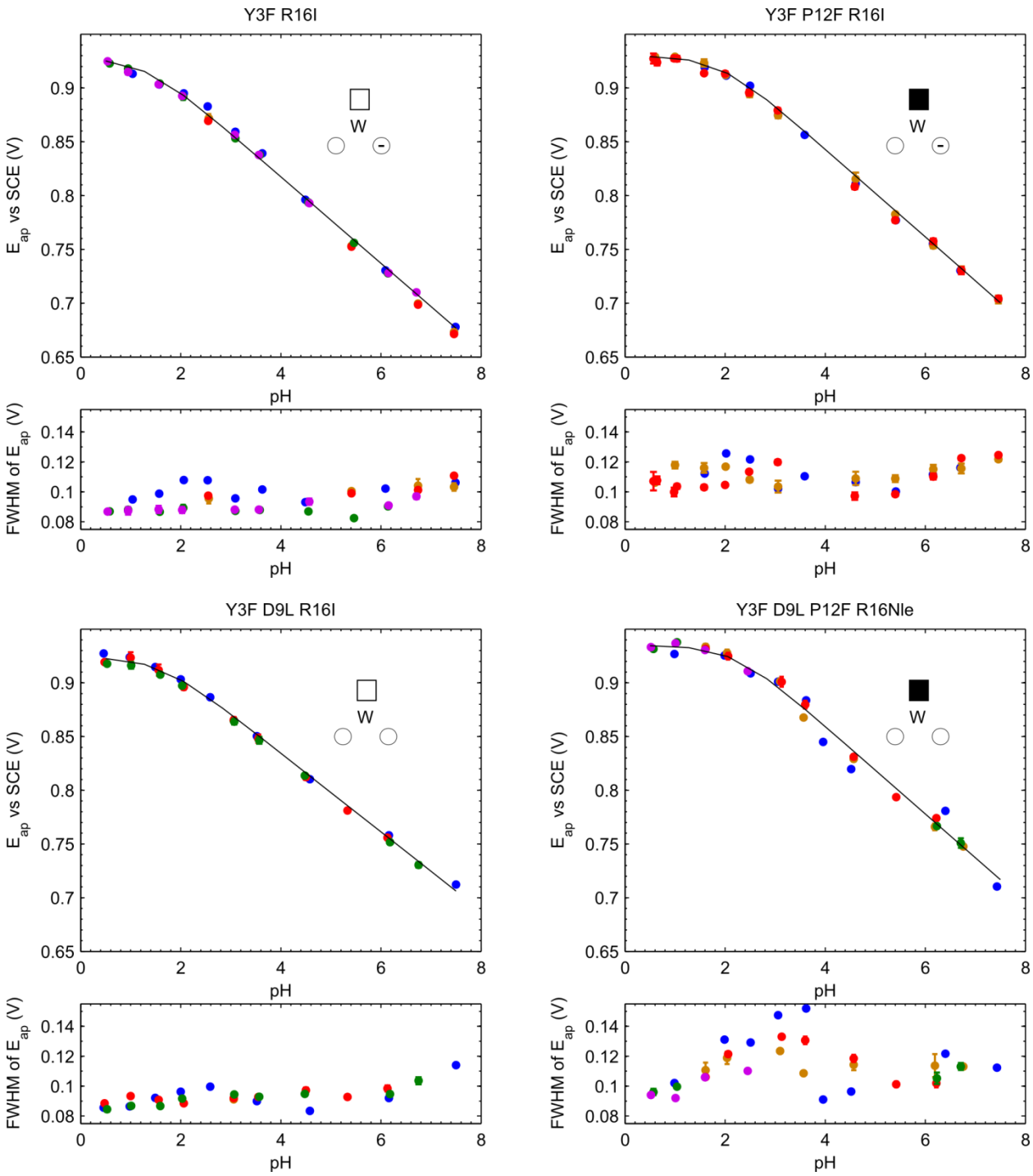

Figure A2.7. Pourbaix diagrams for each of the trp-cage constructs, along with a fit (black line) using equation 2.4. In addition, immediately below each Pourbaix diagram is the FWHM of the Gaussian of each data point. In each Pourbaix diagram and FWHM plot, the points of the same color were samples made from the same stock solution of peptide. The graphic inset within each Pourbaix diagram represents the changes to the 9th, 12th, and 16th residues that affect the microenvironment around tryptophan.

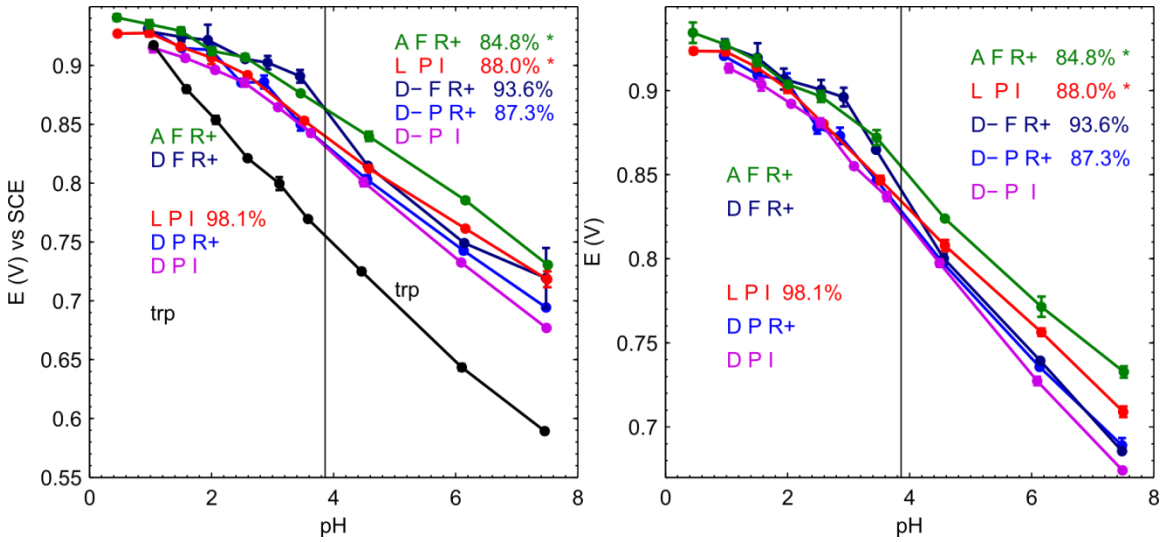

Figure A2.8. Applied potential at current maximum vs. solvent pH for differential pulse voltamograms of trp-cages peptides. The 9th, 12th, and 16th residues were systematically mutated in the peptides and are indicated in the figure. The fold populations are also indicated in percent. The vertical line marks the pK_a of the aspartate side chain. DPV was collected with a 50 mV pulse amplitude and 20 ms pulse width. On the left the voltammograms were collected with a 50 ms period and on the right with a 200 ms period. In addition on the left is a preliminary Pourbaix diagram of L-tryptophan.

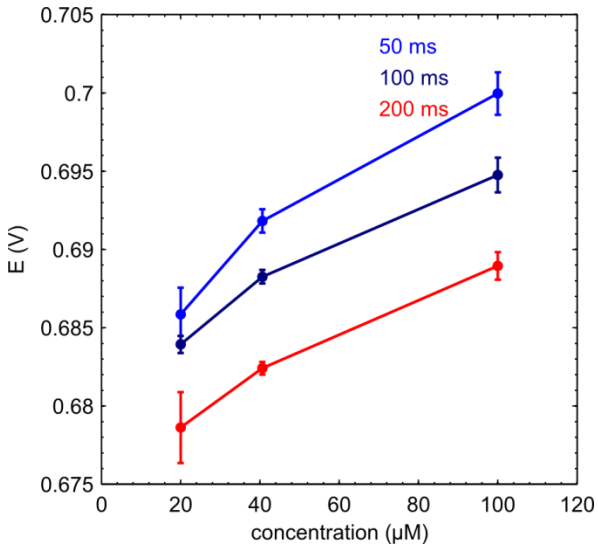

Figure A2.9. Applied potential at current maximum vs. concentration of TC16bY3F. DPV was collected with a 50 mV pulse amplitude, 20 ms pulse width, and the periods indicated in the figure (50ms, 100 ms, 200 ms).

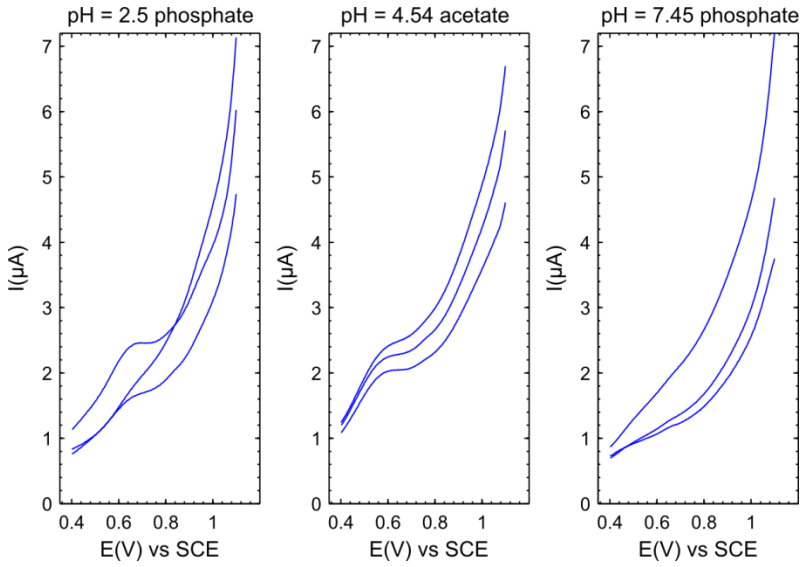

Figure A2.10. Differential pulse voltamograms of the buffers used to measure the redox pototentials of trp-cage and hairpin peptides.Current vs. applied potential vs. concentration of TC16bY3F. DPV was collected with a 50 mV pulse amplitude, 20 ms pulse width, and the periods indicated in the figure (50ms, 100 ms, 200 ms).

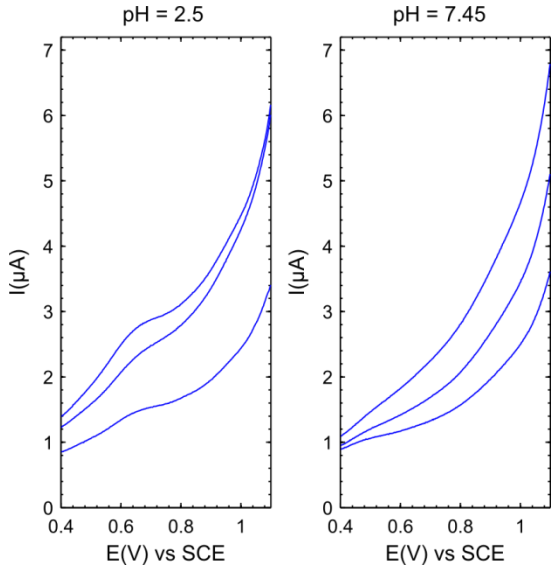

Figure A2.11. Differential pulse voltamograms of TC16bY3FD9LW6FR16Nle. DPV was collected with a 50 mV pulse amplitude, 20 ms pulse width, and periods of 50ms, 100 ms, 200 ms.

A2.3 Ru^{II} phototrigger

A2.3.1 Results

Ru^{II} phototriggers have been used previously to generate tryptophan and tyrosine radicals.[6,7] The mechanism for tryptophan oxidation with a Ru^{II} phototrigger is shown in Scheme A2.1. Ru^{II} has a broad

absorption band from 400-500 nm. Photoexcitation into this absorption band excites Ru^{II} to Ru^{III} by localizing an electron on the bipyridine ligand. An exogenous quencher (in this case $[Co^{III}(NH_3)_5Cl]^{2+}$) abstracts the electron leaving the highly oxidizing Ru^{III} species. If tryptophan is in close enough proximity to Ru^{III} for electron transfer to occur, a tryptophan radical will be generated which can be freeze quenched and studied by EPR spectroscopy.

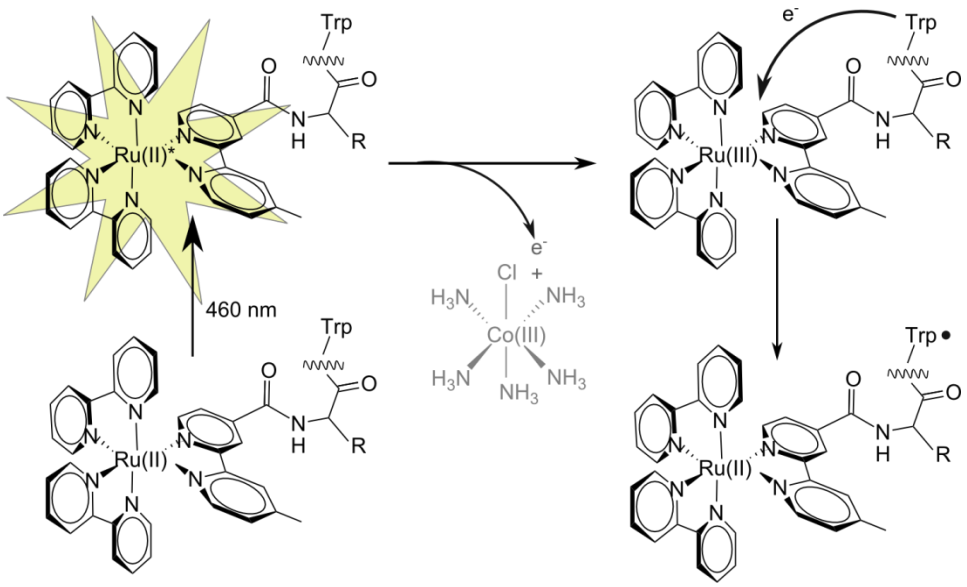

Scheme A2.1. Mechanism for Ru^{II} phototriggered oxidation of tryptophan residues in a peptide.

A trp-cage with Ru^{II} phototrigger covalently attached to the N-terminus of the peptide (sequence $Ru^{II}(2,2'\text{-bpy})_2(2,2'\text{-4-COOH-bpy})$-FAQWLADaGPASaRPPPS) was synthesized and found to be ≈ 82 % folded with 2D NMR experiments at 280 K and pH = 6.4. To test the if tryptophan radicals could be generated via Ru^{III} oxidation, a solution of 1 mM Ru^{II}-peptide and saturated Co^{III} in pH = 8 phosphate buffer was illuminated with visible light (420-600 nm) at room temperature in a quartz LN2 cold finger dewar. After ≈ 1 min of illumination, the sample was frozen by pouring LN2 into the quartz dewar and then immediately removed from the sample from the path of visible radiation. This procedure produced the EPR spectrum shown in Figure A2.12. It is identical in shape to EPR spectra produced by oxidizing trp-cage peptides with Ce^{IV}. The spectra produced with Ce^{IV} have been shown to be tryptophan based via deuterium labeling of the tryptophan indole ring. However, the reaction yield produced by Ru^{II}/Ru^{III}

oxidation is extremely low compared to Ce^{IV} oxidation (note the difference in signal-to-noise ratio of the two spectra).

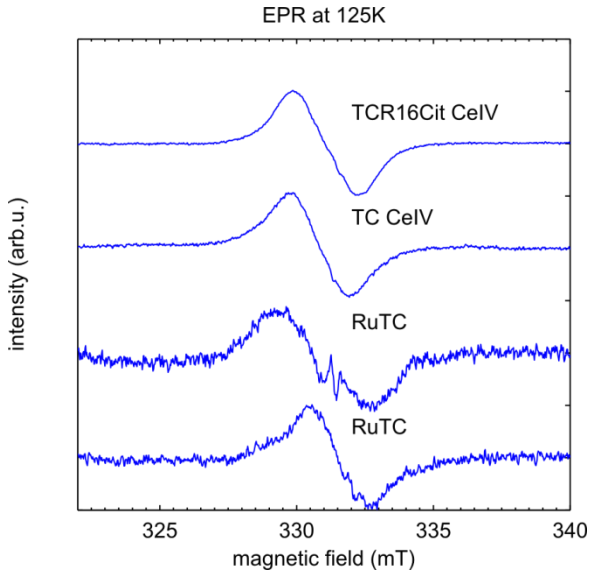

Figure A2.12. 9.38 GHz (bottom spectrum) and 9.29 GHz (second from bottom to top spectra) CW EPR spectra of radicals generated by Ru^{II} photoexcitation (labeled RuTC) or Ce^{IV} chemical oxidation (includes Ce^{IV} in label) of trp-cage peptides. Ru^{II} photooxidation produces a spectrum similar in width to Ce^{IV} oxidation. Spectrometer settings were as follows: modulation amplitude of 3 G or less, and microwave power of ≈ 13 μW.

A2.3.2 Outlook for phototriggered oxidation

The low yield of radicals obtained using Ru^{II}/Ru^{III} photooxidation compared to Ce^{IV} oxidation precluded further studies with this technique. However, one advantage of the phototrigger method of oxidation is its applicability through a range of pH values allowing studies of the neutral and cation tryptophan radical with EPR spectroscopy. Improvements to the yield of radicals may be made in the following ways:

1. Moving the Ru^{II} trigger closer to the tryptophan residue by further truncating the N-terminus of the trp-cage. If it is found that this compromises the folded structure of the trp-cage, a phototrigger may be attached to the hairpin system, where tryptophan is at the N-terminus.
2. Using a laser operating at the absorption maximum (450 nm) of Ru^{II} as the excitation source. This may increase the instantaneous yield of the Ru^{III} excited state and therefore the radical yield.

3. Combining the use of a laser with rapid freeze quench methods.
4. Incorporate a rhenium I phototrigger. The Re^{I}/Re^{II} phototriggers work in much the same way as Ru^{II}/Ru^{III} but have a ≈ 200 mV larger reduction potential which increases the driving force for tryptophan oxidation. The trigger can be covalently attached at either histidine residues or to the peptide N-terminus.[8–10]

A2.3.3 Methods

Synthesis of $Ru^{II}(2,2'\text{-bpy})_2(2,2'\text{-4-COOH-bpy})$ (abbreviated Ru^{II}-COOH). The starting materials cis-dichlorobis(2,2'-bipyridine)ruthenium(II) (abbreviated Ru^{II}) and 2,2'-bipyridine-4-carboxylic acid (abbreviated bipy-COOH) were purchased from Sigma Aldrich and used without further purification. 10 mg of bipy-COOH was suspended in (5 mL of 70 % ethanol in water). To this 27 mg (1:1 molar equivalents) of Ru^{II} was dissolved producing a dark purple color. The mixture was stirred under reflux for 5 hours. During this time, the solid bipy-COOH dissolved presumably as it chelated to Ru^{II}. Leftover solid bipy-COOH was removed by filtration and the solid rinsed with ethanol. The filtrate was a deep red. The presence of Ru^{II}(2,2'-bpy)2(2,2'-4-COOH-bpy) was confirmed by mass spectrometry. The filtrate was used without further purification as leftover Ru^{II} starting material (lacking a carboxyl group) was assumed to not interfere with covalent attachment to TC16bY3F.

Synthesis of Ru^{II}-TC16bY3F. The truncated version of TC16bY3F was prepared on resin by standard solid-state peptide synthesis as described in Section 2.3.4. A test cleavage of an aliquot of resin showed the presence of the desired peptide FAQWLADaGPASaRPPPS by mass spectroscopy. 20 μmol of Ru^{II}-COOH in acetonitrile was transferred to a round bottom flask and the MeCN removed under vacuum. 20 μmol of deprotected FAQWLADaGPASaRPPPS-resin was transferred to the round bottom flask. For coupling, typically 2-3 fold excess of 1-cyano-2-ethoxy-2-oxoethylidenaminooxy)dimethylamino-morpholino-carbenium hexafluorophosphate (COMU), 4-5 fold excess of DIEA per moles of peptide were used. For the 20 μmol preparation, ≈ 25 mg of COMU, 500 μL of NMP, and 25 μL of DIEA were added to the round bottom flask containing resin and Ru^{II}-COOH. The solution was stirred over night at room temperature. The resin was transferred to a reaction vessel equipped with a glass frit and rinsed with DCM. The

remaining resin was bright orange in color. The peptide was cleaved from the resin using the usual cleavage cocktail. Filtration, removal of TFA, and rinsing with diethyl ether was carried in the standard way. The bright orange peptide was dried under N_2 and stored at room temperature in the dark before purification.

Purification was carried using reverse-phase HPLC on a C18 column as described in Section 2.3.5. The presence of Ru^{II}-TC16bY3F was confirmed by mass spectrometry. The volume of purified peptide was reduced by rotary evaporation to ≈ 5 mL. This solution was frozen on dry ice and then lyophilized. The bright orange peptide was stored in powdered form in the dark. The percent fold was characterized by 2D NMR on a Bruker 700 MHz NMR as described in Section 2.3.2.

Synthesis of $[Co^{III}(NH_3)_5Cl]Cl_2$. 4.5 g of NH_4Cl was transferred to a flask to which 5 mL of H_2O was added. 10 mL of NH_4OH (≈ 15 M) was added and the mixture stirred. To this, H_2O was added in 2 mL increments until the NH_4Cl fully dissolved (about 6 mL more H_2O). 3.91 g of Co^{II} hexahydrate was added to the flask which turned the solution a reddish brown. 4mL (by mass) of 30% H_2O_2 was added to the flask and stirred. To this, 12 mL of HCl (14.8 M) was added and the solution stirred. This solution was heated to 80 °C and stirred for 30 minutes which resulted in a dark blue color. After cooling to room temperature. The solution was filtered using a Buechner funnel and rinsed with H_2O. The solid was returned to the reaction flask by rinsing the filter paper with H_2O to a volume of ≈ 40 mL. To this, 12 mL NH_4OH (14 M) and 30 mL HCl (12.8 M) were added and the solution heated to 80 °C for 40 minutes. This solution was cooled in an ice bath until solid began to precipitate. The solid was filtered using Buechner funnel and left to dry. The result was bright pink solid and the mass was confirmed with ESI-MS.

A2.4 Direct UV oxidation of trp

A2.4.1 UV photooxidation without quenchers

The tryptophan indole ring absorbs light at 280 nm. When a frozen sample of L-tryptophan in 10-60% v/v glycerol/ice is exposed to UV radiation, the sample develops an EPR spectrum. This occurs both for samples exposed to UV radiation from a xenon arc lamp or the 266 nm fourth harmonic of an Nd:YAG

laser (see A2.4.4 Methods section below for experimental details). This behavior has been observed previously and the EPR signal attributed to a mixture of tryptophan radicals and hydrated electrons.[11] Glycerol (used as a glassing agent) in water develops only a weak EPR signal during long periods of UV irradiation (≈ 40 min, data not shown), so all EPR signals studied herein are attributed to tryptophan radicals and hydrated electrons. Despite L-tryptophan developing a strong EPR signal when exposed to UV radiation, ENDOR spectroscopy revealed no substantial ^{1}H hyperfine coupling at X-band (data not shown).

Frozen aqueous samples of trp-cage peptides also develop an EPR signal when exposed to UV radiation. Samples of trp-cage peptides were typically prepared at concentrations of 200 μM or less which is favorable to keep the samples magnetically dilute to prevent inter-peptide dipolar coupling and distortion of the signal. It was found that the Nd:YAG laser produced EPR spectra in a shorter amount of time for these samples so it was used primarily as the radiation source.

A2.4.2 UV photooxidation without quenchers: temperature dependence

Shown in Figure A2.13 are the CW-EPR spectra of L-trp, TC16bY3FD9AR16Nva, and TC16bY3FR16Cit produced by UV irradiation. Samples were typically prepared in D_2O ice to reduce the linewidth of the hyperfine features due to the hydrated electron (note the sharpened features in Figure A2.13 of L-trp, D_2O compared to L-trp, H_2O).

The spectra in Figure A2.13 show a large, narrow feature at 331 mT. This feature decreases in intensity when the sample temperature in the EPR cavity is raised from 120 K to 150 K without any additional exposure to radiation. After this irreversible annealing process (i.e. the feature at 331 mT does not grow in if the temperature is lowered back to 120 K) the spectra for L-trp and the trp-cage peptides appear nearly identical.

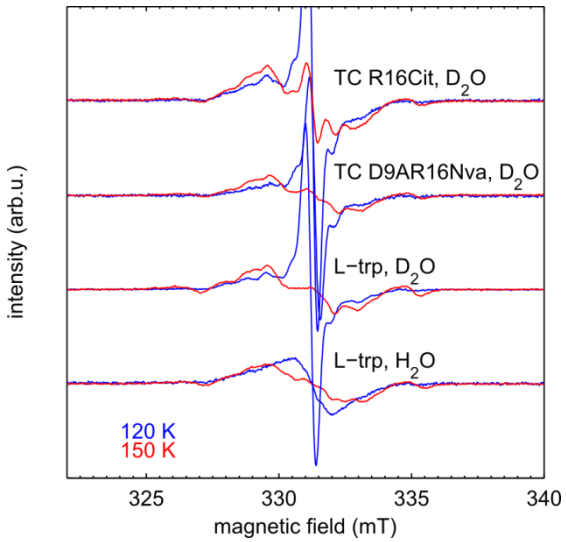

Figure A2.13. 9.3 GHz CW EPR spectra of L-tryptophan and TC16bY3F varients produced by exposing samples to UV radiation (≈ 700 µJ pulses at 266 nm from an Nd:YAG laser operating at 10 Hz) for about 30 seconds at 77 K. Spectrometer settings were as follows: modulation amplitude of 1 G, and microwave power of ≈ 50 µW or less. Spectra are scaled by number of scans, receiver gain, and microwave power.

To studies these photo-induced radicals with ENDOR spectroscopy, the samples were irradiated in an external cold finger at 77 K, then transferred into the pulse EPR spectrometer. During this transfer time, the samples reached an unknown temperature greater than 77 K and as a result, the pulse field-swept spectra (bottom spectra in Figure A2.14) did not show the large narrow feature. ENDOR spectroscopy was carried out on two trp-cage peptides at X-band (data not shown) and Q-band (Figure A2.14). However, ENDOR experiments, carried out at several field positions, did not display the strong (5-34 MHz) hyperfine coupling expected for the ^{1}H atoms on the indole ring and on C_{β} based on the theory and literature.

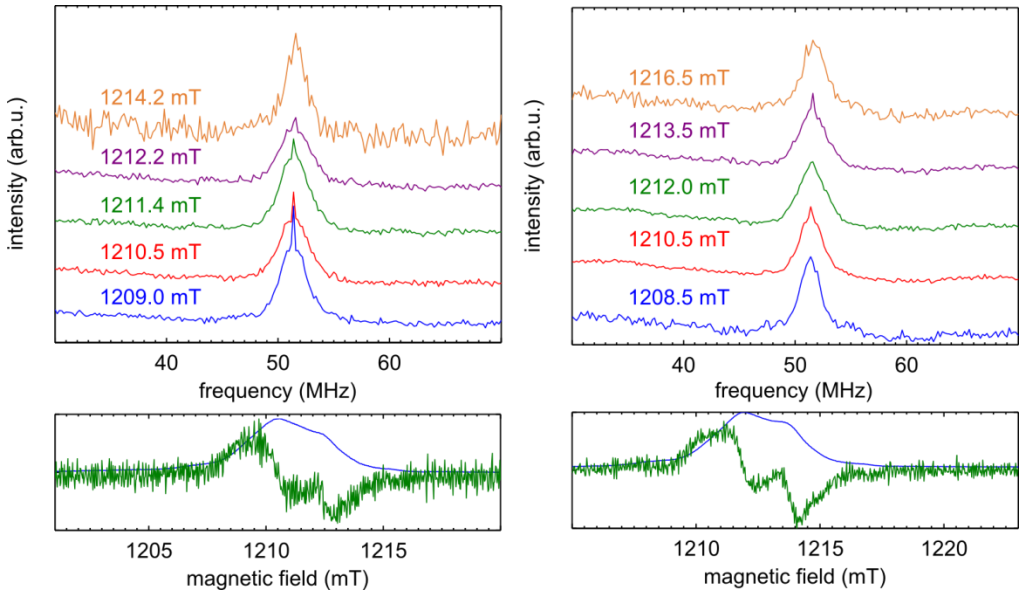

Figure A2.14. 33.9 GHz ENDOR spectroscopy on 200 µM trp-cage peptides (left, TC16bR16Cit; right, TC16bD9AR16Nva) in 60 or 10% glycerol and D_2O. Signals were generated by exposing samples to UV radiation (≈ 500 µJ pulses at 266 nm from an Nd:YAG laser operating at 10 Hz) for about 30 seconds at 77 K. ENDOR was collected at 40 K with the Davies pulse sequence with (200 ns), $\pi/2$(100 ns), (600 ns), shot repetition time (5 ms or 2 ms) and (12 or 12.5 µs) RF pulse. ENDOR was collected at the fields indicated in the figure. The bottom spectra show the 2-pulse echo detected field sweeps (blue) along with first derivatives (green).

A2.4.3 UV photooxidation with quenchers

Due to the presence of the hydrated electron in samples exposed to UV radiation, several electron quencher were added to solutions of tryptophan before UV irradiation. The quenchers (Fe^{III}, Co^{III}, and Cu^{II}) could act as places for the hydrated electron to localize. In their reduced forms, the quenchers are either EPR silent or only have EPR spectra at very low temperatures (≈ 10 K) compared to 120 K used for CW-EPR and 40 K used for ENDOR. However, in control experiments, it was shown that $[Fe^{III}(CN)_6]^{3-}$ and $[Co^{III}(NH_3)_5Cl]^{2+}$ both develop EPR spectra when exposed to UV radiation in the absence of tryptophan, which only complicate the spectra instead of simplifying them (Figure A2.15). The Cu^{II} quencher is EPR active which gives rise to the negative feature at the edge of the spectrum at 323 mT in Figure A2.15. The sample containing Cu^{II} and L-trp developed an EPR spectrum after exposure to UV radiation. However, the spectrum appears similar to the spectra obtained by exposing only L-tryptophan to UV radiation and then annealing (i.e. Figure A2.13 above).

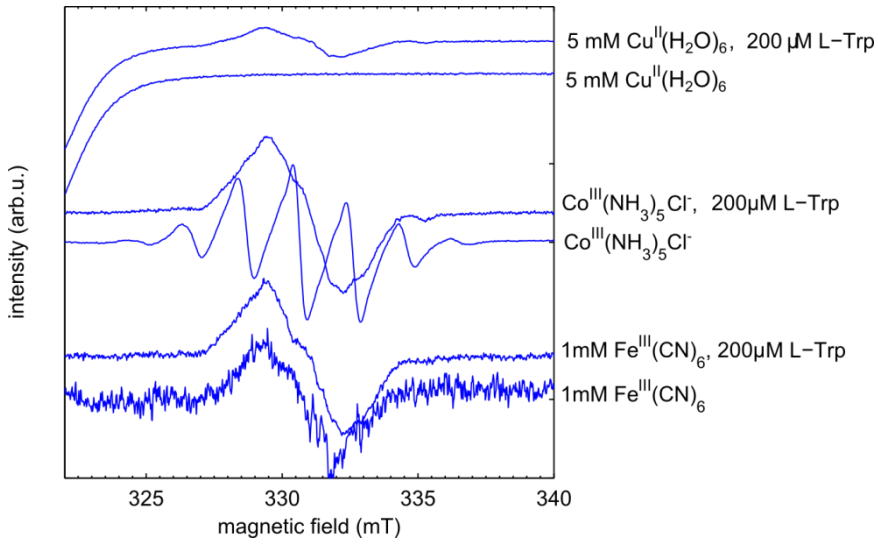

Figure A2.15. 9.3 GHz CW EPR spectra of metal compounds used as hydrated electron quenchers and mixtures of metal quenchers with L-tryptophan. In samples with mixtures, the metal quencher was always added in excess. Signals were generated by exposing samples to UV radiation (≈ 800 µJ pulses at 266 nm from an Nd:YAG laser operating at 10 Hz) for up to 100 seconds at 77 K. However, the spectrum labeled 5 mM $Cu^{II}(H_2O)_6$ was not exposed to UV radiation. EPR spectra were collected at ≈ 125 K. The spectra of $Fe^{III}CN_6$ and $Co^{III}(NH_3)_5Cl$ were collected with 2 mW of microwave power and 3 G modulation amplitude. All other spectra were collected with 50 µW of power or less and 3 G or less modulation amplitude.

A2.4.4 Methods

Sample preparation for photooxidation. Samples were prepared by dissolving L-tryptophan or trp-cage peptides to 1 mM (Sigma-Aldrich) in unbuffered solutions of 0 %, 10 %, or 60 % v/v glycerol to nanopure water. These solutions were then diluted to final concentrations of 100-200 µM and delivered to a 4 mm O.D. quartz EPR tubes (X-band) or 1.5 mm quartz EPR tubes (Q-band). Dioxygen was removed from the sample using three cycles of freeze-pump-thaw under vacuum and argon on a Schlenk line. Samples were frozen before removing from the Schlenk line and used immediately or stored at 77 K for a maximum of two days before performing EPR experiments.

Photooxidation-xenon arc lamp. Samples were exposed to ≈ 20 minutes of continuous UV radiation using a xenon arc lamp equipped with a 260-320 nm dichroic filter through the optical window of the SHQE (Bruker) resonant cavity held at 125 K. The UV power reaching the samples ranged from 30 mW to 55 mW.

Photooxidation-Nd:YAG laser. Samples were oxidized at 77 K with the 266 nm fourth harmonic of a Continuum Surelite Q-switched Nd:YAG laser with pulse power between 300 and 600 uJ operating at 10 Hz. Samples were irradiated between 30-120 seconds, transferred to the EPR spectrometer while frozen and examined at 125 K for CW EPR or 40 K for pulse ENDOR.

CW-EPR Spectroscopy. All samples were checked for microwave power saturation effects spectra were collected at a microwave power below the saturation limit.

A2.5 *In situ* continuous-flow chemical and electrochemical oxidation of tryptophan

The short lifetime of the tryptophan radicals generated in the peptides is evidenced by the irreversible electrochemical experiments. This creates the need for freeze trapping the unstable radicals. However, studying the EPR properties of the radicals at room temperature in solution has the advantage of the anisotropic component of the hyperfine tensors averaging to zero due to tumbling of the molecule. This produces EPR spectra with sharp lines due only to the isotropic component of the hyperfine coupling.[12] As discussed in the introduction, this isotropic coupling can be directly related to the spin density distribution on the tryptophan indole ring.

The oxidation of trp-cage and β-hairpin peptides can be carried out in high yield with Ce^{IV} as oxidizing agent which produces CW and pulse EPR spectra with high signal-to-noise ratios. However, these experiments must be performed at low pH for Ce^{IV} to be sufficiently oxidizing. As all side chain residues are expected to be protonated, this removes the ability to study the influence of a negatively charged microenvironment on the magnetic properties. Instead, electrochemical oxidation offers the opportunity to generate radical species at a wide variety of pH values. As both methods of oxidation have advantages, continuous flow EPR experiments were carried out using both techniques.

There are several factors to consider when designing an *in situ* continuous-flow sample chamber:

1. If one wants to monitor the behavior of tryptophan radicals at various pH values, the experiment must be done in aqueous buffer. The high dielectric constant of water makes it a challenging solvent

to tune the EPR resonator to for experiments. Thus small sample outer diameters (less than ≈ 0.7 mm) are necessary to keep the aqueous buffer out of the high-electric-field areas in the resonator.

2. For electrochemical oxidation, the electrode geometry must be controlled to prevent short circuiting of the cell due to the working electrode and counter electrode coming in contact within the small sample diameter.
3. For chemical oxidation, efficient mixing of the analyte (peptide) and oxidant (Ce^{IV}) must be achieved. In addition, because of the short lifetime of the tryptophan radicals, this must occur very close to the sensitive region of the EPR resonator, so that very little time happens between oxidation and measurement of the species.

The following subsections will discuss the strategies used to overcome these challenges using both electrochemical and chemical oxidation.

A2.5.1 Syringe pump and sample tubing

A dual syringe pump with 30 mL Luer lock tip syringes was used for continuous-flow experiments. Teflon tubing with an inner diameter of 1/32 inch and outer diameter of 1/16 inch was used as the sample tubing in the EPR resonator. Tubing inner diameter of 1/32 inch maximizes the sample outer diameter that can be used without interfering with the electric field component of the microwave radiation. Finally, the Teflon tubing was fed through a quartz tube the length of the EPR resonator before inserting in the resonator. The rigid quartz helped prevent vibrations in the Teflon tubing from changing the tuning in the resonator.

A2.5.2 Electrode design: Testing continuous flow electrochemistry on Q_{10}

Several cell setups have been proposed for electrochemically generating EPR active species in the EPR resonator, and electrodes used here were designed based on these reports.[13,14] A bare platinum wire (125 µm diameter) was used as counter electrode and PFA (perfluoroalkoxy) coated platinum wire (203 µm diameter with coating) was used as working electrode. These wires were attached to copper wire with silver paint and then the copper and joint were wrapped in Teflon tape to prevent short circuiting.

Electrode leads were connected directly to the long copper wire which kept magnetic components out of the magnetic field of the EPR spectrometer. About 10 mm of the PFA coating at the end of the working electrode was removed to expose the platinum surface. When inserted into sample tubes, the working and counter electrodes were offset so that the exposed platinum wires were not touching.

No reference electrode was used in this setup, so the reference electrode lead was connected to the counter electrode. The applied potential is referenced to the open-circuit current of the solution being measured. This means a CV voltammogram must be collected before electrolysis of the solution to know what potential needs to be applied to oxidize or reduce the species of interest. To test the quality of the electrodes, experiments were first carried out on a solution of 1 mM coenzyme Q_{10} (or ubiquinone) in DCM with 100 mM tetrabutylammonium hexafluorophosphate (CAS 3109-63-5) as electrolyte. This solution was loaded into a 30 mL syringe and Teflon tubing fed from the syringe through the top of the EPR resonator. The electrodes were fed through the opening in the bottom of the Teflon tubing and positioned so that the working electrode was centered in the most sensitive part of the resonator. A cyclic voltammogram of this configuration (without flow from the syringe pump) revealed a cathodic peak at roughly -3 V (see top of Figure A2.16). To measure the EPR spectrum, a constant voltage more negative than -3 V was applied to the cell and the solution in the cell was refreshed by turning on the syringe pump. As can be seen in Figure A2.16., an EPR spectrum of reduced Q_{10} grows in once the potential is nearly 1 V more negative than the cathodic peak (spectrum 2). To test that the solution was refreshed, spectra 4 and 5 were collected after letting the sample continue flowing, but turning off the applied potential. Finally, the highest-intensity signal was obtained when a potential of -4.1 V was applied and the flow rate decreased (spectrum 7, presumably because low flow allowed the EPR active species to accumulate).

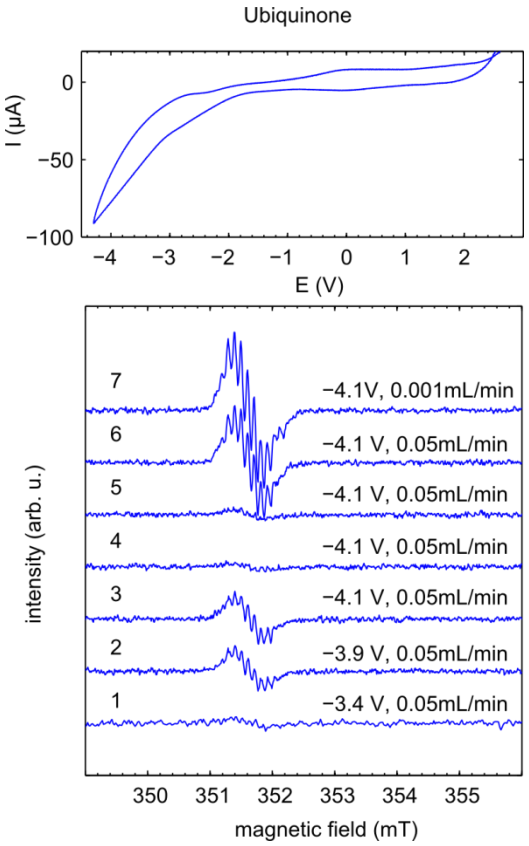

Figure A2.16. *Top:* The cyclic voltammogram of 1 mM Q_{10} in DCM with 100 mM tetrabutylammonium hexafluorophosphate as electrolyte. *Bottom:* The EPR spectrum of Q_{10} produced by applying the constant potentials indicated in the figure.

A2.5.3 Continuous flow electrochemistry on L-trp and peptides

Aqueous solutions between 100 μM to 1 mM of L-tryptophan or trp-cage peptide were prepared with 100 mM KCl as electrolyte. Reactive oxygen was removed from these solutions by purging with N_2 for about 30 minutes. For L-tryptophan, up to 20 mL of this solution was added in to the 30 mL syringe. The solution was added into the EPR cavity suing the syringe pump. At 0 mL/min, a cyclic voltammogram was acquired to determine where the water oxidation peak was located (Figure A2.17). The flow of the syringe pump was then set and a constant potential roughly 1 V greater than the anodic peak due to tryptophan was applied to the continuously flowing sample. With flow rates ranging from 0.1 mL/min to 10 mL/min no EPR active species were observed. A similar experiment was carried out using a solution of a hairpin peptide and similar results were observed. The lack of observable EPR active species could be due to several problems:

1. *Decay of the species.* The volume of sample in the resonator active space is roughly 4 µL assuming a 1 cm resonator active space and 0.035 cm tubing radius. With a flow rate of 10 mL/min the sample volume in the resonator is completely refreshed every ≈ 25 ms. The decay rate of the tryptophan radicals in the trp-cage and β-hairpin peptides is not known exactly but implied to be on the 10 s of ms scale from the irreversible electrochemical experiments. This could be improved with faster flow rates, however, large samples volumes, and therefore large synthetic preparations of peptides, would need to be prepared.
2. *Instantaneous yield of radicals*. Radicals can only be generated at the surface of the electrode. The small surface of the thin platinum wire may not generate enough radicals instantaneously to be observed given the sensitivity of the EPR experiment. This may be improved with mesh electrodes with larger surface area.

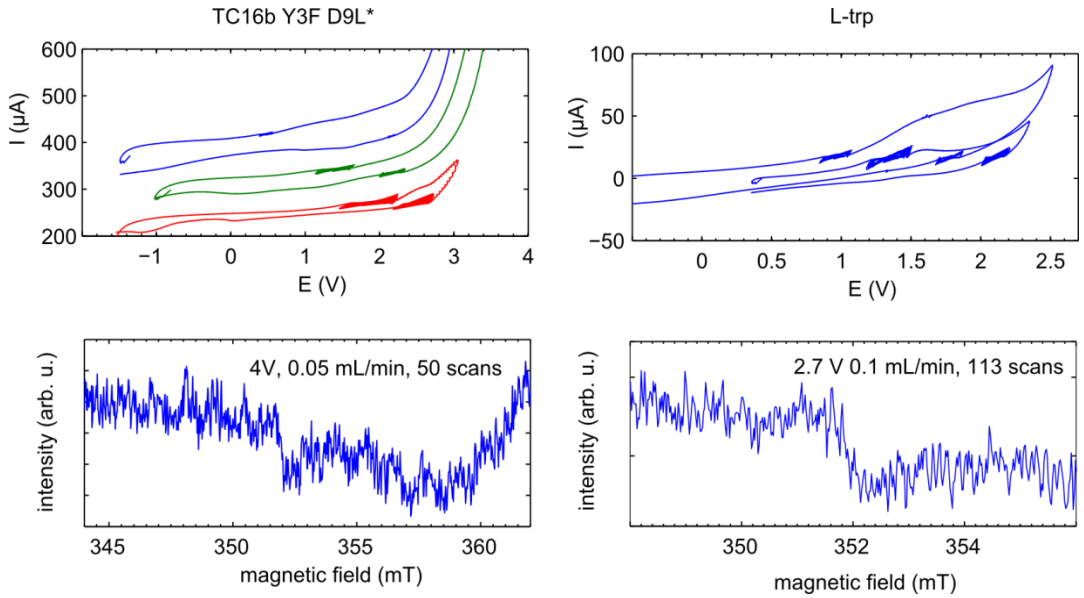

Figure A2.17. *Top:* The cyclic voltammograms of TC16bY3FD9L* (missing the C terminal serine) and L-tryptophan in 100 mM aqueous KCl referenced to the open-circuit potential. CVs were collected with scane rates of 1000mV/s. *Bottom:* EPR spectra of continuously flowing solutions of TC16bY3FD9L* and L-tryptophan in 100 mM aqueous KCl when a constant potential approximately 1 V larger than the anodic peak is applied. EPR spectra were recorded with scan rates of 20 s, modulation amplitudes of 8 G or greater, and microwave power of 20 mW or less.

A2.5.4 Continuous-flow chemical oxidation of L-trp and peptides

Ce^{IV} ammonium nitrate was prepared to a concentration of 10 mM in acetonitrile. A solution of L-trp was prepared in tris buffer to 1 mM concentration. Each solution was degassed on a Schlenk line. The removal of dissolved gases was necessary so that bubbles did not form at the mixing point of the two solvents. 10 mL of each solution was loaded into separate syringes and these were loaded on to the dual syringe pump. Teflon tubing of outer diameter 1/16 in and inner diameter 1/64 in were connected to the Luer lock of each syringe. The ends of each Teflon tube were fitted to an HPLC T-joint. The output of the T-joint was connected to Teflon tubing of 1/32 inner diameter and 1/16 outer diameter. The T-joint was positioned immediately outside the EPR cavity approximately 3 cm above the active space of the resonator.

The syringe pump was switched on with flow rates between 0.1 and 10 mL/min while constantly collecting EPR spectra with scan rates of 20 s, modulation amplitudes of 8 G or greater, and microwave power of 20 mW or less. No EPR active species were observed. This was also attempted in a similar manner with 100 μM solutions of β-hairpin peptide HP8D and again no EPR active species were observed.

A2.6 References

(1) Kier, B. L.; Andersen, N. H. *J. Am. Chem. Soc.* **2008**, *130* (44), 14675.
(2) Kier, B. L.; Shu, I.; Eidenschink, L. A.; Andersen, N. H. *Proc. Natl. Acad. Sci.* **2010**, *107* (23), 10466.
(3) Mcmillan, A. W.; Kier, B. L.; Shu, I.; Byrne, A.; Andersen, N. H.; Parson, W. W. *J. Phys. Chem. B* **2013**, *117*, 1790.
(4) Andersen, N. H.; Neidigh, J. W.; Harris, S. M.; Lee, G. M.; Liu, Z.; Tong, H. *J. Am. Chem. Soc.* **1997**, *119* (36), 8547.
(5) Tommos, C.; Skalicky, J. J.; Pilloud, D. L.; Wand, A. J.; Dutton, P. L. *Biochemistry* **1999**, *38* (29), 9495.
(6) Sjödin, M.; Styring, S.; Wolpher, H.; Xu, Y.; Sun, L.; Hammarström, L. *J. Am. Chem. Soc.* **2005**, *127* (11), 3855.
(7) Irebo, T.; Johansson, O.; Hammarström, L. *J. Am. Chem. Soc.* **2008**, *130* (29), 9194.
(8) Di Bilio, A. J.; Crane, B. R.; Wehbi, W. A.; Kiser, C. N.; Abu-Omar, M. M.; Carlos, R. M.; Richards, J. H.; Winkler, J. R.; Gray, H. B. *J. Am. Chem. Soc.* **2001**, *123* (13), 3181.
(9) Shafaat, H. S.; Leigh, B. S.; Tauber, M. J.; Kim, J. E. *J. Am. Chem. Soc.* **2010**, *132* (26), 9030.
(10) Holder, P. G.; Pizano, A. a; Anderson, B. L.; Stubbe, J.; Nocera, D. G. *J. Am. Chem. Soc.* **2012**, *134* (2), 1172.
(11) Mahmoud, G. S.; Melø, T. B. *J. Photochem. Photobiol. B.* **1990**, *5* (3–4), 467.

(12) Connor, H. D.; Sturgeon, B. E.; Mottley, C.; Sipe, H. J.; Mason, R. P. *J. Am. Chem. Soc.* **2008**, *130* (20), 6381.
(13) Murray, P. R.; Collison, D.; Daff, S.; Austin, N.; Edge, R.; Flynn, B. W.; Jack, L.; Leroux, F.; McInnes, E. J. L.; Murray, A. F.; Sells, D.; Stevenson, T.; Wolowska, J.; Yellowlees, L. J. *J. Magn. Reson.* **2011**, *213* (1), 206.
(14) Morsy, M. A.; Kawde, A. M. *Electrochim. Acta* **2015**, *160*, 22.

Chapter 3

Identifying organic radicals in the spore photoproduct lyase active site

Abstract

The spore photoproduct lyase (SPL) is a 4Fe-4S cluster enzyme that utilizes the cofactor *S*-adenosyl methionine (SAM) to catalyze the repair of a specific UV-photodamage product in DNA known as the spore photoproduct (SP), which is a dimer of thymidine bases. Both the mechanisms of formation and repair of SP are still actively under investigation and suggested to proceed through radical intermediates. The suggested repair mechanism of SP by SPL involves a series of hydrogen atom transfers through a SAM-based radical, a tyrosyl radical, and a cysteinyl radical. Both the 4Fe-4S cluster and the suggested organic radicals are amenable to study with EPR spectroscopy. We made a series of mutations to the relevant amino acid residues in the SPL active site. The changes in binding affinity of SAM due to the various mutations can be correlated with the extent of the spectral changes to the 4Fe-4S cluster EPR spectra. At 40 K, an EPR spectrum characteristic of a carbon-centered radical appears. The identity of this radical is still under investigation.

Contributions

These studies would not have been possible without the contributions from the Lei group at Indiana-University Purdue-University Indianapolis (IUPUI). Linlin Yang performed the mutagenesis, expression, purification, EPR sample preparation, and kinetic studies of the SPL enzyme. In addition, she is currently preparing the enzyme SAM synthetase in preparation for deuterium labeled SAM EPR experiments.

Publications

This work is currently unpublished.

3.1 Introduction

3.1.1 Introduction to 4Fe-4S clusters

SPL belongs to what is now recognized as the large superfamily of radical *S*-adenosyl-L-methionine [4Fe-4S]$^{2+/+}$ cluster enzymes.[1] This superfamily is characterized by the consensus amino acid sequence CXXXCXXC where the conserved cysteine residues coordinate three of the iron ions of the 4Fe-4S cluster. Upon the addition of the cofactor *S*-adenosyl-L-methionine (SAM or AdoMet) the fourth iron undergoes bidentate coordination by the amino nitrogen and carboxylate oxygen of SAM (see Figure 3.1).[2,3] Common to many members of the radical SAM superfamily, when the cluster is in the reduced state [4Fe-4S]$^{+}$ it will donate an electron to the SAM cofactor, cleaving the 5'C_{Ade}–S_{Met} bond to produce methionine and a carbon centered 5'-deoxyadenosyl radical (5'-dA$^{\bullet}$). Upon production of this radical, the many varieties of radical SAM enzymes are poised to perform complicated and diverse chemistry. Although the existence of the 5'-dA$^{\bullet}$ intermediate is widely accepted, its isolation for EPR studies has proven to be challenging, is still actively pursued,[4] and is the main concern of this chapter.

3.1.2 SPL compared to other [4Fe-4S]$^{2+/+}$ cluster enzymes

The SPL enzyme shares many of the features common to the radical SAM superfamily. It has been demonstrated through x-ray crystallography and HYSCORE spectroscopy that the cofactor SAM binds the fourth iron of the cluster in a bidentate fashion (crystal of *Geobacillus thermodenitrificans* SPL (SPL_{Gt}), HYSCORE detected ^{14}N coupling from SAM in *Clostridium acetobutylicum* SPL (SPL_{Ca}))[5,6] and that SAM binding reduces the covalency of the Fe-S bonds in the cluster (through Moessbauer, XAS, and DFT on SPL_{Ca}).[7] After the cluster reduces SAM and generates the 5'-dA$^{\bullet}$ radical, the enzymes' chemistries typically proceed with H atom abstraction from the substrate. Consequently, many of the radical SAM enzymes produce 5'-dAH and methionine (cleaved SAM) as co-products along with the final product of the reaction. In contrast, the SPL enzyme is suggested to use the cofactor catalytically and to regenerate SAM through a unique H atom/radical transfer chain.[8,9]

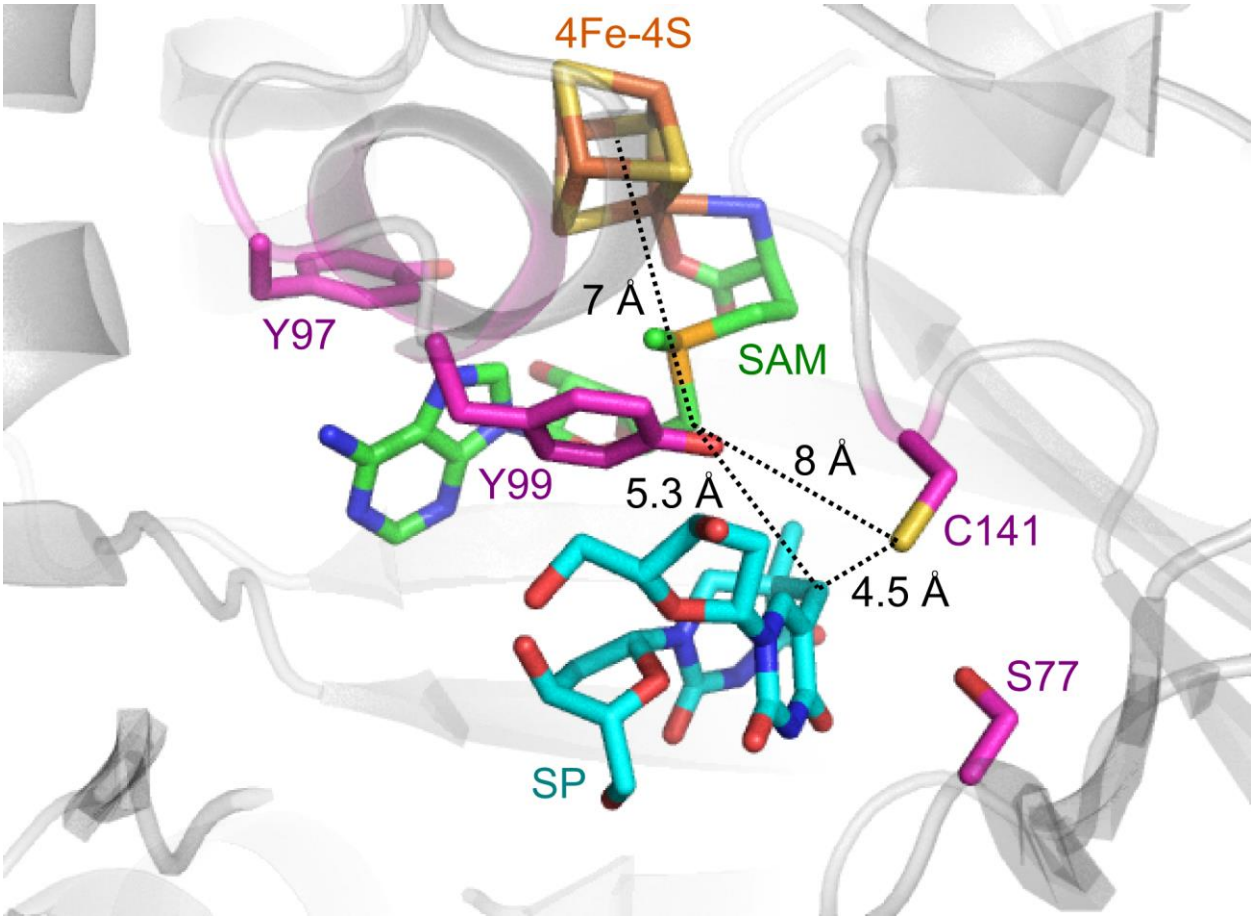

Figure 3.1. The active site of SPL_{Gt} depicting the 4Fe-4S complex (Fe in orange, S in yellow) bound to cofactor SAM (carbons in green) and substrate SP (carbons in cyan). Also shown are the amino acid residues (numbered with the +1 sequence shift in SPL_{Bs}, carbons in magenta) suggested to be important for the radical transfer mechanism and SAM binding. The remaining atoms are colored with nitrogen in blue and oxygen in red. pbd ID 4FHD[6]

3.1.3 The HAT mechanism of spore photoproduct (SP) repair

The enzyme SPL repairs a specific DNA dimer, SP, resulting from UV photodamage that occurs when bacteria enter a dormant endospore state. Currently the repair of SP is suggested to proceed through a radical transfer chain which passes through cofactor, substrate, and active site residues as depicted in Scheme 3.1. Efficient repair of the DNA lesion in endospores is believed to be one of the key factors allowing bacteria to remain viable upon revival from extremely long periods of dormancy.[10,11] To summarize the steps in Scheme 3.1, the $[4Fe\text{-}4S]^{+}$ cluster reduces the SAM cofactor by one electron, generating 5'-dA$^{\bullet}$ ($AdeCH_2^{\bullet}$ in the Scheme). A subsequent H atom transfer (HAT 1) from SP to 5'-dA$^{\bullet}$ produces 5'-dAH ($AdeCH_2H$ in the Scheme) and a radical intermediate of SP which upon rearrangement

abstracts an H atom from a nearby cysteine at position 141 (*Bacillus subtilis* SPL (SPL_{Bs}) numbering) which is highly conserved among spore forming *Bacillaceae*. This produces the repaired thymine bases and a cysteine radical (HAT 2). It is believed that through subsequent HATs from tyrosine 99 to cysteine 141 (HAT 3), and then from 5'-dAH to tyrosine 99 (HAT 4), the 5'-$dA^{\bullet}$ radical is reproduced and recombines with methionine to regenerate the SAM cofactor. Some aspects of this mechanism are well agreed upon and other aspects need further exploration to be fully understood as given in greater detail below.

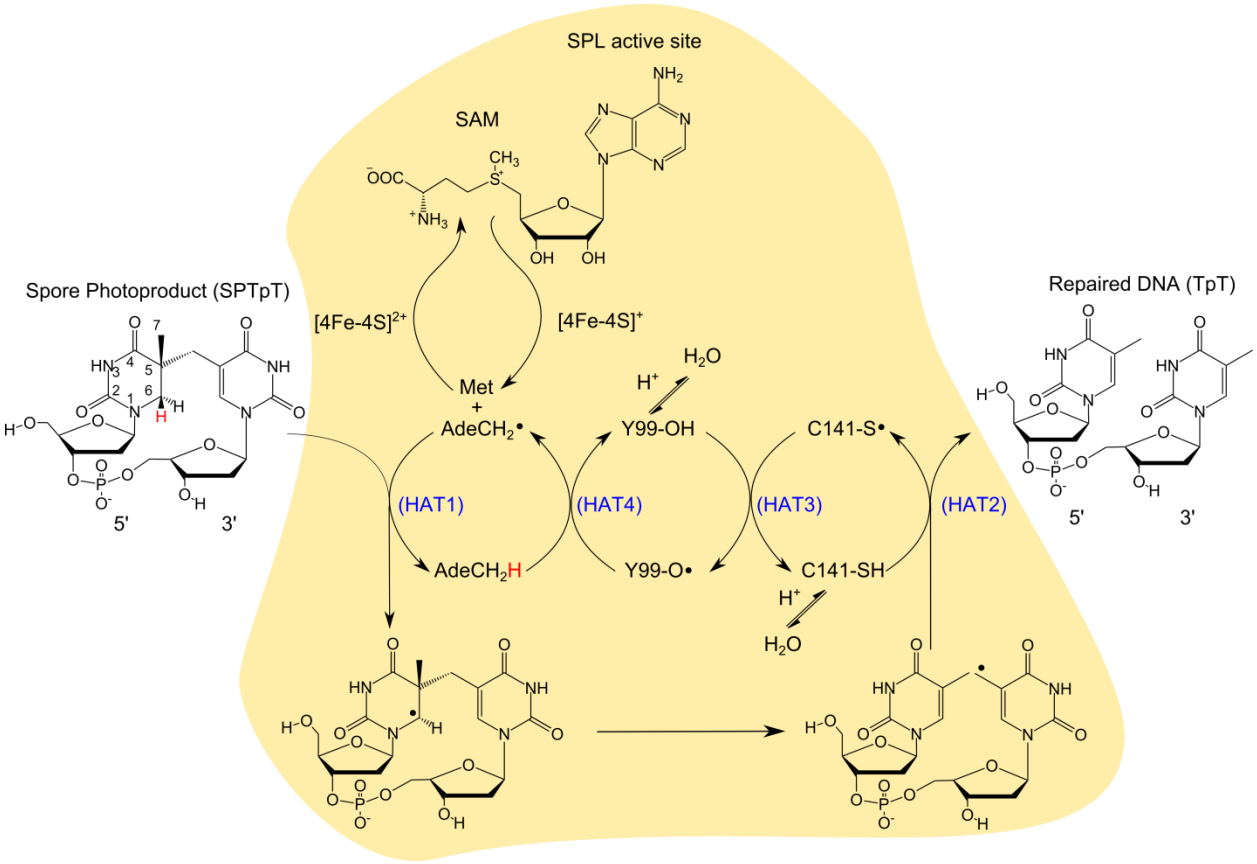

Scheme 3.1. The repair of SP by the SPL enzyme depicting the proposed H-atom transfer chain. The active site is enclosed in the orange region and the structures of the substrate SP and cofactor SAM are depicted.

3.1.4 Practical aspects of studying the enzyme

Studying the catalytic activity and structure of SPL (and 4Fe-4S cluster enzymes in general) presents many challenges due to the O_2 sensitivity of the enzymes. In *in vitro* enzymes preparations, before SAM binds the fourth iron of the cluster, the iron is generally not bound to a residue in the enzyme. This

makes the fourth iron somewhat labile and often laboratory isolation of these enzymes results in a [3Fe-4S]$^{+}$ cluster. However, in the presence of strong reducing agents (sodium dithionite or photoactivated deazariboflavin) and in strict anaerobic environments (2 ppm of O_2 or less), the [3Fe-4S]$^{+}$ cluster can be converted to the [4Fe-4S]$^{+}$ species. The reduced [4Fe-4S]$^{+}$ cluster formally consists of three Fe^{2+} ions (S = 2 each) and one Fe^{3+} ion(S = 5/2) that are antiferromagnetically coupled, resulting in an EPR-active state with total spin S = 1/2.[7] This state has a characteristic EPR signal with typical g values $g_{\parallel}$ = 2.02 and $g_{\perp}$ = 1.9 that must generally be measured at less than 20 K due to the fast relaxation of the cluster. Transferring one electron to the SAM cofactor formally produces the [4Fe-4S]$^{2+}$ state, which is EPR silent (S = 0).

Many activity and structural studies of SPL utilize truncated versions of the spore photoproduct substrate and the studies have been carried out in several homologs of the enzyme. A dinucleotide analogue of SP, which lacks the phosphodiester linkage between the nucleotides, has been shown to crystallize in SPL_{Gt}. This structure is shown in Figure 3.1 with the residues suggested to be relevant for SP repair highlighted.[6] There has been much mechanistic work carried out in SPL_{Gt} as well as SPL_{Bs}, which has a +1 sequence shift relative to SPL_{Gt}. It was shown that the analogue SPTpT which contains the phosphodiester linkage (structure in Scheme 3.1) will act as a minimal substrate for reactivity studies in SPL_{Bs} and this analogue was utilized in our studies. Researchers have also found that in SPL_{Ca} the conserved cysteine residue at positions 141 in SPL_{Bs} is instead an alanine. A cysteine alternatively appears at position 77 in SPL_{Ca}, which in SPL_{Bs} is a serine.[12,13] This has led to ours and others' work in the *Bacillaceae* SPL enzymes exploring whether the reactivity of SPL_{Bs} C141A mutants can be recovered with S77C mutations.[14]

3.1.5 The mechanism in detail

The steps in the mechanism of SP repair have been elucidated by several groups and the details of the experiments which have led to the current understanding of the enzyme are below.

1. *Electron donation from [4Fe-4S]$^{+}$ to SAM*. The quantitative reduction of SAM to 5'-dA$^{\bullet}$ has not been shown in SPL. However, the Broderick group has spin quantitated the [4Fe-4S]$^{+}$ cluster in pyruvate-formate lyase activating enzyme (PFL-AE, another member of the radical SAM super-family) using EPR. With stoichiometric addition of the substrate pyruvate-formate lyase (PFL), they showed quantitative conversion of the [4Fe-4S]$^{+}$ EPR signal in PFL-AE to the expected glycyl radical on PFL.[15]
2. *HAT1*. The first H atom transfer step is proposed to produce 5'-dAH and a radical of the substrate, SP$^{\bullet}$, through removal of an H atom at the C6 position. This radical then rearranges through β-scission of the $^{5'}$C5–$^{3'}$C7 bond to an allylic thymidine radical. This was originally proposed by Begley *et al.* when they demonstrated that an analogue of spore photoproduct (labeled with the leaving group thiophenol at the $^{5'}$C6 position) underwent β-scission of the bond linking the pyrimidines under radical forming conditions and produced the final products.[16] It was later shown in the enzyme that SP labeled with tritium at $^{5'}$C6 incorporated ^{3}H into SAM after the reaction (though how this occurred remained unclear).[8] In greater detail, it was found using SP enantioselectively ^{2}H-labeled at the $^{5'}C6_{HproR}$ and $^{5'}C6_{HproS}$ positions that SPL is enantioselective for the $^{5'}C_{HproR}$ atom.[9]
3. *HAT2*. The thymine allylic radical generated from $^{5'}$C5–$^{3'}$C7 bond scission must be quenched to reach the final product. Although it was originally proposed that SAM could back donate the H-atom, mutational studies demonstrated that C141A mutations to SPL$_{Bs}$ abolished its activity *in vivo* suggested the mechanism was more complicated.[12] *In vitro* studies later showed that C141A-SPL$_{Bs}$ mutants produce TpT-SO_2 from the SPTpT substrate as the major product. The $-SO_2$ group (which came from excess dithionite in solution used as a reducing agent to convert [4Fe-4S]$^{2+}$ to [4Fe-4S]$^{+}$) quenched the thymine allylic radical, which suggested C141 as the direct H-atom donor in the native enzyme.[17,18] Finally, using SPTpT deuterium labeled at $^{5'}$C6, it was shown that deuterium was incorporated into SAM during the repair reaction, but not reincorporated into the repaired thymine bases, suggesting simple back donation of the H atom was not the correct mechanism.[9]
4. *HAT3*. The crystals structure of SPL$_{Gt}$ shows a tyrosine residue (Y99 in SPL$_{Bs}$) in close proximity to C140 (C141 in SPL$_{Bs}$), SP, and SAM. It was suggested that this tyrosine also plays a role in the radical transfer mechanism when UV-Vis studies of wild-type (WT) SPL$_{Gt}$ revealed a feature at 410 nm

(typical for $Tyr^{\bullet}$) that was not present in Y89F-SPL_{Gt}.[19] Reduced catalytic activity in tyrosine mutants of SPL_{Bs} further supported this conclusion. It was found that the mutations Y97F and Y99F reduced the turnover rate of the enzyme roughly 4-fold and 10-fold, respectively. The double mutation Y97F/Y99F reduced the turnover rate roughly 100-fold and the double mutation Y97A/Y99A led to no reactivity, presumably because it disrupted SAM binding in the active site. From this the role of Y99 in the radical transfer mechanism was supported and at least a structural role for Y97 was proposed.[20]

5. *HAT4*. The final H-atom transfer step in the currently proposed mechanism involves regeneration of SAM from the radical 5'-$dA^{\bullet}$. Catalytic regeneration of SAM was first proposed by the Broderick group when they found that adding a limiting amount of SAM to *in vitro* reactions containing SPL and SP still led to substantial substrate repair and very little 5'-dAH production, suggesting a single SAM molecule is involved in hundreds of turn-overs.[8,21] However, when $Tyr^{\bullet}$ was observed in the mechanism, it was proposed that SAM may initiate the first repair of SP, but $Tyr^{\bullet}$ carries out subsequent SP repairs eliminating the energetically unfavorable production of 5'-$dA^{\bullet}$ radicals.[19] This final step is still controversial.

The single electron transfer/H-atom transfer chain in the SPL enzyme makes the mechanism amenable to study with EPR spectroscopy. The 4Fe-4S cluster itself is paramagnetic in the +1 oxidation state and each of the organic radicals in the mechanism can be studied with EPR if they can be trapped in their radical state. The Li group at Indiana-University Purdue University at Indianapolis (IUPUI) prepared a series of SPL_{Bs} enzymes with mutations to the active site residues. We studied the variable temperature EPR spectra of several preparations of SPL mutants including 1) the intact $[4Fe\text{-}4S]^{+}$ cluster produced by reduction with dithionite, 2) the EPR signals produced by reduction with dithionite and incubation with the cofactor SAM, and 3) for select mutants, the reduced mutants incubated with SAM and the substrate SPTpT. Upon incubation with SAM we observed changes to the $[4Fe\text{-}4S]^{+}$ EPR signal and the appearance of an organic radical signal with strong hyperfine coupling features in all of the samples that we believe bind the SAM cofactor. Incubation of mutants with both SAM and SPTpT cause the organic

radical spectrum to disappear, suggesting it is a radical in the catalytic pathway. This radical is tentatively assigned to 5'-dA$^{\bullet}$ based on previous literature and DFT calculations. Below, I describe the experimental evidence for this tentative assignment.

3.2 Results*:* CW EPR spectroscopy

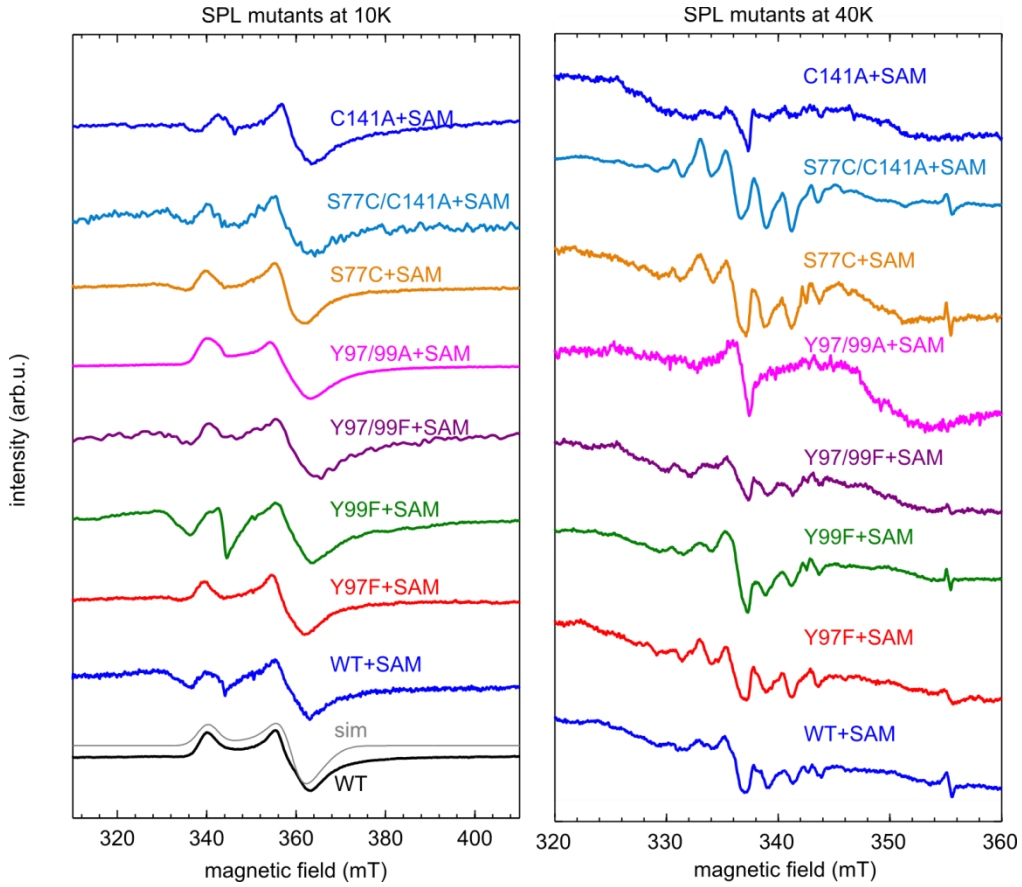

Figure 3.2. The CW EPR spectra at 10 K and 40 K of the SPL enzyme with various mutations made to the active site (indicated in the figure) in the presence of the cofactor SAM (except for bottom left spectrum labeled WT). EPR spectra at 10 K were collected at 9.63 GHz in a dual-mode resonator (except for C141A+SAM which was collected in an SHQE resonator at 9.38 GHz; for clarity, the plotted spectrum is shifted upfield to account for the difference) with 10 mW of microwave power or less and 10 G modulation amplitude or less. EPR spectra at 40 K were collected at 9.38 GHz in an SHQE resonator with 2 mW of power and 5 G modulation amplitude. A simulation of the WT spectrum without SAM is included. Simulation parameters included a slightly rhombic *g* tensor with principal values of 1.89, 1.92, and 2.02. Spectral broadening was including by convoluting the simulation with a Gaussian broadening of 2 mT and additional axial broadening in the form of *g* value strain (0.05, 0.03, and 0.03, respectively).

Samples for CW EPR spectroscopy were prepared in an anaerobic environment by incubating an SPL mutant with 50 to 100 fold excess of sodium dithionite for 30 minutes. Where indicated by the label

"+SAM" in Figure 3.2, samples were then incubated with 10 fold excess of SAM for 5 minutes then frozen in liquid nitrogen.

WT SPL_{Bs} (reduced with dithionite but not incubated with SAM) shows the expected S = 1/2 EPR signal near g = 2 (350 mT) for a reduced $[4Fe\text{-}4S]^{+}$ cluster (for reference this is shown as the bottom spectrum in Figure 3.2 left along with a simulation). In previous studies, it was shown that the introduction of mutations Y97F, Y99F, Y97/99F, and Y97/99A do not affect the $[4Fe\text{-}4S]^{+}$ cluster EPR signal.[20] In the appendix Figure A3.3 we also show that C141A and S77C/C141A constructs maintain the expected $[4Fe\text{-}4S]^{+}$ EPR signal upon reduction with dithionite. This demonstrates that all of these mutants still form an intact FeS cluster. However, these mutations do have a dramatic effect on the reactivity of SPL. In Table 3.1 are the turnover rates of spore photoproduct repair of the various SPL_{Bs} mutants compared to the WT enzyme (column 2, V_{max} (min^{-1})). In all cases the turnover rate is reduced and for the Y97/99A mutations there is no reactivity. The reactivity of the mutants S77C and S77C/C141A are not currently published.

The 10 K CW EPR spectra of the SPL_{Bs} mutants incubated with SAM are shown in Figure 3.2 *left*. After the introduction of the cofactor SAM, most of the EPR spectra show a modified $[4Fe\text{-}4S]^{+}$ cluster signal characterized by changes in line shape and signal intensity compared to the WT spectrum without SAM. This drastic reduction in the $[4Fe\text{-}4S]^{+}$ EPR signal has been observed before upon binding of SAM; however, its origin is unclear.[22] Researchers speculated it occurs due to some of the $[4Fe\text{-}4S]^{+}$ clusters converting to the EPR silent $[4Fe\text{-}4S]^{2+}$ state upon electron transfer to SAM, which would drastically reduce the intensity of the signal. Alternatively, they suggested the $[4Fe\text{-}4S]^{+}$ cluster could occupy higher-spin states (not accessible via typical EPR in perpendicular mode at X band with fields < 1 T) due to structural changes upon SAM binding.[22] The samples with the strongest distortions of the $[4Fe\text{-}4S]^{+}$ signal correspond to mutants that still exhibit substantial turnover rates of SP repair. For instance, the Y97/99A mutant exhibits no turnover and the $[4Fe\text{-}4S]^{+}$ EPR signal appears intact. This indicates that SAM does not bind to the cluster in this mutant and that the aromaticity of the tyrosine residues plays a role in SAM binding, as was previously suggested.[20] As shown in wider sweeps of the magnetic field at 10

K (Appendix Figure A3.1), the mutations that show the distorted spectra exhibit a feature at g = 5.05 (≈ 136.0 mT at 9.63 GHz) potentially indicative of a higher-spin state. This feature increases in intensity as the temperature is lowered to 5 K in the WT+SAM sample (Figure A3.2), suggesting that at least some of the signal reduction is due to high-spin state occupation.

Table 3.1. Turnover rates for SP repair in SPL_{Bs}[20]

SPL_{BS} enzyme	V_{max} (min^{-1})
WT	0.41 ± 0.03
C141A	0.14 ± 0.02
Y97F	0.12 ± 0.01
Y99F	0.06 ± 0.005
Y97/99F	< 0.004
Y97/99A	N.A.

When the sample temperature is raised to 40 K, the 4Fe-4S cluster EPR signal relaxes too rapidly for observation. Instead, a faint six-line signal about 13 mT in full width becomes distinguishable (Figure 3.2 *right*). The symmetric shape and distinct ≈ 2.5 mT splitting indicate this is a carbon-centered organic radical with strongly coupled proton hyperfine features. The organic radical only appears in samples that show the distorted $[4Fe\text{-}4S]^{+}$ cluster signal at 10 K indicative of SAM binding; the Y97/99A mutant believed to not bind SAM does not exhibit the organic radical signal at 40 K.

The introduction of the substrate analogue SPTpT to the reaction mixture results in loss of the organic radical signal at 40 K. In Figure A3.3, we show the EPR spectra at 10 K and 40 K of the C141A and S77C/C141A mutants under three different conditions; reduced with dithionite, reduced with dithionite with SAM added, and reduced with dithionite with the addition of SAM and SPTpT. The organic radical is present in the samples where SAM has been added, but seems to be quenched with the addition of SPTpT. This suggests the samples are still catalytically active and that the reaction proceeds beyond the organic radical intermediate when the substrate is present.

The FeS cluster can be reduced in an alternative manner using photoactivated deazariboflavin and dithiothreitol (DTT). WT and C141A SPL treated with deazariboflavin and DTT produce the same $[4Fe\text{-}4S]^{+}$ EPR spectra as the samples reduced with dithionite (Figure A3.4). In two of the SPL mutants (C141A

and S77C/C141A), the addition of SAM to the deazariboflavin/DTT reaction results in the distorted [4Fe-4S]$^{+}$ cluster EPR signal at 10 K, which is indicative of SAM binding. Warming the samples to 40 K, it is apparent the organic radical is also present (Figure A3.3). However, the yield of the organic radical is significantly lower, therefore dithionite is the preferred reducing condition for further studies on the organic radical. The relevance of the deazariboflavin/DTT reduction has implication beyond the scope of this thesis. These are discussed briefly along with additional EPR spectra in Appendix A3.5.

3.3 Discussion

Based on the observations described above, we can make the following tentative conclusions:

1. The EPR spectrum of the organic radical could potentially be due to 5'-dA$^{\bullet}$ (structure in Figure 3.3). The radical appears in many different SPL mutants, making it unlikely it is centered on any of the residues that have been suggested in the catalytic mechanism (C141, Y97 or Y99). However, we cannot rule out an off-pathway alanine radical (which would have a similar structure and the same number of strongly coupled protons in the EPR spectrum).
2. The organic radical spectrum can be well-simulated using a strong exchange coupling between the radical and the FeS cluster (discussed further in 3.3.1). This indicates the cluster is paramagnetic and, therefore, in the [4Fe-4S]$^{+}$ state. After electron transfer to SAM to generate 5'-dA$^{\bullet}$, the cluster should be in the 2+ state. However, because of the large excess of dithionite in solution (50-100x) it is not unreasonable to think the cluster may be re-reduced to the 1+ state.
3. The strong exchange coupling needed to simulate the organic radical spectrum also indicates the organic radical is in close proximity to the FeS cluster. Given this, and that the radical signal intensity is greatly diminished in samples containing SAM and the substrate SPTpT (Figure A3.3), the organic radical seems to be catalytically relevant to the repair of SP.
4. Although the signal intensity is decreased in the spectra of SPL mutants+SAM at 10 K relative to WT SPL without SAM (Figure 3.2 *left*), it is clear that the [4Fe-4S]$^{+}$ EPR spectrum is still present. Whether this is due to the re-reduced clusters (conclusion 2) or clusters that did not transfer an electron to SAM, we cannot distinguish. In addition, it seems likely that at least some of the signal loss upon

SAM binding is due to the occupation of higher-spin states. A g = 5.05 feature is present at 10 K that grows to a much larger feature at 5 K, which is most likely due to an $S > 1/2$ system (Figures A3.1 and A3.2).

3.3.1 DFT to support our conclusions

Arguably the most exciting (potential) observation is the 5'-dA$^{\bullet}$ radical in close proximity to the FeS cluster. This radical is expected to have strong hyperfine coupling to three protons in the system; two at the 5' carbon and one at the 4' carbon in Figure 3.3. DFT results indicate ≈ 100 % Mulliken spin population on C5' leads to these large hyperfine couplings which are tabulated in Table 3.2. Figure 3.3 shows a simulation of the 5'-dA$^{\bullet}$ radical with the calculated hyperfine couplings. The simulation has five lines while our data clearly show a six-lined spectrum. The sixth line can be accounted for by including a 60 MHz exchange coupling in the simulation. Observing six lines instead of five supports the spectrum belonging to the 5'-dA$^{\bullet}$ radical in the SPL active site.

3.3.2 Relevant literature

Capturing 5'-dA$^{\bullet}$ for characterization with EPR spectroscopy in any radical SAM enzyme has proven difficult. It still remains unclear how the enzymes completely overcome the energetic cost of generating the 5'-dA$^{\bullet}$ radical. The ability of [4Fe-4S]$^{+}$ clusters to reduce the SAM cofactor is surprising because of the ≈ 1.3 V gap in reduction potential between the two when measured separately (trialkylsulfonium reduction potentials are near -1.8 V[23] and [4Fe-4S]$^{2+/+}$ clusters are near -500 mV[24–26]). However, SAM binding in the active site decreases the solvent exposure, polarity, and dielectric constant of the medium around SAM, which has been shown to raise the reduction potentials of redox active organic molecules. Additionally, the covalent binding of SAM to the cluster affects the SAM reduction potential (shown to raise it to -990 mV) and the [4Fe-4S]$^{+}$ cluster reduction potential (shown to lower it to -600mV[27]) which provides a large contribution to closing the reduction potential gap. Finally, the orientation in which SAM binds to the unique iron of the [4Fe-4S]$^{+}$ cluster is thought to provide a direct pathway for SAM cleavage. Spectroscopic evidence suggests the antibonding orbital of the 5'C_{Ade}–S_{Met} bond is oriented so

that it directly overlaps with orbitals of the iron-sulfur cluster. The antibonding orbital can then accept an electron causing homolytic cleavage of the 5'C_{Ade}–S_{Met} bond.[2,28–30]

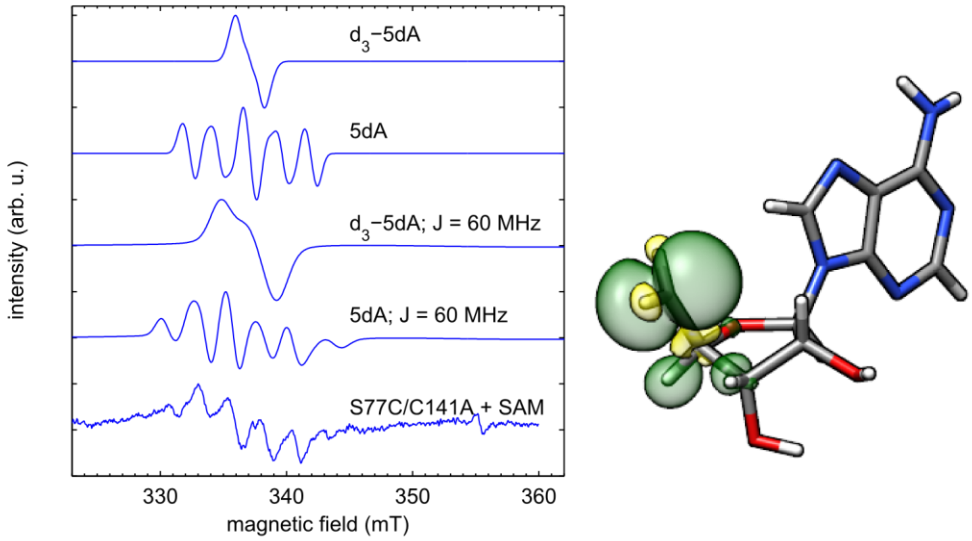

Figure 3.3. CW EPR spectrum of the S77C/C141A+SAM spectrum also shown in Figure 3.2 collected at 40 K. In addition are simulations of the 5'-dA• radical including an electron-electron coupling of 60 MHz (5dA; J = 60 MHz), this same simulation but taking into account deuteration of the protons at C4 and C5 (d_3-5dA; J = 60 MHz), the 5'-dA• radical with no coupling (5dA), and the 5'-dA• radical with deuteration of the protons at C4 and C5 (d_3-5dA).

The earliest success at measuring the EPR properties of 5'-dA• came when the Frey group successfully captured an allylic analogue (5'-deoxy-3',4'-anhydroadenosine-5'-yl) of the 5'-dA• radical in the active site of the [4Fe-4S] cluster enzyme lysine 2,3-aminomutase.[31,32] The EPR spectrum of this analogue revealed a five-line spectrum with splitting of ≈ 2 mT due to strong hyperfine coupling to four protons. The hyperfine coupling of each proton was confirmed with selective ^{2}H isotopic labeling. Very recently, Heidinger *et al.* observed an organic radical in the EPR spectra of C140A-SPL_{Gt} + SAM. The symmetric five-line spectrum with about ≈ 2 mT splitting was indicative of a carbon-centered organic radical. This radical was present only in in the C140A mutant, not WT or Y98F SPL_{Gt} which were also studied. Based on DFT calculations which yielded similar results to ours, this radical was also tentatively assigned as 5'-dA•.[33] Although likely that our groups are observing the same radical, there are differences between the observations of Heidinger *et al.* and those herein, namely, our spectrum contains at least six lines and is observed in many mutants of SPL_{Bs}.

It is of course possible the identity of this organic radical is not 5'-dA$^{\bullet}$; there are a few other likely candidates. First, tyrosine is a common redox active amino acid and there are two tyrosine residues suggested to be on pathway in the repair of SP by SPL. However, we see the radical in samples where these have been mutated out. Instead, the tyrosine radical could be off pathway. We note that tyrosine radicals identified in the literature typically show at most a two-line splitting due to the hyperfine coupling of the C_β protons, making this a less likely candidate for the radical reported here. Second, the spectrum could be due to an off-pathway alanine radical. With the loss of one H atom at C_β, an alanine radical would have the same number of strongly coupled protons (two at C_β and one at C_α) in the same geometry as the proposed 5'-dA$^{\bullet}$. This makes on an off-pathway alanine radical a strong alternative contender for the radical identity.

3.4 Outlook

Although our data is consistent with a 5'-dA$^{\bullet}$ radical, further studies are needed to solidify our conclusions. To complete this study, isotopic labeling of SAM should be performed. Using SAM labeled with deuterium at C5' and C4' positions (commercially available from Cambridge Isotope Laboratories) would produce the EPR spectrum simulated in Figure 3.3 (spectrum labeled d_3-5dA; J = 60 MHz). The hyperfine structure of the strongly coupled protons would collapse, but the splitting due to the electron-electron coupling would remain. This spectrum, with a narrower bandwidth than the protiated spectrum, would be amenable to relaxation induced dipolar modulation (RIDME) spectroscopy which can measure this electron-electron coupling and further confirm that the remaining splitting is due to an electron-electron interaction.[34] At this point, this study would then support the conclusions drawn above.

Up until very recently, there have been no claims of direct observation of the 5'-dA$^{\bullet}$ radical in the large superfamily of radical SAM enzymes.[33] This has been attributed to the highly unstable radical either quickly reacting or degrading before it can be trapped for spectral characterization. If Heidinger *et al*. and we are truly observing 5'-dA$^{\bullet}$, SPL may be a member of a distinct sub-class of these enzymes that react and stabilize 5'-dA$^{\bullet}$ in a unique way compared to those enzymes previously studied. At this point,

work remains to distinguish if 5'-dA$^{\bullet}$ is truly being trapped and why SPL (and potentially other members of the radical SAM superfamily) show this alternative behavior.

3.5 Methods

Enzyme preparation. Preparation of the SPL enzyme was carried out by the Li group at IUPUI and the general methods are described in Yang *et al*.[20,35]

EPR sample preparation. EPR samples were prepared at a concentration of approximately 200 μM protein in a 25 mM tris buffer at pH 7 with 250 mM NaCl and 10-20% glycerol in a 200 μL sample volume. Reduction of the FeS cluster was carried out by incubating the enzyme with 50-fold dithionite for 30 minutes. In samples where the cofactor SAM was present, after incubation with dithionite, 10-fold of SAM was added and the sample allowed to incubate for 5 minutes before flash freezing in liquid nitrogen. In samples where the substrate SPTpT was present (data in Appendix Figure A3.3), after incubation with dithionite, SAM and SPTpT were added to the sample and allowed to incubate for reaction times given with the figure before flash freezing in liquid nitrogen.

Samples reduced with deazariboflavin and DTT were prepared in the same reaction buffer described above. In this case, 3-fold excess deazariboflavin and 25-fold excess DTT were added to the enzyme solution and the solution was illuminated for 25 minutes (Sylvania fluorescent self-ballasted lamp; ESP-23 w; samples ≈10 cm from the lamp) before flash freezing in liquid nitrogen. In the case where only deazariboflavin was present, the same illumination procedure was carried out.

CW EPR spectroscopy. EPR experiments were carried out on a Bruker EleXsys E580 spectrometer in either a dual mode (ER4116DM) or SHQE cavity resonator. Experimental temperatures were achieved with a continuous-flow liquid helium cryostat (Oxford ESR900) and Oxford ITC503S variable-temperature controller. Spectra were collected at a frequency of ≈ 9.63 GHz (dual mode resonator) or 9.38 GHz (SHQE resonator) which is specified in the figure captions. The microwave power and field modulation amplitudes (100 kHz frequency) are specified in the figure captions.

Density Functional Theory (DFT) calculations. Geometry optimization and magnetic properties (*g*-tensors and hyperfine coupling constants) of 5′-dA• were calculated in the ORCA 3.0.3 software with spin unrestricted Kohn-Sham orbitals, the B3LYP functional, and the EPR-II basis set.[36–39] Calculations included the solvent model COSMO with a dielectric constant of 4 to model the interior of a protein and Becke-Johnson dispersion correction using the keyword D3BJ.[40] Calculated Mulliken spin populations were visualized with the Chimera software.[41]

Spectral simulations. EPR spectra of 5′-dA• and d_3-5′-dA• were simulated with the EasySpin[42] software using the model spin Hamiltonian

$$\hat{H} = \mu_B \boldsymbol{B}\boldsymbol{g}\hat{\boldsymbol{S}} + \sum_k h\hat{\boldsymbol{S}}\boldsymbol{A}_k\hat{\boldsymbol{I}}_k \qquad \text{Eq. 3.1}$$

where the first term is the electron Zeeman interaction containing the Bohr magneton, μ_B, the externally applied magnetic field, $\boldsymbol{B}$, the electron spin operator, $\hat{\boldsymbol{S}}$, and the electron *g* tensor, $\boldsymbol{g}$. The second term describes the hyperfine interaction between an electron spin, $\hat{\boldsymbol{S}}$, and a nuclear spin, $\hat{\boldsymbol{I}}_k$, with the hyperfine matrix $\boldsymbol{A}_k$. *k* sums over all nuclei coupled to the electron spin. All tensor orientations used in the simulation were taken from the DFT calculations. These values are summarized in Table 3.2.

In the cases where an electron-electron interaction was included in the simulation, the model spin Hamiltonian

$$\hat{H} = \sum_j \mu_B \boldsymbol{B}\boldsymbol{g}_j\hat{\boldsymbol{S}}_j + \sum_{1,k} h\hat{\boldsymbol{S}}_1\boldsymbol{A}_k\hat{\boldsymbol{I}}_k + \hat{\boldsymbol{S}}_1\boldsymbol{J}\hat{\boldsymbol{S}}_2 \qquad \text{Eq. 3.2}$$

was used, where $\hat{\boldsymbol{S}}_1$ represents the organic radical and $\hat{\boldsymbol{S}}_2$ represents the [4Fe-4S]$^+$ paramagnet. Hyperfine coupling (second term) was assumed to only occur for the organic radical as in Equation 3.1. The third term represents the electron-electron coupling, $\boldsymbol{J}$, between the organic radical and the FeS cluster.

Table 3.2 presents the principal *g* values and hyperfine coupling values used to simulate the 5′-dA• radical. To simulate the deuterated radical d_3-5′-dA•, all of the ^{1}H hyperfine coupling values were scaled

by the ratio of gyromagnetic ratios $\gamma(^2H)/\gamma(^1H)$ to account for deuterium labeling. The *g* values of 1.88, 1.92, and 2.05 were used for the *S* = 1/2 FeS cluster and an isotropic electron-electron exchange coupling of 60 MHz was included. Relaxation of the FeS cluster at 40 K was modeled by broadening the features out using gStrain.

Table 3.2. Principal values of the EPR parameters (hyperfine couplings in MHz) used in the simulations in Figure 3.3

	g (xx, yy, zz)	$C5_{H1}$ (xx, yy, zz)	$C5_{H2}$ (xx, yy, zz)	$C4_{H1}$ (xx, yy, zz)
5'-dA•	2.0022,2.0028, 2.0031	-100, -60, -20	-100, -60, -20	130, 130, 140

3.6 References

(1) Broderick, J. B.; Duffus, B. R.; Duschene, K. S.; Shepard, E. M. *Chem. Rev.* **2014**, *114*, 4229.
(2) Walsby, C. J.; Hong, W.; Broderick, W. E.; Cheek, J.; Ortillo, D.; Broderick, J. B.; Hoffman, B. M. *J. Am. Chem. Soc.* **2002**, *124* (12), 3143.
(3) Walsby, C. J.; Ortillo, D.; Broderick, W. E.; Broderick, J. B.; Hoffman, B. M. *J. Am. Chem. Soc.* **2002**, *124* (38), 11270.
(4) Horitani, M.; Shisler, K.; Broderick, W. E.; Hutcheson, R. U.; Duschene, K. S.; Marts, A. R.; Hoffman, B. M.; Broderick, J. B. *Science* **2016**, *352* (6287), 822.
(5) Chandor, A.; Douki, T.; Gasparutto, D.; Gambarelli, S.; Sanakis, Y.; Nicolet, Y.; Ollagnier-de-Choudens, S.; Atta, M.; Fontecave, M. *Comptes Rendus Chim.* **2007**, *10*, 756.
(6) Benjdia, A.; Heil, K.; Barends, T. R. M.; Carell, T.; Schlichting, I. *Nucleic Acids Res.* **2012**, *40* (18), 9308.
(7) Silver, S. C.; Gardenghi, D. J.; Naik, S. G.; Shepard, E. M.; Huynh, B. H.; Szilagyi, R. K.; Broderick, J. B. *J. Biol. Inorg. Chem.* **2014**, *19*, 465.
(8) Cheek, J.; Broderick, J. B. *J. Am. Chem. Soc.* **2002**, *124* (12), 2860.
(9) Yang, L.; Lin, G.; Liu, D.; Dria, K. J.; Telser, J.; Li, L. *J. Am. Chem. Soc.* **2011**, *133*, 10434.
(10) Setlow, P. *J. Appl. Microbiol.* **2006**, *101*, 514.
(11) Desnous, C.; Guillaume, D.; Clivio, P. *Chem. Rev.* **2010**, *110* (3), 1213.
(12) Fajardo-Cavazos, P.; Rebeil, R.; Nicholson, W. L. *Curr. Microbiol.* **2005**, *51*, 331.
(13) Ollagnier-de-choudens, S.; Atta, M.; Fontecave, M. **2006**, *281* (37), 26922.
(14) Benjdia, A.; Heil, K.; Winkler, A.; Carell, T.; Schlichting, I. *Chem. Commun.* **2014**, *50*, 14201.
(15) Henshaw, T. F.; Cheek, J.; Broderick, J. B. *J. Am. Chem. Soc.* **2000**, *122* (34), 8331.
(16) Mehl, R. A.; Begley, T. P. **1999**, No. Scheme 1, 6.
(17) Chandor-Proust, A.; Berteau, O.; Douki, T.; Gasparutto, D.; Ollagnier-de-Choudens, S.; Fontecave, M.; Atta, M. *J. Biol. Chem.* **2008**, *283* (52), 36361.
(18) Yang, L.; Lin, G.; Nelson, R. S.; Jian, Y.; Telser, J.; Li, L. *Biochemistry* **2012**, *51*, 7173.
(19) Kneuttinger, A. C.; Heil, K.; Kashiwazaki, G.; Carell, T. *Chem. Commun.* **2013**, *49*, 722.
(20) Yang, L.; Nelson, R. S.; Benjdia, A.; Lin, G.; Telser, J.; Stoll, S.; Schlichting, I.; Li, L. *Biochemistry* **2013**, *52*, 3041.
(21) Buis, J. M.; Cheek, J.; Kalliri, E.; Broderick, J. B. *J. Biol. Chem.* **2006**, *281* (36), 25994.
(22) Silver, S. C.; Chandra, T.; Broderick, W. E.; Broderick, J. B.; Spore, Á. S. Á. **2010**, 943.
(23) Colichman, E. L.; Love, D. L. *J. Org. Chemsitry* **1953**, *18* (1), 40.
(24) Ugulava, N. B.; Gibney, B. R.; Jarrett, J. T. *Biochemistry* **2001**, *40* (28), 8343.
(25) Pierrel, F.; Hernandez, H. L.; Johnson, M. K.; Fontecave, M.; Atta, M. *J. Biol. Chem.* **2003**, *278* (32),

29515.
(26) Hinckley, G. T.; Frey, P. A. *Biochemistry* **2006**, *45* (10), 3219.
(27) Wang, S. C.; Frey, P. A. *Biochemistry* **2007**, *46* (45), 12889.
(28) Broderick, J. B.; Duderstadt, R. E.; Fernandez, D. C.; Wojtuszewski, K.; Henshaw, T. F.; Johnson, M. K. *J. Am. Chem. Soc.* **1997**, *119* (31), 7396.
(29) Broderick, J. B. *Nature* **2010**, *465*, 877.
(30) Kampmeier, J. A. *Biochemistry* **2010**, *49* (51), 10770.
(31) Magnusson, O. T.; Reed, G. H.; Frey, P. A. *Biochemistry* **2001**, *40* (26), 7773.
(32) Frey, P. A. *Acc. Chem. Res.* **2014**, *47* (2), 540.
(33) Heidinger, L.; Kneuttinger, A. C.; Kashiwazaki, G.; Weber, S.; Carell, T.; Schleicher, E. *FEBS Lett.* **2016**, *590*, 4489.
(34) Milikisyants, S.; Scarpelli, F.; Finiguerra, M. G.; Ubbink, M.; Huber, M. *J. Magn. Reson.* **2009**, *201* (1), 48.
(35) Yang, L.; Lin, G.; Nelson, R. S.; Jian, Y.; Telser, J.; Li, L. *Biochemistry* **2012**, *51* (36), 7173.
(36) Lee, C.; Yang, W.; Parr, R. G. *Phys. Rev. B* **1988**, *37* (2), 785.
(37) Becke, A. D. *J. Chem. Phys.* **1993**, *98* (2), 1372.
(38) Barone, V. In *Recent Advances in Density Functional Methods, Part I*; Chong, D. P., Ed.; World Scientific: Singapore, 1996.
(39) Neese, F. *WIREs Comput. Mol. Sci.* **2012**, *2*, 73.
(40) Klamt, A.; Schuurmann, G. *J. Chem. Soc. Perkin Trans. 2* **1993**, No. 5, 799.
(41) Pettersen, E. F.; Goddard, T. D.; Huang, C. C.; Couch, G. S.; Greenblatt, D. M.; Meng, E. C.; Ferrin, T. E. *J. Comput. Chem.* **2004**, *25* (13), 1605.
(42) Stoll, S.; Schweiger, A. *J. Magn. Reson.* **2006**, *178* (1), 42.

Chapter 3 Appendix

Identifying organic radicals in the spore photoproduct lyase active site

---

A3.1 Additional data collected for SPL_{Bs} mutants over the course of three months of storage

In wide field-swept spectra of the SPL mutants with SAM (left panel in Figure A3.1), a feature at $g \approx 5.05$ (136 mT, 9.63 GHz) is indicative of higher-spin state occupation by enzymes that bind to SAM. In the Y97/99A+SAM sample, which we expect does not bind SAM, there is no feature at this field value.

Due to several equipment failures, the temperature dependent data of the SPL mutant enzymes was collected over the course of three months. Below are comparisons, where possible, of spectra collected within one week of receiving samples, and spectra collected three months later. During that time samples were stored in a liquid nitrogen storage dewar. As seen at 10 K, three months of storage caused some obvious degradation in the Y97F+SAM, Y97/99F+SAM, Y97/99A+SAM, and S77C/C141A+SAM samples based on the additional low-field features (left panel in Figure A3.1). In the g = 2 region of the FeS cluster EPR signal, it seems that the signal decreased so that organic radical is almost visible in these spectra at 10 K (especially in S77C+SAM and S77C/C141A+SAM; center panel Figure A3.1). Only two samples, WT+SAM and Y99F+SAM, were studied at 40 K when the samples were freshly prepared (right panel Figure A3.1). Both of these samples show the organic radical indicating the radical is not a result of prolonged storage.

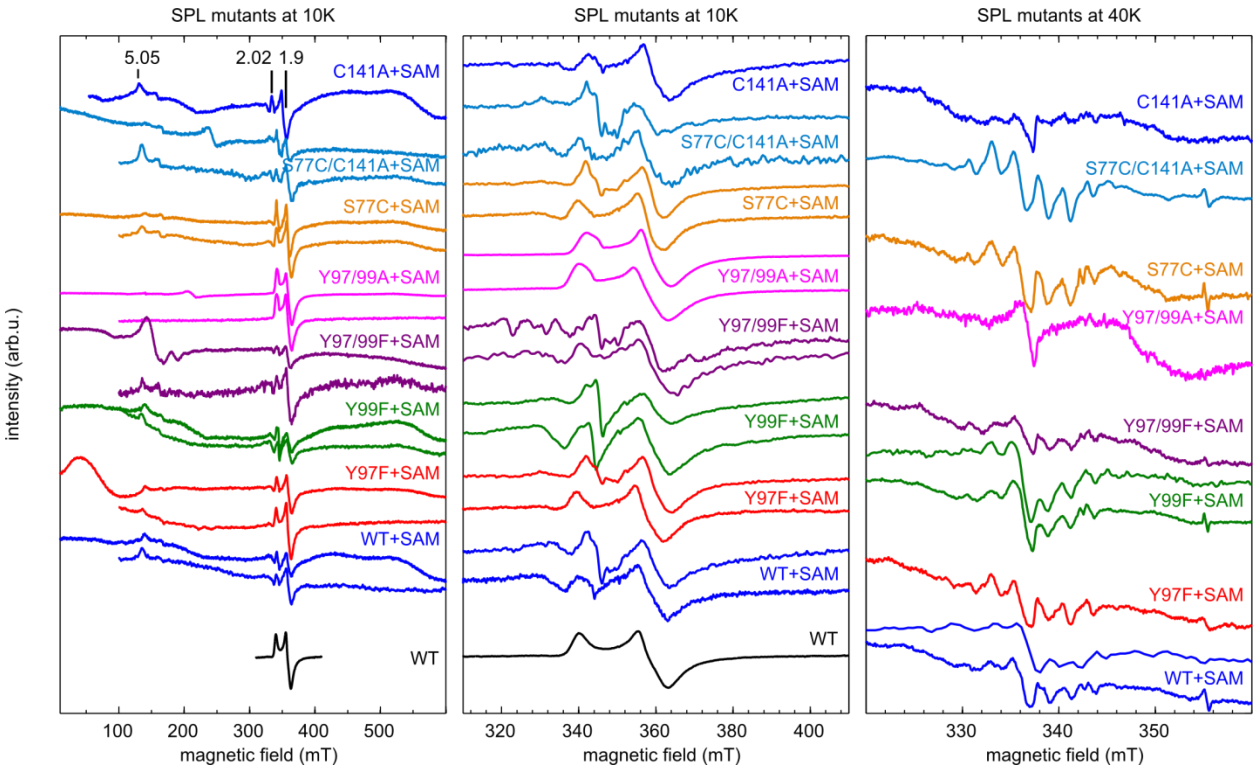

Figure A3.1. The CW EPR spectra at 10 K and 40 K of the SPL enzyme with various mutations made to the active site. The mutations are indicated in the figure. For each sample except WT and C141A+SAM there are two EPR spectra in the left and middle columns. In the left column, the widest spectra spanning 1 to 600 mT (shifted slightly up for each mutant in the figure) were collected three months after sample preparation (samples were stored at 77 K in the interim). The addition of low field features indicates there is some degradation of the Y97F+SAM, Y97/99F+SAM, and S77C/C141A+SAM samples over time. In the middle column is a narrower view of the $g \approx 2$ features at 10 K. Again the spectrum for a given mutant shifted slightly up was collected three months after sample preparation. In the right column, EPR spectra were collected at 40 K. There are two EPR spectra for the WT+SAM and Y99F+SAM samples only. In this case the spectrum shifted slightly up was collected within one week after sample preparation. In addition the C141A+SAM spectrum was collected within a week of preparation. The remaining spectra were collected three months after sample preparation. Spectra are normalized to their most intense feature for clarity.

The EPR spectrometer parameters in Figure A3.1 are listed in the tables below for each spectrum and separated by storage time. The spectra numbering is kept consistent across the panels for each mutant and numbered from the bottom to top (i.e. spectrum 1 = WT, spectrum 2 = WT+SAM, spectrum 3 =Y97F+SAM, etc.).

Figure A3.1 *left*	Microwave Frequency (GHz)	Modulation Amplitude (G)	Microwave Power (mW)
Spectrum 1	9.63	5	2
Spectra 2-8	9.63	10	20
Three months of storage			
Spectra 2-9	9.38	5	2

Figure A3.1 *center*	Microwave Frequency (GHz)	Modulation Amplitude (G)	Microwave Power (mW)
Spectrum 1	9.63	5	2
Spectra 2-3, 6-8	9.63	5	3
Spectra 4-5	9.63	10	10
Three months of storage			
Spectra 2-8	9.38	10	0.05
Spectrum 9	9.38	5	0.05

Figure A3.1 *right*	Microwave Frequency (GHz)	Modulation Amplitude (G)	Microwave Power (mW)
Spectra 2, 4	9.63	10	20
Three months of storage			
Spectra 2-8	9.38	5	2

A3.2 Variable-temperature CW EPR of WT and Y99F SPL_{Bs} with SAM

In the WT+SAM sample of SPL_{BS}, the feature at g = 5.05 (136 mT) seen in many of the SPL constructs (see Figure A3.1) grows in considerably at 5 K (Figure A3.2 *left*). In both WT and C141A SPL_{Bs}, the organic radical only becomes distinguishable at 40 K. At 80 K in the Y99F+SAM sample, the organic radical is not visible, perhaps due to fast relaxation. This is consistent with the organic radical being in close proximity to a paramagnetic state of the 4Fe-4S cluster, which enhances its relaxation rate.

A3.3 Catalytic implications for the organic radical observed at 40 K

In two SPL_{Bs} constructs (C141A and S77C/C141A), the catalytic behavior of the mutants was explored by monitoring samples of the reduced enzymes, the reduced enzymes plus SAM, and the reduced enzymes plus SAM and the substrate SPTpT. Both constructs with only reductant present show the intact S=1/2 $[4Fe\text{-}4S]^{+}$ EPR spectrum similar to reduced WT SPL at 10 K, which relaxes too quickly to be visible at 40 K (blue spectra in Figure A3.3, see the main text for WT spectrum). Upon addition of SAM, the $[4Fe\text{-}4S]^{+}$ signal is distorted (red spectra at 10 K in Figure A3.3). When the temperature is raised to 40 K, an organic radical appears that is not seen at 40 K in samples with the reduced enzyme (compare the blue spectra to the red spectra in Figure A3.3). In reduced samples that have both SAM and SPTpT present,

the [4Fe-4S]$^{+}$ signal is even further distorted at 10 K and at 40 K the organic radical has significantly diminished (purple spectra in Figure A3.3). This behavior indicates the organic radical seen in the samples with enzyme and SAM present (red spectra 40 K) is catalytic since the addition of the substrate quenches the radical (purple spectra at 40 K).

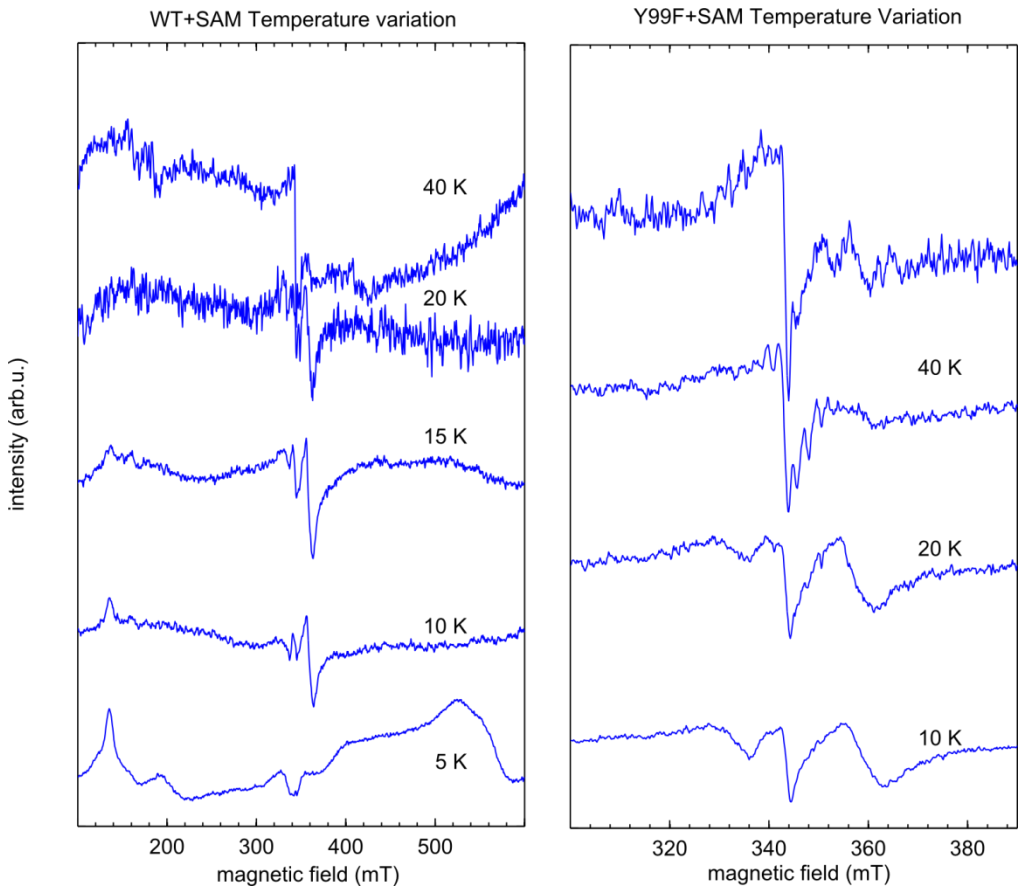

Figure A3.2. Variable-temperature 9.63 GHz CW EPR spectra of WT and Y99F SPL incubated with SAM. The spectra are scaled by microwave power, number of scans, receiver gain, and temperature. Spectra were recorded with modulation amplitude of 1 mT and microwave power of 20 mW (except for WT+SAM at 20 K which was collected at 2 mW).

In addition, in Figure A3.3 we show spectra of samples reduced by an alternative method using illuminated deazariboflavin in the presence of the cofactor SAM. Further details on this preparation and its relevance are present below in section A3.4. Here, these samples simply demonstrate that the organic radical is still present in these samples (green spectra at 40 K) and it is not a byproduct of the reduction using dithionite.

Finally, the EPR spectra in Figure A3.3 are from samples prepared at a different time than the spectra of the organic radical presented in the main text and above (Figure 3.2 and Figure A3.1). This demonstrates the reproducibility of the radical.

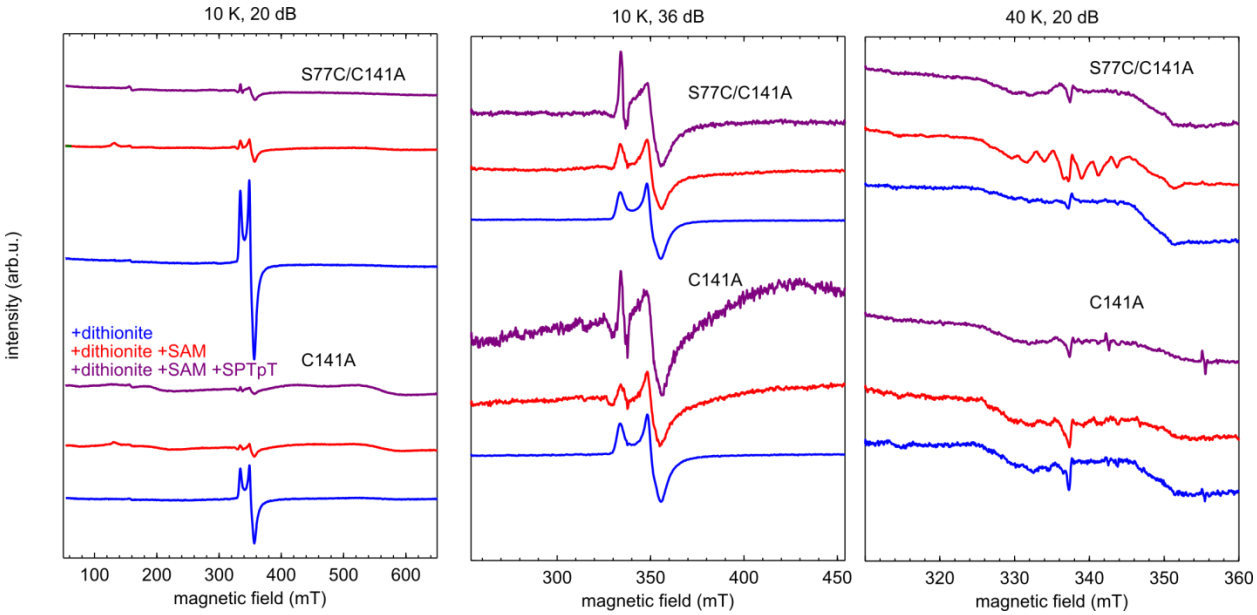

Figure A3.3. CW EPR spectra at 10 K and 40 K of the C141A and S77C/C141A mutants. In blue are samples reduced with dithionite, in red samples reduced with dithionite and with SAM present, and in purple are samples reduced with dithionite and with SAM and SPTpT present. In the left and center panels are the spectra at 10 K showing the 4Fe-4S cluster signal and its distortion upon addition of SAM. In the right panel at 40 K, we see the organic radical in the samples with SAM (red). The organic radical disappears in the samples with the addition of substrate SPTpT (1 minute incubation time, purple). Additional data (not shown) for the C141A mutant shows no signs of an organic radical after incubation with SPTpT for 4, 11, or 30 minutes. In all cases, EPR spectra were recorded with a microwave frequency of 9.38 GHz and modulation amplitude of 0.5 mT. The microwave power was set to 2 mW (*left* panel), 50 µW (*center* panel), and 2 mW (*right* panel). Spectra in the *left* panel are scaled by number of scans, gain and microwave power. Spectra in the *center* and *right* panels are scaled to their most intense feature for clarity.

A3.4 Rescue of the C141A-SPL$_{Bs}$ reactivity in samples reduced with illuminated deazariboflavin in the presence of thiols as electron donors

The Li group at IUPUI pursued reactivity studies of C141 and S77 mutants of SPL$_{Bs}$. In *Clostridia* SPL enzymes such as SPL$_{Ca}$, the highly conserved C141 residue in *Bs* is instead alanine and a cysteine is located at the residue corresponding to S77 in SPL$_{Bs}$. Thus far, they have found that C141A SPL$_{Bs}$ has reduced activity (see Table 3.1 in main text). However, in the presence of illuminated deazariboflavin

and thiols, the activity of this mutant is restored. The reactivity of the enzymes is not restored to the same extent when DTT is absent from the reaction.

Once in the reduced state, deazariboflavin is a strong enough reductant to reduce the as-isolated FeS cluster. The Li group currently hypothesizes that in the presence of UV light thiols ultimately donate electrons to deazariboflavin which then reduces the cluster. We used EPR spectroscopy to determine the ultimate electron donors which reduce the FeS cluster in the illuminated deazariboflavin reaction by comparing the spectra of the $[4Fe\text{-}4S]^{+}$ clusters in the absence and presence of dithiothreitol (DTT).

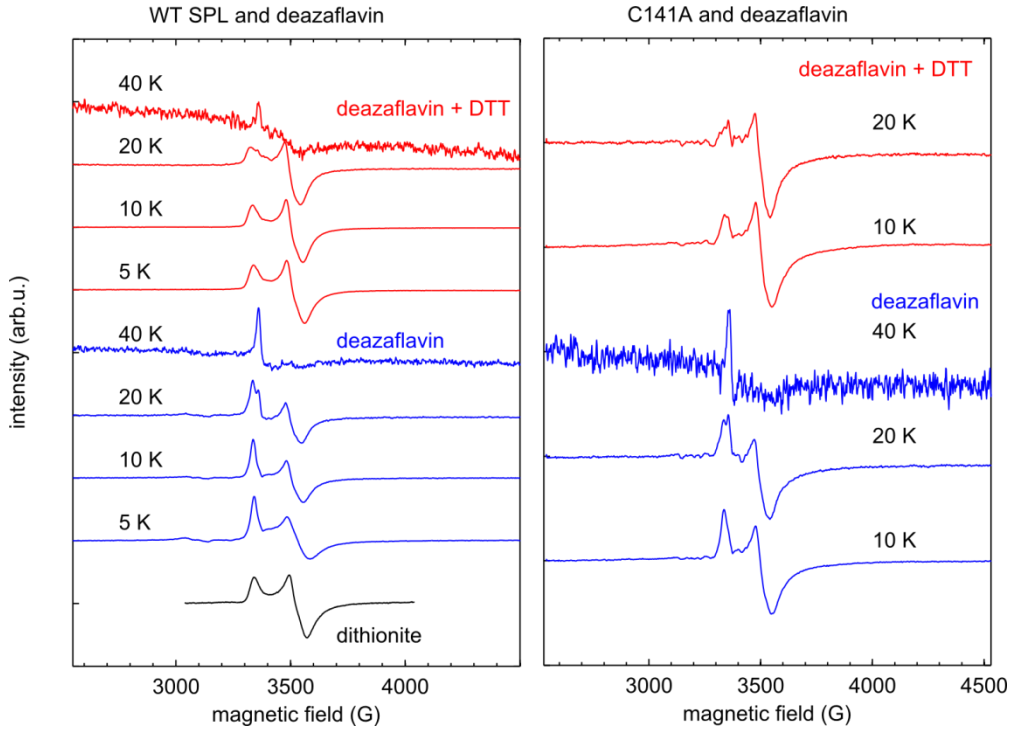

Figure A3.4. CW EPR spectra at 10 K to 40 K of WT and the C141A mutant reduced using deazaflavin and DTT illuminated for 25 minutes (no SAM or SPTpT present). For comparison on the left, the WT spectrum of the 4Fe-4S cluster reduced with dithionite is shown (bottom trace). The 4Fe-4S cluster is successfully reduced in this alternative manner using deazaflavin and DTT. Notice that DTT must be present for the reduction to occur. The spectra taken with only deazaflavin present (blue) are distorted compared to the expected signal for the WT reduced with dithionite. EPR spectrometer parameters on *left* include microwave frequency of 9.38 GHz, modulation amplitude of 10 G, and a microwave power of 50 µW. On the *right*, spectrometer settings were a microwave frequency of 9.38 GHz, modulation amplitude of 10 G, and a microwave power of 50 µW.

In Figure A3.4 are temperature dependent spectra of WT SPL $_{Bs}$ and C141A SPL $_{Bs}$ reduced with illuminated deazariboflavin in the absence and presence of DTT. In the presence of DTT, the spectra

closely resemble the WT SPL_{Bs} spectrum produced through reduction with dithionite (compare the black spectrum and the red spectra in Figure A3.4). Without DTT, the spectra are distorted such that the lowest-field feature at 330 mT is more intense than in the typical WT SPL_{Bs} spectrum produced through reduction with dithionite. This increase is in part due to a sharp organic radical attributed to deazariboflavin which is seen at 40 K. However, the EPR intensity of this radical is weak compared to the FeS cluster and does not seem intense enough to distort the spectra collected with deazariboflavin and DTT at 5 K (WT) or 10 K (C141A).

The additional distortion of the FeS spectrum when DTT is absent is attributed to a $[3Fe\text{-}4S]^+$ cluster signal, which is expected to occur in as-isolated enzymes that have not been reduced. These spectra typically show one strong feature at g = 2.01 (i.e. overlapping with the lowest-field feature of the $[4Fe\text{-}4S]^+$ signal).[1] In Figure A3.5 *left* we show an attempt to quantitate the $[3Fe\text{-}4S]^+$ cluster signal in samples without DTT present by simulating the $[4Fe\text{-}4S]^+$ signal in samples with both deazariboflavin and DTT. It is clear in the experimental spectra (compare green and blue spectra in the top figure of Figure A3.5 *top left*) that an additional low-field feature is present is samples lacking DTT. By simulating the $[4Fe\text{-}4S]^+$ spectrum, integrating the spectra, and subtracting the area of the simulated $[4Fe\text{-}4S]^+$ cluster signal (red spectrum in Figure A3.5 *bottom left*) from the samples lacking DTT (green spectrum in Figure A3.5 *bottom left*) we derive a rough estimate for the percentage of $[3Fe\text{-}4S]^+$ as 40% of the spectrum. Very apparent baseline issues prevent this method of quantitation from being fully reliable; however, it is overall apparent some $[3Fe\text{-}4S]^+$ contributes to the signals seen in the samples lacking DTT. In addition, when wider sweeps of the SPL_{Bs} C141A are collected, there is considerably more "junk iron" (or adventitiously bound Fe^{3+}) present which is characterized by the feature at g = 4.2 (160 mT) in Figure A3.5 *right*. This indicates the $[4Fe\text{-}4S]^+$ does not form to the same extent in samples lacking DTT and that thiols can act as the ultimate electron donor in reactions where the FeS cluster is reduced with illuminated deazariboflavin. Much work remains to be done to elucidate the mechanism which restores the activity of C141A SPL_{Bs} in the presence of illuminated deazariboflavin. EPR has played a role in

determining the extent to which thiols are necessary for reduction of the cluster which is ultimately necessary for repair of SP to occur.

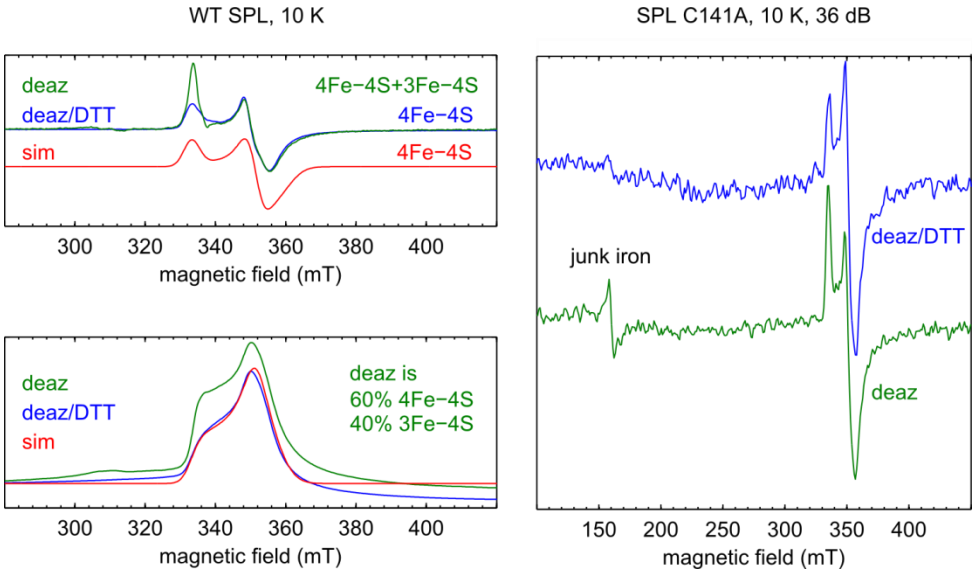

Figure A3.5. *Left, top* The same experimental spectra of WT SPL_{Bs} reduced by illuminated deazariboflavin in the presence and absence of DTT (blue and green spectra respectively) as presented in Figure A3.4. In addition, a simulation of the $[4Fe\text{-}4S]^{+}$ cluster using typical parameters (red spectrum, see simulation parameters in Figure 3.2). *Left, bottom* Integrated spectra from the *Left, top* figure. By subtracting the simulated spectrum ($[4Fe\text{-}4S]^{+}$ only, red) from the spectrum lacking DTT (mixture of $[4Fe\text{-}4S]^{+}$ and $[3Fe\text{-}4S]^{+}$, green) we find that the $[3Fe\text{-}4S]^{+}$ signal makes up (very roughly) ≈ 40 % of the signal. *Right* In addition, samples prepared by reduction with illuminated deazariboflavin in the absence of DTT (green) show an increase in a feature typically attributed to "junk iron" relative to the spectra of samples prepared with DTT present (blue). This also supports the conclusion that a thiol enhances the reduction of the cluster by providing the electron to reduce the FeS cluster.

A3.5 References

(1) Payne, K. A. P.; Quezada, C. P.; Fisher, K.; Dunstan, M. S.; Collins, F. A.; Sjuts, H.; Levy, C.; Hay, S.; Rigby, S. E. J.; Leys, D. *Nature* **2015**, *517*, 513.

Chapter 4

EPR study of UV-irradiated thymidine microcrystals supports radical intermediates in spore photoproduct formation

Abstract

Spore photoproduct is a thymidine dimer formed when bacterial endospore DNA is exposed to ultraviolet (UV) radiation. The mechanism of formation of this thymidine dimer has been proposed to proceed through a radical-pair intermediate. The intermediate forms when a methyl-group hydrogen atom of one thymidine nucleobase is transferred to the C6 position of an adjacent thymidine nucleobase, forming two species, the TCH_2 and TH radicals, respectively. Using a series of thymidine isotopologues and electron paramagnetic resonance (EPR) spectroscopy, we show that microcrystals of thymidine exposed to UV radiation produce these two radical species. We observe three sources which donate the additional hydrogen at the C6 position of the TH radical. One of the three sources is the methyl group of another thymidine molecule in a significant fraction of the TH species. This lends support to the radical pair intermediate proposed in the formation of spore photoproduct.

Contributions

Yajun Jian from Lei Li's group at Indiana University – Purdue University Indianapolis synthesized the deuterium-labeled thymidine.

Publications

Reproduced with permission from Hayes, E. C.; Jian, Y.; Li, L.; Stoll, S., *J. Phys. Chem. B.*, **2016**, 120 (42), 10923-10931. Copyright 2016 American Chemical Society.

4.1 Introduction

The spore photoproduct (SP) is a unique DNA lesion formed when two adjacent thymidine bases dimerize upon exposure to UV radiation. Although the pyrimidine bases have been observed to form

different classes of dimers, including cyclobutane pyrimidine dimers and pyrimidine 6-4 pyrimidone photoproducts,[1] the SP, or 5-thyminyl-5,6-dihydrothymine (see Scheme 4.1) is the dominant photoproduct in bacterial endospore DNA.[2,3] A combination of the low hydration level of DNA, DNA saturation by small acid-soluble proteins, and a high calcium dipicolinate concentration in dormant endospores creates an environment that favors the A conformation of DNA and formation of the 5*R* enantiomer (due to DNA helical structure) of SP over other thymidine photoproducts.[4–6] During spore germination, the 5*R*-SP is efficiently repaired by the 4Fe-4S cluster enzyme spore photoproduct lyase.[7–13] The unique structure of SP and its efficient repair make bacterial endospores resistant to the deleterious effects of UV light on DNA for extremely long periods of time.[14,15] Given the utilization of UV light in sterilization processes,[16–18] it is important to fully understand the mechanisms of formation and repair of the spore photoproduct.

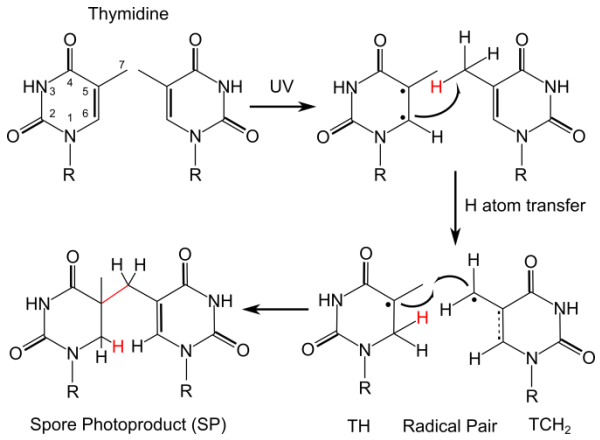

Scheme 4.1: Proposed mechanism for spore photoproduct formation.

A long history of progress has led to the current understanding of the dimerization mechanism which forms SP. Originally, a sequential mechanism was suggested that involved the recombination of two thymine radicals; the oxidation product (an allylic 7-yl radical abbreviated TCH_2) and the reduction product (a 5,6-dihydro-thymid-5-yl radical abbreviated TH).[19,20] These radicals had been previously observed by continuous-wave electron paramagnetic resonance (EPR) spectroscopy in crystals of thymidine and DNA strands irradiated with gamma and UV radiation.[21,22] These radicals share the

structure of the components of the SP dimer (Scheme 4.1) making them likely intermediates during dimerization. However, the source of the additional C6 hydrogen of the TH component was unclear.[23]

To resolve this, Cadet and co-workers irradiated thymidine-d_3 (deuterated at the nucleobase methyl group) in an ice matrix with UV light and found 60% incorporation of deuterium at the C6 position of the TH moiety of the final product SP (highlighted in red in Scheme 4.1).[5,24] The incomplete incorporation of deuterium at the C6 position was puzzling until recently when Lin *et al.* performed similar UV irradiation experiments on thin films of methyl deuterated dinucleotide thymine dinucleoside monophosphate (d_4-TpT or d_3-TpT). Upon analyzing the structure of the photoproducts, they discovered the 5*R*-SP with complete deuterium incorporation in a stereoselective manner from the methyl group of the 3' thymidine to the C6 position of the 5' thymidine.[25] Further studies revealed a substantial kinetic isotope effect (KIE) in SP formation, suggesting that trace unlabeled thymidine-d_3 was the reason for the previously observed incomplete deuterium incorporation at C6.[26] A more detailed mechanism was suggested based on these observations. As depicted in Scheme 4.1, the H atom transfer from the methyl group of the 3' thymidine to the C6 position of the 5' thymidine is postulated to form an intermediate TCH_2/TH radical pair which then recombines to the SP. Despite the establishment of the mechanism, these radicals have not yet been directly observed in the SP photochemistry.

In samples of methyl-deuterated mononucleotide thymidine, Ames *et al.* showed that 5*S*-SP forms through the same H atom transfer mechanism as the biologically relevant 5*R*-SP.[26] Jian *et al.* further showed that dry microcrystals of thymidine monomers, in which the thymine bases stack in a left-handed manner, form the 5*S*-SP as the dominant photoproduct in high yields (≈ 85 %) upon exposure to UV radiation at room temperature.[27,28] The base stacking conformation in microcrystals is believed to mimic that found in spore DNA even though these two systems exhibit an opposite chirality (left-handed yielding 5*S*-SP versus right-handed yielding 5*R*-SP, respectively). Considering the purity and high product yield of the 5*S*-SP in thymidine microcrystals exposed to UV radiation, we used this sample preparation in the studies described here to search for the suggested radical intermediates in the SP formation mechanism in Scheme 4.1.

Table 4.1. TH radical hyperfine coupling and g values [a]

starting material	ionization conditions	*g*	$^{1}H_{C6}$	$^{1}H_{C6}$	$^{1}H_{C7}$ (3x)
thymidine[21]	γ	2.0024	113.4	113.4	57.4
	--	2.0030	113.4	113.4	57.4
		2.0042	113.4	113.4	57.4
thymidine[30]	x-ray RT	--	123.2	117.8	--
			113.6	107.4	
			111.6	106.0	
thymidine[32]	x-ray 10 K	--	123.8	118.3	--
			114.6	107.7	
			112.5	105.9	
thymine[33]	x-ray 10 K	--	133.9	97.0	61.3
			124.4	86.5	53.7
			122.3	85.2	53.3
thymidine[b,c]	UV 120 K	2.0021	114(10)	110(10)	54(5)
		2.0067	114(10)	110(10)	56(5)
		2.0080	117(10)	113(10)	64(5)

[a] Hyperfine coupling principal values are in MHz

[b] Simulation parameters from this study

[c] Error in g values is ± 0.003 (due to 0.5 mT magnet error); error in hyperfine coupling based on varying simulations

Table 4.2. TCH_2 radical hyperfine coupling and *g* values[a]

starting material	ionization conditions	*g*	$^{1}H_{C7}$	$^{1}H_{C7}$	$^{1}H_{C6}$	$^{14}N1$
thymidine[31]	x-ray RT	--	65.8	67.0	42.2	--
			42.8	42.5	29.7	
			21.0	22.0	14.3	
thymidine[32]	x-ray 10 K	--	-70.2	-65.4	-41.8	--
			-42.8	-42.9	-29.7	
			-22.2	-20.4	-14.0	
1-methyl-thymine[32]	x-ray 10 K	--	-72.5	-67.7	-37.4	--
			-44.1	-43.6	-27.1	
			-23.1	-21.0	-13.1	
thymine[33]	x-ray 10 K	--	-66.6	-71.1	-43.5	--
			-43.2	-44.3	-31.2	
			-22.0	-22.3	-15.1	
thymidine[34]	UV 77 K	--	-64.4	-64.4	-39.2	--
			-42.0	-42.0	-28.0	
			-19.6	-19.6	-14.0	
thymidine[b,c]	UV 120 K	2.0045	-56(5)	-56(5)	-36(5)	-1(5)
		2.0055	-42(5)	-42(5)	-28(5)	-1(5)
		2.0065	-19(5)	-22(5)	-20(5)	5(5)

[a] Hyperfine coupling principal values are in MHz

[b] Simulation parameters from this study

[c] Error in g values is ± 0.003 (due to 0.5 mT magnet error); error in hyperfine coupling based on varying simulations

We used electron paramagnetic resonance (EPR) spectroscopy and isotopically labeled thymidine to probe the radical nature of the proposed intermediates in SP formation. Upon exposing samples of dry microcrystalline powders of thymidine to UV radiation, we observed EPR spectra characteristic of the TCH_2 and TH radicals. Previous studies have thoroughly characterized the structure of the two radical intermediates we observed.[21,29–31] However, here we use sample preparations known to cleanly form the 5*S*-SP[28] and an extensive set of thymidine isotopologues. Site-specific labeling allowed us to identify three sources of the hydrogen at the C6 position of the TH radical: an intermolecular methyl group (on the proposed SP pathway), exchangeable hydrogens (off the proposed pathway), and an ambiguous source we term "other" (possibly off the proposed pathway). Applying UV radiation over a wide range of temperatures (120 K, 210 K, and 250 K) results in only a small variation in the ratio of these sources. The observation of TH radicals formed by C6 hydrogen addition from the methyl group of another thymidine molecule lends support to the mechanism of SP formation involving the TCH_2/TH radical pair intermediate.

4.2 Results

Selective deuterium labeling of thymidine can be used to determine the source of the additional hydrogen at the C6 position of the proposed TH radical intermediate. Deuterium has a nuclear spin of 1, but due to its decreased gyromagnetic ratio, has hyperfine coupling strengths ≈ 6.5 times smaller than protium. The mechanism of spore photoproduct formation suggested in Scheme 4.1 indicates the additional hydrogen at the C6 position of the TH radical will come from the methyl group of an adjacent thymidine (which becomes the TCH_2 radical). However, other possible off-pathway sources of the additional hydrogen at C6 of TH are the exchangeable hydrogens of thymidine at N3 of the base and O3' and O5' of the sugar. Here we use four isotopologues of thymidine to distinguish these hydrogen sources; "thy" is the fully protiated thymidine, "H/D-thy" is thymidine deuterated at the positions with exchangeable hydrogens, "thy-d_3" is thymidine deuterated at the C5 methyl group, and "H/D-thy-d_3" is thymidine deuterated at the C5 methyl group and at positions with exchangeable hydrogens. The EPR spectra resulting from UV irradiation (266 nm, 4.66 eV) of microcrystals of these four thymidine

isotopologues at 120 K, 210 K, and 250 K are shown in Figure 4.1. In all cases, after exposure to UV radiation at the temperatures indicated in the figure, the EPR spectra were recorded at 120 K to increase the signal-to-noise ratio.

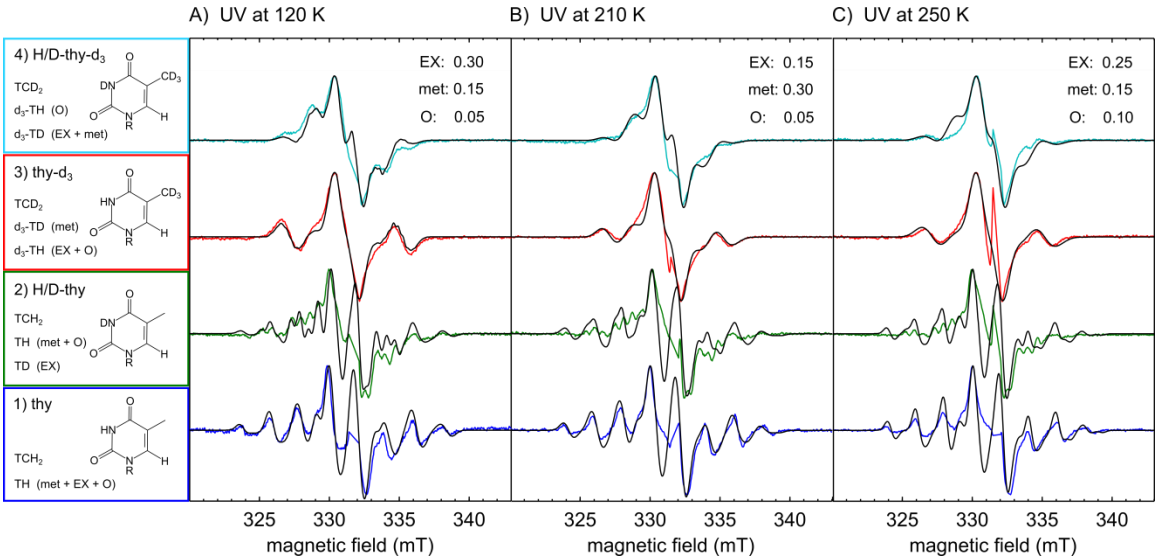

Figure 4.1. Continuous-wave EPR spectra of microcrystalline powder samples of thymidine (blue), H/D-thymidine (green), thymidine-d_3 (red), and H/D-thymidine-d_3 (cyan) photodamaged with 266 nm laser pulses at 120 K, 210 K, and 250 K indicated at the top of each set of axes. In all cases, EPR measurements were carried out at 120 K. The structures of the starting materials are shown in the left column. The isotopologues of the TCH_2 and TH radicals that are used to simulate the spectra are indicated to the left of each starting material. In addition, the hydrogen sources (met, EX, or O defined in main text) that lead to particular TH isotopologues for each starting material are indicated in parenthesis. Simulations were done assuming the restrictive model (defined in main text) and the fractions of hydrogen sources producing TH isotopologues at a given temperature of UV irradiation are indicated at the top right corner of each panel. Simulated spectra are shown in black. EPR spectrometer settings were as follows: microwave power of 0.1 mW to avoid power saturation; microwave frequency between 9.297-9.304 GHz (simulations take in to account the frequency variation between samples); typically 30-100 scans were needed to achieve the signal-to-noise ratio of the spectra shown. In all cases the spectra were normalized to their most intense feature for clarity. At the center of each experimental spectrum was a feature attributed to a quartz-based radical which was removed for clarity.

With our choices in isotopologues of thymidine starting material we can distinguish three sources of the additional hydrogen at C6 of the TH radical; the methyl group (abbreviated “met”, on proposed SP formation pathway), the exchangeable hydrogens (abbreviated “EX”, off proposed SP pathway), or any other hydrogens in the system (abbreviated “O”, possibly off proposed SP pathway). In total, only two spectroscopically distinct isotopologues of the TCH_2 radical (TCH_2 and TCD_2) and four isotopologues of the TH radical (TH, TD, d_3-TH, and d_3-TD, structures in Figure 4.2) can form. The starting materials will

produce predictable isotopologues of the TH radicals depending on the source of the additional hydrogen at C6. In the left column of boxes in Figure 4.1, we summarize which TCH_2 and TH isotopologues will form in a given starting material. In addition, the source of the additional C6 hydrogen (either met, EX, or O) which forms the TH isotopologues is indicated in parentheses.

In order to gain an understanding of the magnetic properties of the suggested radical intermediates in SP formation we performed density functional theory (DFT, B3LYP, 6-311G) calculations. For TCH_2, DFT calculations reveal substantial spin density on C5, C6, and C7 which results in strong hyperfine coupling to the protons at positions 6 and 7. For TH, DFT calculations show substantial spin density on C5 which results in hyperfine coupling to the three methyl protons and very strong couplings to the two protons at the C6 position (Figure 4.3 and Tables 4.1 and 4.2).

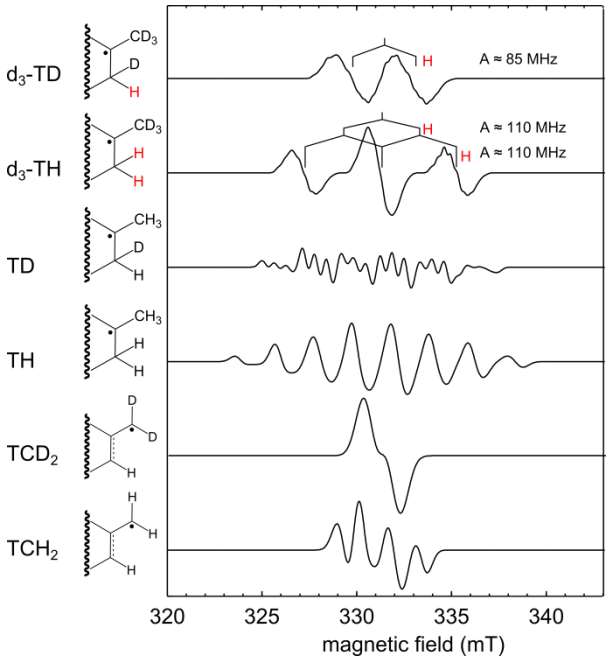

Figure 4.2. Simulations of the 9.3 GHz EPR spectra of the six radicals (two TCH_2 isotopologues, four TH isotopologues) that appear as components in the mixtures that give the spectra of Figure 4.1. Simulated spectra are area normalized.

To begin spectral simulations, the bottom spectrum in Figure 4.1A (thy starting material) was simulated as a 1:1 ratio of the TCH_2 and TH radicals using the results of DFT calculations for EPR properties of the TCH_2 and TH radicals. Then the principal values of the magnetic parameters were varied until adequate

agreement between the simulated and experimental spectra was achieved. This produced the magnetic property values of the primary isotopologues which are in reasonable agreement with the literature values in Tables 4.1 and 4.2 (also see Appendix A4.1). To simulate EPR spectra of TCH_2 and TH isotopologues we scaled down the appropriate proton hyperfine coupling values of the primary isotopologues using the ratio of gyromagnetic ratios $\gamma_{1_H}/\gamma_{2_H}$ ≈ 6.5. In the case of the d_3-TD isotopologue, the hyperfine coupling of the one strongly coupled proton was scaled down to 75% of the hyperfine coupling of the primary TH isotopologue. The scaled-down value (A_{iso} ≈ 85 MHz) is within the range of C6 proton couplings reported in the literature (see Table 4.1). The Fermi contact term of these hyperfine coupling values are expected to depend strongly on the dihedral angle C7-C5-C6-H_{C6}. Structural variation when one deuterium nucleus is present at C6 may be the cause for the decrease. The hyperfine coupling values of all isotopologues are summarized in the supplementary information (Tables A4.1a and A4.1b).

For clarity, the spectra of TCH_2 and TH isotopologues are separately simulated in Figure 4.2. The d_3-TH radical has a triplet pattern with features at ≈ 327 mT, ≈ 331 mT, and ≈ 335 mT. This is due to strong coupling, *A*, to two protons at C6. The d_3-TD spectrum is distinguished by strong hyperfine coupling to one proton at C6. This produces a doublet pattern with features at 330 mT and 333 mT. This radical can form in thy-d_3 only when "met" is the hydrogen source. It is the presence of the d_3-TD radical in the UV-photodamaged products of thy-d_3 that will lend support to the mechanism of SP formation in Scheme 4.1 involving the radical pair intermediate.

It is clear that the experimental spectra in Figure 4.1 are mixtures of the individual spectra simulated in Figure 4.2. We developed a "restrictive model" to quantitate these mixtures of TCH_2 and TH isotopologues. To perform simulations, we assumed an equal ratio (1:1) of the TCH_2:TH isotopologues in each spectrum to account for the expected stoichiometry of oxidation and reduction (transfer of one electron and hydron) which we call the "1:1 restriction". In addition, we assumed that the ratio of hydrogen sources "met", "EX", and "O" leading to the reduction products (TH isotopologues) was identical for all starting materials at a given UV irradiation temperature. As this assumption essentially

excludes kinetic isotope effects, we call it the “isotope effect restriction”. These assumptions allowed us to simultaneously simulate the four spectra collected at a particular temperature. We found one set of fractions of the three hydrogen sources (which produce predictable TH isotopologues with respect to the particular starting material) that yielded an adequate simulation for each of the four spectra.

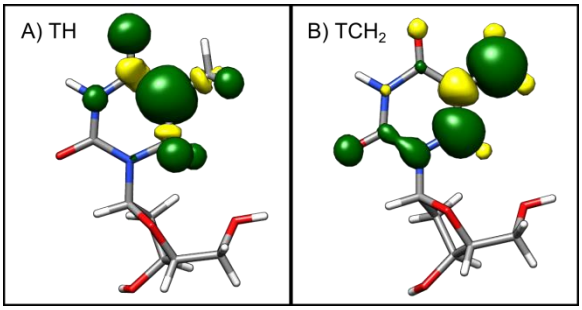

Figure 4.3. Calculated spin density distributions (isosurface contoured at $\pm 0.0025\ a_0^{-3}$) of the TH and TCH_2 radicals. Positive spin density is shown in green and negative spin density is shown in yellow.

The spectrum for H/D-thy-d_3 in Figure 4.1A reveals the percentage of TH isotopologue which forms due to the “O” hydrogen source (5 %), as this is the only way to produce the d_3-TH radical in this material. The spectrum for thy-d_3 in Figure 4.1A reveals the percentage of TH isotopologues (15 %) which form due to the “met” hydrogen source, as this is the only way to produce to the d_3-TD radical from this starting material. Finally, the “EX” hydrogen source was used to account for the remaining 30 % of TH isotopologues which should be produced assuming the 1:1 restriction. The ratios of hydrogen sources which produce the TH radicals are summarized at the top right corner of Figure 4.1A next to the abbreviations “met”, “EX”, and “O”. With the same assumptions and methodology, the ratios of hydrogen sources producing TH isotopologues at 210 K and 250 K were determined and the results listed in the top right corners of Figures 4.1B and 4.1C.

Despite the limiting assumptions in our model, the agreement between experimental and simulated spectra is satisfactory. However, as there are obvious visual disagreements, we also performed less restrictive simulations. In Figure A4.1, we show the same data as in Figure 4.1, simulated without assuming either the isotope effect restriction or the 1:1 restriction. In addition, the hyperfine coupling of the TH isotopologues were altered slightly from the primary isotopologue (TH formed from UV

irradiation at 120 K) but still kept within 25% of the primary values (parameters in Tables A4.2a and A4.2b). Removing these restrictions allows for better visual agreement with the experimental spectra. Generally, the new simulations indicate that the ratio of TCH_2:TH isotopologues is roughly 1:1 after UV irradiation at 120 K, but increases to 2:1 after UV irradiation at 250 K. In addition, the relative contribution of TH radicals produced with the "O" hydrogen source compared to TH radicals produced by the "met"+"EX" sources increases at warmer temperatures of UV irradiation. Most importantly, the simulations for thy-d_3 exposed to UV radiation at all three temperatures must include some contribution from the d_3-TD radical, indicating a methyl group source for the additional hydrogen at the C6 position of the TH isotopologues which supports TH formation through the mechanism shown in Scheme 4.1.

We explored the reproducibility of our results. In general, for a particular starting material UV irradiated at a given temperature, the identities of radical isotopologues present in the spectra are reproducible (see Figures A4.2 and A4.3). However, the ratio of radicals varies. For instance, in Figure A4.4 we show four different trials of thy-d_3 irradiated at 120 K which we simulated using three different schemes. We find the percentage of d_3-TD varies from 0 % to 25 % among the four sample trials. Although it is tempting to try to draw quantitative conclusions from our simulations, the poor reproducibility as shown in Figure A4.4 precludes extensive interpretation.

UV radiation was applied at 120 K to trap higher yields of intermediates. However, since the reaction in spore DNA takes place at biological temperatures, we also applied UV radiation at the warmer temperatures of 210 K and 250 K. We note the features due to the d_3-TD radical in thy-d_3 (evidence for the "met" hydrogen source which supports the suggested SP mechanism) are most prominent in the sample irradiated at 210 K indicating this may be the best temperature we tested for trapping this intermediate. Applying UV radiation at 250 K led to decreased signal intensity and spectral broadening; therefore, UV irradiation temperatures above 250 K were not pursued.

We also explored the temperature dependence of the spectra after completion of the irradiation. This helped to identify the reason for increased broadening in the spectra of samples exposed to UV radiation at temperatures greater than 120 K. The increased line width may be due to two different

types of broadening. First, there is the homogeneous broadening that occurs due to spin relaxation which should become more pronounced at warmer temperatures. Indeed, increasing the EPR measurement temperature to 260 K for material UV irradiated at 120 K broadens out the hyperfine features (Appendix Figure A4.5A). Second, there is site-to-site inhomogeneity in the microcrystalline lattice. There is more thermal energy in starting material exposed to UV radiation at warmer temperatures which may allow the radicals to populate a wider range of conformations as the photodamage occurs. For example, although the features of material UV irradiated at 210 K and 250 K sharpen as the measurement temperature is dropped to 120 K (decreased homogeneous broadening as stated above, Appendix Figure A4.5B and C) the spectra do not reach the sharpness observed for samples exposed to UV radiation at 120 K. Importantly, variation of the EPR measurement temperatures shows no new species are formed when UV is applied at variable temperatures.

Therefore, we also performed measurements on thin film samples (Appendix Figures A4.2 and A4.3), since UV irradiation of thymidine thin films (formed by evaporation of methanol) has also been shown to produce the SP dimer.[26] The results show the same formation of TCH_2 and TH radical isotopologues, but generally with broadened spectral features compared to the microcrystal samples, supporting the idea that some of the broadening is caused by structural heterogeneity.

4.3 Discussion

Site-selective isotopic labeling has more clearly established the sources of the additional hydrogen at the C6 position of the TH radicals formed when microcrystals of thymidine are exposed to UV radiation. We modeled these sources of hydrogen with restrictive spectral simulations of our data in Figure 4.1. Fits are improved with an unrestrictive model where we relaxed the 1:1 restriction and the isotope effect restriction (Figure A4.1). In Figure A4.6, we graphically represent the ratio of isotopologues used in the restrictive and unrestrictive models in Figures 4.1 and A4.1. Using the two models and the graphical representation of the results, we understand the underlying reasons for the misfits in Figure 4.1 and can identify trends in the data. We will now discuss our findings in the context of previous

literature concerning both the formation of spore photoproduct and the more general effects of ionizing radiation on thymidine.

4.3.1 Observation of the "met" hydrogen source.

It is not surprising that a mixture of sources ("met", "EX", and "O") donate the additional hydrogen at C6 of the TH isotopologues. Previously, it was observed that crystals of thymidine grown in D_2O (H/D-thy) formed the TD isotopologue (our "EX" source) when X-ray radiation was applied at 77 K. Alternatively, when UV radiation (320 nm) was applied to H/D-thy at 77 K, the TH isotopologue (our "met" or "O" source in H/D-thy) was the dominant product.[34] This latter result is in contrast to our measurements where we see TD as the dominant isotopologue formed in H/D-thy upon UV irradiation at or above 120 K. Although this latter result from the literature is indicative of the "met" source, in these studies isotopic labeling of the methyl group was not performed to confirm the source of the C6 hydrogen in TH. It was observed that dry films of thymidine-d_3 and DNA labeled with thymine-d_3 formed the d_3-TH isotopologue when exposed to UV radiation at 77 K[22] (analogous to our "EX" and "O" in thy–d_3). The poor resolution of these early experiments did not allow observation of the d_3-TD radical (our "met" source) if it was present. Our simulations have allowed us to quantitate the contributions of three C6 hydrogen sources which lead to the TH isotopologues. Compared to other studies we observe the "met" source of the additional hydrogen at C6 of the TH radical which is indicative of radical intermediates in SP formation.

4.3.2 Relaxing the isotope effect restriction

Using the unrestrictive model, simulations of the data are improved when the ratios of hydrogen sources are allowed to vary for different thymidine isotopologues at a given temperature of UV radiation. This is likely due to isotope effects. SP formation has a KIE of 3.5 in dinucleotide thymidine (TpT) thin films exposed to UV radiation.[25] This deuterium discrimination triples for monomeric thymidine thin films.[26] Considering this, formation of the TH radical via the SP mechanism ("met") should be more favorable in thymidine with protiated methyl group than in thymidine with deuterated methyl group. In our samples, this would manifest as a larger relative ratio of TH ("met" + "O") in H/D-

thy than the ratio of d_3-TD ("met") in thy-d_3 for a given temperature of UV irradiation. However, in Figure A4.6 (right) we can see the ratio of d_3-TD in thy-d_3 is larger at all three temperatures. One could speculate that non-deuterated starting material is more likely to proceed to the final product, SP, thus quenching more of the TH radicals in H/D-thy samples.

4.3.3 Isotope effects: the "O" source of hydrogen

The large deuterium discrimination in SP formation potentially accounts for our "O" source of hydrogen. The "met" and "O" sources may be equivalent with the "O" source resulting from the trace ^{1}H impurities in the synthesis of thymidine-d_3 (99.5 % pure).[26] If this is the case, the impurities account for ≈ 25 %, 14 %, and 40 % of the TH isotopologues formed by the SP mechanism ("met" or "O") at 120 K, 210 K, and 250 K, respectively (using the hydrogen source fractions obtained from our restrictive model in Figure 4.1). With a 0.5 % impurity, this would indicate 50-fold, 28-fold, and 80-fold deuterium discriminations, respectively. As these numbers are larger than the reported discrimination, there may also be incomplete labeling of the exchangeable positions in the H/D-thy-d_3 sample which we use to measure the percentage of TH isotopologues formed by the "O" source of hydrogen.

In addition, there is a larger relative fraction of TH isotopologues produced by the "O" source at warmer temperatures of UV irradiation using either the restrictive or unrestrictive model. Previous EPR studies have been carried out on thymidine crystals grown in D_2O (analogous to our starting material H/D-thy). Gamma irradiation of these single crystals at 77 K produced the TD isotopologue (our "EX" source).[35] Upon annealing these samples to warmer temperatures, the deuterium began to exchange for protium at room temperature and fully exchanged after annealing to 373 K forming the TH isotopologue. Our EPR spectra do not show obvious signs of H/D exchange upon warming the samples irradiated at 120 K to 260 K (Figure A4.2). However, the increase in the ratio "O"/"met+EX" (0.25 at 120 K to 0.65 at 250 K, unrestrictive model) in H/D-thy-d_3 samples may be indicative of deuterium-to-protium exchange occurring during the photodamage process at warmer temperatures of UV irradiation.

4.3.4 Relaxing the 1:1 restriction

Relaxing the 1:1 restriction in our model also improves the agreement of the simulations with the experimental spectra (compare Figure 4.1 to Figures A4.1 and A4.4). In several previous studies, the TCH_2 radical is reported as a minor species in comparison to the TH radical.[21,31,34] In addition, the TCH_2 radical has been reported to form as a radical pair in gamma irradiated single crystals of thymine where H_2 is believed to form in the process.[36] In this instance, two oxidation products form without the generation of a reduction product. The graphic in Figure A4.6 (right) illustrates that the ratio TCH_2:TH trends from 1:1 to 2:1 as the UV irradiation temperature is increased in our experiments. This is in contrast to the literature where the TCH_2 radical is reported as a minority species in single crystals of irradiated thymidine at cryogenic temperatures and at room temperature.

4.3.5 The "EX" source of hydrogen

Previous literature suggests a possible mechanism for the "EX" source. The T^- radical (one electron addition) is a potential precursor to the TH radical (one electron, one proton addition). The T^+ radical (one electron loss) is a potential precursor to the TCH_2 radical (one electron loss, deprotonation at the methyl group). Holroyd and Glass observed the TH and TD radicals in glasses of thymidine in H_2O and D_2O, respectively, which they postulated to form through hydronation of the T^- radical.[37] Further studies by Sevilla established that the T^- and T^+ radical can form in frozen aqueous solutions of thymine exposed to UV radiation (77 K).[38–41] In these studies, T^+ and T^- were observed to decay to the TCH_2 and TH radicals, respectively, upon increasing the temperature to 143 K.[38] Hydronation at the C6 position of the anion radicals of thymine and uracil has also been followed at room temperature by both electronic absorption and solution state EPR spectroscopies.[42,43] It is possible that our TH isotopologues produced by the "EX" source of hydrogens also form through hydronation of the T^- radical. However, the literature results were obtained for aqueous samples of thymine (not thymidine) exposed to UV radiation. In solvent-free thymidine crystals, the T^- radical, along with the TCH_2 and TH radicals, have been observed at irradiation (x-ray) and EPR measurement temperatures of 10 K and lower.[30,32,33,44,45] Warming these samples to 40 K caused decay of the anion radical but did not lead to observable increase in the

concentration of TH radical[32,33,45] suggesting that in the solid state the anion does not clearly decay into the TH radical. Our temperature variation studies did not reveal changes in radical species, so we cannot conclude that our "EX" source is equivalent to hydronation of the T^- radical (Figures A4.2, A4.3, and A4.5).

4.3.6 Presence of alternative radicals: T^- and T^+

The substantial improvement in simulations we achieve after relaxing our restrictions helps substantiate our assumption that only TCH_2 and TH isotopologues are present in our system. However, as stated, the T^+ and T^- radicals are relevant species in solution and the T^- radical (Appendix Figure A4.7) is a relevant product in the irradiation of DNA strands.[46,47] Given the simplicity of the T^- EPR spectrum (Appendix Figure A4.7) we cannot completely rule out its presence in our spectra, but we can adequately simulate our data without it. The T^+ radical would produce a more distinct spectrum (Appendix Figure A4.7) so it seems unlikely that it is present in our spectra. In a more complicated situation, Malone *et al.* irradiated thymidine monophosphate at 77 K in aqueous perchlorate glass and found a mixture of TCH_2, TH, and anion radicals. Warming this sample to 240 K caused decay of the TH radical with no observable successor and decay of the TCH_2 radical to a quintet species.[48] Despite these observations in other systems, we do not need to include additional radical species to achieve better simulations of our data.

4.3.7 Lack of expected radical pair interaction

We do not see evidence in our spectra for the strong electron-electron interaction expected for the radical pair intermediate directly on the proposed pathway to SP in Scheme 4.1. Previously, Dulčić *et al.* observed very-low-intensity signals assigned to pairs of TCH_2 radicals ≈ 5 Å apart in thymidine crystals with dipolar splitting on the order of ≈ 15 mT.[36] Based on the crystal structure by Young *et al*.,[27] the atoms of adjacent thymidine rings are ≈ 3-4 Å apart which would result in a dipolar splitting of 30-60 mT for a radical pair in our microcrystals. Our spectra are adequately simulated without any electron-electron coupling. Our simulations utilize line broadenings less than about 1 mT which corresponds to radicals at least 12 Å apart. Previous studies[25] and theoretical calculations[49] of the SP formation mechanism also suggest that an excited triplet state forms prior to the rate-limiting H-atom abstraction

step which forms the radical pair. Here, we saw no evidence of a triplet state (no half field signal, data not shown).

Although high yields of SP have been achieved in room temperature suspensions of thymidine microcrystals exposed to UV light for 12 hours or longer, we see a low radical yield (requiring measurement times of ≈ 1 hour) after about 45 minutes of UV irradiation.[28] Our low yield is likely due to excitation of thymidine molecules limited to the outermost layer next to the EPR sample tube, similar to the observation made by Jian *et al.* in the thymidine film photoreactions.[28] We suggest that the radicals produced by the "met" source are left over after on-SP pathway H-atom transfer has occurred, though how these radicals become trapped remains unclear. Similarly, the TH isotopologues produced by the "O" hydrogen source may be equivalent to the "met" source (therefore on the SP pathway) and due to trace ^{1}H impurities in thymidine-d_3. The TH radicals produced by the "EX" source form through a mechanism that is not on the suggested pathway to SP formation.

4.4 Conclusions

In previous studies of deuterium-labeled thymidine, spore photoproduct was observed to form when one thymidine molecule abstracted an H atom from the methyl group of an adjacent thymidine onto its C6 position on route to the final product. This H atom abstraction is suggested to form the TCH_2 and TH as a radical pair intermediate. We have shown that the TCH_2 and TH radicals both form in thymidine microcrystals exposed to UV radiation under a dry argon atmosphere. We did not observe the dipolar or exchange interactions expected for a radical pair. However, using selective isotopic labeling, we did observe several sources of the additional hydrogen at the C6 position of the TH radical isotopologues, including the methyl group of another thymidine molecule. This is consistent with the mechanism in Scheme 4.1 and lends support to the proposed radical nature of the intermediates. Although both radicals were observed in previous EPR studies, the experimental finding that *5S*-SP is generated as the sole photoproduct in UV irradiated thymidine microcrystals as used here establishes the biological relevance of the study to the SP photochemistry for the first time.

4.5 Materials and Methods

Sample Preparation. All chemicals were used without further purification after purchase. Gaseous nitrogen and argon were passed through a desiccant drying line before use in sample preparation. Glassware was dried in an oven overnight before use. Water vapor was avoided in sample preparation as relative humidity has been reported to influence the radicals produced in irradiated films of thymine and DNA.[22,50] To prepare samples of thymidine in Figure 4.1, microcrystals of thymidine (Sigma-Aldrich) were suspended in diethyl ether (99%, Sigma-Aldrich) and pipetted to the bottom of a 4 mm O.D. quartz EPR sample tube. The ether was removed on a vacuum manifold for a minimum of 5 hours. The EPR tube was pump-purged for three cycles under vacuum and argon and flame sealed under a low-pressure argon environment with a propane oxygen torch. A similar procedure was used for thymidine-d_3. Thymidine-d_3 was synthesized as previously described.[26]

To prepare H/D-thy, thymidine was dissolved in methanol-d_4 (Cambridge Isotopes, 99.8% D) to a ratio of $\geq$300:1 exchangeable deuterons:protons in an EPR sample tube. To prevent exposure to atmospheric water, the sample tube was stored in a desiccated environment under a constant flow of nitrogen for 24 hours, after which the methanol-d_4 was pumped off on a vacuum manifold with tip-off manifold adapter. This procedure was repeated two more times. On the final exchange, the methanol-d_4 was allowed to slowly evaporate over the course of 1-2 days by directing dry nitrogen into the EPR tube with a syringe needle. This produced powdery white crystals of H/D-thy. The exchange in methanol-d_4 appears complete as indicated by ^{1}H NMR (Figure A4.8). The same procedure was used to prepare H/D-thy-d_3 from thymidine-d_3.

Radical generation. Paramagnetic signals were generated using the 266 nm wavelength of an Nd:YAG laser (Continuum, Surelite EX). Laser pulses (less than 800 μJ per pulse, 3-5 ns pulse length, 10 Hz repetition rate, 10 mm spot size; 10 mW/cm^2) were passed through space into a 2 mm aperture on a Bruker SHQE cavity EPR resonator held at the desired temperature. Low-power laser pulses make biphotonic processes unlikely in this system.[51] Samples were irradiated for 5 minutes, then the sample tube was rotated to increase sample exposure to UV radiation. This was done up to a total irradiation

time of 45 minutes. Samples in Figure 4.1A were irradiated at 120 K. The radiation was then removed and EPR spectra collected. The samples in Figure 4.1B (4.1C) were irradiated at 210 K (250 K) then radiation was removed. The cavity was then cooled to 120 K and allowed to equilibrate for 5 minutes followed by collection of EPR spectra without any additional UV radiation.

EPR spectroscopy. EPR experiments were carried out on a Bruker EMX spectrometer in an SHQE cavity resonator equipped with a variable-temperature insert. Experimental temperatures of 120 K, 210 K, 250 K, and 260 K were measured on a thermocouple ≈ 2 cm below the sample. The desired temperature was reached with a temperature controller utilizing the flow of evaporated nitrogen through a quartz transfer line as coolant. Spectra were collected at a frequency of ≈ 9.3 GHz (specified in figure captions) with the microwave power set to prevent saturation (see figure captions for more detail). Additional spectrometer parameters for all spectra collected were field modulation with 0.2 mT peak-to-peak amplitude and 100 kHz frequency, time constant of 40.96 ms, and sweep rate of ≈ 0.7 mT/s.

UV irradiation of the samples produced a sharp feature at the center of the EPR spectra attributed to radicals generated in the quartz tubes. The central 25 or fewer points were removed in the spectra plotted in Figure 4.1 for clarity. This central feature can be seen in the data presented in the Appendix. In all cases, the spectra presented are normalized to their most intense feature (in some cases the quartz feature, Appendix Figures A4.2 and A4.3) for clarity.

Density Functional Theory (DFT) calculations. Geometry optimization calculations were carried out on the Gaussian09 software[52] with spin unrestricted orbitals, the B3LYP functional, and the 6-311G basis set for the TCH_2 and TH radicals. Using the output geometry of the optimized TH radical, geometry optimization dependent on the methyl group rotation was carried out at the same level of theory. This was done by simultaneously incrementing the three dihedral angles from C6-C5-C7-H1, C6-C5-C7-H2, and C6-C5-C7-H3, freezing the dihedral angles and performing a geometry optimization on the remaining structure. This was performed in 10 degree increments for 11 steps generating an output file of 12 optimized structures. The magnetic properties including g-tensors and hyperfine coupling constants were calculated using coupled-perturbed Kohn-Sham approach for the TCH_2 geometry and

each of the 12 TH optimized geometries in ORCA 3.0 with spin unrestricted orbitals, the B3LYP functional, and the 6-311G basis set.[53–56] Calculated Mulliken spin populations are visualized with the Chimera software.[57]

Spectral simulations. EPR spectra were simulated with the EasySpin software[58] using the model spin Hamiltonian

$$\hat{H} = \mu_{\mathrm{B}} \boldsymbol{B} \boldsymbol{g} \hat{\boldsymbol{S}} + \sum_{k} h \hat{\boldsymbol{S}} \boldsymbol{A}_k \hat{\boldsymbol{I}}_k \qquad \text{Eq. 4.1}$$

where the first term is the electron Zeeman interaction containing the Bohr magneton, μ_{B}, the externally applied magnetic field $\boldsymbol{B}$, the electron spin operator $\hat{\boldsymbol{S}}$, and the electron g tensor, $\boldsymbol{g}$. The second term describes the hyperfine interaction between an electron spin, $\hat{\boldsymbol{S}}$, and a nuclear spin, $\hat{\boldsymbol{I}}_k$, with the hyperfine matrix $\boldsymbol{A}_k$. k sums over all coupled nuclei. All tensor orientations used in the simulation were taken from the DFT calculations. The tensor orientation for each of the three methyl group hydrons in the TH isotopologues is the average orientation of the three hydrons further averaged over all twelve optimized structures. Hyperfine principal values and g principal values were varied manually to the values listed in Tables 4.1 and 4.2 for TCH_2 and TH simulations. The hyperfine coupling principal values were adjusted for deuterium nuclei (described in Results section and summarized in Appendix A4.1) for simulation of isotopologues.

4.6 References

(1) Kneuttinger, A. C.; Kashiwazaki, G.; Prill, S.; Heil, K.; Müller, M.; Carell, T. Formation and Direct Repair of UV-Induced Dimeric DNA Pyrimidine Lesions. *Photochem. Photobiol.* **2014**, *90*, 1–14.

(2) Donnellan, J. E.; Setlow, R. B. Thymine Photoproducts but Not Thymine Dimers Found in Ultraviolet-Irradiated Bacterial Spores. *Science* **1965**, *149*, 308–310.

(3) Varghese, A. J.; Wang, S. Y. Ultraviolet Irradiation of DNA in Vitro and in Vivo Produces a Third Thymine-Derived Product. *Science* **1967**, *156*, 955–957.

(4) Kim, S. J.; Lester, C.; Begley, T. P. Synthesis of the Dinucleotide Spore Photoproduct. *J. Org. Chem.* **1995**, *60*, 6256–6257.

(5) Desnous, C.; Guillaume, D.; Clivio, P. Spore Photoproduct: A Key to Bacterial Eternal Life. *Chem. Rev.* **2010**, *110*, 1213–1232.

(6) Setlow, P.; Li, L. Photochemistry and Photobiology of the Spore Photoproduct : A 50-Year Journey. *Photochem. Photobiol.* **2015**, *91*, 1263–1290.

(7) Buis, J. M.; Cheek, J.; Kalliri, E.; Broderick, J. B. Characterization of an Active Spore Photoproduct Lyase, a DNA Repair Enzyme in the Radical S -Adenosylmethionine Superfamily. *J. Biol. Chem.*

2006, *281*, 25994–26003.
(8) Chandor-Proust, A.; Berteau, O.; Douki, T.; Gasparutto, D.; Ollagnier-de-Choudens, S.; Fontecave, M.; Atta, M. DNA Repair and Free Radicals, New Insights into the Mechanism of Spore Photoproduct Lyase Revealed by Single Amino Acid Substitution. *J. Biol. Chem.* **2008**, *283*, 36361–36368.
(9) Chandra, T.; Silver, S. C.; Zilinskas, E.; Shepard, E. M.; Broderick, W. E.; Broderick, J. B. Spore Photoproduct Lyase Catalyzes Specific Repair of the 5R but Not the 5S Spore Photoproduct. *J. Am. Chem. Soc.* **2009**, *131*, 2420–2421.
(10) Benjdia, A.; Heil, K.; Barends, T. R. M.; Carell, T.; Schlichting, I. Structural Insights into Recognition and Repair of UV-DNA Damage by Spore Photoproduct Lyase, a Radical SAM Enzyme. *Nucleic Acids Res.* **2012**, *40*, 9308–9318.
(11) Kneuttinger, A. C.; Heil, K.; Kashiwazaki, G.; Carell, T. The Radical SAM Enzyme Spore Photoproduct Lyase Employs a Tyrosyl Radical for DNA Repair. *Chem. Commun.* **2013**, *49*, 722–724.
(12) Yang, L.; Nelson, R. S.; Benjdia, A.; Lin, G.; Telser, J.; Stoll, S.; Schlichting, I.; Li, L. A Radical Transfer Pathway in Spore Photoproduct Lyase. *Biochemistry* **2013**, *52*, 3041–3050.
(13) Yang, L.; Li, L. Spore Photoproduct Lyase: The Known, the Controversial, and the Unknown. *J. Biol. Chem.* **2015**, *290*, 4003–4009.
(14) Cano, R. J.; Borucki, M. K. Revival and Identification of Bacterial Spores in 25- to 40-Million-Year-Old Dominican Amber. *Science* **1995**, *268*, 1060–1064.
(15) Setlow, P. Spores of Bacillus Subtilis : Their Resistance to and Killing by Radiation, Heat and Chemicals. *J. Appl. Microbiol.* **2006**, *101*, 514–525.
(16) Marshall, M. M.; Hayes, S.; Moffett, J.; Sterling, C. R.; Nicholson, W. L. Comparison of UV Inactivation of Spores of Three Encephalitozoon Species with That of Spores of Two DNA Repair-Deficient *Bacillus Subtilis* Biodosimetry Strains. *Appl. Environ. Microbiol.* **2003**, *69*, 683–685.
(17) Nicholson, W. L.; Galeano, B. UV Resistance of Bacillus Anthracis Spores Revisited: Validation of *Bacillus Subtilis* Spores as UV Surrogates for Spores of *B. Anthracis* Sterne. *Appl. Environ. Microbiol.* **2003**, *69*, 1327–1330.
(18) Guerrero-Beltràn, J. A.; Barbosa-Cànovas, G. V. Review : Advantages and Limitations on Processing Foods by UV Light. *Food Sci. Technol. Int.* **2004**, *10*, 137–147.
(19) Rahn, R. O.; Hosszu, J. L. Photoproduct Formation in DNA at Low Temperatures. *Photochem. Photobiol.* **1968**, *8*, 53–63.
(20) Varghese, A. J. 5-Thyminyl-5,6-Dihydrothymine from DNA Irradiated with Ultraviolet Light. *Biochem. Biophys. Res. Commun.* **1970**, *38*, 484–490.
(21) Pruden, B.; Snipes, W.; Gordy, W. Electron Spin Resonance of an Irradiated Single Crystal of Thymidine. *Proc. Natl. Acad. Sci.* **1965**, *53*, 917–924.
(22) Pershan, P. S.; Shulman, R. G.; Wyluda, B. J.; Eisinger, J. Electron Spin Resonance of Irradiated DNA. *Science* **1965**, *148*, 378–380.
(23) Varghese, A. J. Photochemistry of Thymidine in Ice. *Biochemistry* **1970**, *9*, 4781–4787.
(24) Cadet, J.; Vigny, P. The Photochemistry of Nucleic Acids. In *Bioorganic Photochemistry: Photochemistry and the Nucleic Acids*; Morrison, H., Ed.; J. Wiley & Sons: New York, **1990**; Vol. 1, pp 96-99.
(25) Lin, G.; Li, L. Elucidation of Spore-Photoproduct Formation by Isotope Labeling. *Angew. Chem. Int. Ed.* **2010**, *49*, 9926–9929.
(26) Ames, D. M.; Lin, G.; Jian, Y.; Cadet, J.; Li, L. Unusually Large Deuterium Discrimination during Spore Photoproduct Formation. *J. Org. Chem.* **2014**, *79*, 4843–4851.
(27) Young, D. W.; Tollin, P.; Wilson, H. R. The Crystal and Molecular Structure of Thymidine. *Acta Crystallogr. Sect. B Struct. Crystallogr. Cryst. Chem.* **1969**, *25*, 1423–1432.

(28) Jian, Y.; Ames, D. M.; Ouyang, H.; Li, L. Photochemical Reactions of Microcrystalline Thymidine. *Org. Lett.* **2015**, *17*, 824–827.
(29) Herak, J. N.; Galogaza, V. Radical Transformation in Irradiated DNA and Its Constituents. *Proc. Natl. Acad. Sci. U. S. A.* **1969**, *64*, 8–12.
(30) Box, H. C.; Budzinski, E. E.; Potter, W. R. ENDOR Characterization of the Free Radical in Irradiated Thymidine. *J. Chem. Phys.* **1974**, *61*, 1136–1139.
(31) Herak, J. N.; McDowell, C. A. ENDOR Study of the Minority Radicals Formed in X-Ray-Irradiated Single Crystals of Thymidine. *J. Magn. Reson.* **1974**, *16*, 434–438.
(32) Hole, E. O.; Sagstuen, E.; Nelson, W. H.; Close, D. M. Primary Reduction and Oxidation of Thymine Derivatives. ESR/ENDOR of Thymidine and 1-Methylthymine X-Irradiated at 10 K. *J. Phys. Chem.* **1991**, *95*, 1494–1503.
(33) Sagstuen, E.; Hole, E. O.; Nelson, W. H.; Close, D. M. Radiation-Induced Free-Radical Formation in Thymine Derivatives. EPR/ENDOR of Anhydrous Thymine Single Crystals X-Irradiated at 10 K. *J. Phys. Chem.* **1992**, *96*, 1121–1126.
(34) Flossmann, W.; Zehner, H.; Müller, A. Radicals Produced in Single Crystals of Thymine Derivatives by UV and X-Rays. *Z. Naturforsch.* **1980**, *35*, 20–29.
(35) Herak, J. N. EPR Study of Radiation Damage of Deuterated Single Crystal of Thymidine. *J. Chem. Phys.* **1970**, *52*, 6440–6441.
(36) Dulcic, A.; Herak, J. N. Radiation-Induced Pair-Wise Radical Formation in Single Crystals of Thymine. *Biochim. Biophys. Acta* **1973**, *319*, 109–115.
(37) Holroyd, R. A.; Glass, J. W. Radicals Formed by Electron Transfer to Pyrimidine Derivatives. *Int. J. Radiat. Biol.* **1968**, *14*, 445–452.
(38) Sevilla, M. D. An Electron Spin Resonance Study of the Photoionization of Thymine. The Thymine Cation and Anion Radicals. *J. Phys. Chem.* **1971**, *75*, 626–631.
(39) Sevilla, M. D.; Van Paemel, C.; Nichols, C. An Electron Spin Resonance Study of Several Base Cation Radicals Produced by Photoionization. *J. Phys. Chem.* **1972**, *76*, 3571–3577.
(40) Sevilla, M. D.; Van Paemel, C.; Zorman, G. Reactions of the Cation and Anion Radicals of Several DNA Bases. *J. Phys. Chem.* **1972**, *76*, 3577–3582.
(41) Adhikary, A.; Kumar, A.; Heizer, A. N.; Palmer, B. J.; Pottiboyina, V.; Liang, Y.; Wnuk, S. F.; Sevilla, M. D. Hydroxyl Ion Addition to One-Electron Oxidized Thymine: Unimolecular Interconversion of C5 to C6 OH-Adducts. *J. Am. Chem. Soc.* **2013**, *135*, 3121–3135.
(42) Deeble, D. J.; Das, S.; von Sonntag, C. Uracil Derivatives: Sites and Kinetics of Protonation of the Radical Anions and the UV Spectra of the C(5) and C(6) H-Atom Adducts. *J. Phys. Chem.* **1985**, *89*, 5784–5788.
(43) Novais, H. M.; Steenken, S. ESR Studies of Electron and Hydrogen Adducts of Thymine and Uracil and Their Derivatives and of 4,6-Dihydroxypyrimidines in Aqueous Solution. Comparison with Data from Solid State. The Protonation at Carbon of the Electron Adducts. *J. Am. Chem. Soc.* **1986**, *108*, 1–6.
(44) Box, H. C.; Budzinski, E. E. Primary Radiation Damage in Thymidine. *J. Chem. Phys.* **1975**, *62*, 197–199.
(45) Sagstuen, E.; Hole, E. O.; Nelson, W. H.; Close, D. M. Structure of the Primary Reduction Product of Thymidine after X Irradiation at 10 K. *J. Phys. Chem.* **1989**, *93*, 5974–5977.
(46) Cullis, P. M.; Evans, P.; Malone, M. E. Electron Addition to DNA-Thymine vs Cytosine Radical Anion? *Chem. Commun.* **1996**, 985–986.
(47) Adhikary, A.; Kumar, A.; Becker, D.; Sevilla, M. D. Understanding DNA Radicals Employing Theory and Electron Spin Resonance Spectroscopy. *Encyclopedia of Radicals in Chemistry, Biology and Materials*, 2012, 1–26.
(48) Malone, M. E.; Symons, M. C. R.; Parker, A. W. An EPR Study of Photoionised Thymine and Its

Derivatives at 77 K. *J. Chem. Soc. Perkin Trans. 2* **1993**, 2067–2075.
(49) Du, Q.; Zhao, H.; Song, D.; Liu, K.; Su, H. Consecutive Reaction Mechanism for the Formation of Spore Photoproduct in DNA Photolesion. *J. Phys. Chem. B* **2012**, *116*, 11117–11123.
(50) Rahn, R. O.; Hosszu, J. L. Influence of Relative Humidity on the Photochemistry of DNA Films. *Biochim. Biophys. Acta* **1969**, *190*, 126–131.
(51) Angelov, D.; Berger, M.; Cadet, J.; Getoff, N.; Keskinova, E.; Solar, S. Comparison of the Effects of High-Power U.V.-Laser Pulses and Ionizing Radiation on Nucleic Acids and Related Compounds. *Internatial J. Radiat. Appl. Instrum. Part C* **1991**, *37*, 717–727.
(52) Gaussian 09, Revision C.01, Frisch, M. J.; Trucks, G. W.; Schlegel, H. B.; Scuseria, G. E.; Robb, M. A.; Cheeseman, J. R.; Scalmani, G.; Barone, V.; Mennucci, B.; Petersson, G. A.; *et al.* Gaussian, Inc., Wallingford CT, **2010**.
(53) Neese, F. The ORCA Program System. *WIRES: Comput. Mol. Sci.*, **2012**, *2*, 73-78.
(54) Lee, C.; Yang, W.; Parr, R. G. Development of the Colle-Salvetti Correlation-Energy Formula into a Functional of the Electron Density. *Phys. Rev. B* **1988**, *37*, 785–789.
(55) Becke, A. D. A New Mixing of Hartree–Fock and Local Density-Functional Theories. *J. Chem. Phys.* **1993**, *98*, 1372–1377.
(56) Krishnan, R.; Binkley, J. S.; Seeger, R.; Pople, J. A. Self-Consistent Molecular Orbital Methods. XX. A Basis Set for Correlated Wave Functions. *J. Chem. Phys.* **1980**, *72*, 650–654.
(57) Pettersen, E. F.; Goddard, T. D.; Huang, C. C.; Couch, G. S.; Greenblatt, D. M.; Meng, E. C.; Ferrin, T. E. UCSF Chimera--A Visualization System for Exploratory Research and Analysis. *J. Comput. Chem.* **2004**, *25*, 1605–1612.
(58) Stoll, S.; Schweiger, A. EasySpin, a Comprehensive Software Package for Spectral Simulation and Analysis in EPR. *J. Magn. Reson.* **2006**, *178*, 42–55.

Chapter 4 Appendix

EPR study of UV-irradiated thymidine microcrystals supports radical intermediates in spore photoproduct formation

---

A4.1 Simulation parameters for EPR spectra

Table A4.1a. EPR parameters (g values and hyperfine coupling values) for simulations of TCH_2 isotopologues in Figure 4.1 [a,b,c,d]

	species	*g*	g frame	H_{C6}	H_{C6} frame	H_{C7}	H_{C7} frame	H_{C7}	H_{C7} frame	$^{14}N1$	$^{14}N1$ frame	LWPP [e] (mT)
DFT	TCH_2	2.0024 2.0029 2.0033	-66° 26° -42°	-49 -38 -15	17° 40° -36°	-75 -51 -19	138° 15° -162°	-70 -50 -18	166° 130° 148°	-4 5 -5	168° 101° -113°	N.A.
120K	TCH_2	2.0045 2.0055 2.0065	-66° 26° -42°	-36 -28 -20	17° 40° -36°	-56 -42 -19	138° 15° -162°	-56 -42 -22	166° 130° 148°	-1 -1 5	168° 101° -113°	0.6
	TCD_2	P	P	P	P	P·D	P	P·D	P	P	P	0.8
210K	TCH_2	P	P	P	P	P	P	P	P	P	P	0.7
	TCD_2	P	P	P	P	P·D	P	P·D	P	P	P	0.8
250K	TCH_2	P	P	P	P	P	P	P	P	P	P	0.6
	TCD_2	P	P	P	P	P·D	P	P·D	P	P	P	0.9

[a] All hyperfine values are in MHz

[b] "P" indicates the value is the same as the value for the primary isotopologue in the 3rd row of the table (TCH_2 at 120 K)

[c] P·D = P·$\gamma_{2_H}/\gamma_{1_H}$, D is the ratio of gyromagnetic ratios for ^2H and ^1H, approx. 0.1535

[d] All frames are the Euler angles of the rotation matrices computed in Orca

[e] Peak-to-peak line width

Table A4.1b. EPR parameters for simulations of TH isotopologues in Figure 4.1 [a,b,c,d]

	species	*g*	g frame	H_{C7} (methyl)	H_{C7} frame	H_{C6}	H_{C6} frame	H_{C6}	H_{C6} frame	LWPP[e] (mT)
DFT	TH	2.0023 2.0044 2.0056	142° 20° -66°	54 55 63	4° 82° 104°	58 59 70	86° 12° -69°	119 120 132	180° 43° -114°	N.A.
120K	TH	2.0021 2.0067 2.0080	142° 20° -66°	54 56 64	4° 82° 104°	114 114 117	86° 12° -69°	110 110 113	180° 43° -114°	0.6
	TD	P	P	P	P	P	P	P·D	P	0.4
	TH-d_3	P	P	P·D	P	P	P	P	P	0.3
	TD-d_3	P	P	P·D	P	P·0.75	P	P·D	P	0.3
210K	TH	P	P	P	P	P	P	P	P	0.7
	TD	P	P	P	P	P	P	P·D	P	0.4
	TH-d_3	P	P	P·D	P	P	P	P	P	0.6
	TD-d_3	P	P	P·D	P	P·0.75	P	P·D	P	0.7
250K	TH	P	P	P	P	P	P	P	P	0.5
	TD	P	P	P	P	P	P	P·D	P	0.5
	TH-d_3	P	P	P·D	P	P	P	P	P	1.0
	TD-d_3	P	P	P·D	P	P·0.75	P	P·D	P	0.7

[a] All hyperfine values are in MHz

[b] "P" indicates the value is the same as the value for the primary isotopologue in the 3rd row of the table (TH at 120 K)

[c] P·D =P· $\gamma_{2_H}/\gamma_{1_H}$, D is the ratio of gyromagnetic ratios for ^{2}H and ^{1}H, approx. 0.1535

[d] All frames are the Euler angles of the rotation matrices computed in Orca

[e] Peak-to-peak line width

A4.2 Alternative model for EPR simulations of data in Figure 4.1

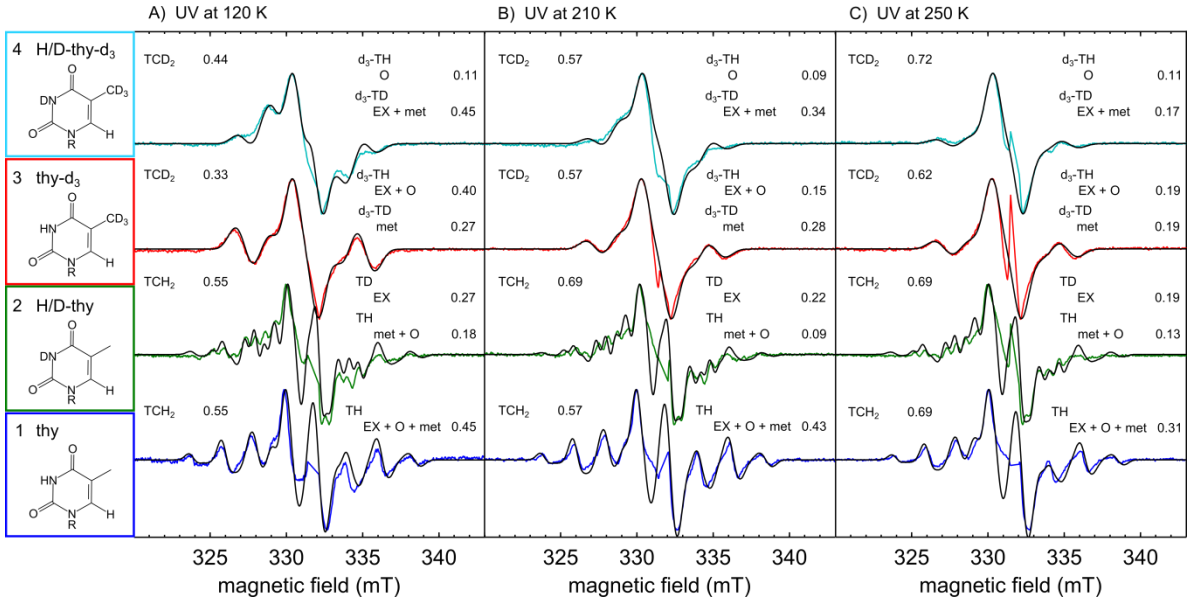

Figure A4.1. Continuous-wave EPR spectra collected at 120 K of microcrystalline powder samples of thymidine, H/D-thymidine, thymidine-d_3, and H/D-thymidine-d_3 photodamaged with 266 nm laser pulses at variable temperatures (120 K, 210 K, 250 K) indicated at the top of each set of axes (identical spectra to those presented in Figure 1 of the main text, see main text for additional experimental details). The structures of the starting materials are shown in the left column. The ratio of isotopologues of the TCH_2 and TH radicals that are used to simulate the spectra are indicated within the figure. In addition, the pathways ("met", "EX", or "O") that lead to a specific TH isotopologue for each starting material are indicated. In contrast to the simulations in Figure 4.1 of the main text, the simulations here do not assume the 1:1 restriction or the isotope effect restriction (defined in the main text). In all cases the spectra and simulations were normalized to their most intense feature for clarity. See main text (Discussion Section) for a discussion of the relevance of these simulations.

Table A4.2a. EPR parameters for simulations of TCH_2 isotopologues at variable temperatures in Figure A4.1 [a,b,c,d]

	species	*g*	g frame	H_{C6}	H_{C6} frame	H_{C7}	H_{C7} frame	H_{C7}	H_{C7} frame	$^{14}N1$	$^{14}N1$ frame	LWPP [e] (mT)
120K	TCH_2	2.0045 2.0055 2.0065	-66° 26° -42°	-36 -28 -20	17° 40° -36°	-56 -42 -19	138° 15° -162°	-56 -42 -22	166° 130° 148°	-1 -1 5	168° 101° -113°	0.7
	TCD_2	P	P	P	P	P·D	P	P·D	P	P	P	0.9
210K	TCH_2	P	P	P	P	P	P	P	P	P	P	0.8
	TCD_2	P	P	P	P	P·D	P	P·D	P	P	P	1.0
250K	TCH_2	P	P	P	P	P	P	P	P	P	P	0.8
	TCD_2	P	P	P	P	P·D	P	P·D	P	P	P	1.0

[a] All hyperfine values are in MHz

[b] "P" indicates the value is the same as the value for the primary isotopologue in the 2nd row of the table (TCH_2 at 120 K)

[c] P·D =P· $\gamma_{2_H}/\gamma_{1_H}$, D is the ratio of gyromagnetic ratios for ^2H and ^1H, approx. 0.1535

[d] All frames are the Euler angles of the rotation matrices computed in Orca

[e] Peak-to-peak line width

Table A4.2b. EPR parameters for simulations of TH isotopologues at variable temperatures in Figure A4.1 [a,b,c,d]

	species	*g*	g frame	H_{C7} (methyl)	H_{C7} frame	H_{C6}	H_{C6} frame	H_{C6}	H_{C6} frame	LWPP[e] (mT)
120K	TH	2.0021 2.0067 2.0080	142° 20° -66°	54 56 64	4° 82° 104°	114 114 117	86° 12° -69°	110 110 113	180° 43° -114°	0.6
	TH	P	P	P	P	P	P	P·D	P	0.4
	TD	P	P	P·D	P	P·0.95	P	P	P	0.6
	TH-d_3	P	P	P·D	P	P·0.80	P	P·D	P	0.5
210K	TD-d_3	P	P	P	P	P	P	P	P	0.6
	TH	P	P	P	P	P	P	P·D	P	0.4
	TD	P	P	P·D	P	P·0.95	P	P	P	0.6
	TH-d_3	P	P	P·D	P	P·0.75	P	P·D	P	0.6
250K	TD-d_3	P	P	P	P	P	P	P	P	0.6
	TH	P	P	P	P	P	P	P·D	P	0.4
	TD	P	P	P·D	P	P	P	P	P	0.7
	TH-d_3	P	P	P·D	P	P·0.75	P	P·D	P	0.7

[a] All hyperfine values are in MHz

[b] "P" indicates the value is the same as the value for the primary isotopologue in the 2rd row of the table (TH at 120 K)

[c] P·D =P· $\gamma_{2_H}/\gamma_{1_H}$, D is the ratio of gyromagnetic ratios for ^2H and ^1H, approx. 0.1535

[d] All frames are the Euler angles of the rotation matrices computed in Orca

[e] Peak-to-peak line width

A4.3 Reproducibility of radicals produced in thymidine microcrystals and thin films exposed to UV radiation

A4.3.1 Spectra acquired after UV irradiation at 120 K

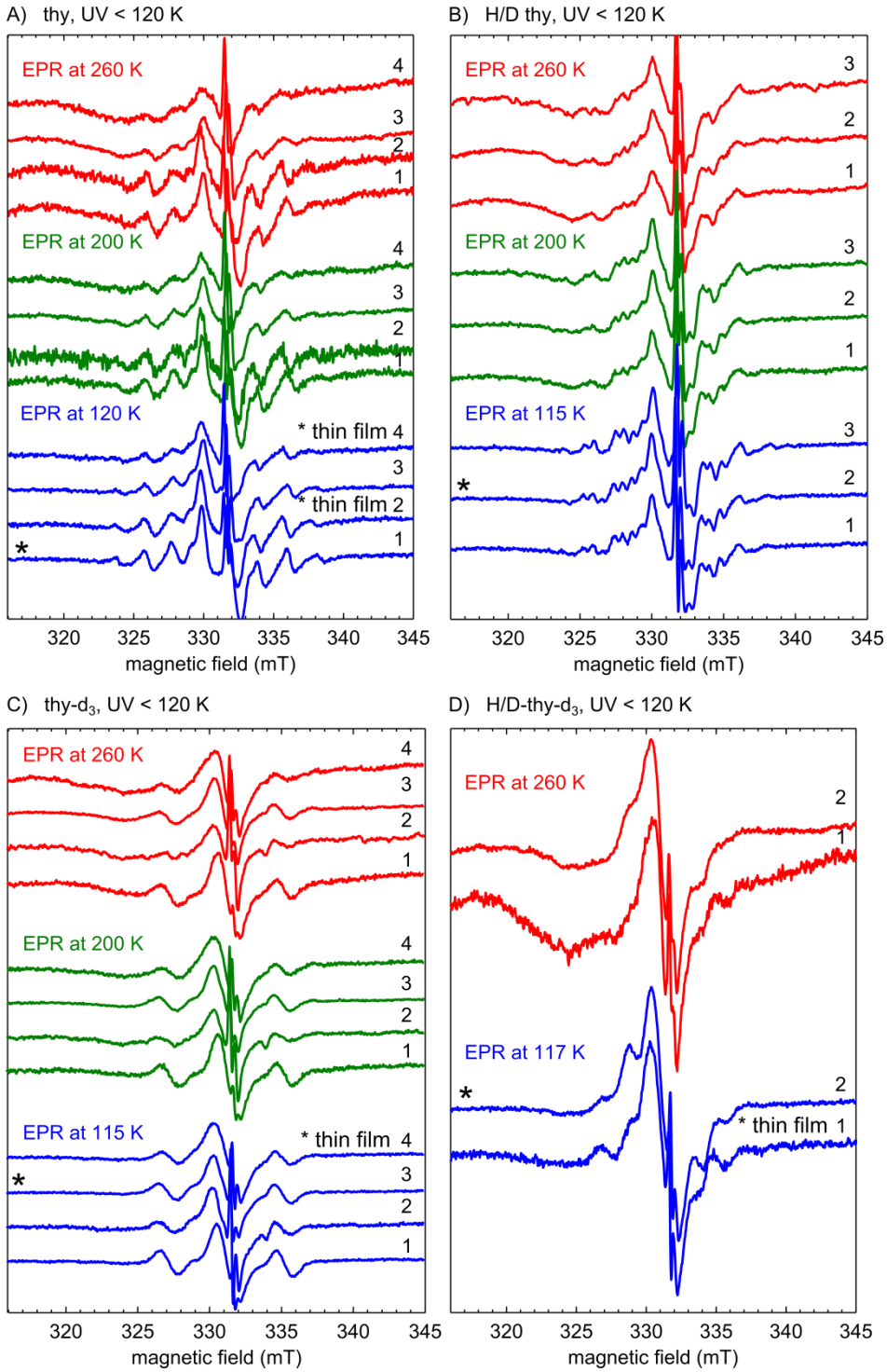

Figure A4.2. Multiple trials of UV irradiation (266 nm, 10 Hz, ≈ 30 min) at less than or equal to 120 K of thymidine, H/D thymidine, thymidine-d_3, and H/D thymidine-d_3. Within each figure (A, B, C, D), spectra marked with the same number are of the same sample but the temperature was raised in the EPR cavity from 120 K (blue), to 200 K (green), to 260 K (red) without removing the sample from the EPR cavity. Except where indicated, all samples are microcrystalline powder samples prepared as described in the main text. Thin film samples are prepared as described below. Spectrometer settings were as follows: microwave attenuation was 33 dB for spectra recorded below 120 K, greater than or equal to 25 dB for spectra recorded at 200 K, and greater than or equal to 20 dB for spectra recorded at 260 K; sweep rates of ≈ 40 seconds over 30 mT; microwave frequency near 9.3 GHz; modulation amplitude of 0.2 mT and frequency of 100 kHz; typically 30-100 scans were needed to achieve the signal to noise ratio of the spectra shown. Spectra marked with a star (*) are spectra shown in Figure 4.1 of the main article.

This figure shows that thin-film preparation of samples generally leads to broader features in the spectra. Thin-film samples 2 and 4 in Figure A4.2A, 4 in Figure A4.2C, and 1 in Figure A4.2D all have broadened features compared to their microcrystalline analogues. However, the yield of radical isotopologues of TCH_2 and TH does not appear to depend on the preparation between thin film and microcrystal.

A4.3.2 Spectra acquired after UV irradiation at 210 and 250 K

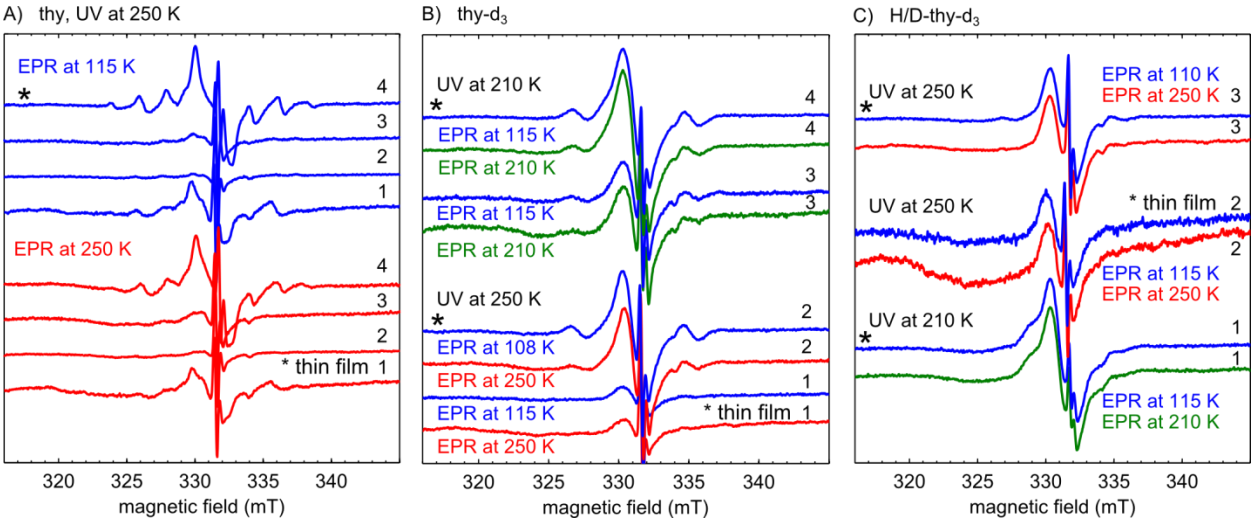

Figure A4.3: Multiple trials of UV irradiation (266 nm, 10 Hz, ≈ 30 min) at 210 K and 250 K of thymidine, thymidine-d_3, and H/D thymidine-d_3. Within each figure (A,B,C) spectra marked with the same number are of the same sample but the temperature was lowered in the EPR cavity from either 250 K or 210 K (red or green, respectively) to 120 K (blue) without removing the sample from the EPR cavity. Except where indicated, all samples are microcrystalline powder samples prepared as described in the main text. Thin film samples are prepared as described below. Spectrometer settings were as follows: microwave attenuation was 33 dB for spectra recorded below 120 K, greater than or equal to 25 dB for spectra recorded at 200 K, and greater than or equal to 20 dB for spectra recorded at 250 K; sweep rates of 40 seconds for 30 mT; microwave frequency near 9.3 GHz; modulation amplitude of 0.2 mT and frequency of 100 kHz; typically 30-100 scans were needed to achieve the signal to noise ratio of the spectra shown. Spectra marked with a star (*) are spectra shown in Figure 4.1 of the main article.

This figure shows that, once again, thin film preparation of samples generally leads to broader features in the spectra (compare thin film sample 1 in A to microcrystal sample 4 in A). Cooling both thin film and microcrystalline samples after UV irradiation always sharpens the features (especially sample 4 in A, samples 2 and 4 in B, samples 1 and 3 in C).

A4.3.3 Thin film sample preparation

Thin-film samples of were prepare by dissolving thymidine or thymidine-d_3 in methanol (Fisher, 0.01% H_2O) or d_4-methanol (Cambridge, 99.8% D). Approximately 200 µL of this solution was transferred to a quartz EPR sample tube. The methanol was pumped out from the sample tube under vacuum, leaving a thin film of thymidine, thymidine-d_3, or H/D-thymidine-d_3 on the bottom 3 cm of the sample tube. Removal of visible solvent required about 10 minutes under vacuum. The sample was then left for an

additional 3 hours under vacuum to remove residual solvent. The EPR sample tube was then flame sealed under a low-pressure argon atmosphere.

A4.4 Various models of the quantity of the d_3-TD radical in irradiated thy-d_3

There is a difference in yield of isotopologues even between similar preparations. In the context of spore photoproduct formation, the most important sample for determining the source of H atom donation to the C6 position of thymidine is the thymidine-d_3 sample. Presence of the d_3-TD radical indicates the methyl group of an adjacent thymidine is the donor of the additional hydron at the TH C6 position and supports the sequential radical pair mechanism for spore photoproduct formation discussed in the main text. Simulations (Figure A4.4, simulation parameters summarized in Table A4.3a and b) of the blue spectra (EPR at 120 K) in Figure A4.2C indicate that the ratio of d_3-TD radical varies slightly among different trials.

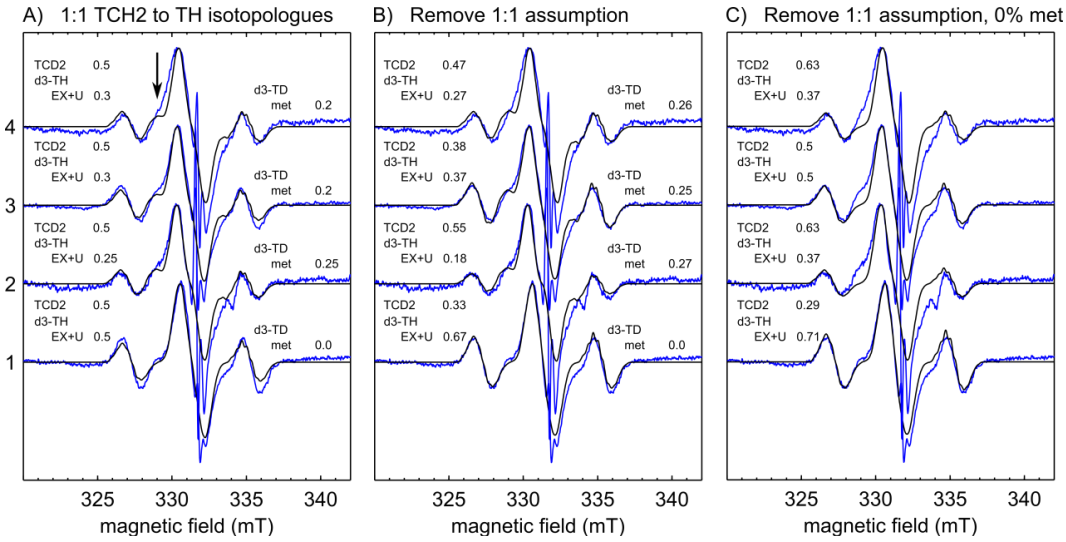

Figure A4.4. Three ways of simulating the blue spectra in Figure A4.2C (thy-d_3, UV irradiation temperature < 120 K, EPR temperature < 120 K) are shown. Experimental spectra are shown in blue and simulations in black. For thy-d_3 the oxidation product will be the TCD_2 isotopologue. The reduction products will be the d_3-TH isotopologue formed by the "EX" and "O" pathway and the d_3-TD radical formed by the "met" pathway (see main text for a discussion of the pathway abbreviations). A) First, using the restrictive scheme we assumed a 1:1 ratio of TCH_2:TH isotopologues. We find the percentage of d_3-TD in the simulation varies from 0 % to 25 % among the four trials. B) Next, we removed the 1:1 restriction which resulted in visually better simulations of the experimental data. In these simulations, the d_3-TD radical still made up between 0 % and 27 % of the radicals present among the four trials. C) Spectra are simulated by relaxing the assumption of a 1:1 ratio of TCH_2:TH isotopologues, but assuming no d_3-TD isotopologues are present (i.e. the "met" pathway of TH isotopologue formation is not active). In this case, the simulations for spectra 2-4 do not adequately model the spectral features we attribute to the d_3-TD radical present at 329 mT (marked by an arrow in A) and 334 mT. In A, B, and C simulation parameters (Table A4.3) are identical except for the ratio of TCH_2 and TH isotopologues included.

Table A4.3a. Simulation parameters for the TCD_2 isotopologue used in Figure A4.4[a,b,c]

species	g	g frame	H_{C6}	H_{C6} frame	H_{C7}	H_{C7} frame	H_{C7}	H_{C7} frame	$^{14}N1$	$^{14}N1$ frame	LWPP[d] (mT)
TCD_2	P	P	P	P	P·D	P	P·D	P	P	P	0.8

[a] "P" indicates the value is the same as the value for the primary isotopologue in the 3rd row of Table A4.1a

[b] $P{\cdot}D = P{\cdot}\gamma_{2_H}/\gamma_{1_H}$, D is the ratio of gyromagnetic ratios for ^2H and ^1H, approx. 0.1535

[c] All frames are the Euler angles of the rotation matrices computed in Orca

[d] Peak-to-peak line width

Table A4.3b. Simulation parameters for the TH isotopologues used in Figure A4.4 [a,b,c]

species	g	g frame	H_{C7} (methyl)	H_{C7} frame	H_{C6}	H_{C6} frame	H_{C6}	H_{C6} frame	LWPP[d] (mT)
TH-d_3	P	P	P·D	P	P	P	P	P	0.3
TD-d_3	P	P	P·D	P	P·0.75	P	P·D	P	0.3

[a] "P" indicates the value is the same as the value for the primary isotopologue in the 3rd row of Table A4.1b

[b] $P{\cdot}D = P{\cdot}\gamma_{2_H}/\gamma_{1_H}$, D is the ratio of gyromagnetic ratios for ^2H and ^1H, approx. 0.1535

[c] All frames are the Euler angles of the rotation matrices computed in Orca

[d] Peak-to-peak line width

A4.5 Temperature dependence of radical signals in microcrystalline thymidine

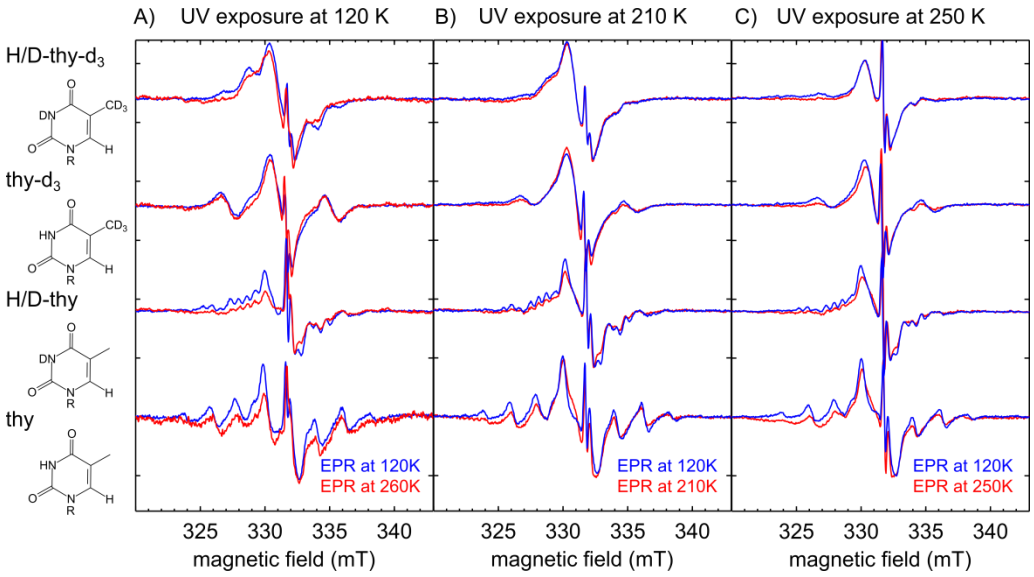

Figure A4.5: Shown in blue are the same spectra as in Figure 4.1 of the main text where EPR was recorded at 120 K. Shown in red is the EPR spectrum taken at a warmer temperature indicated in the figure (260 K in A, 210 K in B, and 250 K in C). In Figure A4.5A, after recording the EPR spectrum at 120 K, the sample was warmed to 250 K and the EPR spectrum recorded without any additional UV radiation applied. In Figure A4.5B, the sample was UV irradiated at 210 K and the EPR spectrum recorded. Then the sample was cooled to 120 K and the EPR spectrum was recorded without any additional UV radiation applied. In Figure A4.5C, the sample was UV irradiated at 250 K and the EPR spectrum recorded. Then the sample was cooled to 120 K and the EPR spectrum was recorded without any additional UV radiation applied. Spectrometer settings were as follows: microwave attenuation was 33 dB for spectra recorded below 120 K, 25 dB for spectra recorded at 210 K and 250 K; sweep rates of 40 seconds for 30 mT; microwave frequency between 9.302-9.336 GHz; modulation amplitude of 0.2 mT and frequency of 100 kHz; typically 30-100 scans were needed to achieve the signal to noise ratio of the spectra shown. In all cases the spectra were normalized to their most intense feature, so relative quantitation of number of radicals should not be made from this figure.

A4.5.1 Effects of warming samples UV irradiated at 120 K (Figure A4.5A)

The spectra of thymidine used in Figure A4.5A broadened upon warming but the position of the dominant features did not shift indicating no new radical species formed upon warming. The broadening is attributed to structural rearrangement of the radicals upon warming that could not occur at 120 K. This idea is substantiated by the EPR data collected on thin film samples of thymidine exposed to UV radiation. Thin film samples are more structurally amorphous than microcrystals and the spectra collected for thin film samples under identical UV irradiation were consistently broadened compared to microcrystalline samples of the same material (Appendix A4.3).

Of particular importance is the broadening of the features due to the d_3-TD radical in thymidine-d_3 irradiated at 120 K upon warming to 250 K. These features at 329 and 333 mT broaden considerably upon warming, but look very similar to the spectra for thymdine-d_3 in Figure A4.5B where UV radiation was applied at 210 K. This supports our approach of simulating the spectra using the same isotopologues in different ratios at different temperatures, but simply broadening the features when UV radiation is applied at warmer temperatures (see simulation parameters in Tables A4.1a and A4.1b).

A4.5.2 Effects of cooling samples UV irradiated at 210 K and 250 K (Figures A4.5B and A4.5C)

In contrast to irradiating the samples at 120 K, each of the isotopically labeled thymidine starting materials was irradiated with UV light at 210 K and 250 K in Figures A4.5B and C, respectively. Cooling to 120 K increased the signal intensity and required data collection at lower microwave power to prevent saturation.

When thymidine-d_3 and H/D-thymidine-d_3 are irradiated and measured at warmer temperatures, the features due to the d_3-TH isotopologue at 327 and 336 mT are broadened nearly beyond detection, in particular in panel C. However, these features do sharpen and become detectable at 120 K. It is unexpected that in spectrum 4 of panel C there appears to be very little of the d_3-TD radical with features expected at 329 and 333 mT given it is so prominent in spectrum 4 in both panel A and B. However, this may be due to these broadening effects at warmer temperatures.

A4.6 Graphical representation of pathway models

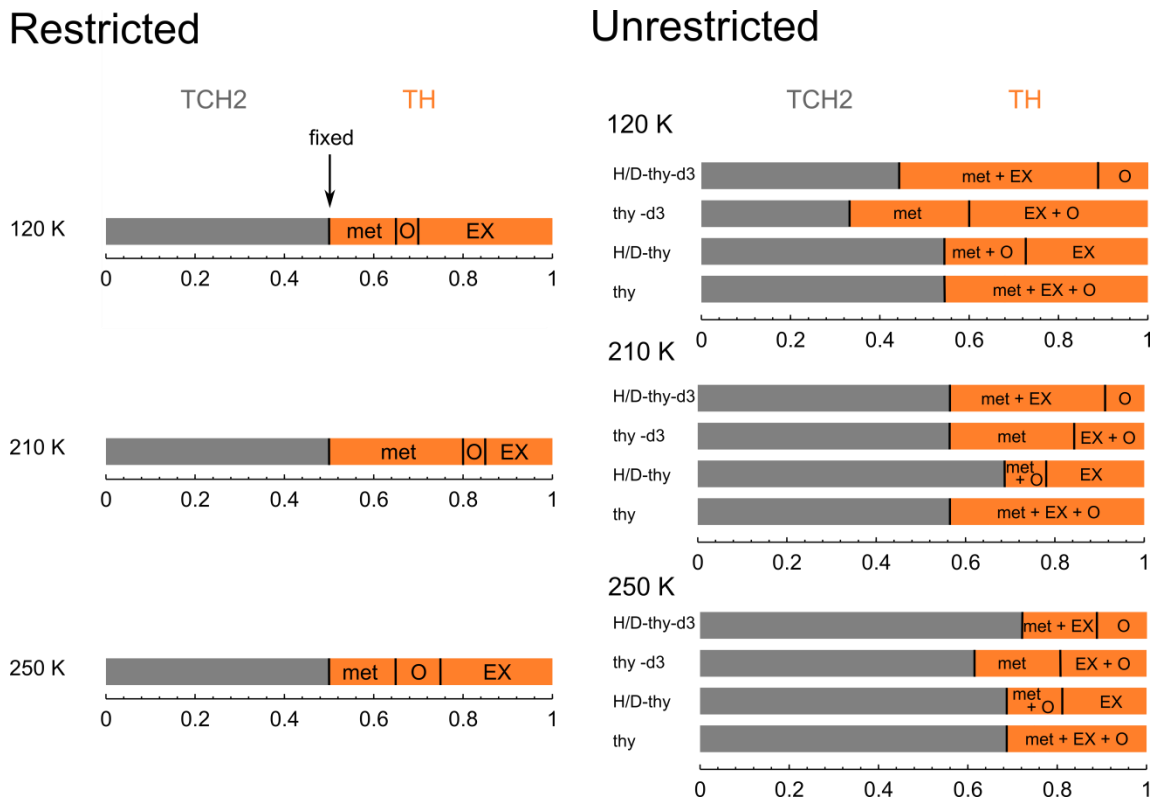

Figure A4.6. Left: A graphical representation of the restrictive model of radical formation in thymidine (with 1:1 restriction and isotope effect restriction, as defined in the main text) used in simulations shown in Figure 4.1. Right: A graphical representation of the unrestrictive model of radical formation in thymidine used in simulations shown in Figure A4.1. The gray bars represent the percentage of TCH_2 isotopologue present in each sample. The burnt-orange bars represent the percentage of TH isotopologues which form for a given pathway indicated by text in the figure. See the main text (results section) for a detailed account of which TH isotopologues will form for a given starting material and pathway.

A4.7 Structures, property calculations, and simulations of EPR spectra of anion (T^-) and cation (T^+) thymidine radicals

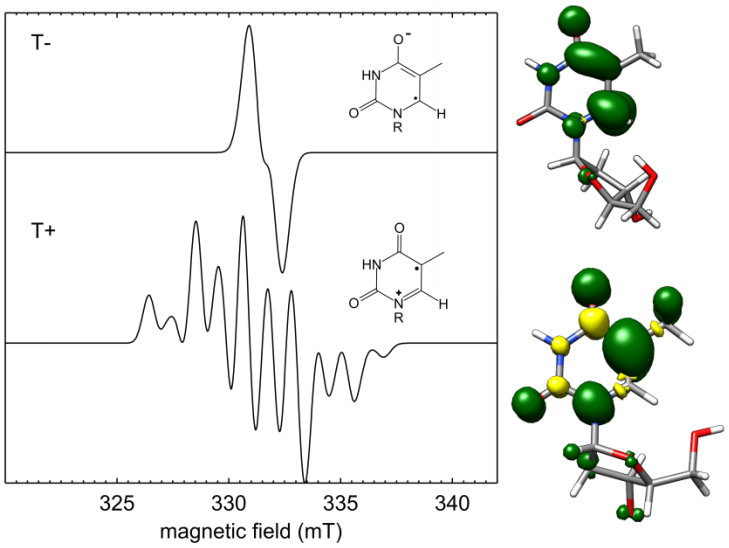

Figure A4.7: Simulations of the EPR spectra of the anion and cation radical formed from one electron reduction and oxidation of thymidine, respectively. EPR properties were calculated using the Orca 3.0 quantum computing software (details below). Simulations of the anion radical use the full g tensor and the hyperfine coupling of the proton at the N3 position, the proton at the C6 positon, and the methyl group protons at C5. Simulation of the cation radical use the full g tensor and hyperfine coupling tensors of the N1 nitrogen, the methyl group protons at C5, and the proton at the carbon bound to N1 (on the sugar moiety). In all cases the full tensors were used to account for the Euler angles between the principal values. Simulations used an arbitrary microwave frequency of 9.3 GHz in both cases. Principal values of the properties are listed in Table A4.4.

Table A4.4. Principal values of the calculated g tensor and hyperfine couplings (MHz) of the anion and cation thymidine radicals[a]

species	*g*	H_{C5} (methyl)[b]	H_{N3}	H_{C6}	LWPP (mT)
T^-	2.0023 2.0036 2.0047	2 3 8	1 -7 -7	7 -16 -36	0.6
	g	H_{C5} (methyl)[b]	$H_{C1'}$	N1	LWPP (mT)
T^+	2.0025 2.0053 2.0074	59 60 65	31 32 38	-0.5 -1 40	0.6

[a] Hyperfine coupling principal values are in MHz
[b] Average hyperfine coupling of the three methyl protons

Density Function Theory Calculations: Geometry optimization calculations were carried out using Gaussian09 software[1] with spin unrestricted orbitals, B3LYP functional, and 6-311++G basis set for the T^-

radical and the 6-311G basis set for the T^+ radical. The magnetic properties including g-tensors and hyperfine coupling constants were calculated for the optimized geometries using ORCA 3.0[2] with spin unrestricted orbitals, the B3LYP functional, and 6-311G basis set for T^- and T^+. Simulations of EPR spectra were performed with the full 3×3 g and hyperfine tensors as input parameters to the EasySpin software. Only certain nuclei, indicated in Table A4.4, with substantial hyperfine coupling strengths were used in simulations. For the methyl group protons, the average of the full tensors was computed and used as the hyperfine coupling tensor for each of the three protons. The average principal values are reported in Table A4.4.

A4.8 Exchange of protons in deuterated methanol

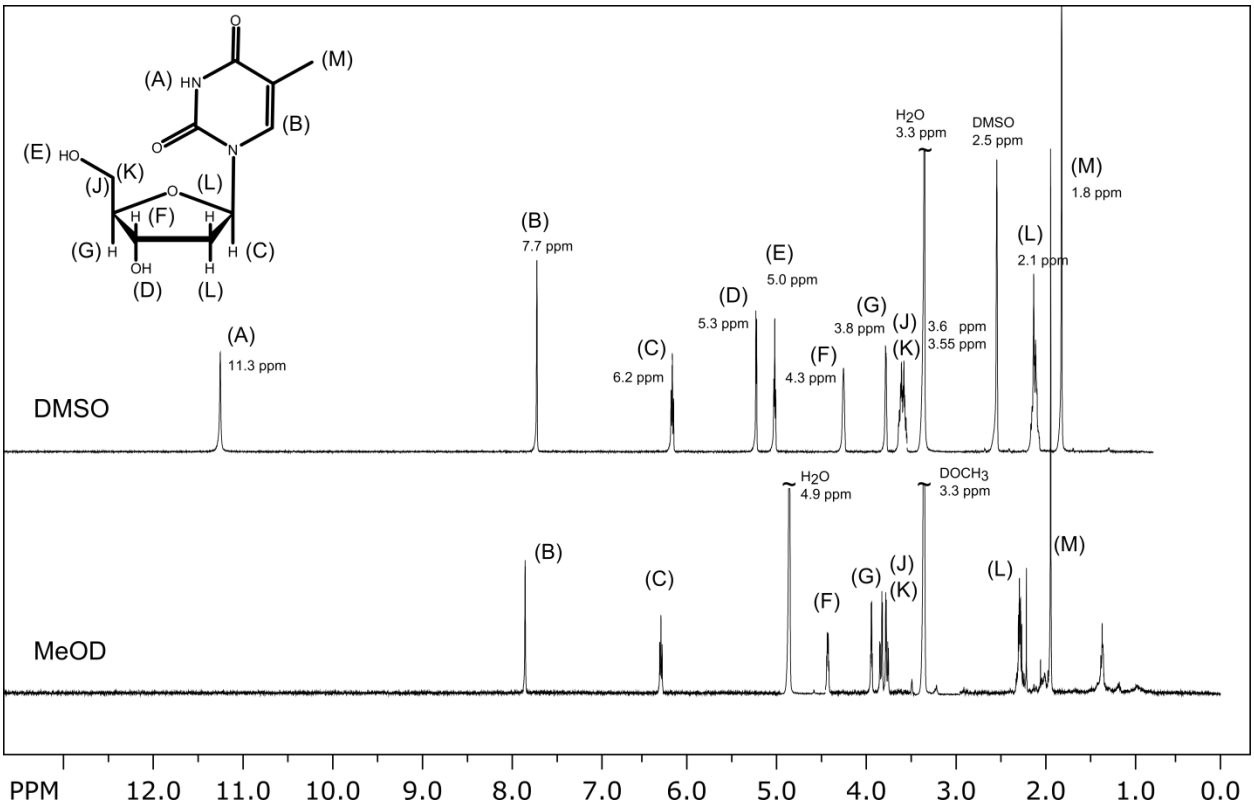

Figure A4.8: 499 MHz NMR of thymidine (structure in top left). Top spectrum: Thymidine in $(CD_3)_2SO$ (Cambridge Isotopes, 99.9%). The spectrum was assigned based on manufacturer and database spectra.[3,4] Bottom spectrum: Thymidine in $DOCD_3$ (Cambridge Isotopes, 99.8%). As can be seen by the disappearance of peaks (A), (D), and (E), the secondary amine and hydroxyl protons exchange readily in deuterated methanol. The intensity of solvent peaks denoted "~" were cut off for clarity.

A4.9 References

(1) M. J. Frisch, G. W. Trucks, H. B. Schlegel, G. E. Scuseria, M. A. Robb, J. R. Cheeseman, G. Scalmani, V. Barone, B. Mennucci, G. A. Petersson, H. Nakatsuji, M. Caricato, X. Li, H. P. Hratchian, A. F. Izmaylov, J. Bloino, G. Zheng, J. L. Sonnenberg, M. Had, and D. J. F. Gaussian 09, Revision C.01, **2010.**

(2) Neese, F. The ORCA Program System. *WIREs Comput. Mol. Sci.* **2012**, *2*, 73–78.

(3) Ulrich, E. L.; Akutsu, H.; Doreleijers, J. F.; Harano, Y.; Ioannidis, Y. E.; Lin, J.; Livny, M.; Mading, S.; Maziuk, D.; Miller, Z.; *et al.* BioMagResBank. *Nucleic Acids Res.* **2008**, *36*, D402–D408.

(4) Thymidine(50-89-5)1HNMR, http://www.chemicalbook.com/SpectrumEN_50-89-5_1HNMR.htm.

Chapter 5

EPR characterization of a $Mn^{III}Mn^{IV}$ intermediate during O-O bond activation by a small molecule thiolate-ligated Mn^{II} compound

Abstract

A metastable intermediate in O-O bond activation by a small molecule Mn^{II} compound, Mn^{II}-6MeODPEN, has been identified with UV-Vis and EPR spectroscopy. The EPR spectrum indicates the intermediate is a $Mn^{III}Mn^{IV}$ dimer. The intermediate forms when Mn^{II}-6MeODPEN is exposed to atmosphere and abstracts an H atom from either solvent or H atom donors. The bridging motif and the location of the abstracted H atom are under active investigation with further EPR experiments described here. Understanding the full structure of this intermediate will provide insight into the mechanism of O-O bond activation in this small molecule.

Contributions

The original 6MeODPEN ligand synthesis and preliminary investigations into the reactivity of Mn^{II}-6MeODPEN with O_2 was established by Audra L. Johansen (Kovacs Group at UW). Continuation of these studies has been performed by Chaau Yan (Penny) Poon (Kovacs Group at UW). Broken-symmetry DFT calculations were initiated by Julian A. Rees (Kovacs Group at UW) and subsequent analysis of the output done in collaboration. W-band EPR spectra were collected at the Max Planck Institute for Chemical Energy Conversion in the Biophysical Chemistry Department (Director Dr. Wolfgang Lubitz). Dr. Nicholas Cox provided insight and expertise in the study of manganese clusters with EPR and EDNMR spectroscopy. All other EPR experiments and spectral simulations were performed by ECH.

Publications

This work is currently unpublished.

5.1 Introduction

The formation and activation of dioxygen bonds are key steps in biological molecular processes and Nature has selected manganese as the redox-active metal involved. Dioxygen bond activation is exemplified in photosynthetic O_2 production (O-O bond formation) by the tetranuclear Mn cluster of the Oxygen Evolving Complex (OEC) as well as in class Ib ribonucleotide reductases (O-O bond cleavage), which are responsible for DNA repair.[1,2] Dioxygen activation by manganese metalloenzymes in Nature often proceeds through a series of Mn-O_2 intermediates, including Mn-superoxo, -peroxo, and $Mn^{III}Mn^{IV}$ and $Mn^{IV}Mn^{IV}$-μ-oxo/hydroxo moieties.[3–5] These intermediates, which are challenging to isolate even in synthetic model systems, are often highly reactive, which hampers their structural and spectroscopic characterization. Due to the complex and transient nature of these biological systems, bioinorganic chemists investigate the chemistry of synthetic small-molecule Mn-O_2 systems. One key aspect of working with synthetic systems is that these small molecules can be rationally modified to control the progression of reactivity, thus allowing the exploration of a larger bio-inspired chemical space.

Detailed insights into the chemistry of Mn and O_2 may help in designing better systems for energy conversion and other molecular transformations. For this purpose, members of the Kovacs group at the University of Washington predictively designed a series of small-molecule Mn^{II} complexes which activate and cleave the O-O bond in dioxygen. Each of the Mn^{II} compounds presented in Scheme 5.1 proceeds to an analogous final product, an unsupported μ-oxo $Mn^{III}Mn^{III}$ dimer which has been characterized with x-ray diffraction (XRD)). However, depending on the ligand structure (see Scheme 5.1; ligand structures L1, L2, L3 and L4) around the Mn^{II} ion, the complexes exhibit different metastable intermediates which are observable at cold temperatures (typically less than 243 K).

Rational ligand design stems in part from a previous Kovacs lab study which correlated the degree of O-O bond activation with metrical parameters in a series of $LXMn^{III}$-OOR compounds (where the identity of –OOR was inconsequential and LX ligands were variants of the QuinoEN and 6MeDPEN ligands in Scheme 5.1). They found that the shorter the N-heterocyclic amine—Mn bond length (N_{Ar}—Mn) the longer the O-O bond length of the alkylperoxo ligand, indicating increased bond activation.[6,7]

The N_{Ar}—Mn bond length reflects the electron-donating character of the N-heterocyclic amines of the ligands and for the compounds in Scheme 5.1, this metric is best compared in the N_{Ar}—Mn bond lengths of the final products (see Scheme 5.1). In 6MeDPENMn$^{III}_2$O (ligand L3), the N_{Ar}—Mn bond length is more than 0.3 Å longer than in 6HDPENMn$^{III}_2$O (ligand L1). As such, Mn^{II}6MeDPEN is less activating of O-O bonds allowing observation of a metastable intermediate (not observed during Mn^{II}-6HDPEN reactivity with dioxygen) which was characterized as a Mn_2(III,III)-*trans*-μ-1,2-peroxo dimer (Mn^{III}-O-O-Mn^{III} in Scheme 5.1) using XRD and resonance Raman (rR) spectroscopy. The UV-Vis absorption of the intermediate (λ_{max} = 640 nm) gives it a distinct green color.[8,9]

Based on this structural and spectroscopic insight, rational ligand modification was made to further enhance O_2 activation by increasing the electron donating character of the pyridine bond. This resulted in the newly designed system Mn^{II}-6MeODPEN (L4 in Scheme 5.1) which at room temperature reacts with O_2 immediately to form the Mn^{III}-O-Mn^{III} final product. Comparing the crystal structures of the final products of L3 and L4, the N_{Ar}—Mn bond length is nearly 0.2 Å shorter in 6MeODPEN than in 6MeDPEN. Upon lowering the O_2 reaction temperature, the predicted result was observed: a more activated O-O bond, as evidenced by the significantly shorter-lived green intermediate (proposed to be the peroxo-bridged intermediate Mn^{III}-O-O-Mn^{III}). Unexpectedly, the 6MeODPEN ligand system also stabilizes a previously unobserved intermediate species (following the green intermediate) which is distinguished by a dark red color (λ_{max} = 505 nm). EPR spectroscopy has provided evidence suggesting this intermediate is a Mn^{III}Mn^{IV} dimer (drawn as "Mn^{III}-O-Mn^{IV}-OH ?" in Scheme 5.1).

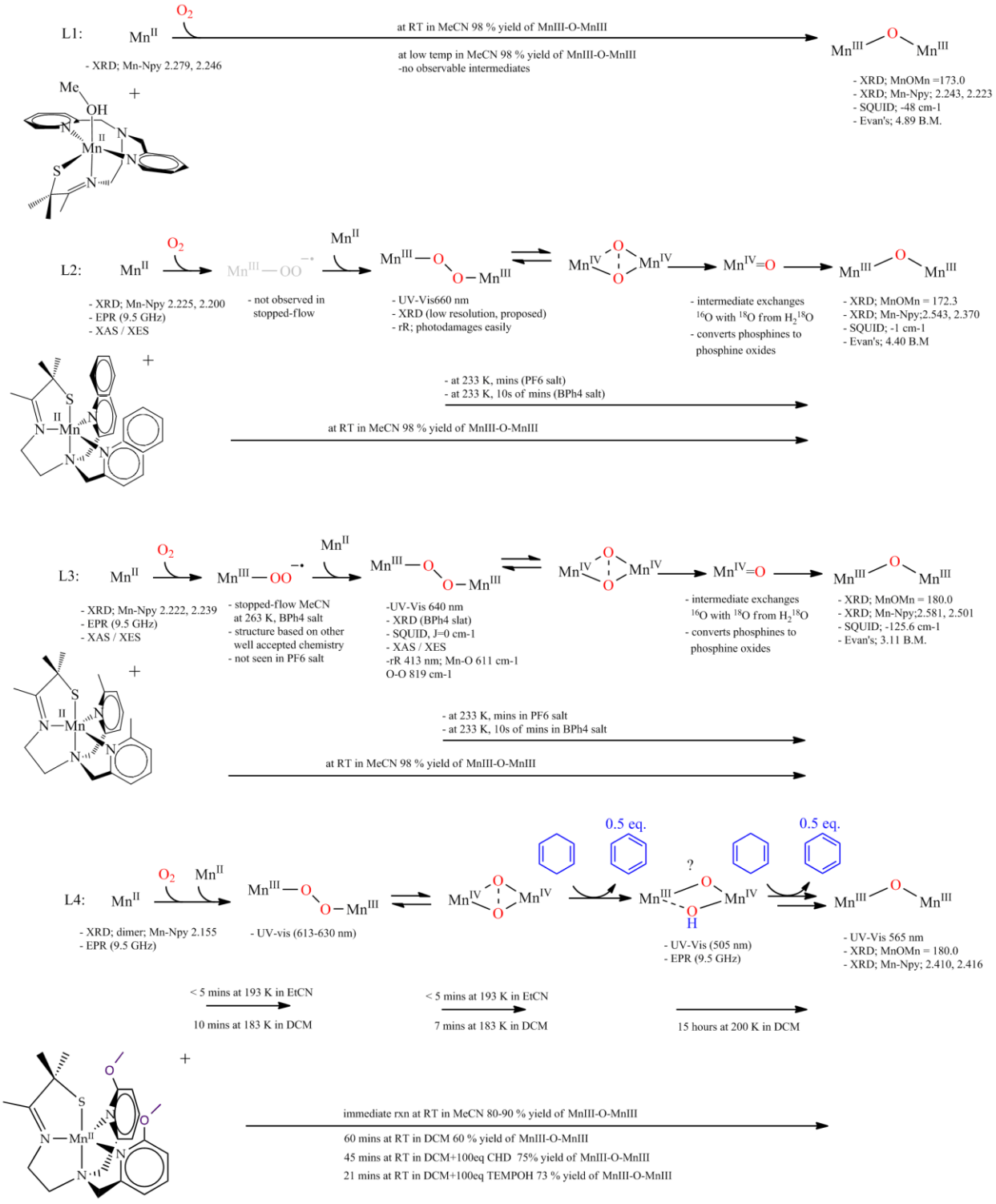

Scheme 5.1. Ligand structures and reaction pathways of Mn^{II} compounds with O_2. The details of this scheme are discussed in more depth in Introduction 5.1.

The list below enumerates some of the key observations and experimental details concerning the reactivity of Mn^{II}-6MeODPEN in comparison to Mn^{II}-DPEN, Mn^{II}-6MeDPEN, and Mn^{II}-QuinoEN as illustrated in Scheme 5.1. Although some of the synthetic preparations and reactivity studies remain unpublished, a thorough recounting of these details is beyond the scope of this thesis.

1. *Sample preparation and monitoring reactivity*. The manganese starting materials are synthesized in an anaerobic environment. When exposed to atmosphere at room temperature, the Mn^{II} compounds shown in Scheme 5.1, which are colorless solutions, change quickly to a purple color ($\lambda_{max} \approx 560$ nm). This species in all cases has been shown to be an unsupported Mn^{III}-O-Mn^{III} dimer through XRD. Upon lowering the temperature at which the reaction occurs, some of the compounds proceed to the final product through intermediate compounds. The intermediates discussed here are obvious by the clear change in color of the solution. The low-temperature reactivity described below is monitored on a UV-Vis spectrometer equipped with a dip-probe. The reaction vessels are held in cold baths to maintain the reaction temperatures described.
2. *Green intermediate in Mn^{II}-6MeDPEN and Mn^{II}-QuinoEN*. When the reaction temperature is lowered to 233 K, instead of proceeding directly to the final product, a green species develops (detected by UV-Vis). This meta-stable intermediate has been characterized in the 6MeDPEN ligand with both rR and XRD and shown to be the first structurally characterized Mn^{III}_2-*trans*-μ-1,2-peroxo dimer (in QuinoEN, the resolution of the XRD experiment is too low to confirm the structure). Over the course of tens of minutes at 233 K, the green intermediate proceeds to the final product. Although no metastable intermediates form after Mn^{III}-O-O-Mn^{III}, further reactivity studies have shown that phosphines are oxidized to phosphine oxides when added to Mn^{III}-O-O-Mn^{III}. In addition, if $H_2{}^{18}O$ is added to a solution of the green intermediate, a significant proportion of the final product Mn^{III}-O-Mn^{III} contains ^{18}O. Both of these observations are indicative of the type of chemistry expected of a high-valent Mn species, currently proposed to be a Mn^{IV}=O.[10–12]
3. *Green to red intermediate in Mn^{II}-6MeODPEN*. When Mn^{II}-6MeODPEN is exposed to atmosphere at $\approx$ 200 K, a green intermediate with absorption maximum similar to the previously characterized

Mn^{III}-O-O-Mn^{III} grows in over the course of 10 minutes. However, this intermediate is far less stable than in the 6MeDPEN ligand scaffold and concomitantly grows in with a new intermediate with absorption maximum at 505 nm. Over the course of another 7 minutes the green intermediate fully converts to the 505 nm intermediate (characterized by a distinct red color). In DCM at ≈ 200 K this new red intermediate is stable for ≈ 15 hours. In acetonitrile the reactivity proceeds more rapidly, presumably because of the warmer reaction temperature needed to prevent MeCN from freezing.

4. *H atom abstraction in Mn^{II}-6MeODPEN*. Recent studies have shown that when Mn^{II}-6MeODPEN reacts with O_2 in the presence of an H atom donor, the complex will abstract H atoms. This was shown by monitoring the formation of benzene from 1,4-cyclohexadiene (CHD), a two-H atom abstraction process, by GC-MS in solutions of Mn^{II}-6MeODPEN in DCM. The formation of one equivalent of benzene (in the presence of 100 equivalents of CHD) suggests that two H atom abstractions occur during the full course of the reaction. Quenching the reaction immediately upon the formation of the red intermediate showed one half equivalent of benzene present. This indicates one H atom abstraction occurs *en route* to formation of the red intermediate and the other after formation of the red intermediate. 2,2,6,6-tetramethyl-1-piperidinol (TEMPOH) has also been shown to act as an H atom donor, forming $TEMPO^{\bullet}$ in the process. The reaction proceeds more rapidly than with CHD; however, TEMPOH also reacts with O_2 to form $TEMPO^{\bullet}$ complicating stoichiometric quantitation of the H atom abstraction. Overall the reaction proceeds with relatively high yield of final product (> 70 %). As shown in Scheme 5.1, it is tentatively proposed that a $Mn^{IV}Mn^{IV}$ bis-μ-oxo species could perform the H atom abstraction, resulting in a one-electron reduction of the Mn dimer to the $Mn^{III}Mn^{IV}$ intermediate observed with EPR spectroscopy. Efforts to locate the abstracted hydrogen in the $Mn^{III}Mn^{IV}$ species and further characterization of the bridging motif are principal goals of the experiments described in this chapter.

Currently the results suggest that this perturbation to the ligand scaffold has significantly altered the mechanism of O_2 bond activation in Mn^{II}-6MeODPEN compared the other Mn^{II} compounds in Scheme 5.1. Mn^{II}-6MeODPEN seems to promote O-O bond cleavage through a $Mn^{III}Mn^{IV}$ intermediate, while

Mn^{II}-6MeDPEN is proposed to pass through an unobserved Mn^{IV}=O species. We propose the intriguing and somewhat controversial species shown in Scheme 5.2 as contenders for the bridging motif between the Mn^{III} and Mn^{IV} ions in the red intermediate.

Although the first contender (bis-μ-oxo-μ-hydroxo $Mn^{III}Mn^{IV}$) contains a μ-hydroxo bridge which has been observed in $Mn^{II}Mn^{II}$, $Mn^{II}Mn^{III}$, $Mn^{III}Mn^{III}$, and $Mn^{IV}Mn^{IV}$ dimers,[13–16] it has been argued that the bridge of a bis-μ-oxo $Mn^{III}Mn^{IV}$ dimer should not be basic enough to support protonation[17] (a bis-μ-oxo-μ-hydroxo $Mn^{III}Mn^{IV}$ compound has been reported by Boucher *et al.* though to the best of our knowledge no magnetic data exists for this compound).[18] However, thiolates form extremely covalent metal-ligand bonds relative to other biologically relevant ligating atoms (i.e. N and O). The Kovacs group has shown that these ligands can promote unexpected spin states (i.e. low-spin non-heme Fe^{III}), increase the basicity of transition metal ions, and lower the transition metal redox potential.[19] In one such study, in a thiolate-containing ligand scaffold (related to those in Scheme 5.1), H atom abstraction was studied in Mn^{III}-OR compounds (same ligand scaffold, unique ligand R = $^{p}NO_2Ph$, Ph, Me, and H). In this study, as the oxidizing strength (more positive cathodic peak potential) of the compounds decreased, the compounds were more likely to abstract H atoms (forming the alcohol analogue of the -OR ligands) indicating increasing pK_as. In this way, increased basicity, a result of the thiolate ligand, was found to offset the less oxidizing redox potential allowing H atom abstraction to occur.[20]

Second, the results of broken-symmetry density functional theory (BS DFT) calculations have led us to propose a $Mn^{III}Mn^{IV}$-μ-oxo bridged dimer with terminal hydroxo on the Mn^{IV} ion. Although not a common bridging motif for $Mn^{III}Mn^{IV}$ dimers, it has been observed (one example found in the literature in Table 5.1).[21] This species is also well-poised to continue to the final product, Mn^{III}-O-Mn^{III}. Finally, we also acknowledge that protonation of the compound due to H atom abstraction may not happen at the bridging oxygen(s). Protonation may occur at the pyridine nitrogen atoms (resulting in structures bis-μ-oxo $Mn^{III}Mn^{IV}$, $N_{py}H$ and bis-μ-oxo $Mn^{III}Mn^{IV}$, $N_{py}H$ H-bond in Scheme 5.2).

This chapter presents the CW and pulse EPR spectra of the red intermediate. In some cases, the spectra have been simulated and the spin Hamiltonian parameters, including *g* values and manganese hyperfine

coupling, are presented. In addition, preliminary pulse EPR spectra aimed at measuring the hyperfine coupling of the abstracted H atom via deuterium labeling are shown. The results of broken-symmetry DFT calculations are presented to guide interpretation of the results. Appendix 5 contains details concerning the behavior of the red intermediate's EPR spectrum in different solvents and in the presence of H atom donors. Finally, the EPR spectra of the starting material Mn^{II}-6MeODPEN, an impurity in 6MeODPENMn^{III}_2O (believed to be the oxidation product 6MeODPEN$Mn^{III,IV}$O), and a species which appears to have an S = 3/2 ground state have all been observed during these studies. These all complicate interpretation of the results, and conclusions on confirming the identity of each of these spectra are in Appendix 5.2.

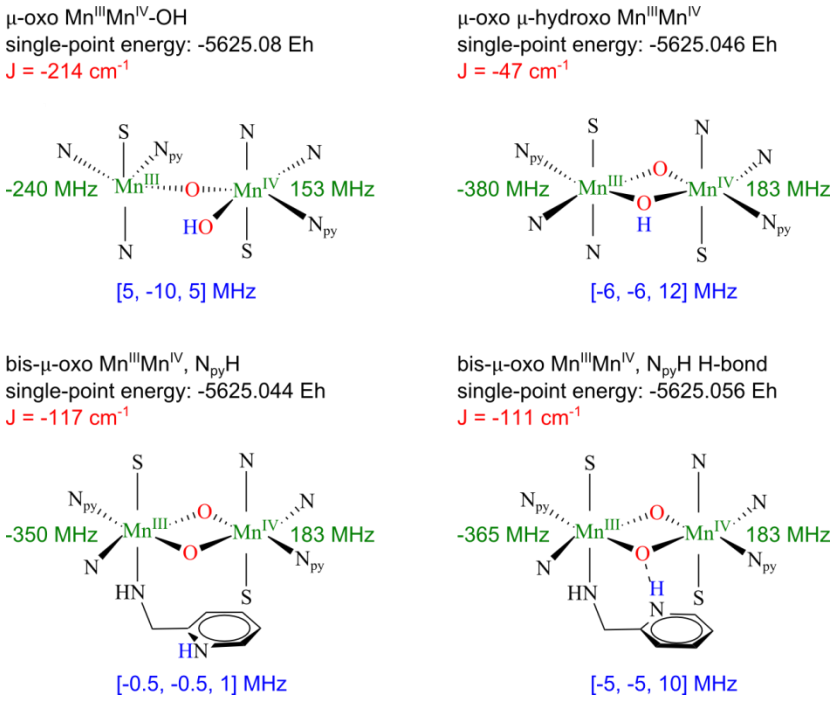

Scheme 5.2. Proposed structures for the red intermediate in the reaction of Mn^{II}6MeODPEN with O_2. The calculated single–point energy (BS DFT), exchange coupling J (BS DFT), ^{55}Mn isotropic hyperfine coupling values (BS DFT), and ^{1}H dipolar hyperfine coupling of the abstracted H atom in various positions (extended point-dipole approximation) are given. Structures are based on the optimized geometries from BS DFT calculations and metrical parameters used in the extended point dipole approximation are taken from these geometries. Note that the Mn^{III} in μ-oxo $Mn^{III}Mn^{IV}$-OH is five-coordinate as per the optimized structure.

5.2 Results

5.2.1 General considerations for EPR sample preparation

In the following sections, the EPR experiments are described. Several different solvent matrices and a variety of temperatures were used for the different experiments. The use of different solvent matrices changed as our understanding of the mechanism at work developed. Initially, nitrile-type solvents were used for sample preparation because this allowed for high-concentration samples to be prepared. However, it was determined that high concentrations (≈ 5 mM) led to strong dipolar broadening in the X-band CW EPR spectrum that distorted the manganese hyperfine coupling (see Appendix Figure A5.1 for a comparison). Around the same time, it was determined that Mn^{II}-6MeODPEN was performing H atom abstraction *en route* to the final product. As listed in Scheme 5.1, the weaker CH bonds of acetonitrile means it could act as the H atom donor, obscuring the true H atom abstraction character when H atom donors such as CHD and TEMPOH are used in the reaction. These two discoveries led to the use of DCM and toluene as the solvent mixture for EPR sample preparation (Mn^{II}-6MeODPEN is not as soluble in DCM but DCM has stronger CH bonds). However, a recent comprehensive comparison of DCM and MeCN solvents shows that MeCN generally leads to enhanced resolution of the manganese hyperfine features in X-band CW EPR spectra and in Q-band pulse EPR spectra. In addition, it seems that incomplete reaction of the Mn^{II} starting material and a weak EPR signal in the Mn^{III}-O-Mn^{III} final product lead to overlapping spectra with what we believe to be the true $Mn^{III}Mn^{IV}$ spectra shown in Figure 5.1. These factors have all complicated sample preparation. A more detailed account of these problems is discussed in Appendix Sections A5.2 and A5.3.

The short T_1 relaxation time of the red intermediate (≈ 10 μs at 15 K) means temperatures near 5 K are ideal for pulse EPR experiments such as ENDOR, 3P-ESEEM, and HYSCORE. While some experiments were performed at appropriate temperatures (X-band and W-band data), others were performed between 10 K and 20 K (Q-band data). Any experiments performed at these warmer temperatures were done on a new cryogen-free system installed on our pulse spectrometer that only reaches ≈ 12 K at the sample, not because these are ideal temperatures for the sample.

5.2.2 Field-swept EPR and ^{55}Mn hyperfine spectroscopy: magnetic parameters of manganese ions

Shown in Figure 5.1 are the field-swept EPR spectra of the red intermediate collected at 9.64, 33.86 and 94.02 GHz (X-, Q-, and W-band, respectively). The X-band spectrum was collected on a CW spectrometer. The Q- and W-band spectra were collected on pulse spectrometers and either FID detected or Hahn echo detected. The Q-band spectrum was collected using the typical one-dimensional FID-detected field sweep (see Chapter 1). In contrast, the W-band spectrum was collected using a two-dimensional detection scheme where the full echo transient was collected at each field value. This detection is advantageous because it allows for more efficient separation of the desired $Mn^{III}Mn^{IV}$ spectrum from an overlapping Mn^{II} (S = 5/2) signal. Further details on this detection and data processing are given in Appendix A5.4 along with a brief discussion on observing and removing unwanted Mn^{II} background signals in manganese samples.[22]

The spectra shown in Figure 5.1 are dominated by the hyperfine couplings of the unpaired electron to the two manganese nuclei. The low frequency/field spectrum (X-band), where the hyperfine interaction is large compared to small g anisotropy, is roughly symmetric, suggesting fairly isotropic manganese hyperfine coupling values. However, the hyperfine interaction is not magnetic field dependent. At higher static applied magnetic fields (W-band), asymmetry in the spectrum caused by the anisotropic g-values becomes more apparent. This demonstrates the advantage of using multiple field/frequency experiments to increase the resolution of different parameters in the spin Hamiltonian.[22,23] The spectra in Figure 5.1 are simulated using the same set of g and hyperfine coupling values (listed in Figure 5.1 and in Table 5.1) and the decent agreement between simulated and experimental spectra in the case of the X-band and W-band spectra provides some confidence in the simulation parameters. The simulated Q-band spectrum, however, has poor agreement with experiment which may be due to insufficient removal of an underlying Mn^{II} impurity spectrum and resonator background contributions (see Appendix A5.3 for more details).

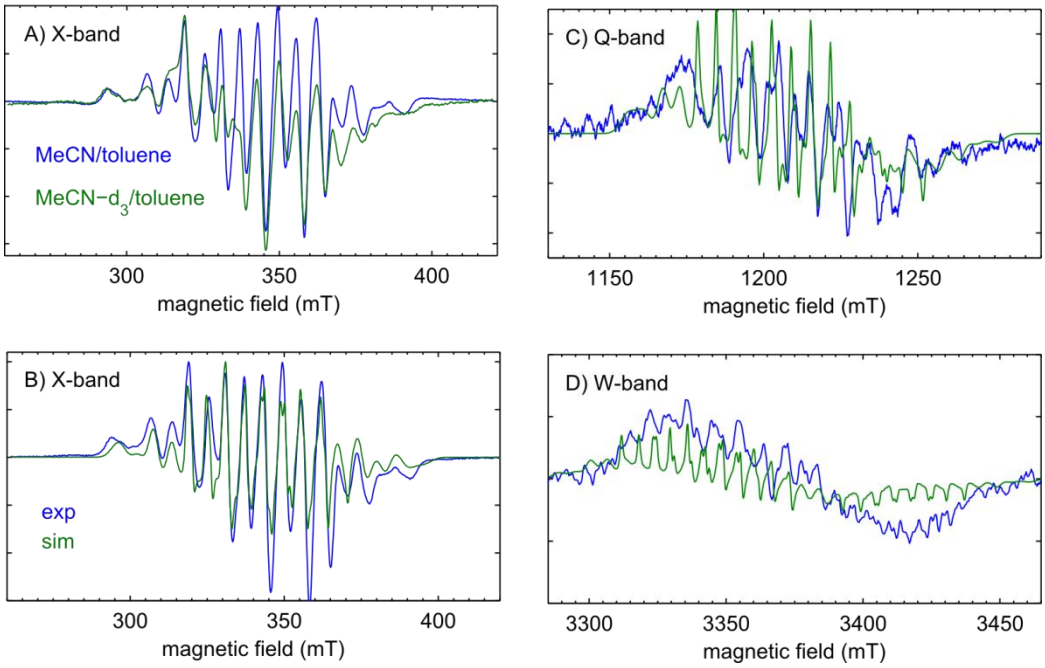

Figure 5.1. Experimental X-, Q-, and W-band field swept spectra (blue): A) The continuous-wave 9.64 GHz EPR spectrum of the red intermediate in a 1:1 solution of MeCN/toluene or MeCN-d_3/toluene at a starting material concentration of ≈ 0.5 mM. After exposure to atmosphere and formation of the red intermediate, the sample was flash frozen in liquid nitrogen and the spectra recorded at 6.6 K with a microwave power of 0.2 mW and modulation amplitude of 0.7 mT. B) The same continuous-wave 9.64 GHz EPR spectrum of the red intermediate in a 1:1 solution of MeCN/toluene as in A). C) FID-detected field-swept pulse EPR spectrum at 33.864 GHz of the red intermediate in MeCN/toluene with a starting material concentration of ≈ 5mM. Spectrum was collected at 7 K with a 1 μs excitation pulse and a 2 ms repetition rate (typical T_1 ≈ 0.7 ms at this temperature). D) 2D transient-detected field-swept pulse EPR spectrum at 94.018 GHz of the red intermediate in MeCN/toluene with a starting material concentration of ≈ 0.5 mM. Spectrum was collected at 4.7 K with the sequence π/2 – τ – π – detection using π/2 (π) pulse lengths of 80 (160) ns and 1 ms repetition rate. Further details on collection and post-processing of the 2D data set to achieve the spectrum shown above are described in Appendix A5.4. In green are simulated spectra for each of the different field/frequency measurements. The simulations were performed using the EasySpin software for an effective S = ½ system with anisotropic g tensor of 1.967, 2.004, and 2.015. Purely isotropic hyperfine couplings for two manganese nuclei were used with values $^{Mn}A_{iso}$= 325 MHz and $^{Mn}A_{iso}$ = 180 MHz. Spin Hamiltonian parameters were the same for the simulated spectra at all field/frequency combinations.

Despite what seems like good agreement between the simulated and experimental spectra, the Q- and W-band field-swept spectra are quite noisy (the spectra shown are derivatives of the absorption-shaped experimental data). To gain additional confidence in the magnetic parameters, the hyperfine coupling of the manganese nuclei can be probed directly with the ELDOR-detected nuclear magnetic resonance (EDNMR, see Chapter 1) experiment which is especially useful for detecting large hyperfine couplings.

Shown in Figure 5.2 are the field-dependent EDNMR spectra collected at Q and W band. The manganese nuclei are in the strong hyperfine coupling regime ($^{55Mn}A >> {}^{55Mn}\nu_L$) where resonances appear centered at $A/2$ and split by twice the Larmor frequency of the nucleus.

Table 5.1. Experimentally determined magnetic properties of Mn and mix metal dimers

Metal Ions	System	Bridging Ligands	J (cm^{-1})	^{55Mn}A Mn^{III} (MHz)	^{55Mn}A Mn^{IV} (MHz)	$^{1H}A_{iso}$, bridging (MHz)	$^{1H}A_{dip}$, H_2O (MHz)
$^{1}Mn^{III}Fe^{III}$	R21ox	μ-hydroxo; bis-μ-carboxylato	-1.8 to -8	263	--	21	7
$^{2}Mn^{II}Mn^{III}$	small molecule	μ-hydroxo; μ-(piv)2	-8.6	264	-564 (Mn^{II})	--	--
$^{3}Mn^{II}Mn^{III}$	PSII	?	10	220	-625 (Mn^{II})		
$^{4}Mn^{II}Mn^{III}$	Mn Catalase	?		223	-587 (Mn^{II})		
$^{5}Mn^{III}Mn^{IV}$	small molecule	bis-μ-oxo	-150	-400	218	--	--
$^{6}Mn^{III}Mn^{IV}$	small molecule	mono μ–alkoxo	-10	-337	197	--	8.4; 7.4
$^{7}Mn^{III}Mn^{IV}$	small molecule	μ-oxo	-177	381	183	--	--
$^{8}Mn^{III}Mn^{IV}$	small molecule	bis-μ-oxo	-150	452	219	--	--
$^{9}Mn^{III}Mn^{IV}$	small molecule	bis-μ-oxo	-134	451	220	--	--
$^{10}Mn^{III}Mn^{IV}$	small molecule	bis-μ-oxo	-155	408	230	--	--
$^{11}Mn^{III}Mn^{IV}$	small molecule	bis-μ-oxo	-139	456	216	--	--
$^{12}Mn^{III}Mn^{IV}$	small molecule	bis-μ-oxo	-140	413	218	--	--
$^{13}Mn^{III}Mn^{IV}$	small molecule	bis-μ-oxo	-151	430	210	--	--
$^{14}Mn^{III}Mn^{IV}$	small molecule	?	--	325	180	--	--

(1) Shafaat, *et al*., *JACS*, **2014**, 136, 13399.
(2) Cox, *et al*., *IC*, **2011**, 50, 8238.
(3) Sarrou, *et al*., *Biochem,* **1998**, 37, 3581.
(4) Zheng, *et al.*, *IC*, **1994**, 33, 382.
(5) Randall, *et al*., *JACS*, **1995**, 117, 11780.
(6) Larson, *et al.*, *JACS*, **1992**, 114, 6263.
(7) Horner, *et al., IC*, **1999**, 38, 1222.
(8) Jensen, *et al.*, *IC*, **1995**, 34, 4244.; Schafer, *et al*., *JACS*, **1998**, 120, 13104.
(9) Manchanda, *et al*., *IC*, **1994**, 33, 5157.; Schafer, *et al*., *JACS*, **1998**, 120, 13104.
(10) Hureau, *et al*., *JACS*, **2003**, 125, 11637.
(11) Frapart, *et al.*, *JACS*, **1996**, 118, 2669.
(12) Goodson, *et al.*, *IC*, **1990**, 29, 503.
(13) Susuki, *et al.*, *Chem Lett*, **1988**, 1763.
(14) This study.

The simulations shown in green in Figure 5.2 use the same hyperfine coupling parameters used for the field-swept simulations in Figure 5.1 which do not include any anisotropy of the ^{55}Mn hyperfine coupling. However, especially in the W-band spectra, there is some obvious field dependence of the resonance position of the features, which may indicate anisotropic components to the hyperfine coupling. The spectra in Figure 5.2 are simulated with the EasySpin function *salt* typically used for Davies ENDOR and not expected to accurately capture the intensity of transitions. However, it should capture the resonance frequencies. Currently, the simulations are not satisfactory and ongoing efforts include producing a common set of spin Hamiltonian values for accurately and simultaneously simulating all the spectra in Figures 5.1 and 5.2.

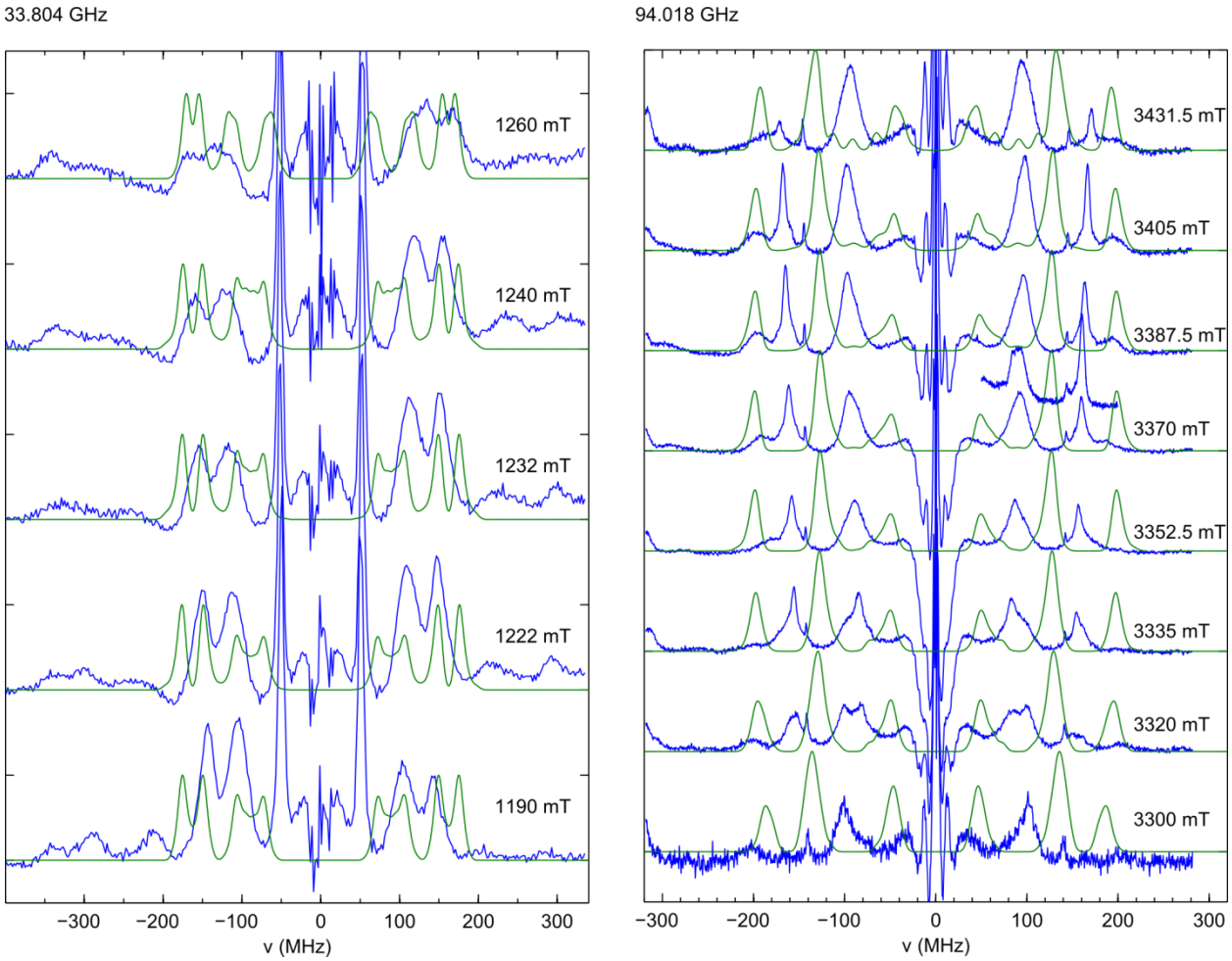

Figure 5.2. *Left*: the 33.804 GHz EDNMR spectra at different static magnetic field values of the red intermediate (≈ 500 μM starting material formed from exposure to atmosphere in the presence of the H atom donor TEMPOH) in DCM/toluene. Spectra were collected using a 15 μs HTA (full ELDOR channel power) pulse and echo detected 3 μs later with softer π/2 (π) pulse lengths of 50 (100) ns. The temperature was 11 K and the repetition rate was 1 ms. A strong ^{1}H resonance occurs at ≈ 50 MHz. *Right*: the 94.018 GHz ED-NMR spectra at different static magnetic field values of the red intermediate (< 500 μM starting material formed from exposure to atmosphere) in MeCN/toluene. Spectra were collected using a 2.5 μs HTA (ELDOR channel attenuated to 12 dB) pulse and echo detected 2.5 μs later with π/2 (π) pulse lengths of 80 (160) ns. The temperature was 4.6 K and the repetition rate was 0.5 ms. A weak, sharp ^{1}H resonance occurs at ≈ 140 MHz.

5.2.3 ^{1}H and ^{2}H hyperfine spectroscopy: locating the abstracted H atom

In addition to characterizing the magnetic properties of the manganese intermediate, we are interested in understanding the reactivity of Mn^{II}-6MeODPEN. This compound reacts with dioxygen and the reactivity studies suggest the compound abstracts at least one hydrogen atom *en route* to the $Mn^{III}Mn^{IV}$ intermediate. If this H atom binds in close proximity to the unpaired electron delocalized across the

manganese ions, its hyperfine coupling interaction should be measureable with EPR spectroscopy and the strength of the hyperfine coupling should be indicative of its location (expected dipolar hyperfine coupling is summarized in Scheme 5.2). In addition, with deuteration of H atom donors such as CHD(CHD-d_8) or TEMPOH(D), assignment of the hyperfine coupling belonging to this H atom becomes more definitive.

Shown in Figure 5.1 is also the X-band CW spectrum of the red intermediate prepared in deuterated acetonitrile (d_3-MeCN) and toluene. Even the largest expected ^{1}H hyperfine coupling for the protonated bis-μ-oxo bridge (≈ 50 MHz) corresponds to less than a 2 mT splitting in the CW spectrum and it is unlikely this would be well resolved. Therefore, the spectrum of the sample prepared in deuterated solvents is expected to appear similar to the sample prepared in protiated solvents. However, there are some small differences between the two.

To gain better resolution of ^{1}H and ^{2}H hyperfine coupling values, we used electron-nuclear double resonance (ENDOR), three-pulse electron spin echo envelope modulation (3P ESEEM), and hyperfine subcorrelation (HYSCORE) spectroscopies at Q- and W-band to search for the abstracted H atom. Shown in Figure 5.3 are the Mims and Davies ENDOR spectra of samples prepared in a variety of concentrations and solvent conditions, and measured at a variety of temperatures (see caption for details). Although the CW EPR spectra appear to be distorted due to inter-dimer dipolar coupling when they are in high concentration (see Appendix Figure A5.1), electron-electron dipolar coupling is not probed in the ENDOR experiment and does not distort these spectra. The Mims ENDOR spectrum in MeCN/Tol shows a ^{1}H nucleus with a hyperfine coupling of about 8 MHz. Davies ENDOR of this same sample, which is a better experiment for detecting strong hyperfine coupling, shows a spectrum with the same ≈ 8 MHz coupling. However, the inherently lower sensitivity of the Davies ENDOR experiment (compared to Mims) results in a noisy baseline. There are some features split by ≈ 30 MHz in the Davies spectrum recorded on a sample prepared in DCM/Tol/NH_4BF_6. This may indicate a strongly coupled proton in this sample; however, given the noise, deuterium labeling is needed to confirm the identity of these (potential) resonances. Q-band ENDOR samples were also prepared in deuterated solvents (top two spectra in

Figure 5.3, left) and studied with Mims ENDOR (the resonator temperature of 15 K precluded studies with the inherently lower signal-to-noise of the Davies experiment). Intriguingly, the smaller ≈ 8 MHz coupling is not detected in these samples. Ongoing efforts will focus on performing these experiments at lower temperatures with both Mims and Davies ENDOR. Generally, the Q-band ENDOR data indicate that the spectra in these experiments are not sensitive to MeCN:toluene versus DCM:toluene solvent mixtures. Finally, the Mims and Davies ENDOR spectra collected at W-band (data not shown) show no resolved ^{1}H coupling. The sample for these experiments was prepared at low concentration in MeCN:toluene and measured at ≈ 4.5 K. The reason for the lack of features remains unclear.

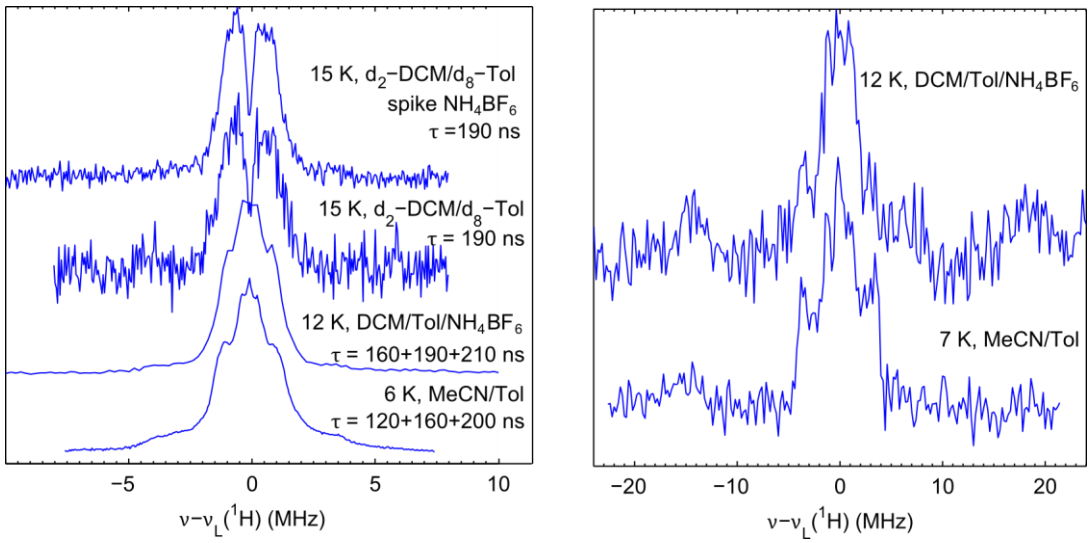

Figure 5.3. *Left*: Mims ENDOR at ≈ 33.9 GHz of the red intermediate prepared in different solvents as indicated in the figure. The spectra were collected at 1 or 3 τ values (as indicated) and where appropriate the spectra are the summations. The pulse sequence $\pi/2 - \tau - \pi/2 - T - \pi/2 - \tau$– echo was used with π/2 pulse lengths between 16 and 30 ns, an RF pulse applied during *T* with lengths between 12 and 15 μs, and repetition rates of 2 to 5 ms. *Right*: Davies ENDOR at ≈ 33.9 GHz of the red intermediate prepared in different solvents as indicated in the figure. The pulse sequence $\pi - T - \pi/2 - \tau - \pi - \tau$– echo was applied using π/2 (π) pulse lengths of 50 (100) ns (MeCN/Tol spectrum) or 40 (80) ns (DCM/Tol spectrum) with RF pulses applied during *T* of lengths between 12.5 and 15 μs at a repetition time of 2 ms or longer. The bottom spectra on both the left and right are of the same sample, as are the second from the bottom spectra.

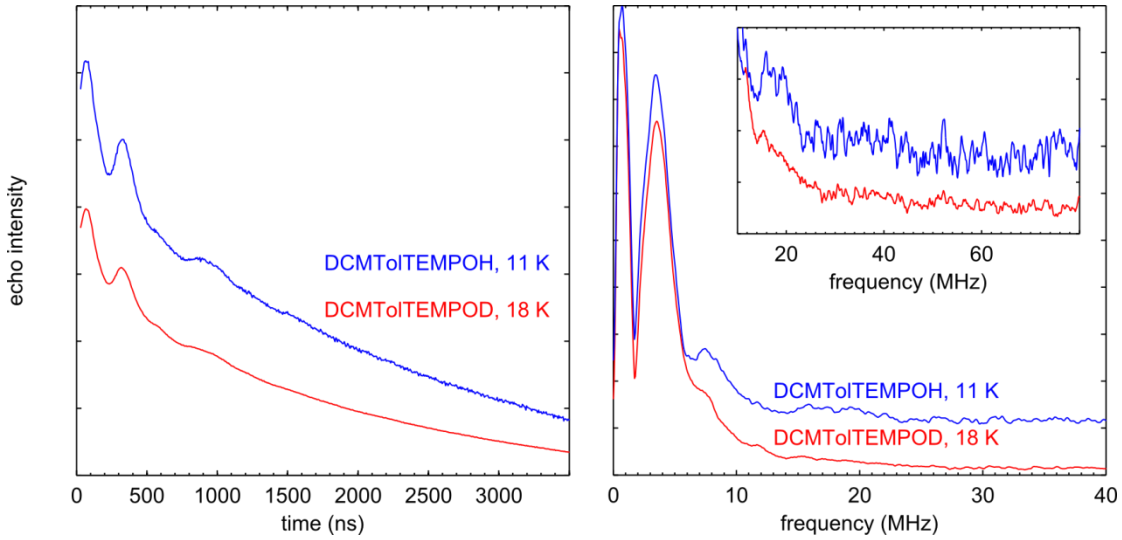

Figure 5.4. 3P ESEEM time traces (left) and spectra after Fourier transformation (right) of the red intermediate (500 μM starting material concentration) in DCM:toluene exposed to atmosphere in the presence of either TEMPOH or TEMPOD. A second-order polynomial was fit and subtracted from the time traces on the left followed by multiplication with the right side of an exponential apodization window and zero filling before Fourier transformation to produce the spectra on the right. 3P ESEEM was acquired with the pulse sequence $\pi/2 - \tau - \pi/2 - t_1 - \pi/2 - \tau$– echo where t_1 was varied in 6 ns steps and the π/2 pulse lengths were 16 ns. The spectra were collected at 8 different τ values starting at 124 ns and increasing in 6 ns steps. Static field values were 1230 mT (TEMPOD) and 1232 mT (TEMPOH) and the repetition rates were 0.5 ms.

In addition to ENDOR, the 3P ESEEM experiment can reveal hyperfine and (in the case of deuterium with nuclear spin I = 1) quadrupole coupling. The 3P ESEEM spectra of the red intermediate prepared in the presence of TEMPOH and TEMPOD are shown in Figure 5.4 along with their Fourier transforms. The Fourier transforms are essentially identical at frequencies between 1 and 12 MHz; the region dominated by the ^{14}N hyperfine and quadrupole coupling. At the applied magnetic fields used for the 3P ESEEM, the nuclear Larmor frequencies of ^{1}H and ^{2}H are about 52.4 MHz and 8 MHz, respectively. Similar to the ENDOR experiments, hyperfine coupling should appear as resonances symmetrically split about the nuclear Larmor frequencies. These large frequencies are more difficult to probe with the ESEEM experiment and it is expected that if any hydrogen resonances are present, they should be very weak compared to the ^{14}N resonances (see an example simulation in Appendix Figure A5.8). Zooming in to the baseline of the experimental Fourier transforms (inset in Figure 5.4, right) between 20 and 80 MHz shows mostly noise. There is a peak at the Larmor frequency of ^{1}H in the sample prepared in the presence of TEMPOH and several peaks surrounding this feature. However, the noise precludes further

interpretation of the features in this region. In addition, the sample prepared with TEMPOD should still show a ^{1}H Larmor frequency feature and features from the smaller ^{1}H hyperfine couplings from the ligand (as measured in the ENDOR experiments), but this area seems featureless. This indicates the ^{1}H ESEEM effect is not efficient enough to be measured. ESEEM at X-band has the potential to drive the transitions due to ^{1}H and ^{2}H coupling more efficiently than at Q-band.

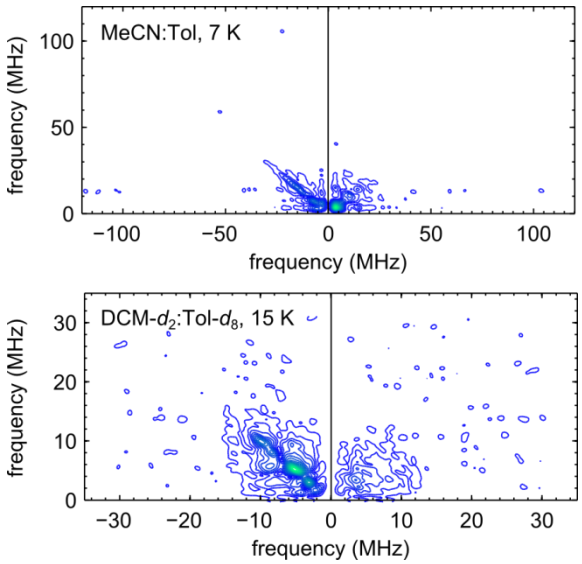

Figure 5.5. *Top*: HYSCORE spectrum of the red intermediate in MeCN and toluene (≈ 5 mM starting material concentration exposed to atmosphere) at 33.822 GHz. The time trace was recorded with the pulse sequence $\pi/2 - \tau - \pi/2 - t_1 - \pi - t_2 - \pi/2 - \tau$ – echo where t_1 and t_2 were varied in 2 ns increments starting at 80 ns, the $\pi/2$ (π) pulse lengths were 30 (30) ns (using different microwave channels), τ = 80 ns, and the repetition rate was 2 ms. *Bottom*: HYSCORE spectrum of the red intermediate in fully deuterated DCM and toluene (≈ 0.5 mM starting material concentration exposed to atmosphere) at 33.924 GHz. t_1 and t_2 were varied in 16 ns increments starting at 200 ns, the $\pi/2$ (π) pulse lengths were 40 (40) ns (using different microwave channels), τ = 200 ns, and the repetition rate was 1.5 ms.

Finally, the 2D Fourier transforms of HYSCORE spectroscopy are shown in Figure 5.5. These spectra are preliminary and the two samples used differ not only in the solvent composition, but also in concentration. Interestingly, in the second quadrant of the top spectrum, where nuclei in the strong-coupling regime resonate, there are two features split by ≈ 80 MHz, at ≈(-100, 15) MHz and ≈(-15, 100) MHz. However, this splitting of 85 MHz is smaller than expected for a proton in the strong coupling regime at Q band fields ($2 \times {}^{1H}\nu_L \approx 100$ MHz). Although intriguing, further experiments on comparable samples in the same conditions with both protiated and deuterated solvents are necessary. Similarly to

the ESEEM experiments, the next steps should focus on performing experiments at X-band where the ^{1}H and ^{2}H ESEEM effects may be more efficiently driven.

5.2.4 DFT results

To help guide our expectations for the hyperfine coupling of both the manganese nuclei and the abstracted proton, we performed broken-symmetry DFT (BS DFT) calculations on the proposed structures in Scheme 5.2. The broken-symmetry method is necessary for obtaining accurate property calculations of strongly exchange-coupled systems. After the calculations have finished, additional post-processing steps must be performed to reliably compare experimental and calculated results. The details of applying BS DFT for geometry optimizations and magnetic property calculations along with the necessary post-processing steps are summarized in Appendix A5.6.

Geometry optimization. The workflow to produce the results of BS DFT calculations is visually summarized in Appendix A5.7 and Scheme A5.1. We started by performing all-atom geometry optimizations of three proposed structures; the μ-oxo-μ-hydroxo-bridge, the bis-μ-oxo bridge with protonated pyridine ring, and an H-bonding interaction between a protonated pyridine ring donor to the bis-μ-oxo bridge. All starting geometries were constructed "by hand" in Avogadro using the crystal structure of $Mn^{III}OMn^{III}$ as a guide.[24] The latter two structures successfully optimized to the desired geometry. However, the μ-oxo-μ-hydroxo-bridge optimized to a structure best described as a μ-oxo bridged $Mn^{III}Mn^{IV}$ dimer with a terminal hydroxo on Mn^{IV}. This structure contains a somewhat unrealistic five-coordinate Mn^{III} ion; however, it is the lowest-energy structure of the three. Starting from this optimized geometry, we adjusted by hand one of the pyridine rings so that the Mn^{III} ion was a more realistic six-coordinate ion and performed an all-atom geometry optimization on this structure (this calculation is still running so results are unavailable). Finally, in order to probe the effects of bis-μ-oxo bridge protonation on magnetic properties, we again took the μ-oxo-μ-hydroxo-bridged dimer starting geometry and performed an optimization for only the H atoms, to forcibly maintain the protonated bis-μ-oxo bridge structure.

Exchange coupling. Using BS DFT, the Heisenberg exchange coupling between the two manganese ions was calculated for all of the optimized structures based on the Hamiltonian

$$\hat{H} = -2J\hat{\boldsymbol{S}}_1\hat{\boldsymbol{S}}_2 \qquad \text{Eq. 5.1}$$

The Orca program uses the single-point energies of the high-spin and broken-symmetry states to calculate the exchange coupling *J* based on three previously reported methods for its calculation. The Yamaguchi[25] method

$$J = -\frac{E_{\mathrm{HS}} - E_{\mathrm{BS}}}{\langle \hat{S}^2 \rangle_{\mathrm{HS}} - \langle \hat{S}^2 \rangle_{\mathrm{BS}}} \qquad \text{Eq. 5.2}$$

is reported to give the closest agreement to experimental values and is the value reported in Scheme 5.2 and Table A5.1. Of the optimized structures, all except the μ-oxo-μ-hydroxo-bridged dimer can be classified as strongly exchange coupled where it is valid to describe the total spin of the system as *S* = 1/2. As discussed in Section 5.3.1 this limit must hold in order to use the projection factors for the Hamiltonian in the coupled basis as described by Bencini and Gatteschi.[26] As discussed next and in detail in Appendix 5.6, this strong-exchange limit must also hold for applying the standard post-processing procedures (which involve scaling by the spin expectation values at each Mn site in the dimer) to obtain calculated hyperfine coupling values that can be compared to experimental values from BS DFT.

^{55}Mn hyperfine couplings. The hyperfine coupling values of the manganese ions and the proton of interest (shown in Scheme 5.2 for each structure) were calculated using BS DFT. As has been reported in detail[27,28] and is summarized in Appendix 5.6 of this thesis, the raw hyperfine values from the BS DFT calculation must be post-processed before making meaningful comparisons to experimentally determined hyperfine coupling values. The procedure was applied for the isotropic components of the BS DFT-calculated ^{55}Mn hyperfine coupling values, and the values are summarized in Table A5.2 for each structure. Most of the structures are in the strong-exchange limit and the post-processing resembles the description of moving from the uncoupled to coupled basis as summarized in 5.3.1. However, for the μ-oxo-μ-hydroxo-bridged dimer in the intermediate exchange coupling regime, the ^{55}Mn hyperfine

coupling values reported in Table A5.2 should be considered a lower limit as described in more detail in Appendix 5.6.

In general, each of the structures has ^{55}Mn hyperfine coupling values that are smaller in magnitude than reports of both calculated and experimentally determined ^{55}Mn couplings in $Mn^{III}Mn^{IV}$ dimers (compare Tables 5.1 and A5.2). In Mn^{III}-O-Mn^{IV}-OH with five-coordinate Mn^{III}, the Mn^{III} coupling is considerably lower (|180| MHz compared to ≈ |400| MHz) than literature values. This may be due to the five-coordinate environment compared to the literature structures which are six-coordinate. The calculated hyperfine coupling values of the rest of the proposed structures agree well with the isotropic hyperfine coupling used to simulate the experimental data in Figure 5.1 (all compared in Table A5.2).

A similar projection of the anisotropic components of the BS DFT-calculated manganese hyperfine couplings can also be carried out. However, since the simulations of the experimental data in Figure 5.1 are adequate with only isotropic hyperfine couplings included, this has not yet been performed. Techniques for spin projection of the raw hyperfine couplings of terminal and bridging nuclei (specifically ^{17}O) have also been explored.[29] For terminal ligands, the same projection factors as used for the individual manganese nuclei can be used since the terminal ligand can be well described as belonging to a specific spin center (i.e. to whichever manganese nucleus it is bound). For bridging nuclei, it is not as clear cut which local spin system the hyperfine coupling should be projected with, and both averaging and summing the projected hyperfine values have been suggested.[29] However, since as of this writing there is no experimentally confirmed hyperfine coupling for the abstracted proton, we have not undertaken these calculations for the BS DFT results (however, we have used the projection factor weighted extended point-dipole approximation to predict the dipolar ^{1}H coupling as described below). Instead, the ^{1}H hyperfine coupling values reported in Table A5.1 are the raw values from the BS DFT calculation.

5.3 Discussion

5.3.1 Understanding the 16-line spectrum of $Mn^{III}Mn^{IV}$ dimers

Although a manganese dimer can exhibit a spectrum with up to 36 lines (due to two I = 5/2 nuclei with 6 possible transitions each), $Mn^{III}Mn^{IV}$ dimers have been found to exhibit a characteristic 16-line spectrum due to overlap of some of the transitions.[30,31] This can be understood by considering the transition from the spin Hamiltonian in the uncoupled to the coupled basis. Equation 5.3 shows a spin Hamiltonian in the uncoupled basis describing the interaction of a Mn^{III} (S_1 = 2, four unpaired electrons) and a Mn^{IV} ion (S_2 = 3/2, three unpaired electrons) including the electron Zeeman interaction, ^{55}Mn hyperfine coupling, nuclear Zeeman interaction, the exchange interaction, and the zero field interaction (this ignores ^{55}Mn quadrupole coupling and hyperfine coupling from other nuclei).

$$\widehat{H} = \mu_{\mathrm{B}} \sum_{i=1,2} \boldsymbol{B}_0 \boldsymbol{g}_i \widehat{\boldsymbol{S}}_i + \sum_{i=1,2} \hat{\boldsymbol{I}}_i \boldsymbol{a}_i \widehat{\boldsymbol{S}}_i - g_{\mathrm{N}} \mu_{\mathrm{N}} \sum_{i=1,2} \boldsymbol{B}_0 \hat{\boldsymbol{I}}_i - 2J \widehat{\boldsymbol{S}}_1 \widehat{\boldsymbol{S}}_2 + \sum_{i=1,2} \widehat{\boldsymbol{S}}_i \boldsymbol{d}_i \widehat{\boldsymbol{S}}_i \qquad \text{Eq. 5.3}$$

However, when J is large (typical values for $Mn^{III}Mn^{IV}$ dimers are on the order of -150 cm^{-1}) so that all of the transitions in the measured EPR spectrum can be assumed to be within one spin manifold, this Hamiltonian can be simplified to the coupled basis and be treated as an effective S_t = 1/2 system.[32] Moving to the coupled basis, the Hamiltonian simplifies to the more familiar form in equation 5.4.

$$\widehat{H} = \mu_{\mathrm{B}} \boldsymbol{B}_0 \boldsymbol{G} \widehat{\boldsymbol{S}}_t + \sum_{i=1,2} \hat{\boldsymbol{I}}_i \boldsymbol{A}_{\mathrm{i}} \widehat{\boldsymbol{S}}_t - g_{\mathrm{N}} \mu_{\mathrm{N}} \sum_{i=1,2} \boldsymbol{B}_0 \hat{\boldsymbol{I}}_i \qquad \text{Eq. 5.4}$$

The tensors $\boldsymbol{G}$, $\boldsymbol{A}_1$ and $\boldsymbol{A}_2$ in equation 5.4 are the ones measured during an EPR experiment. These values are related to the intrinsic $\boldsymbol{g}_i$ and $\boldsymbol{a}_{\mathrm{i}}$ tensors in equation 5.3 through the relations

$$\boldsymbol{G} = \sum_{i=1,2} \rho_i \boldsymbol{g}_i \quad \text{and} \quad \boldsymbol{A}_{i=1,2} = \rho_i \boldsymbol{a}_i \qquad \text{Eq. 5.5}$$

where ρ_i are projection factors which can be determined using the equation

$$\rho_i = \frac{S_{\mathrm{t}}(S_{\mathrm{t}}+1) + S_i(S_i+1) - S_{3-i}(S_{3-i}+1)}{2S_{\mathrm{t}}(S_{\mathrm{t}}+1)} \qquad \text{Eq. 5.6}$$

which includes the spin of the two ions (S_i and S_{3-i}) and the total spin (S_t). In uncoupled systems, Mn^{III} and Mn^{IV} ions do not have significantly different intrinsic hyperfine couplings.[26] However, when interpreting the spin Hamiltonian in the coupled representation, these intrinsic hyperfine coupling values become scaled by the projection factors. For a $Mn^{III}Mn^{IV}$ system with S = 2 (Mn^{III}), S = 3/2 (Mn^{IV}), and total spin S = ½, the projection factors are 2 and -1 for the Mn^{III} and Mn^{IV} ions, respectively. Knowing that the hyperfine coupling values of the two ions will be in a 2:1 ratio, it is easy to visualize with the splitting diagram shown in Figure A5.9 that the 16 line spectrum is expected and diagnostic of a $Mn^{III}Mn^{IV}$ dimer.

5.3.2 Approximating ^{1}H coupling with projection factors

Although it is clear from the X-band CW spectrum in Figure 5.1 that the red intermediate is a $Mn^{III}Mn^{IV}$ dimer, the bridging motif and the location of the abstracted H atom are still unknown. The current data are inconclusive concerning the hyperfine coupling values of the H atom that the compound purportedly abstracts and deuterium labeling will be necessary to confirm these values. Regardless, the hyperfine coupling values can be predicted for the proposed structures shown in Scheme 5.2.

First, as an electron is necessary for the conversion from the Mn^{III}-O-O-Mn^{III} green intermediate into the proposed bis-μ-oxo bridged $Mn^{III}Mn^{IV}$ dimer, it seems reasonable that the proton could land on the O-O bridge resulting in the μ-oxo-μ-hydroxo bridge. A proton on the bridge would have a strong dipolar hyperfine coupling due to its close proximity to the Mn ions and potentially a very large isotropic hyperfine coupling if the spin density on the O-O bridge is large. Table 5.1 summarizes some of the experimentally known hyperfine coupling values for –OH or H_2O ligands bound to manganese and mixed-metal dimers. In the one case with a hydroxo-bridged $Fe^{III}Mn^{III}$ dimer, the proton has an isotropic hyperfine coupling around 21 MHz due to the spin population on the bridging oxygen. It has been shown that the point-dipole approximation can be used to predict the anisotropic hyperfine coupling of protons in close proximity to dinuclear $Mn^{III}Mn^{IV}$ sites assuming equal spin density at the two manganese nuclei.[33,34] The results are often quite accurate and in agreement with experimental and

theoretical calculations despite the simplicity assumed for the distribution of spin density.[35] Using the extended point-dipole approximation for exchange-coupled metal dimers

$$A(\mathrm{MHz}) = C \cdot \mathrm{diag}\left(-\delta, -\Gamma + \frac{\delta}{2}, \Gamma + \frac{\delta}{2}\right) \qquad \text{Eq. 5.7}$$
$$\delta = 2r_{\mathrm{HA}}^{-3} - r_{\mathrm{HB}}^{-3}$$
$$\Gamma = \frac{3}{2}\sqrt{4r_{\mathrm{HA}}^{-6} - 4r_{\mathrm{HA}}^{-3}r_{\mathrm{HB}}^{-3}\cos(2\theta) + r_{\mathrm{HB}}^{-6}}$$
$$C = \frac{g_{\mathrm{e}}\mu_{\mathrm{B}}g_{\mathrm{N}}\mu_{\mathrm{N}}}{h} = 79.2\ \mathrm{MHz/\AA}$$

where r_{HA} and r_{HB} are the distances in angstroms from the ^{1}H nucleus to the Mn^{III} and Mn^{IV} nuclei, respectively, and θ is the angle Mn^{III}-H-Mn^{IV} in radians (taken from the BS DFT-optimized geometry), a dipolar hyperfine coupling T_{dip} of 6 MHz is obtained (where the relation $A_{dip} = T_{dip} \times$ diag[-1 -1 2] applies to obtain the traceless dipolar tensor). However, as shown in the BS DFT calculations and evidenced by known μ-hydroxo bridge $Mn^{II}Mn^{III}$ dimers, protonation of the bis-μ-oxo bridge should drastically decrease the exchange coupling, affecting the appropriate values for projection factors. As argued above and discussed in Appendix A5.6, the projection factors used in this calculation likely produce a lower limit for the dipolar hyperfine coupling.

The next proposed structures are related: a protonated pyridine nitrogen acting as an H bond donor to the bis-μ-oxo bridge (N_{py}–H - - O) or a protonated pyridine nitrogen that has swung away from the bridge. The latter structure with the proton not directly in the superexchange pathway, would likely have a weak isotropic hyperfine coupling. Depending on how far the pyridine arm has swung from the O-O bridge, the anisotropic component may also be very small. Using the BS DFT geometry for a protonated pyridine nitrogen, a dipolar coupling T_{dip} of 0.5 MHz is obtained. For the case of N_{py}–H - - O, the spin projection-weighted distributed point-dipole approximation in equation 5.7 can be used to predict a dipolar coupling T_{dip} of 5 MHz. Here, again the distances r_{HA} and r_{HB} and the angle θ were taken from the optimized geometry.

Finally, the hyperfine coupling of the proton on the terminal hydroxo of Mn^{III}-O-Mn^{IV}-OH can also be predicted. Using equation 5.7 and the BS DFT-optimized geometry a dipolar coupling T_{dip} of 5 MHz is predicted for this proton.

All of the distances r_{HA} and r_{HB} and the angles θ are summarized in the Appendix Scheme A5.1. In addition, the dipolar coupling of selected ^{1}H atoms on the 6MeODPEN ligand were investigated. For the methyl group near the sulfur atom, the $-CH_2$ group off the secondary amine, and the $-CH_2$ group off the tertiary amine, dipolar couplings of 1.3 MHz, 1.7 MHz, and 2.8 MHz were calculated, respectively. All of these values are small enough that they should not be confused with the dipolar coupling of a proton associated with the bridging motif. In addition, these ^{1}H atoms should not be exchangeable with deuterium so isotopic labeling should effectively distinguish these hydrons.

5.3.3 Conclusions from the experimental and calculated data

The g values and ^{55}Mn and ^{1}H hyperfine coupling values from these experiments are summarized in Table 5.1 and compared to literature g and ^{55}Mn hyperfine values for several $Mn^{III}Mn^{IV}$ compounds. Also included in this table are the ^{55}Mn and ^{1}H hyperfine coupling of $Mn^{II}Mn^{III}$ compounds which support μ-hydroxo bridges. As shown in this table, the isotropic hyperfine couplings of Mn nuclei are typically much larger than the isotropic hyperfine coupling used to simulate the spectra of the red intermediate shown in Figure 5.1 (compare $\approx$ 420 to 325 MHz for Mn^{III} and $\approx$ 200 to 180 MHz for Mn^{IV}, respectively). The smaller isotropic hyperfine coupling of the red intermediate corresponds better to decreased hyperfine coupling found in a μ-oxo bridged $Mn^{III}Mn^{IV}$ dimer. However, all of the structures presented herein for which Mn hyperfine coupling values have been computed with BS DFT display lower-magnitude coupling, regardless of bridging motif. These structures all share the 6MeODPEN ligand scaffold. We attribute the lower magnitude of the ^{55}Mn hyperfine coupling values to the covalent thiolate bonds (which will pull spin density off of the manganese nuclei) of the 6MeODPEN system. To the best of our knowledge, there are no examples in the literature of thiolate-ligated $Mn^{III}Mn^{IV}$ dimers with which to compare the ^{55}Mn hyperfine coupling values of the red intermediate.

Although reliable data for a strongly coupled proton in the red intermediate does not exist, the dipolar hyperfine couplings predicted using the extended point-dipole approximation indicate that different structures may be distinguishable in some cases if the dipolar coupling can be measured. A very small or indistinguishable dipolar coupling is indicative of the bis-μ-oxo $Mn^{III}Mn^{IV}$ with protonated pyridine nitrogen. In addition, this structure will likely have a weak isotropic component as well. The distances r_{HA} and r_{HB} for the N_{py}–H - - O structure and the proton on the μ-oxo-μ-hydroxo structure are similar, and thus the dipolar hyperfine coupling is similar. However, in the N_{py}–H - - O structure, the proton is not covalently bound to the bridge, so the isotropic hyperfine coupling will likely be smaller. Therefore, an experimentally measured isotropic coupling may distinguish between these two structures. It is difficult to predict whether μ-oxo $Mn^{III}Mn^{IV}$-OH will be distinguishable from these two situations. Overall, a generally strong T_{dip} > 5 MHz and strong isotropic hyperfine coupling should indicate the abstracted proton is closely associated with the Mn ions or the bridging motif.

The Appendix to this chapter shows some of the difficulties in reproducing the EPR spectrum of the red intermediate including what seems to be overlap with Mn^{II}6MeODPEN EPR signals and unidentified species present in the Mn^{III}-O-Mn^{III} final product which show intense g = 2 and g = 4 EPR signals. Conclusions concerning these species are presented in the appendix where appropriate.

5.4 Outlook

Although bis-μ-oxo bridged $Mn^{III}Mn^{IV}$ dimers are far more common in the literature, geometry optimizations with BS DFT predict that the lowest-energy (possible) structure of the red intermediate is μ-oxo-bridged $Mn^{III}Mn^{IV}$ dimer with terminal hydroxo. This is an intriguing intermediate as there are few examples of unsupported μ-oxo bridged manganese dimers in the literature. However, it is not entirely surprising since the Kovacs lab has shown previously that the DPEN series of ligands readily stabilize the final product, a μ-oxo bridged $Mn^{III}Mn^{III}$ dimer. Several obvious experiments should be performed to help more completely characterize this intermediate and to complete the mechanistic understanding of O-O bond activation.

1. *EPR spectroscopy*. To clarify the location of the abstracted proton, hyperfine spectroscopy combined with deuterium labeling should be performed as described at the end of each subsection in 5.2 Results.

2. *IR or rR spectroscopy to characterize the bridging motif*. The μ-oxo-bridged $Mn^{III}Mn^{IV}$ dimer with terminal hydroxo should have a distinct O-^{1}H vibrational mode readily probed by IR spectroscopy. As this hydroxyl group forms through H atom abstraction, the deuterium labeled O-^{2}H frequency can also be probed. This experiment presents the technical difficulty of performing the measurement at a temperature where the red intermediate is stabilized (240 K or colder). Another option is rR spectroscopy where the diamond-core breathing mode in the bis-μ-oxo bridged dimer or the –OH stretching frequency could be potentially measured. In the case of the diamond-core breathing mode in the bis-μ-oxo bridged dimer, the frequency may be influenced by deuterium labeling if the bridge is indeed protonated (i.e. the μ-oxo-μ-hydroxo bridge). These experiments can be performed in the frozen-solution state at 77 K.

3. *Characterizing final product EPR signal*. As shown in Figure A5.1 and Figure A5.3, the final product, proposed to be a Mn^{III}-O-Mn^{III} based on metrical parameters from XRD, has a weak EPR signal which is clearly due to a manganese dimer because of the ≈ 21 hyperfine lines at g = 2 and ≈ 14 hyperfine lines at g = 4, many more than the six hyperfine lines expected for a monomer. This EPR spectrum also resembles a spectrum we had attributed to overly concentrated EPR samples and inter-dimer magnetic coupling (see Appendix sections 5.1 and 5.2 for more details). In the 6HDPEN, QuinoEN, and 6MeDPEN Mn^{II} compounds, it was shown that final product Mn^{III}-O-Mn^{III} compounds are S = 2 (via Evans method) which should not give EPR signals using the standard perpendicular-mode EPR spectroscopy. However, it was also shown that these compounds along with the final product of the 6MeODPEN ligand could be oxidized via electrochemical methods to a proposed $Mn^{III}Mn^{IV}$ dimer. This was further explored by monitoring the formation of a new species (absorption maximum ≈ 485 nm) upon stoichiometric oxidation with $N(C_7H_7)_3PF_6$. These electrochemical redox reactions were shown to be reversible except for in the 6MeODPEN compound. One should test if the low-intensity EPR signal observed in the final product 6MeODPEN-$Mn^{III}{}_2O$ is an oxidation impurity of the

compound by purposefully adding $N(C_7H_7)_3PF_6$ to EPR samples and checking for increased intensity in the EPR spectrum. Additional simulations and alternative explanations are presented in Appendix 5.2. Fully understanding the origin of this spectrum is necessary for a complete understanding of the reactivity of Mn^{II}-6MeODPEN.

4. *Measurement of exchange coupling, J*. Protonation of oxo-bridges has been shown in $Mn^{II}Mn^{III}$, $Mn^{IV}Mn^{IV}$ and $Mn^{III}Fe^{III}$ dimers (see Table 5.1) to decrease the magnitude of the exchange coupling.[36,37] BS DFT calculations presented here predict a similar trend. An experimental measurement of *J* using SQUID magnetometry would help confirm the protonation state of the bridge. This presents a technical challenge in sample preparation as SQUID requires pristine solid samples. Attempts thus far to crystallize the red intermediate have been unsuccessful.
5. *BS DFT results for fully hexa-coordinate Mn ions in μ-oxo-$Mn^{III}Mn^{IV}$-OH*. As is indicated in the BS DFT workflow diagram presented in Appendix Scheme A5.1, the structure μ-oxo-$Mn^{III}Mn^{IV}$-OH described herein is pentacoordinate around the Mn^{III} ion. This structure closely resembles the final product Mn^{III}-O-Mn^{III}, and it is known that in this structure both Mn ions are hexacoordinate. A calculation with hexacoordination around Mn^{III} in μ-oxo-$Mn^{III}Mn^{IV}$-OH should be performed and these results taken into account in this analysis once available.

5.5 Experimental Section

The synthesis, reactivity, and crystallographic (starting and final product) characterization of O-O bond activation by Mn^{II}6MeODPEN will be reported in a future publication by the Kovacs lab and is beyond the scope of this thesis.

5.5.1 EPR sample preparation

Q-band sample preparation. EPR samples were prepared by dissolving Mn^{II}6MeODPEN in either MeCN:toluene or DCM:toluene to ≈ 700 μM or less in an anaerobic atmosphere (< 1 ppm O_2) in a volume of ≈ 5 mL in a sealed reaction vessel. Where indicated in specific figure captions, H atom donors such as CHD or TEMPOH were added to these solutions. The vessel was transferred out of the glove box to a UV-Vis spectrometer equipped with a dip-probe detector in a cold bath. The vessel was exposed to

atmosphere or O_2 from a gas cylinder and changes in the UV-Vis spectrum were monitored. Visually, the solution passed from colorless, to green, to red. Once the solution had reached maximum concentration of the red intermediate (as monitored by UV-Vis spectroscopy), an aliquot was extracted into a Q-band EPR sample tube via capillary action, quickly sealed with wax (Bruker) and frozen in liquid nitrogen. Samples were used immediately or stored in liquid nitrogen until use in EPR experiments.

X-band and W-band sample preparation. Mn^{II}-6MeODPEN was dissolved in MeCN:toluene to a concentration of ≈ 5 mM anaerobic atmosphere (< 1 ppm O_2). The solution (sealed) was removed from the glove box and placed in a cold bath. The flask was opened to atmosphere and the clear solution changed to green and then swiftly to the red intermediate. Precooled MeCN:toluene was then added to the reaction to reduce the concentration about 10-fold. For the X-band sample, solution was drawn out of the reaction vessel and quickly deposited into a 4 mm OD quartz EPR tube that had the bottom portion submerged in the cold bath. The sample was then frozen in liquid nitrogen. For the W-band sample, capillary action was used to load a < 1 mm OD quartz capillary by dipping the tube into the red solution. This sample was then frozen in liquid nitrogen.

5.5.2 EPR spectroscopy

CW X-band spectra were collected on a Bruker EMX spectrometer in a dual-mode resonator. Experimental temperatures were reached with a liquid helium continuous-flow cryostat (Oxford ESR 900) equipped with an ITC503S temperature controller. Additional spectrometer settings are provided in the figure captions.

Pulse Q-band spectra were recorded on a Bruker ElexSys X/Q spectrometer in an EN 5107D2 resonator. Experimental temperatures were reached with either an Oxford CF905O liquid helium cryostat and an ITC503S temperature controller or a Bruker ColdEdge cryogen-free system with a Mercury iTC temperature controller. Echo-detected field-swept spectra were recorded with the pulse sequence $\pi/2 - \tau - \pi - \tau -$ echo; Davies ENDOR experiments were carried out with the pulse sequence $\pi - T - \pi/2 - \tau - \pi - \tau -$ echo with the radiofrequency pulse applied during *T*; HYSCORE experiments were carried out

with the pulse sequence $\pi/2 - \tau - \pi/2 - t_1 - \pi - t_2 - \pi/2 - \tau -$ echo; 3P ESEEM experiments were carried out with the sequence $\pi/2 - \tau - \pi/2 - T - \pi/2 - \tau -$ echo; EDNMR experiments were carried out with the pulse sequence $\pi_{HTA} - t - \pi/2 - \tau - \pi - \tau -$ echo and the microwave frequency of π_{HTA} was varied.

Pulse W-band spectra were collected on a Bruker ElexSys E680 spectrometer cooled with liquid helium to $\approx$ 5 K. Two-dimensional transient-detected field-swept spectra were recorded with the pulse sequence $\pi/2 - \tau - \pi - t -$ detection; Davies ENDOR experiments were carried out with the pulse sequence $\pi - T - \pi/2 - \tau - \pi - \tau -$ echo with the radiofrequency pulse applied during *T*; EDNMR experiments were carried out with the pulse sequence $\pi_{HTA} - t - \pi/2 - \tau - \pi - \tau -$ detection and the microwave frequency of π_{HTA} was varied. A Mn^{II} impurity, common to most EPR sample preparations, is visible in the Q- and W-band pulse EPR spectra. The pulse two-dimensional transient-detected field-swept spectrum at W-band was used to minimize this contribution. Details on the data processing and methods for eliminating unwanted Mn^{II} signals from pulse EPR spectra are discussed in Appendix A5.4.

5.5.3 Spectral simulations

X-band, Q-band, and W-band field-swept EPR spectra were simultaneously simulated using the EasySpin[38] software with the spin Hamiltonian for the coupled representation in the *S* = 1/2 ground state

$$\hat{H} = \mu_B \boldsymbol{B}\boldsymbol{g}\hat{\boldsymbol{S}}_T + \sum_{i=1,2} \hat{\boldsymbol{S}}_T \boldsymbol{A}_i \hat{\boldsymbol{I}}_i \qquad \text{Eq. 5.8}$$

where *i* is the index for the two manganese nuclei.

5.5.4 Broken symmetry density functional theory

Broken-symmetry DFT calculations were performed with the Orca 4.0 quantum computing software to produce the optimized geometries, exchange coupling, and hyperfine coupling values of the possible structures of the red intermediate.[39] Geometry optimization used the BP86 functional with def2-TZVP(-f) basis set and the CPCM solvent model for dichloromethane. The resolution of identity (keyword RI) approximation and the Becke-Johnson dispersion (keyword D3BJ) correction were applied. The calculation was initiated using the high-spin state (spin multiplicity = 8). The broken-symmetry

wavefunction was obtained using the keyword “FlipSpin” in the %scf block to obtain a final spin state of S = 1/2. The grid size was set to 4, SCF convergence criteria was set to 1×10^{-8} E_h and geometry converge tolerance set to 5×10^{-6} E_h.

The exchange coupling, J, was computed using the optimized geometries and the molecular orbitals from the geometry optimization calculation as a starting wavefunction. Broken symmetry was again called using the “FlipSpin” keyword in the %scf block and the high-spin state used as the starting spin multiplicity. The TPSSh functional with the resolution of identity and chain of spheres approximations (RIJCOSX) for the Coulomb and exact exchange, respectively, were used. The def2-TZVP(-f) basis set was used on all atoms and the CPCM solvent model for dichloromethane was applied.

The hyperfine coupling values were computed using the optimized geometries and the molecular orbitals from the geometry optimization calculation as a starting wavefunction. The broken-symmetry state (low spin, spin multiplicity 2) was used as the spin multiplicity. The TPSSh functional with the resolution of identity and chain of spheres approximations (RIJCOSX) for the Coulomb and exact exchange, respectively, were used. The def2-TZVP(-f) basis set was used on all atoms except the manganese atoms where the CP(PPP) basis was used to more accurately model core spin polarization. The CPCM solvent model for dichloromethane was applied.

5.6 References

(1) Christianson, D. W. *Prog. Biophys. Mol. Biol.* **1997**, *67* (2–3), 99.
(2) Mcevoy, J. P.; Brudvig, G. W. *Chem. Rev.* **2006**, *106* (11), 4455.
(3) Pecoraro, V. L.; Baldwin, M. J.; Gelasco, A. *Chem. Rev.* **1994**, *94* (3), 807.
(4) Wu, A. J.; Penner-Hahn, J. E.; Pecoraro, V. L. *Chem. Rev.* **2004**, *104* (2), 903.
(5) Leto, D. F.; Jackson, T. A. *J. Biol. Inorg. Chem.* **2014**, *19*, 1.
(6) Coggins, M. K.; Kovacs, J. A. *J. Am. Chem. Soc.* **2011**, *133*, 12470.
(7) Coggins, M. K.; Martin-Diaconescu, V.; Debeer, S.; Kovacs, J. A. *J. Am. Chem. Soc.* **2013**, *135*, 4260.
(8) Coggins, M. K.; Toledo, S.; Shaffer, E.; Kaminsky, W.; Shearer, J.; Kovacs, J. A. *Inorg. Chem.* **2012**, *51*, 6633.
(9) Coggins, M. K.; Sun, X.; Kwak, Y.; Solomon, E. I.; Rybak-Akimova, E.; Kovacs, J. A. *J. Am. Chem. Soc.* **2013**, *135*, 5631.
(10) Gordon-Wylie, S. W.; Collins, T. J. *J. Am. Chem. Soc.* **1989**, *111* (12), 4511.
(11) Parsell, T. H.; Behan, R. K.; Green, M. T.; Hendrich, M. P.; Borovik, A. S. *J. Am.* **2006**, *128*, 8728.
(12) Taguchi, T.; Gupta, R.; Lassalle-Kaiser, B.; Boyce, D. W.; Yachandra, V. K.; Tolman, W. B.; Yano, J.; Hendrich, M. P.; Borovik, A. S. *J. Am. Chem. Soc.* **2012**, *134*, 1996.

(13) Wieghardt, K.; Bossek, U.; Nuber, B.; Weiss, J.; J Bonvoisin; Corbella, M.; Vitols, S. E.; Girerd, J. J. *J. Am. Chem. Soc.* **1988**, *110* (22), 7398.
(14) Baldwin, M. J.; Stemmler, T. L.; Riggs-Gelasco, P. J.; Kirk, M. L.; Penner-Hahn, J. E.; Pecoraro, V. L. *J. Am. Chem. Soc.* **1994**, *116* (25), 11349.
(15) Cheng, B.; Fries, P. H.; Marchon, J.-C.; Scheidt, W. R. *Inorg. Chem.* **1996**, *35* (4), 1024.
(16) Cox, N.; Ames, W.; Epel, B.; Kulik, L. V; Rapatskiy, L.; Neese, F.; Messinger, J.; Wieghardt, K.; Lubitz, W. *Inorg. Chem.* **2011**, *50*, 8238.
(17) Larsen, A. S.; Wang, K.; Lockwood, M. A.; Rice, G. L.; Won, T.-J.; Lovell, S.; Sadilek, M.; Turecek, F.; Mayer, J. M. *J. Am. Chem. Soc.* **2002**, *124* (34), 10112.
(18) Boucher, L. J.; Coe, C. G. *Inorg. Chem.* **1976**, *15* (6), 1334.
(19) Kovacs, J. A.; Brines, L. M. *Acc. Chem. Res.* **2007**, *40* (7), 501.
(20) Coggins, M. K.; Brines, L. M.; Kovacs, J. A. *Inorg. Chem.* **2013**, *52*, 12383.
(21) Horner, O.; Anxolabehere-Mallart, E.; Charlot, M.-F.; Tchertanov, L.; Guilhem, J.; Mattioli, T. A.; Boussac, A.; Girerd, J. *Inorg. Chem.* **1999**, *38* (6), 1222.
(22) Schaefer, K.-O. Exchange Coupled Manganese Complexes: Model Systems for the Active Centres of Redoxproteins Investigated with EPR Techniques, Technical University of Berlin, 2002.
(23) Schaefer, K.-O.; Bittl, R.; Lendzian, F.; Barynin, V.; Weyhermueller, T.; Wieghardt, K.; Lubitz, W. *J. Phys. Chem. B* **2003**, *107* (5), 1242.
(24) Hanwell, M. D.; Curtis, D. E.; Lonie, D. C.; Vandermeersch, T.; Zurek, E.; Hutchison, G. R. *J. Cheminform.* **2012**, *4*, 17.
(25) Yamanaka, S.; Kawakami, T.; Nagao, H.; Yamaguchi, K. *Chem. Phys. Lett.* **1994**, *231*, 25.
(26) Bencini, A.; Gatteschi, D. *Electron Paramagnetic Resonance of Exchange Coupled Systems*; Springer: Berlin, 1990.
(27) Orio, M.; Pantazis, D. A.; Petrenko, T.; Neese, F. *Inorg. Chem.* **2009**, *48* (15), 7251.
(28) Pantazis, D. A.; Orio, M.; Petrenko, T.; Zein, S.; Bill, E.; Lubitz, W.; Messinger, J.; Neese, F. *Chem. A Eur. J.* **2009**, *15*, 5108.
(29) Rapatskiy, L.; Ames, W. M.; Perez-Navarro, M.; Savitsky, A.; Griese, J. J.; Weyhermueller, T.; Shafaat, H. S.; Hoegbom, M.; Neese, F.; Pantazis, D. A.; Cox, N. *J. Phys. Chem. B* **2015**, *119*, 13904.
(30) Randall, D. W.; Sturgeon, B. E.; Ball, J. A.; Lorigan, G. A.; Chan, M. K.; Klein, M. P.; Armstrong, W. H.; Britt, R. D. *J. Am. Chem. Soc.* **1995**, *117* (47), 11780.
(31) Schaefer, K.-O.; Bittl, R.; Zweygart, W.; Lendzian, F.; Haselhorst, G.; Weyhermu, T.; Wieghardt, K.; Lubitz, W. *J. Am. Chem. Soc.* **1998**, *120* (50), 13104.
(32) Wieghardt, K. *Angew. Chem. Int. Ed.* **1989**, *28*, 1153.
(33) Randall, D. W.; Gelasco, A.; Caudle, M. T.; Pecoraro, V. L.; Britt, R. D. *J. Am. Chem. Soc.* **1997**, *119* (19), 4481.
(34) Randall, D. W.; Chan, M. K.; Armstrong, W. H.; Britt, R. D. *Mol. Phys.* **1998**, *95* (6), 1283.
(35) Sinnecker, S.; Neese, F.; Noodleman, L.; Lubitz, W. *J. Am. Chem. Soc.* **2004**, *126* (8), 2613.
(36) Pantazis, D. A.; Krewald, V.; Orio, M.; Neese, F. *Dalt. Trans.* **2010**, *39*, 4959.
(37) Shafaat, H. S.; Griese, J. J.; Pantazis, D. A.; Roos, K.; Andersson, C. S.; Popovic-Bijelic, A.; Graslund, A.; Siegbahn, P. E. M.; Neese, F.; Lubitz, W.; Hogbom, M.; Cox, N. *J. Am. Chem. Soc.* **2014**, *136*, 13399.
(38) Stoll, S.; Schweiger, A. *J. Magn. Reson.* **2006**, *178* (1), 42.
(39) Neese, F. *WIREs Comput. Mol. Sci.* **2012**, *2*, 73.

Chapter 5 Appendix

EPR characterization of a $Mn^{III}Mn^{IV}$ intermediate during O-O bond activation by a small molecule thiolate-ligated Mn^{II} compound

---

A5.1 Comparison of the X-band EPR spectra of Mn^{II}-6MeODPEN, the red intermediate, and the final product 6MeODPENMn^{III}_2O

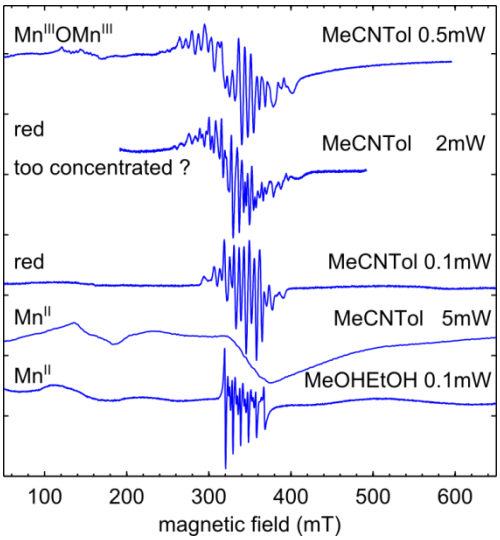

Figure A5.1. X-band EPR spectra of Mn^{II}-6MeODPEN, the red intermediate, and 6MeODPENMn^{III}_2O. The spectra were collected at the microwave powers indicated in the figure, modulation amplitudes of 0.7 mT or less, and at 5 K. There were differences in the microwave frequencies at which each spectrum was collected. The field axis of each spectrum was shifted accordingly to compare the spectra.

The starting material (labeled Mn^{II}, bottom two spectra) shows a 6-line spectrum at $g \approx 2$ (340 mT) typical for high-spin Mn^{II} in a solvent matrix of MeOH/EtOH. In MeCN/toluene, the distinct spectrum at $g \approx 2$ is not visible. However, there is a half-field feature at 150 mT that becomes more distinct. See A5.2.1 for further discussion.

The middle spectrum of the red intermediate is the same as the spectrum shown in Figure 5.1 of the main text. The additional spectrum of the red intermediate (fourth from the bottom) shows a spectrum

with ≈ 21 lines, many more than the 16 lines expected for a $Mn^{III}Mn^{IV}$ dimer. This sample was prepared in a solution of starting material at ≈ 5 mM, whereas the spectrum below it is 10-fold diluted. This 21 line spectrum was thus potentially attributed to inter-dimer dipolar coupling.

However, the final product $Mn^{III}OMn^{III}$ (top spectrum) has a very similar ≈ 21 line EPR spectrum at $g \approx 2$ and also a distinct spectrum with visible Mn hyperfine coupling at $g \approx 4$ (shown in more detail in Figure A5.4). As discussed at the end of Chapter 5 and below in A5.2.3, it is known that $Mn^{III}OMn^{III}$ can be electrochemically oxidized to what is proposed to be a $Mn^{III}Mn^{IV}$ dimer. The 21-line spectrum may be a $Mn^{III}Mn^{IV}$ dimer resulting from oxidized final product.

A5.2 Temperature dependent and solvent dependent X-band CW EPR spectra of the starting material, red intermediate, and final product

A5.2.1 EPR spectra of the starting material, Mn^{II}-6MeODPEN

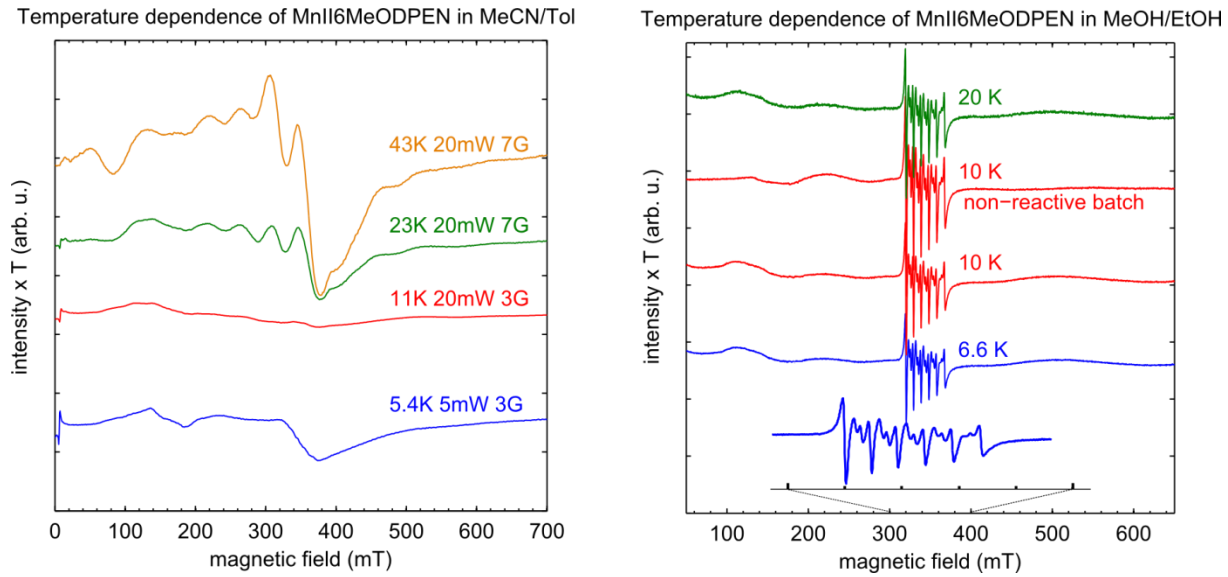

Figure A5.2. Temperature dependent CW spectra of ≈ 5 mM starting material Mn^{II}-6MeODPEN in MeCN/toluene (left) and MeOH/EtOH (right). Spectra are scaled by 1/number of scans, 1/video gain, 1/square root of the microwave power, and temperature. The modulation amplitude and microwave powers used are indicated in the figure on the left and on the right. A microwave power of 0.1 mW and a 0.3 mT modulation amplitude were used.

The Mn^{II} starting material crystallizes as a dimer. If it is a dimer in solution, one would not expect to see EPR features at $g \approx 2$ because antiferromagnetic coupling would produce an $S = 0$ ground state (EPR silent), and ferromagnetic coupling would produce an $S = 5$ ground state (not observed in perpendicular

mode EPR). The spectra in MeCN/Tol do not show any typical Mn^{II} hyperfine features. However, in MeOH/EtOH the starting material shows a six-line spectrum, as is typical for high-spin S = 5/2 Mn^{II} compounds. It may be that MeOH, a relatively good ligand, binds to Mn^{II}-6MeOPEN making it a monomer in the MeOH/EtOH solvent matrix compared to in MeCN/toluene. However, this distinct 6-line pattern was also seen in a batch of starting material that did not react with air. This indicates the spectrum may be due to $Mn^{II}SO_4$ leftover from the synthesis.

A5.2.2 The red intermediate

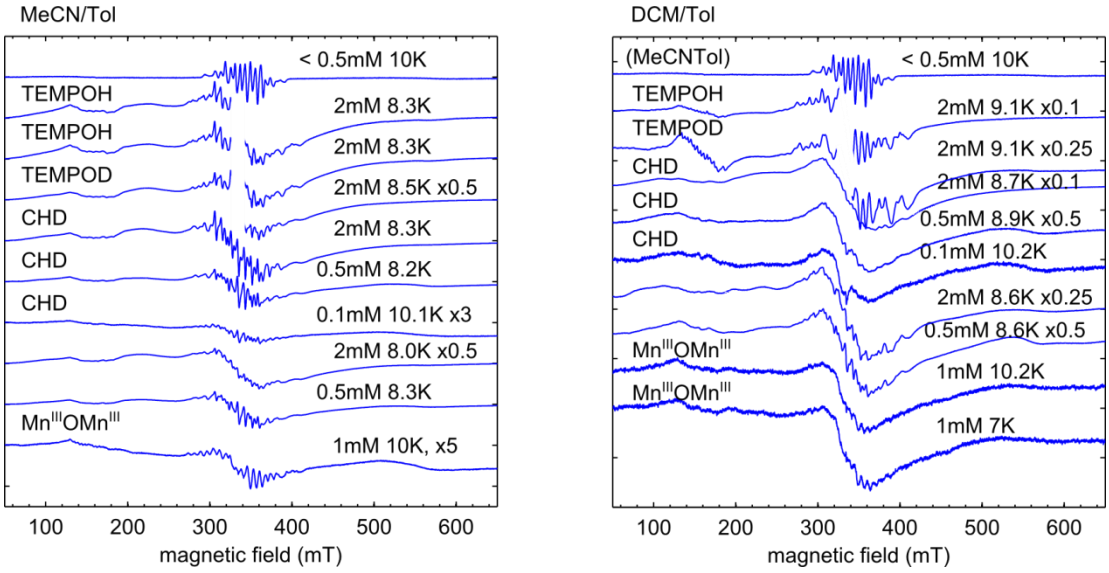

Figure A5.3. CW EPR spectra of the red intermediate formed by exposing Mn^{II}-6MeODPEN to O_2 from a cylinder. As indicated by the figure labels, the reaction was performed in MeCN/Tol in the left figure and DCM/Tol in the right figure. Labels on the left side of each figure indicate the addition of a $^1H(^2H)$ atom donor CHD or TEMPOH(D) (TEMPO• signal is cut out in these spectra) to the reaction mixture. The bottom spectra in both the left and right figures show the final product $Mn^{III}OMn^{III}$ EPR spectra (prepared by dissolving crystalline $Mn^{III}OMn^{III}$ to 1 mM in the respective solvents). Finally, for reference on both the right and the left, the top spectrum shown is the currently hypothesized "clean" EPR spectrum of the red intermediate proposed to be a $Mn^{III}Mn^{IV}$ dimer and shown in Figure 5.1. In almost all cases, the samples appeared distinctly red in color upon freezing. However, the samples prepared in the presence of TEMPOH(D) were purple in color when frozen, more similar to the final product color (noting that TEMPO• is light yellow in color). Spectra were collected with 2 mW of microwave power and a 5 G modulation amplitude (except the top spectrum in both figures). Spectra are scaled by 1/number of scans, 1/video gain, and 1/square root of the microwave power. In addition, for clarity, some spectra are scaled by the factors indicated on the far right of each spectrum label.

Figure A5.3 demonstrates the difficulties encountered in reliably reproducing the $Mn^{III}Mn^{IV}$ spectrum shown at the top of both figures and in Figure 5.1 and A5.1. Initially, it was believed that the 21-line

spectrum labeled “too concentrated” in Figure A5.1 was due to a highly concentrated sample producing magnetic coupling between dimers. The “clean” spectrum was achieved simply by diluting the red intermediate (formed in highly concentrated solutions of the starting material exposed to atmosphere) with cold solvent. The different concentrations indicated in Figure A5.3 were achieved by performing a similar dilution, but the “clean” spectrum was not reproduced. This discrepancy may be caused by two things. First, the final concentration of the clean spectrum was not well known and was perhaps well below the concentrations tested in Figure A5.3. However, in Figure A5.3 the lowest concentration used, 0.1 mM, does not show any reduction in the number of lines, but simply decreased intensity. Second, the main difference between the sample preparations was the exposure of the samples in Figure A5.3 to O_2 from a gas cylinder instead of by simply opening the reaction vessel to atmosphere. This may cause the reaction to proceed more rapidly to the impurity spectrum seen in the final product. However, the 21-line spectrum in Figure A5.1 was produced in samples exposed to atmosphere so using pure O_2 does not seem to be the cause of this inconsistency.

Finally, this series of spectra reveal a distinct half-field feature with ≈ 14 lines in the sample in DCM/Tol in the presence of TEMPOH(D). This half-field feature is also clearly evident in the final product $Mn^{III}OMn^{III}$ in MeCN/Tol, but the hyperfine features are not as sharp. The temperature dependence of this species is explored in Figure A5.4.

A5.2.3 The final product, 6MeODPENMn$^{III}_2$O

The “16-line spectrum rule” for $Mn^{III}Mn^{IV}$ dimers presented in 5.3.1 can be broken in different situations. It is especially common to see more than 16 lines if the *g* and *A* tensors are not collinear.[1] However, here we will present two other situations that are relevant for the structures proposed herein where the number of hyperfine lines deviates from 16.

First, in the only known X-band EPR spectrum of a mono-μ-oxo bridged $Mn^{III}Mn^{IV}$ dimer, there are 18 distinct lines and the intensity pattern of these lines resembles the $g \approx 2$ spectrum seen in 6MeODPENMn$^{III}_2$O.[2] This spectrum (reproduced by simulation in Figure A5.5) has notably small isotropic

^{55}Mn hyperfine coupling values (380 and 180 MHz) with significant rhombic hyperfine anisotropy on Mn^{III}. As discussed in 5.4, 6MeODPENMn^{III}_2O can be electrochemically oxidized to a proposed $Mn^{III}Mn^{IV}$ dimer presumably maintaining the mono-μ-oxo bridge. The impurity spectrum noted in A5.1 is compared to the known mono-μ-oxo bridged $Mn^{III}Mn^{IV}$ and the agreement in the $g \approx 2$ region suggests this impurity is due to oxidized $Mn^{III}OMn^{III}$.

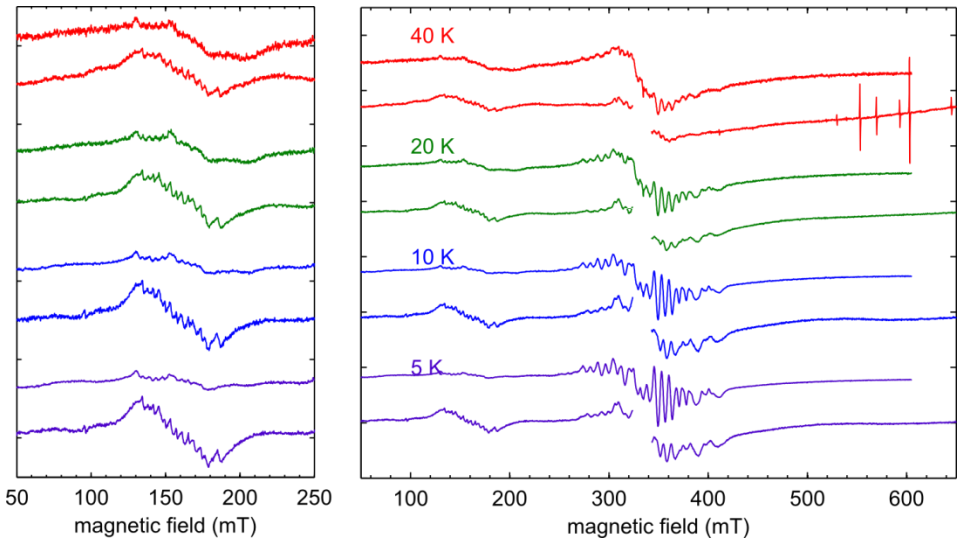

Figure A5.4. Temperature dependent CW spectra of 1 mM final product $Mn^{III}OMn^{III}$ in MeCN/Toluene (uninterrupted spectra) and of the red intermediate in DCM/Tol in the presence of TEMPOD (spectra with TEMPO• removed for clarity; 2 mM starting material exposed to O_2; the frozen sample appeared purple, much like the final product, indicating the reaction may have proceeded beyond the red intermediate). Spectra are scaled by 1/number of scans, 1/video gain, 1/square root of the microwave power, and temperature. The spectra of the final product were collected with 0.5 mW of microwave power and a 5 G modulation amplitude. The spectra in the presence of TEMPOD were collected with 0.02 mW of microwave power at 5 K and 10 K, 0.2 mW of power at 20 K and 40 K, and a 5 G modulation amplitude for all.

Oxidized $Mn^{III}OMn^{III}$ should have very strong exchange coupling due to the linear Mn–O–Mn structure (the exchange coupling in the literature μ-oxo bridged $Mn^{III}Mn^{IV}$ is –177 cm^{-1} and the exchange coupling in 6MeDPENMn^{III}_2O is –125 cm^{-1}, both with Mn-O-Mn angles of 180°). As such, it seems unlikely that S = 3/2 transitions (expected to appear at half field or $g \approx 4$) should be observed in this dimer. In this case, the half-field signal observed herein is currently unassigned. However, its temperature dependence shown in Figure A5.4 (decreasing as temperature is raised) indicates it is an S = 3/2 ground state species.

Also noteworthy, when Mn^{II}6MeODPEN is exposed to O_2 in the presence of TEMPOH(D) the reactions proceed quickly through the green and red intermediates (even at ≈ 200 K (DCM) or ≈ 240 K (MeCN)) so that the samples used in the EPR measurements always appear to have a purple color, indicative of the final product. These samples exhibit very similar EPR spectra (with the $g \approx 2$ and $g \approx 4$ signal) as the neat $Mn^{III}OMn^{III}$ sample, albeit with much higher intensity. It seems TEMPOH(D) drives formation of oxidized $Mn^{III}OMn^{III}$ and the currently unassigned $S = 3/2$ species. As the spectra are very similar in the absence and presence of TEMPOH(D), we currently propose that this signal does not show any magnetic coupling between the Mn dimers and TEMPO• produced during the reaction with O_2.

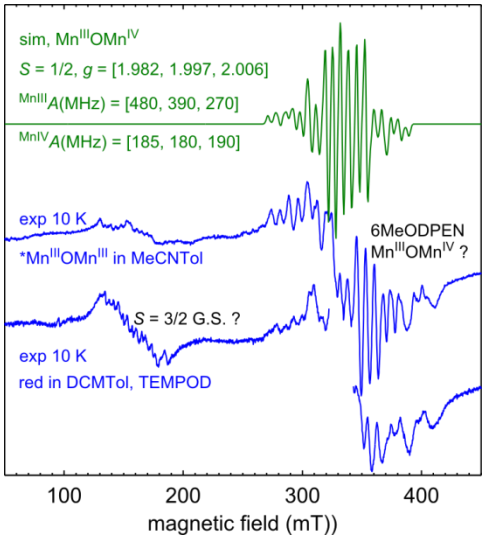

Figure A5.5. In green, a simulation reproducing a $Mn^{III}OMn^{IV}$ EPR spectrum from the literature. Simulation parameters are given in the figure. In blue, the same experimental spectra of 1 mM final product $Mn^{III}OMn^{III}$ in MeCN/toluene and of the red intermediate in DCM/Tol in the presence of TEMPOD collected at 10 K as shown in Figure A5.4.

Second, the 16-line rule has been broken in a $Mn^{III}Mn^{IV}$ dimer with a small exchange coupling of –10 cm^{-1}.[3] In this case, only 12 lines are observed at $g \approx 2$ (and $S = 1/2$ ground state) and as the temperature of the X-band experiment is raised, a signal at $g \approx 4$ grows in due to thermally populating the $S = 3/2$ state. Although the red intermediate spectrum presented in Figure 5.1 is approaching a reduced number of lines (≈ 14), this may be due to an overall reduced ^{55}Mn hyperfine coupling from the covalent thiolate bonds instead of weak exchange coupling.

In conclusion, it seems overall in the reactivity of Mn^{II}-6MeODPEN with O_2 there are at least two $Mn^{III}Mn^{IV}$ dimers (the red intermediate and the oxidized final product) and a structurally unidentified *S* = 3/2 ground state species.

A5.3 Solvent dependent Q-band pulse EPR spectra of the starting material and red intermediate

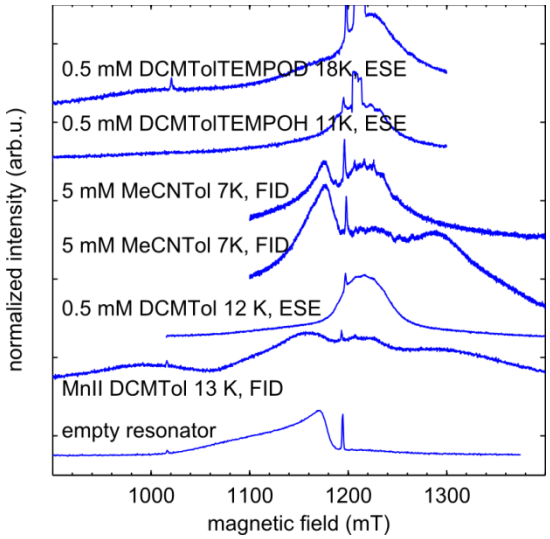

Figure A5.6. Echo- or FID-detected pulse field-swept spectra of the resonator background signal (bottom spectrum), the Mn^{II}-6MeODEN (second from bottom spectrum), and the red intermediate (all other spectra) in various solvent conditions and concentrations collected at ≈ 33.9 GHz. The data marked FID were collected with the sequence $\pi/2$—detection using $\pi/2$ pulse lengths of 1 μs. The echo-detected spectra (marked ESE) were collected with the sequence $\pi/2 - \tau - \pi - \tau$ detection using $\pi/2$ (π) pulse lengths of 16-18 (32-36) ns and typical τ values around 170 ns. Repetition rates were typically between 0.5 and 2 ms.

In Figure A5.6, the bottom spectrum labeled “empty resonator” shows a Cu^{II} background spectrum in the Q-band resonator. The spectrum labeled “MnII...” shows the starting material EPR signal at Q-band. The fourth spectrum up from the bottom shows how both the Cu^{II} background signal and unreacted starting material can interfere with the desired spectrum of the red intermediate. In DCM/Tol, the spectrum of the red intermediate is narrower and has fewer features than the red intermediate in MeCN/Tol. This is consistent with the CW X-band spectra in Figure A5.3 which show that expected features of the red intermediate in DCM are much less distinct.

A5.4 Processing 2D transient detected pulse field swept W-band spectrum

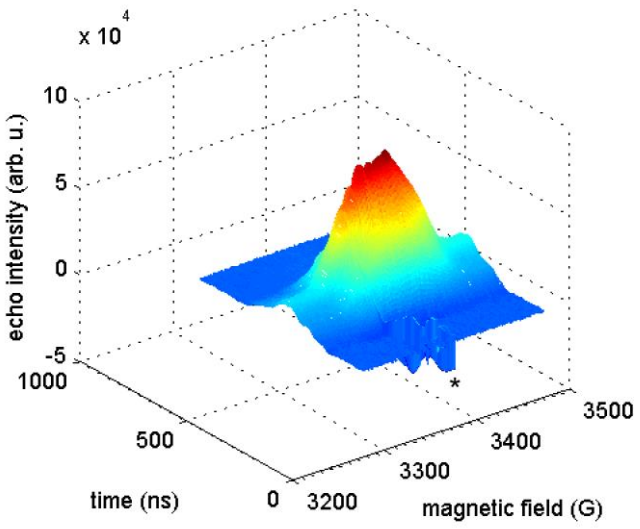

Figure A5.7. The 2D echo transient detected field-swept spectrum of the red intermediate in MeCN/Tol (diluted to 0.5 mM after exposing starting material to atmosphere) at 94.021 GHz. The 2D data set was collected with the sequence $\pi/2-\tau-\pi-$detection using $\pi/2$ (π) pulse lengths of 80 (160) ns and a τ value of 648 ns. The full echo transient was collected at each field value. In this spectrum, the features due to an over-rotated Mn^{II} impurity are more obvious and are marked by an asterisk. To achieve a CW-like field-swept spectrum, the echoes here were integrated over an interval to minimize the contribution from the Mn^{II} signal, then convoluted with a Bessel function of the first kind to simulate a 3.5 mT modulation amplitude to produce the W-band spectrum in Figure 5.1 of the main text. When T_m relaxation rates are short for Mn^{II} impurities relative to the desired Mn EPR signal, longer τ values can be used to minimize the Mn^{II} signal. However, this did not help separate the signals in this case.

A5.5 Representative 3P ESEEM simulations

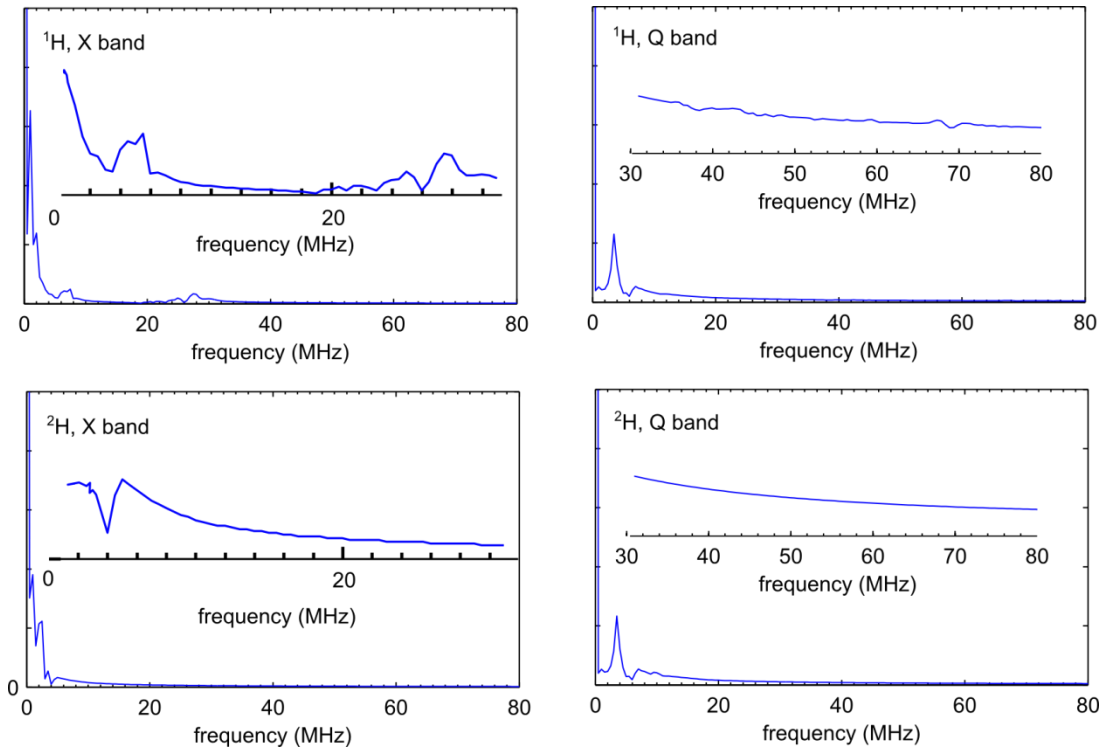

Figure A5.8. The Fourier-transformed time domain traces of a simulated 3P ESEEM experiment. The simulation includes the hyperfine coupling of one ^{14}N nucleus (A_{iso} = 2 MHz and A_{dip} = 2 MHz) and one ^{1}H nucleus (A_{iso} = 20 MHz and A_{dip} = 5 MHz). To show the expected effects of deuterium labeling, where indicated, a ^{2}H nucleus (coupling scaled from $^{1H}A_{iso}$ = 3 MHz and $^{1H}A_{dip}$ = 0.8 MHz) was included in the simulation in place of the ^{1}H nucleus. The pulse sequence $\pi/2 - \tau - \pi/2 - t_1 - \pi/2 - \tau$– echo was simulated where t_1 was varied in 4 ns steps, the $\pi/2$ pulse lengths were 10 ns, and τ was 100 ns. In all cases, the inset is an expanded view of the region where ^{1}H or ^{2}H resonances are expected. In all the spectra, the features between 0 and 10 MHz due to the ^{14}N nucleus dominate the intensity. This figure shows that it is expected for the ESEEM resonances of ^{1}H and ^{2}H features at Q-band to be very weak. Moving to X-band may increase the intensity of these features for the abstracted proton in the red intermediate.

A5.6 Broken-symmetry DFT for exchange coupled spin centers

Applying DFT calculations to systems where two or more spin centers couple antiferromagnetically requires some special considerations. DFT calculations require a single determinant as input. However, in a system with many unpaired electrons in different spatial orbitals, only the high-spin state can be expressed as a single determinant and used as input to a DFT calculation. This represents ferromagnetic coupling, but in the real world, antiferromagnetic coupling is encountered more frequently. To perform DFT calculations on these systems, broken-symmetry DFT (BS DFT) is utilized in the Orca quantum chemical software package. Below is a guide to performing these calculations along with some thoughts on best practices. As an example, the process of performing a geometry optimization, computing EPR properties, and computing the exchange coupling *J* for an antiferromagnetically coupled Mn^{III}(*S*=2)Mn^{IV} (*S*=3/2) dimer will be used.

1. *Geometry optimization*: The user creates the typical Orca input file with level of theory, functionals, basis sets and molecular coordinates specified. The same functionals which are adequate for geometry optimization on transition metal complexes using DFT (BP or BP86) can typically be used with BS DFT. The user should specify the high-spin spin multiplicity (in the case of 7 unpaired electrons, this is 8). A broken-symmetry calculation can be called in the %scf block by using the "FlipSpin" and "FinalMs" options. Orca will perform a single-point calculation on the high-spin state. After, the program will, at the user-defined nucleus specified in the FlipSpin option, flip spins until the desired spin state (specified in the FinalMs option) is reached. This is then a "guess" wavefunction with the same spatial components but different spin components as the high-spin solution. The spatial components of this "guess" wavefunction are then allowed to "relax" and are no longer required to be orthonormal. This results in the broken-symmetry wavefunction. At this point, if one has called for a geometry optimization, the geometry will be relaxed. One should check that the calculation finishes in the BS wavefunction by confirming the spin populations on the metal ions of interest (in this example, one could confirm that the Mulliken spin population at on Mn nucleus (0) is roughly +4 and the spin population at Mn nucleus (1) (where it is requested in the example input file below that spin be flipped) is roughly -3).

```
! UKS Opt BP86 RI def2-TZVP(-f) AutoAux CPCM(ch2cl2) XYZFile PAL8
! SlowConv TightSCF D3BJ Grid4 NoFinalGrid NormalPrint
%scf
        MaxIter 1500
        Flipspin 1              # nucleus where electron spin will flip
        FinalMs 0.5             # desired final m_s
end
```

```
%geom MaxIter 200
        Convergence tight
end
* xyzfile 2 8 geominput.xyz        # high spin should be specified to start calculation
```

2. *Exchange coupling*: If one wants to calculate the exchange coupling, one must perform a single-point calculation on both the high-spin and broken-symmetry state using the optimized geometry. The input file will look nearly identical (especially the %scf block will still contain the FlipSpin and FlipMs options) to that set-up in step one, but the ! Opt keyword will be removed. In addition, the optimized geometry from step one should be used and the wavefunction from step one should be the starting wavefunction (use MOInput and the .gbw file). Once the calculation is completed, search the output file for the word “magnetic” and one will find the exchange coupling printed out. Notice that step one will also result in a printed exchange coupling value. However, since step one was performed on a non-optimized geometry, these values are typically unreliable.

```
! UKS BP86 RI def2-TZVP(-f) AutoAux CPCM(ch2cl2) XYZFile PAL8
! SlowConv TightSCF D3BJ Grid4 NoFinalGrid NormalPrint
! MORead
%moinp "moinput.gbw"
%scf
        MaxIter1500
        Flipspin 1              # nucleus where electron spin will flip
        FinalMs 0.5             # desired final m_s
end
%geom MaxIter 200
        Convergence tight
end
* xyzfile 2 8 optimizedgeominput.xyz     # high spin should be specified to start calculation
```

3. *Property calculations*: Once the initial calculation in step one has finished, the wavefunction is in the low-spin (or final requested spin) broken-symmetry state and the optimized geometry can be used for further property calculations, such as for EPR parameters. An example input file is:

```
! UKS TPSSh RIJCOSX def2-TZVP(-f) AutoAux CPCM(ch2cl2) XYZFile PAL8
! SlowConv TightSCF D3BJ Grid4 NoFinalGrid NormalPrint
! MORead SOMF(1X)
%moinp "moinput.gbw"
%basis
  newGTO Mn "CP(PPP)" end
end
%method
 specialGridAtoms 25
```

```
 specialGridIntAcc 7
end
* xyz 2 2          # use the low spin configuration; use the geometry optimized from step 1
%eprnmr....
end
```

An investigation of the accuracy of EPR property calculations using different functionals was carried out by Orio *et al.* for the case of $Mn^{III}Mn^{IV}$ dimers.[4] Here they demonstrated that many of the results from different functionals deviated from experimental results in a systematic fashion. They were able to apply and recommend correction factors. Generally, the TPSSh functional produces the results most in line with experimental results.

4. *Correction and projection of raw hyperfine coupling values; strong exchange coupling*: The hyperfine coupling values obtained from the BS DFT calculations must be corrected in several ways to be meaningfully compared to experimental values. Methods for these corrections have been outlined in detail and an extensive study on the agreement between experimental and calculated hyperfine coupling values for $Mn^{III}Mn^{IV}$ dimers has been performed.[4,5] For the isotropic component of the hyperfine coupling the relevant equation for projection of the raw HFCs is

$$A_{\mathrm{iso}}^{(k)} = A_{\mathrm{iso,site}}^{(k)} \left(\frac{\langle S_z^{(\mathrm{A})} \rangle}{S_{\mathrm{t}}} \right) \qquad \text{Eq. A5.1}$$

where *k* represents a nucleus in the system, A represents a spin site (in this system *A* for *S* = 2 (Mn^{III}) or *B* for *S* = 3/2 (Mn^{IV})), S_t is the total spin in the coupled representation, and $A_{\mathrm{iso,site}}^{(k)}$ is related to the as-calculated BS hyperfine couplings through

$$A_{\mathrm{iso,site}}^{(k)} = \pm A_{\mathrm{iso,BS}}^{(k)} \left(\frac{\langle S_z \rangle_{\mathrm{BS}}}{S_{\mathrm{A}}} \right) \qquad \text{Eq. A5.2}$$

where S_A is the spin at site A, $\langle S_z \rangle_{\mathrm{BS}}$ is the expectation value of the broken-symmetry state (in this case ½), and the positive or negative sign is applied if the site is expected to have majority α or β spin (so positive for Mn^{III} and negative for Mn^{IV}). For the site A and B in a $Mn^{III}Mn^{IV}$ dimer the term $\pm\left(\frac{\langle S_z \rangle_{\mathrm{BS}}}{S_{\mathrm{A}}}\right)$ becomes 1/4 for Mn^{III} and $-1/3$ for Mn^{IV}.

For most of the proposed structures in Scheme 5.2 of the main text and Scheme A5.1 below, the negative, or antiferromagnetic, exchange coupling is strong (magnitude greater than 75 cm^{-1} using the $-2JS_1S_2$ convention). In this case, the on-site expectation value $\left(\frac{\langle S_z^{(\mathrm{A})} \rangle}{S_{\mathrm{t}}}\right)$ in equation A5.1 simplifies to the well-known spin projection coefficients proposed by Bencini and Gatteschi[6] and explained in Section 5.3.1 of the main text. For Mn^{III} (site A) and Mn^{IV} (site B) ions these projection coefficients are

$$C_{\mathrm{MnIII}} = \frac{\langle S_z^{(\mathrm{A})} \rangle}{S_\mathrm{t}} = \frac{S_\mathrm{t}(S_\mathrm{t}+1) + S_\mathrm{A}(S_\mathrm{A}+1) - S_\mathrm{B}(S_\mathrm{B}+1)}{2S_\mathrm{t}(S_\mathrm{t}+1)} = \frac{\frac{3}{4} + 6 - \frac{15}{2}}{\frac{6}{4}} = 2 \qquad \text{Eq. A5.3}$$

$$C_{\mathrm{MnIV}} = \frac{\langle S_z^{(\mathrm{B})} \rangle}{S_\mathrm{t}} = \frac{S_\mathrm{t}(S_\mathrm{t}+1) + S_\mathrm{B}(S_\mathrm{B}+1) - S_\mathrm{A}(S_\mathrm{A}+1)}{2S_\mathrm{t}(S_\mathrm{t}+1)} = \frac{\frac{3}{4} + \frac{15}{2} - 6}{\frac{6}{4}} = -1 \qquad \text{Eq. A5.4}$$

Combining the above coefficients, the raw broken-symmetry hyperfine couplings can be projected using

$$A_{\mathrm{iso}}^{(\mathrm{MnIII})} = A_{\mathrm{iso,BS}}^{(\mathrm{MnIII})} \times \frac{1}{4} \times 2 \qquad \text{Eq. A5.5}$$

$$A_{\mathrm{iso}}^{(\mathrm{MnIV})} = A_{\mathrm{iso,BS}}^{(\mathrm{MnIV})} \times \left(-\frac{1}{3}\right) \times (-1) \qquad \text{Eq. A5.6}$$

Finally, it has been observed that BS DFT systematically underestimates the manganese hyperfine coupling values by constant coefficients that depend on the functional used for the calculation and whether or not relativistic effects are included in the calculation. A scaling factor of 1.49 has been determined for the functional TPSSh without the inclusion of relativistic effects.[4]

5. *Correction and projection of raw hyperfine coupling values; weak or intermediate exchange coupling*: When the exchange coupling is in the weak to intermediate regime, i.e. $|J_{AB}| \leq 75$ cm^{-1}, the expectation values $\langle S_z^{(\mathrm{A})} \rangle$ and $\langle S_z^{(\mathrm{B})} \rangle$ do not simplify to the spin projection coefficients as the zero-field splitting value for the Mn^{III} nucleus (which contributes the majority of the anisotropy in the system because it is not spherically symmetric) must be included in the effective Hamiltonian. The details on including these parameters have been generalized.[4,5] Looking at the results of our DFT calculations in Table A5.1, this may become relevant for a μ-oxo-μ-hydroxo bridged $Mn^{III}Mn^{IV}$ dimer where the calculated exchange coupling is ≈ 3x smaller then for the μ-oxo bridged dimer, the bis-μ-oxo bridged dimer with the protonated pyridine, or the proton shared between the pyridine and bis-μ-oxo bridge.

   It has been shown that for typical strengths of the zero field-interaction between 1 and 4 cm^{-1} the expectation values are typically slightly larger than the values found in the strong exchange limit. We have not explicitly calculated $\langle S_z^{(\mathrm{A})} \rangle$ and $\langle S_z^{(\mathrm{B})} \rangle$ for the μ-oxo-μ-hydroxo bridged dimer but used the values for the strong-exchange limit. In this case, the ^{55}Mn hyperfine coupling in Table A5.1 can be considered a lower limit.

A5.7 DFT workflow

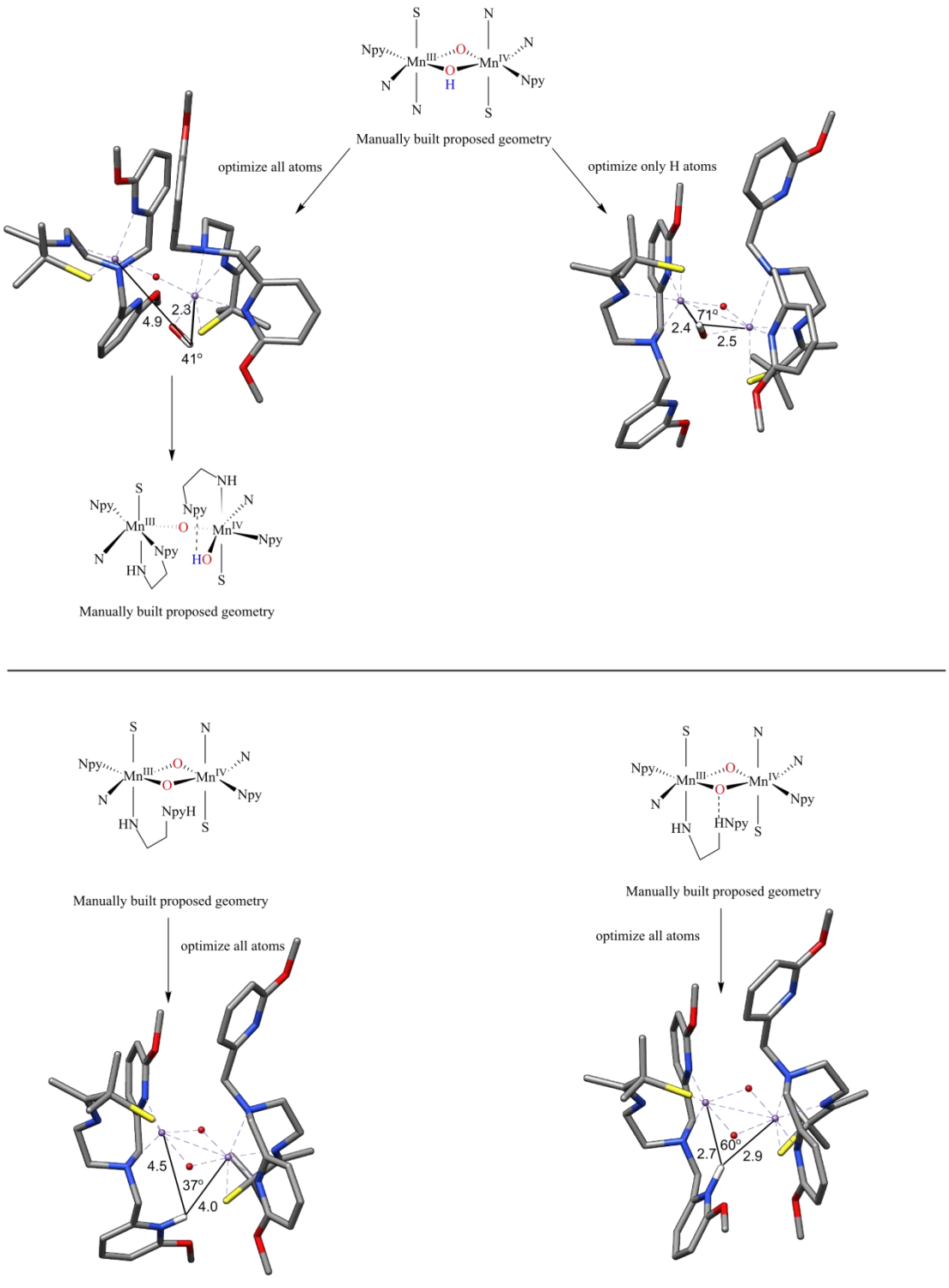

Scheme A5.1. A visual workflow and summary of the results of BS DFT calculations. Of the variety of structures tested, the μ-oxo $Mn^{III}Mn^{IV}$-OH dimer has the lowest single-point energy.

A5.8 DFT results

Table A5.1. Raw BS DFT results for *g* values, ^{55}Mn and abstracted ^{1}H hyperfine coupling (*A* in MHz, Euler angles (EA)[a] in degrees), and exchange coupling (*J* in cm^{-1} for the exchange Hamiltonian $-2JS_1S_2$) in proposed structures of the $Mn^{III}Mn^{IV}$ red intermediate.

Structure	Single-point energy (E_h)[b]	J[c]	*g*	Mn^{III} A and EA		Mn^{IV} A and EA		^{1}H A_{iso}, $A_{spin\ dipolar}$, and EA		
μ-oxo$Mn^{III}Mn^{IV}$-OH	A1: -5625.072	-213	1.994	-40	43	348	15		-31	18
	J1: -5625.080	-166	2.006	-260	8	319	76	-9	14	34
		-214	2.020	-424	4	260	47		17	-34
μ-oxo-μ-hydroxo $Mn^{III}Mn^{IV}$	A1: -5625.038	-46	1.979	-674	-16	364	5		-45	-30
	J1: -5625.046	-36	1.995	-297	37	311	14	-2	-3	32
		-47	2.013	-553	-75	438	42		48	-53
6 coord MnIII μ-oxo$Mn^{III}Mn^{IV}$-OH										
bis-μ-oxo $Mn^{III}Mn^{IV}$	A1: -5625.036	-116	1.982	-621	0	413	-36		0	42
	J1: -5625.045	-90	2.002	-498	84	339	66	-0.5	6.5	65
		-117	2.018	-291	10	354	-31		-7	8
bis-μ-oxo $Mn^{III}Mn^{IV}$ N_{Ar}—H Hbond	A1: -5625.047	-109	1.979	-653	6	426	-34		34.5	13
	J1: -5625.056	-85	1.996	-516	88	344	84	2	-31.5	74
		-111	2.020	-314	0	347	-11		-3	-35

[a] Euler angles for rotation of hyperfine tensor to *g* tensor

[b] Single-point energy from EPR properties calculation marked A1; Single-point energy from exchange coupling calculation marked J1

[c] The exchange coupling calculated from three different methods; $(E_{HS}-E_{BS})/S_{max}^{2}$; $(E_{HS}-E_{BS})/(S_{max}(S_{max}+1))$; and $(E_{HS}-E_{BS})/(\langle S^2\rangle_{HS}-\langle S^2\rangle_{BS})$

Table A5.2. Corrected isotropic ^{55}Mn hyperfine coupling (MHz) from BS DFT calculations.

Structure		Mn^{III}	Mn^{IV}
μ-oxo $Mn^{III}Mn^{IV}$-OH	raw	-240	310
	site	-60	-103
	projected	-120	103
	scaled	-180	153
μ-oxo-μ-hydroxo $Mn^{III}Mn^{IV}$	raw	-510	370
	site	-127.5	-123
	projected	-255	123
	scaled	-380	183
bis-μ-oxo $Mn^{III}Mn^{IV}$	raw	-470	370
	site	-117.5	-123
	projected	-235	123
	scaled	-350	183
bis-μ-oxo $Mn^{III}Mn^{IV}$	raw	-490	370
	site	-122.5	-123
	projected	-245	123
	scaled	-365	183
experiment		325	180

A5.9 The 16-line EPR spectrum for $Mn^{III}Mn^{IV}$ dimers with strong exchange coupling

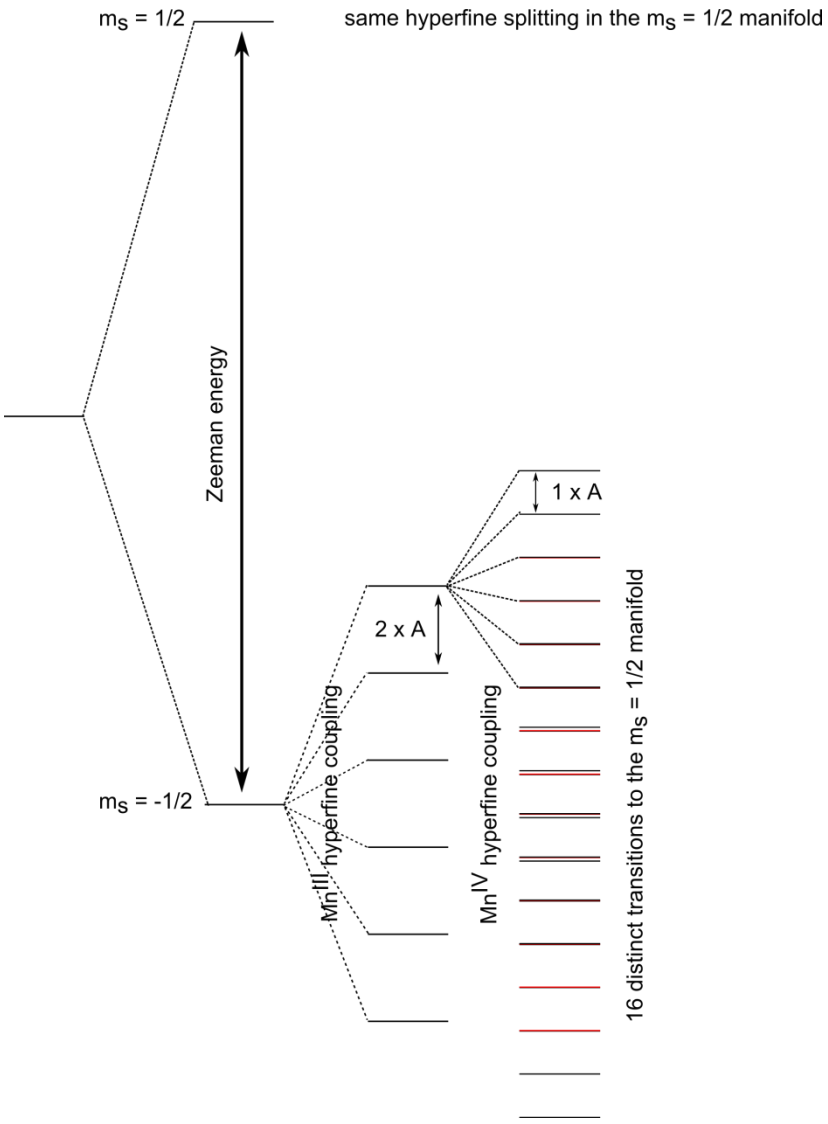

Figure A5.9. The expected 16 distinct transitions for a $Mn^{III}Mn^{IV}$ dimer in the strong exchange limit where the projection factor ratio 2:1 applies.

A5.10 References

(1) Schaefer, K.-O.; Bittl, R.; Zweygart, W.; Lendzian, F.; Haselhorst, G.; Weyhermu, T.; Wieghardt, K.; Lubitz, W. *J. Am. Chem. Soc.* **1998**, *120* (50), 13104.

(2) Horner, O.; Anxolabehere-Mallart, E.; Charlot, M.-F.; Tchertanov, L.; Guilhem, J.; Mattioli, T. A.; Boussac, A.; Girerd, J. *Inorg. Chem.* **1999**, *38* (6), 1222.

(3) Larson, E.; Haddy, A.; Kirk, M. L.; Sands, R. H.; Hatfied, W. E.; Pecoraro, V. L. *J. Am. Chem. Soc.* **1992**, *114* (15), 6263.

(4) Orio, M.; Pantazis, D. A.; Petrenko, T.; Neese, F. *Inorg. Chem.* **2009**, *48* (15), 7251.

(5) Pantazis, D. A.; Orio, M.; Petrenko, T.; Zein, S.; Bill, E.; Lubitz, W.; Messinger, J.; Neese, F. *Chem. A Eur. J.* **2009**, *15*, 5108.

(6) Bencini, A.; Gatteschi, D. *Electron Paramagnetic Resonance of Exchange Coupled Systems*; Springer: Berlin, 1990.

Chapter 6

Electronic structure of a Cu^{II}-alkoxide complex modeling intermediates in copper-catalyzed alcohol oxidations

Abstract

In the copper-catalyzed oxidation of alcohols to aldehydes, a Cu^{II}-alkoxide (Cu^{II}-OR) intermediate is believed to modulate the αC-H bond strength of the deprotonated substrate to facilitate the oxidation. As a structural model for these intermediates, we characterized the electronic structure of the stable compound $Tp^{tBu}Cu^{II}(OCH_2CF_3)$ (Tp^{tBu} = (hydro-tris (3-tert-butyl-pyrazolyl) borate) and investigated the influence of the trifluoroethoxide ligand on the electronic structure of the complex. The compound exhibits an electron paramagnetic resonance (EPR) spectrum with an unusually large g_{zz} value of 2.44 and a small copper hyperfine coupling A_{zz} of $40 \cdot 10^{-4}$ cm^{-1} (120 MHz). Single-crystal electron nuclear double resonance (ENDOR) spectra show that the unpaired spin population is highly localized on the copper ion (≈ 68 %), with no more than 15 % on the ethoxide oxygen. Electronic absorption and magnetic circular dichroism (MCD) spectra show weak ligand-field transitions between 5000 and 12000 cm^{-1} and an intense ethoxide-to-copper charge transfer (LMCT) transition at 24000 cm^{-1}, resulting in the red color of this complex. Resonance Raman (rR) spectroscopy reveals a Cu-O stretch mode at 592 cm^{-1}. Quantum chemical calculations support the interpretation and assignment of the experimental data. Compared to known Cu^{II}-thiolate and Cu^{II}-alkylperoxo complexes from the literature, we found an increased σ interaction in the Cu^{II}-OR bond that results in the spectroscopic features. These insights lay the basis for further elucidating the mechanism of copper-catalyzed alcohol oxidations.

Contributions

The synthesis of and reactivity studies utilizing the copper compounds were performed by Thomas R. Porter in the Mayer group (UW). The MCD experiments were performed in collaboration with Charles J. Barrows from the Gamelin group (UW). The Spiro group, especially George Blouin, set-up the resonance

Raman equipment and was very helpful in teaching the technique and discussing the results. Werner Kaminsky solved the X-ray structures of the copper compounds and determined the single-crystal orientations of EPR samples.

Publications

Reproduced with permission from Hayes, E. C.; Porter, T. R.; Barrows, C. J.; Kaminsky, W.; Mayer, J. M.; Stoll, S., *J. Am. Chem. Soc.*, **2016**, 138 (12), 4132-4145. Copyright 2016 American Chemical Society.

Porter, T. R.; Hayes, E. C.; Kaminsky, W.; Mayer, J. M. *Dalton Trans.,* **2017**, 46, 2551-2558.

6.1 Introduction

Copper(II)/radical systems are important catalysts for the oxidation of alcohols to aldehydes in both biology and synthesis. In nature, the fungal copper enzyme galactose oxidase (GAO) converts primary alcohols to aldehydes.[1,2] In organic synthesis, Cu/nitroxyl systems catalyze the same oxidation.[3–5] The currently accepted mechanisms of both biological and synthetic alcohol oxidation propose Cu^{II}-alkoxide complexes as relevant intermediates.[6,7] Deprotonation of the alcohol when it binds to copper is expected to significantly weaken the substrate αC-H bond strength in preparation for oxidation.[8]

During substrate oxidation in GAO, an alcohol binds to the Cu^{II} site and is deprotonated by an axially bound tyrosinate ligand, producing the proposed CuII-alkoxide intermediate. Ultimately H-atom transfer (HAT) to a coordinated 3′-(S-cysteinyl)tyrosinate radical[9,10] and electron transfer produce the aldehyde product and CuI, but the order and extent of kinetic coupling between the steps is still under investigation.[6,11] For the synthetic Cu/nitroxyl systems, several mechanisms of alcohol oxidation have been discussed in the literature. They all include a Cu^{II}-alkoxide as the first intermediate and differ in the binding mode of the exogenous nitroxyl moiety (which abstracts the αC-H hydrogen of the substrate producing the aldehyde product). [12–16]

Understanding the geometric and electronic structure of these intermediates, including the extent to which the αC-H bond in the alcohol substrate is activated by copper, is of crucial importance to gain fur-

ther insight into the mechanisms of both GAO and the synthetic Cu/nitroxyl systems. However, a detailed electronic structure characterization has not been performed on these intermediates and very few small molecule Cu^{II}-alkoxide complexes are known in the literature to serve as models.[17–20]

As a step toward understanding the structure of the intermediates in Cu-mediated alcohol oxidation, we examined a Cu^{II}-alkoxide complex, $Tp^{tBu}Cu^{II}(OCH_2CF_3)$[21] (abbreviated Cu^{II}-O(TFE) throughout). This complex does efficient H-atom abstraction when treated with H-atom donors such as TEMPO-H, yielding the corresponding radical, trifluoroethanol, and Cu^{I}. While this complex is not a direct functional model (i.e. alkoxide oxidation does not occur upon treatment with external oxyl radical H-atom acceptors),[21] it serves as a general structural model for the proposed intermediates in Cu/radical alcohol oxidation systems. The complex, shown in Figure 6.1, features a tridentate Tp^{tBu} (Tp^{tBu} = (hydro-tris (3-tert-butyl-pyrazol-1-yl) borate) ligand scaffold[22–24] and a 2,2,2-trifluoroethoxide ligand. Structurally, the bulky Tp^{tBu} ligand mimics the catalyst/enzyme supporting ligands, and the alkoxide functions as a substrate model. The complex has an approximately trigonal monopyramidal coordination geometry with a long Cu-N_{axial} bond[21] (similar to type 1 copper sites).[25]

Here, we characterized the electronic structure of Cu^{II}-O(TFE). We used powder and single-crystal electron paramagnetic resonance (EPR) spectroscopy to probe the paramagnetic $S = 1/2$ ground state. This revealed the identity of the singly occupied molecular orbital (SOMO), the $d_{x^2-y^2}$, and its orientation within Cu^{II}-O(TFE). It also revealed a large shift in g_{zz} (one of the largest recorded for copper in a biologically relevant ligand scaffold) and a small copper hyperfine $^{Cu}A_{zz}$, (similar in magnitude to type 1 blue copper sites[25]). Using electron nuclear double resonance (ENDOR) spectroscopy, we measured the hyperfine couplings to determine the strength of the interaction between the unpaired electron and nearby magnetic nuclei (^{1}H, ^{19}F, ^{14}N). With these values, we mapped the extent of delocalization of the unpaired electron onto the Tp^{tBu} and trifluoroethoxide ligands and found much of the spin population localized on copper. Using UV-Vis/NIR, magnetic circular dichroism (MCD), and resonance Raman (rR) spectroscopies, we assigned the electronic transitions and characterized the nature of the Cu-O bond. We show Cu^{II}-O(TFE) has a near-UV ethoxide-to-copper charge transfer transition, giving it a red color,

reminiscent of biological red copper sites (nitrosocyanin[26] and BSco[27,28]). We compare Cu^{II}-O(TFE) to analogous thiolate (Cu^{II}-SR) and peroxo (Cu^{II}-OOR) ligated copper compounds to understand the influence of the ethoxide ligand on electronic structure. In addition, we summarize how the identifying spectroscopic features (large g_{zz}, small $^{Cu}A_{zz}$, near-UV transition) are related to biological copper sites.

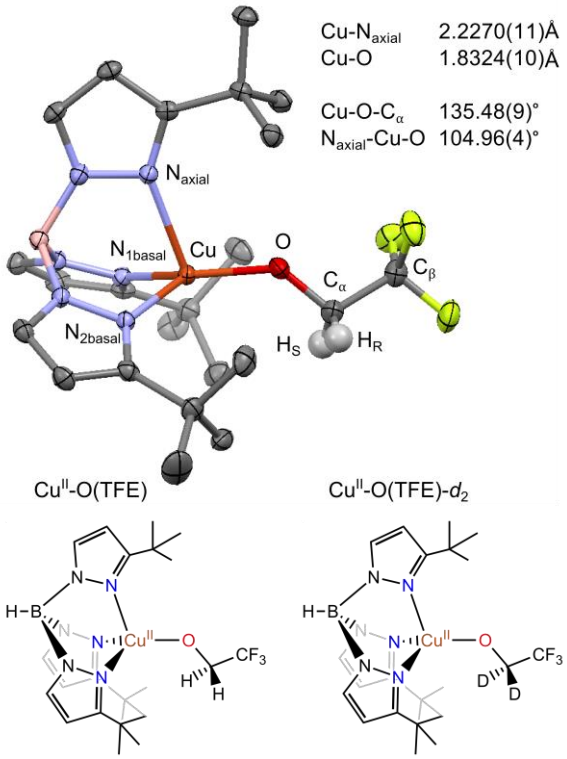

Figure 6.1. (Top) Crystal structure of $Tp^{tBu}Cu^{II}(OCH_2CF_3)$ with ellipsoids at the 50 % probability level and primary bond lengths and angles listed, from ref. 21. Hydrogen atoms are omitted for clarity, except on the trifluoroethoxide ligand. Additional relevant structural features include the bond lengths Cu-N_{1basal} (1.9717(11) Å) and Cu-N_{2basal} (1.9638(11) Å), and the dihedral angles Cu-O-C_α-H_S (37.43°) and Cu-O-C_α-H_R (−81.06°). (Bottom) Lewis structures of Cu^{II}-O(TFE) and Cu^{II}-O(TFE)-d_2 reproduced from ref. 21.

Our data allow the following conclusions to be made. First, the spin population on the ethoxide ligand is small, leaving much of the spin localized on copper. The absence of substantial spin population on the ethoxide ligand suggests a relatively ionic Cu-O bond compared to related Cu^{II} complexes with similar distorted tetrahedral ligand environments. Despite the relatively ionic Cu-O bond, the αC-H bond of the trifluoroethoxide is not activated enough to promote ligand oxidation.[21] Second, the Cu-O bond has contributions from both Cu d_{xy}/O(TFE) pseudo-σ and Cu $d_{x^2-y^2}$/O(TFE) p_π interactions. The σ bonding interaction between the O(TFE)-based pseudo-σ (abbreviated $p_{\sim\sigma}$) and the copper-based d_{xy} orbitals re-

duces the energy gap between the dominantly d_{xy} antibonding orbital and the singly occupied $d_{x^2-y^2}$ orbital. This results in the small difference in energy, $E_{x^2-y^2} - E_{xy}$, observed by MCD spectroscopy, that drives the large shift in g_{zz}. Overall, these insights contribute to the understanding of the role of alkoxide intermediates in Cu^{II}-catalyzed alcohol oxidations.

6.2 Results

6.2.1 Field-swept EPR.

A combination of 9.2 GHz (X-band) and 34 GHz (Q-band) EPR spectroscopies reveal the magnetic parameters of the Cu^{II}-alkoxide. The continuous-wave (CW) 9.2 GHz EPR spectrum of Cu^{II}-O(TFE) in a frozen solution of toluene at 120 K is shown in Figure 6.2A. This spectrum resolved the unusually large g_{zz} = 2.44(1) and small Cu hyperfine coupling A_{zz} = 120(10) MHz ($40(3)\cdot10^{-4}$ cm^{-1}).[21] 34 GHz EPR, shown in Figure 6.2B, of Cu^{II}-O(TFE) in DCM:toluene at 10 K further resolved the principal g values to g_{xx} = 2.060(6), g_{yy} = 2.093(6) and g_{zz} = 2.447(6) (simulation parameters in Table A6.1A). Based on the ligand field theory for a d^9 system, the large g_{zz} shift away from the free electron g value (g_e = 2.0023) indicates that the molecule is in a $d_{x^2-y^2}$ ground state.[29]

To determine the orientation of the *g* tensor principal axes and ultimately of the $d_{x^2-y^2}$ orbital within the molecule, 34 GHz pulse field-swept EPR spectra of a doped single crystal sample were collected (1% Cu^{II}-O(TFE) in the zinc analog Zn^{II}-O(TFE)). In these experiments, a series of thirteen spectra were acquired by rotating a single crystal sample in the EPR spectrometer in 15° increments (Figure 6.2C). In each spectrum, two peaks from two sites in the unit cell are observed due to the P21/n space group of the crystal. Using the principal *g* values obtained from the powder 34 GHz spectrum, the orientation of the g tensor in the molecule was determined by a simultaneous least-squares fitting of the thirteen spectra with a model generated using the simulation parameters in Table A6.1B (fitting details in Experimental section). It was necessary to use g_{zz} = 2.453(4), slightly shifted compared to the frozen solution, to achieve adequate simulations of the data. This is likely due to slight structural differences between a frozen solution and a crystal. The data and simulations indicate the z axis of the *g* tensor (z_g) is tilted ≈ 10° away from the Cu-N_{axial} bond toward the ethoxide ligand and the y axis (y_g) is tilted ≈ 22°

away from the Cu-O bond (shown in Figure 6.3). Least-squares fits of a data set from a second single crystal (Figure A6.2, Table A6.1B, using a g_{zz} value of 2.463(6)) produced a nearly identical g frame orientation. As a result, we determined the lobes of the singly occupied $d_{x^2-y^2}$ orbital lie in a plane normal to the z_g axis and nearly normal to the long Cu-N_{axial} bond. Figure A6.6A shows the orientations of the static field in the molecule for this set of spectra.

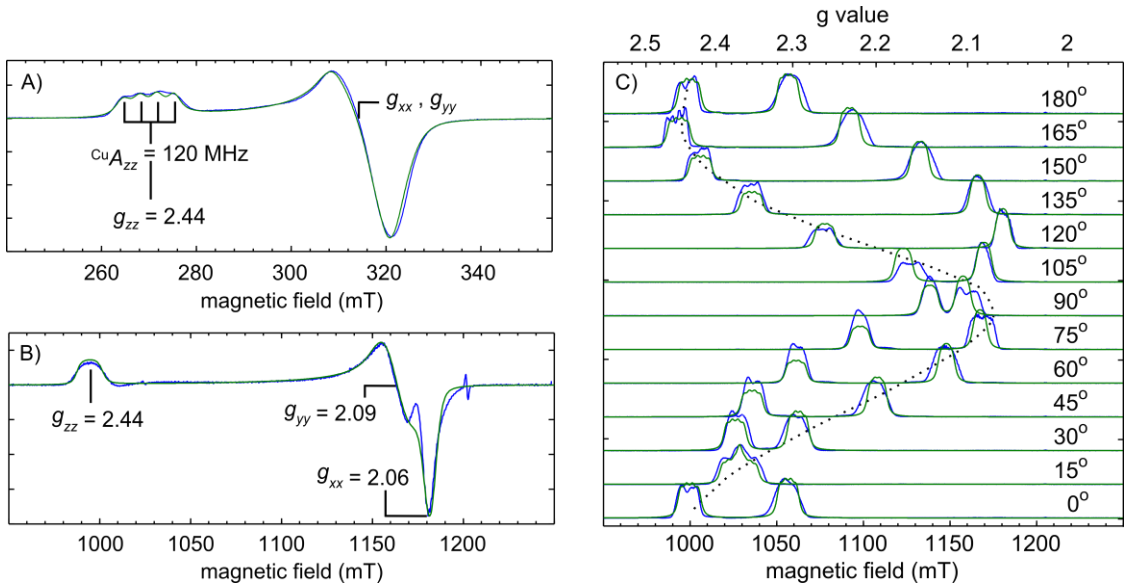

Figure 6.2. The copper hyperfine coupling, principal *g* values, and *g* tensor frame are resolved with multi-frequency and single-crystal EPR. A) Field-modulated 9.22 GHz CW EPR spectrum of a frozen solution of Cu^{II}-O(TFE) in a toluene glass acquired at 120 K with a microwave power of 2 mW (reported previously in ref. 21). B) First derivative of an echo-detected [π/2(30 ns) – τ(240 ns) – π(60 ns) – τ – echo] 34.061 GHz pulse field-swept spectrum of a frozen solution of Cu^{II}-O(TFE) in a DCM:toluene glass (10 K, 3 ms repetition time). C) FID-detected [π/2(1 μs) – FID] pulse field-swept spectra of 1% Cu^{II}-O(TFE) in a Zn^{II}-O(TFE) single-crystal (10 K, 2 ms repetition time, 0.1 mT steps). Spectra were acquired at 34.151 GHz (0°-75°) and 34.143 GHz (90°-180°). In all cases, experimental traces are shown in blue and simulations in green. Simulation parameters are summarized in Tables A6.1A, B.

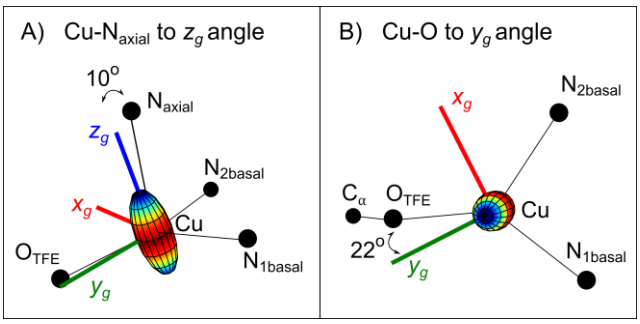

Figure 6.3. Orientation of the *g* tensor in Cu^{II}-O(TFE) determined from single-crystal EPR. An axial *g* tensor ellipsoid is centered on copper and the x_g, y_g, and z_g axes of the tensor are shown as thick red, green, and blue lines, respectively. A) The z_g axis lies 10° off the Cu-N$_{axial}$ bond in crystal 1 (10° in crystal 2, see Appendix). B) The y_g axis lies 22° off the Cu-O bond in crystal 1 (37° in crystal 2, see Appendix).

6.2.2 ENDOR

^{1}H ENDOR. To quantify the distribution of unpaired spin population in the molecule, we measured the hyperfine coupling interaction between the unpaired electron and surrounding magnetic nuclei using ENDOR spectroscopy. Frozen-solution ENDOR spectra of Cu^{II}-O(TFE) revealed broad ^{1}H peaks split by ≈ 25 MHz and centered around the ^{1}H Larmor frequency (peaks at ± 12 MHz in Figure A6.4). In ENDOR spectra of Cu^{II}-O(TFE)-d_2, these features shifted to lower frequency (centered at the ^{2}H Larmor frequency). This indicates these features originate from the αC-H protons on the trifluoroethoxide ligand and these protons have isotropic hyperfine couplings of about 25 MHz.

To determine the full hyperfine tensors of the two protons, including principal values and tensor orientations, we measured ^{1}H ENDOR on a doped single crystal (1% CuII-O(TFE), 99% ZnII-O(TFE)). The corresponding spectra in Figure 6.4 show two pairs of orientation-dependent hyperfine lines due to the two ethoxide protons which we named H$_R$ and H$_S$ (referring to the prochirality of the hydrogens pictured in Figure 6.1). The total hyperfine coupling A_{tot} for each proton is modelled as the sum of an isotropic term and an anisotropic dipolar term, $A_{\mathrm{tot}} = A_{\mathrm{iso}} + A_{\mathrm{dip}}$. The dipolar term of the hyperfine coupling produces the curved path of the peaks in the series of spectra collected as the orientation of the single crystal is rotated in the magnetic field.

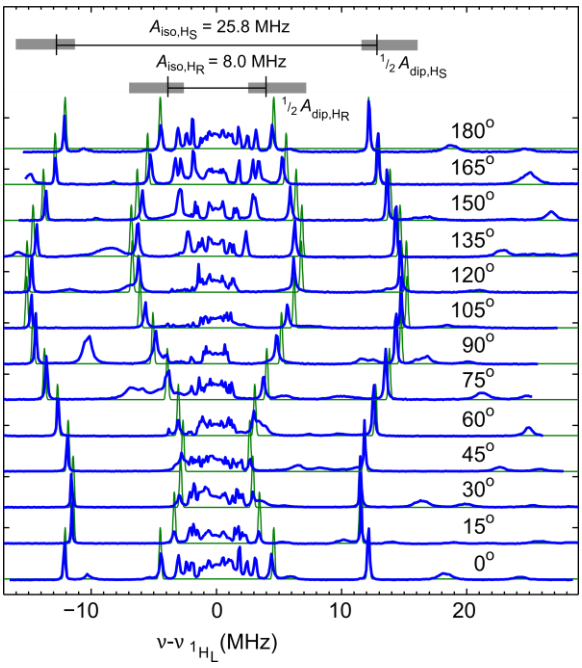

Figure 6.4. Single-crystal ^{1}H ENDOR resolves the hyperfine tensors of the trifluoroethoxide ligand protons H_R and H_S. (Top) The isotropic hyperfine couplings are marked by a black line and the spread of the dipolar hyperfine couplings ($A_{dip} \approx 9$ MHz) is marked by a gray box. Shown in blue are echo-detected Davies ENDOR spectra [π(80 ns) – T – π/2(40 ns) – τ(230 ns) – π(80 ns) – τ – echo] of 1% Cu^{II}-O(TFE) in a Zn^{II}-O(TFE) single-crystal. Spectra were acquired at 34.151 GHz (0°-75°) and 34.143 GHz (90°-180°) (10 K, 3 ms repetition time). A 13 μs RF pulse was applied to excite nuclear transitions and was stepped in 0.1 MHz increments. Spectra were acquired at the g values corresponding to the transitions marked with a dotted line in Figure 6.2C. Simulations are shown in green (parameters in Table A6.1C).

Importantly, the dipolar term depends on the distance between the ^{1}H nucleus and the unpaired spin, which is delocalized in the molecule. We modelled the dipolar hyperfine coupling with a distributed point-dipole approximation assuming the spin population was distributed across the copper, the oxygen of the trifluoroethoxide ligand, and the two basal nitrogen atoms of the Tp^{tBu} ligand. For each proton, H_R and H_S, the total dipolar hyperfine tensor is the sum of four dipolar sub-tensors

$$A_{\mathrm{dip,H}} = \sigma_{\mathrm{Cu}} A_{\mathrm{dip,CuH}} + \sigma_{\mathrm{O}} A_{\mathrm{dip,OH}} + \sigma_{\mathrm{N1}} A_{\mathrm{dip,N1H}} + \sigma_{\mathrm{N2}} A_{\mathrm{dip,N2H}}\,, \qquad \text{Eq. 6.1}$$

where σ_i represents the spin population on atom i. Each sub-tensor was calculated using the point-dipole approximation

$$A_{\mathrm{dip,CuH}} = \frac{\mu_0}{4\pi} \mu_{\mathrm{B}} \mu_{\mathrm{N}} g_{\mathrm{N}} g \frac{1}{r_{\mathrm{CuH}}^3} \left[\left(\frac{3\boldsymbol{r}_{\mathrm{CuH}} \boldsymbol{r}_{\mathrm{CuH}}^{\mathrm{T}}}{r_{\mathrm{CuH}}^2} - \mathrm{I} \right) \right]. \qquad \text{Eq. 6.2}$$

Here μ_B is the Bohr magneton, μ_N is the nuclear magneton, g_N is the nuclear *g* value, I is the 3x3 identity matrix, μ_0 is the vacuum permeability, and *g* is the full 3x3 *g* tensor obtained from fitting the single crystal pulse-field swept spectra. The distance vectors $\boldsymbol{r}_{i\mathrm{H}}$ were taken directly from the coordinates of the X-ray crystal structure.[21] In our simulations, the isotropic hyperfine coupling values ($A_{\mathrm{iso,H_R}}$, $A_{\mathrm{iso,H_S}}$) and the spin populations (σ_{Cu}, σ_O, σ_{N1}, and σ_{N2}) were adjustable parameters.

The proximity of the oxygen atom to the ^{1}H nuclei meant the dipolar contribution to the simulation was affected most significantly by the spin population on oxygen, σ_O. Even after significantly decreasing the spin density on copper (σ_{Cu} = 0.4), values for σ_O any larger than 0.15 produced simulations with too large a dipolar component. However, because the results of ^{14}N ENDOR spectroscopy (in agreement with DFT calculations, see below) place upper bounds of 0.10 on both σ_{N1} and σ_{N2}, it is reasonable to conclude σ_{Cu} is no less than 0.6. With σ_{Cu} = 0.6, values of σ_O any greater than 0.13 produced simulations with too large a dipolar coupling, allowing us to use this as an upper bound for spin population on oxygen in the single crystal.

Specifically, the values σ_{N1} = 0.09 (or 9 %) and σ_{N2} = 0.05 (or 5 %) were chosen based on ^{14}N ENDOR data and are supported by DFT calculations as discussed below. Isotropic couplings, $A_{\mathrm{iso,H_R}}$ = 25.8 MHz and $A_{\mathrm{iso,H_S}}$ = 8 MHz, were used in the simulations and translate to spin populations on the protons of 0.018 (1.8 %) and 0.006 (0.6 %) respectively.[30] The remainder of the spin population (0.836, 83.6 %) was split between oxygen and copper. The simulations in Figure 6.4 used σ_O = 0.10(3) and σ_{Cu} = 0.73(3), or spin populations of 10±3 % and 73±3 %. Using these spin population values for σ_{Cu}, σ_O, σ_{N1}, and σ_{N2}, the principal values of the dipolar coupling were computed as (−3.3, −2.6, 6.3) MHz for H_S and (−2.5, −3.1, 5.5) MHz for H_R using Eq. (1) and (2) (tensor orientations shown in Figure A6.7). The resulting principal values of the hyperfine coupling are (4.7, 5.4, 14) MHz for H_S and (23, 23, 31) MHz for H_R (summarized in Table A6.1C). These values for $A_{\mathrm{iso,H_R}}$, $A_{\mathrm{iso,H_S}}$, σ_{Cu}, σ_O, σ_{N1}, and σ_{N2} also produced satisfactory simulations of ^{1}H ENDOR spectra for a second single crystal (Figure A6.3, Table A6.1C). These data suggest a relatively ionic Cu-O bond with little spin delocalization onto the trifluoroethoxide ligand.

The hyperfine couplings for H_R and H_S are dependent upon the site in the crystal unit cell used for the calculations. The two sites are related by a mirror plane which exchanges the dihedral angles (i.e. Cu-O-C-H_R = −81.06° and Cu-O-C-H_S = 37.43° become Cu-O-C-H_R = −37.43° and Cu-O-C-H_S = 81.06°). This exchanges the values of the hyperfine coupling and spin populations of the two protons.

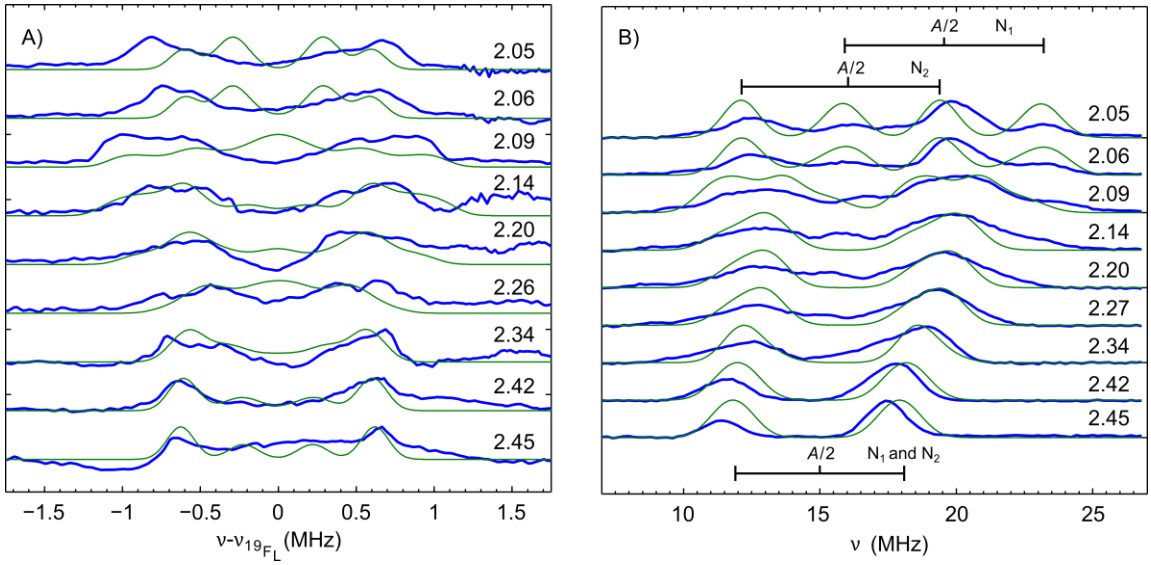

Figure 6.5. ^{19}F and ^{14}N ENDOR spectra of a frozen solution of Cu^{II}-O(TFE)-d_2 (A) and Cu^{II}-O(TFE) (B) in a DCM:toluene glass (10 K, 3 ms repetition time). A) Shown in blue are echo-detected Davies ENDOR spectra [π(100 ns) – T – π/2(50 ns) – τ(240 ns) – π(100 ns) – τ – echo] acquired at 34.068 GHz at the fields corresponding to g values listed in the figure. A 15 µs RF pulse was applied in 0.05 MHz steps. The ^{19}F dipolar hyperfine coupling for simulations (green, parameters in Table A6.1D) were calculated with the distributed point dipole approximation assuming spin populations of σ_O = 0.15 and σ_{Cu} = 0.68. B) Shown in blue are echo-detected Davies ENDOR spectra [π(80 ns) – T – π/2(40 ns) – τ(240 ns) – π(80 ns) – τ – echo] acquired at 34.118 GHz at the fields corresponding to g values listed in the figure. A 14.5 µs RF pulse was applied. The ^{14}N hyperfine couplings for simulations (green, parameters in Table A6.1D) are marked at the A/2 value (nitrogen in the strong coupling regime) for spectra acquired at g = 2.45 (bottom) and g = 2.05 (top). These coupling correspond to spin populations on the basal Tp^{tBu} nitrogen atoms of σ_{N1} = 0.09 and σ_{N2} = 0.05.

^{19}F ENDOR. Higher resolution ENDOR spectra of a frozen solution of Cu^{II}-O(TFE) near the ^{1}H Larmor frequency show a peak pattern that is slightly asymmetric (Figure A6.5). This is due to fluorine peaks centered at the ^{19}F Larmor frequency, which is 2.9 MHz lower than the ^{1}H Larmor frequency at 1160 mT. To separate the fluorine peaks from the proton peaks, the higher frequency half of the ^{1}H ENDOR spectrum, which contains purely proton features, was subtracted from the lower frequency half of the ENDOR spectrum. This yielded the difference spectrum in Figure 6.5A with ^{19}F peaks only. Due to the

three- to four-bond distance between the fluorine nuclei and the majority of the spin density, the isotropic hyperfine coupling was assumed to be negligible. Satisfactory simulations of these data were performed assuming a purely dipolar hyperfine coupling. The dipolar coupling principal values were computed using the distributed point-dipole approximation as described above using distance vectors obtained from crystal coordinates. To achieve the simulations shown in Figure 6.5A, the spin population of oxygen, σ_O, was increased to 0.15(3) and the spin population of copper, σ_{Cu}, decreased to 0.68(3) while the nitrogen spin populations were kept as 0.09 and 0.05. Principal ^{19}F hyperfine values of (−1.1, −1.4, 2.4) MHz, (−0.65, −0.75, 1.4) MHz, and (−1.1, −1.3, 2.2) MHz were calculated (Table A6.1D). Hyperfine tensor frames were defined using the crystal structure coordinates assuming the unique axis A_{zz} points toward the copper nucleus (see Experimental section for details) and are visualized in Figure A6.7. These simulations reproduce the orientation dependence and width of the spectra well, which supports the small σ_O and allows us to place an upper bound of 15±3 % spin population on oxygen when Cu^{II}-O(TFE) is in a frozen solution consistent with the small σ_O observed for the single crystal.

^{14}N ENDOR. Orientation-dependent 34 GHz 14N ENDOR supports the spin delocalization onto the TptBu ligand (Figure 6.5B). At the low-field position (993 mT, g_{zz} = 2.45) where strong orientation selection is expected, the ENDOR spectrum shows only two features at 11.5 MHz and 17.5 MHz. These features are split by twice the Larmor frequency of ^{14}N (3.05 MHz) and centered at ≈ 15 MHz, half the hyperfine coupling, A, for nitrogen in the strong coupling regime. At the highest field edge (g = 2.05), the ^{14}N ENDOR spectrum splits into four lines indicating two nitrogen atoms are responsible for the coupling. Two less intense lines are centered at $A/2$ ≈ 20 MHz and two more intense lines are centered at $A/2$ ≈ 16 MHz (corresponding to axial hyperfine values for $N1_{basal}$ of A_{zz} ≈ 40 MHz, $A_{xx,yy}$ ≈ 30 MHz and for $N2_{basal}$ of A_{zz} ≈ 32 MHz, $A_{xx,yy}$ ≈ 30 MHz).

Observing only two peaks in the ENDOR spectrum collected at g_{zz} = 2.45 indicates that the two nitrogen nuclei contributing to the spectrum have identical hyperfine couplings in the direction of the z_g axis, known to be almost parallel to the long Cu-N_{axial} bond. For nitrogen atoms, we expect an approximately axial tensor, where the axis of the largest principal value (z_A) points toward copper and the majority of

the spin density. In this case, only the two basal nitrogen atoms ($N1_{basal}$ and $N2_{basal}$ in Figure 6.1) will have equivalent hyperfine coupling in the z_g direction and are assigned as the source of these ^{14}N features. Using this definition of the hyperfine tensor frames (details in Experimental section) and the values for *A* listed above in an initial simulation, the hyperfine couplings were adjusted to the final values (29, 29, 41) MHz and (30, 30, 35) MHz for $N1_{basal}$ and $N2_{basal}$, respectively, to achieve the simulation in Figure 6.5B (parameters in Table A6.1D). From the DFT calculations, quadrupole couplings are expected to be small (see Table A6.1E) and were not included in the simulation.

The majority of the ^{14}N hyperfine coupling comes from spin density in the 2s and 2p orbitals of the nitrogen atom of interest. Following Morton and Preston[30], one can calculate 2s orbital spin populations from the isotropic hyperfine couplings A_{iso} = 33 and 32 MHz for $N1_{basal}$ and $N2_{basal}$, respectively. Similarly, one can use the dipolar values of the coupling (A_{zz} = 41 and 35 MHz and $A_{xx,yy}$ = 29 and 30 MHz for $N1_{basal}$ and $N2_{basal}$, respectively) to compute the 2p spin population (details in Appendix Section A6.1.6). The result yields a 2s orbital spin population of 0.02 for each nitrogen and 2p spin populations of 0.07 and 0.03 producing total spin populations of 0.09 (9 %) and 0.05 (5 %) on $N1_{basal}$ and $N2_{basal}$, respectively. Contributions to the ^{14}N hyperfine tensors due to dipolar coupling between nitrogen and spin population on other atoms (Cu, O, other N) were determined to be negligible (< 1 MHz) using the point-dipole approximation. In addition, we observed weak modulations in an ESEEM experiment (see Appendix A6.1.7, Figure A6.8) that are likely due to the axial nitrogen. Since hyperfine coupling and spin population on the axial nitrogen are expected to be weak based on DFT calculations (A_{iso} < 1 MHz), this was not considered in the distributed point dipole approximation.

6.2.3 Electronic spectroscopy

With a combination of room temperature electronic absorption (RT ABS),[21] low temperature electronic absorption (LT ABS), and MCD spectroscopy, we resolved the near-UV and near-IR electronic transitions of Cu^{II}-O(TFE) (Figure 6.6). The RT ABS spectrum (Figure 6.6A) shows an intense near-UV transition at 24000 cm^{-1} (ε > 3000 M^{-1} cm^{-1}) which is not present in the precursor $Tp^{tBu}Cu^{II}(OTf)$.[21] Additional weak near-IR features (ε < 300 M^{-1} cm^{-1}) are seen below 13000 cm^{-1}. In the MCD spectrum (Figure 6.6C), two

transitions underlying the near-UV transition become distinguishable. The near-IR features in the MCD spectrum are resolved into four distinct features which grow in intensity relative to the near-UV features.

Based on the resolution of the MCD spectrum we chose to model our electronic transitions as six Gaussian bands (see dashed lines in Figure 6.6) where each band consists of a peak center (transition energy), width, and integrated intensity. To constrain the simultaneous Gaussian fit of our model, we assumed the energy of the transitions did not change between the RT ABS, LT ABS, and MCD spectra, but allowed the width and integrated intensity of each band to vary freely. The near-IR bands 1-4 of the RT ABS and MCD spectra were simultaneously fit. In the LT ABS spectrum (Figure 6.6B), these features were detected with substantial noise and were not considered in the fit. Separately, the near-UV bands 5-6 of the RT ABS, LT ABS, and MCD spectra were simultaneously fit. Fitting parameters are summarized in Table A6.2. We found λ_{max} at 5200 cm^{-1}, 7050 cm^{-1}, 9400 cm^{-1}, 11800 cm^{-1}, 23200 cm^{-1}, and 26100 cm^{-1} for bands 1-6, respectively. Significant figures in the near-IR region are based on a less than 100 cm^{-1} measurement step size below 12500 cm^{-1} and a less than 50 cm^{-1} step size below 8000 cm^{-1}. Significant figures in the near-UV region are based on a less than 200 cm^{-1} measurement step size.

Several factors allow assignment of bands 1-4 as d → d in character and bands 5-6 as trifluoroethoxide to copper charge transfer (CT) in character. First, bands 1-4 in the RT ABS are low intensity (ε < 300 M^{-1} cm^{-1}) compared to bands 5-6. In transition metal complexes with incompletely filled d orbitals, low intensity features are usually the electric dipole forbidden d → d transitions. In contrast, the high intensity bands 5-6 are likely electric dipole allowed transitions such as from a ligand p orbital to a copper d orbital. Next, the relative intensities of the features in the RT ABS and MCD spectra suggest the near-IR transitions are predominantly d → d in character.[31,32] As shown in Figure A6.9, the intensity of all transitions in the MCD spectrum are temperature dependent indicating they are all C-term features. In low-symmetry sites, where all the electronic states are expected to be non-degenerate, C-term intensity is driven by spin-orbit coupling. The spin-orbit coupling is larger for copper than the ligand atoms (ξ_{Cu} = 830 cm^{-1}, $\xi_{O,N}$ ≈ 150, 76 cm^{-1} for the free ions).[29] The magnitudes of intensities of copper-based d → d

transitions are expected to increase relative to CT transitions when going from the RT ABS to the MCD spectrum. The ratio C_0/D_0 is commonly used to make this comparison between the C-term intensity (MCD), C_0, and the dipole transition strength (RT ABS), D_0, for each band.[33–35] Here, we use peak intensity maxima from the Gaussian fits to approximate C_0/D_0 ratios as MCD/ RT ABS ratios for bands 1-6. The MCD/ RT ABS ratios are larger in magnitude for bands 1-4 (MCD/ RT ABS = $0.076 \cdot 10^{-3}$, $0.16 \cdot 10^{-3}$, $-0.053 \cdot 10^{-3}$, and $-0.12 \cdot 10^{-3}$ respectively) compared to bands 5-6 (MCD/ RT ABS = $-0.009 \cdot 10^{-3}$ and $-0.02 \cdot 10^{-3}$ respectively) which supports the assignment of the low energy peaks as transitions within the d manifold.

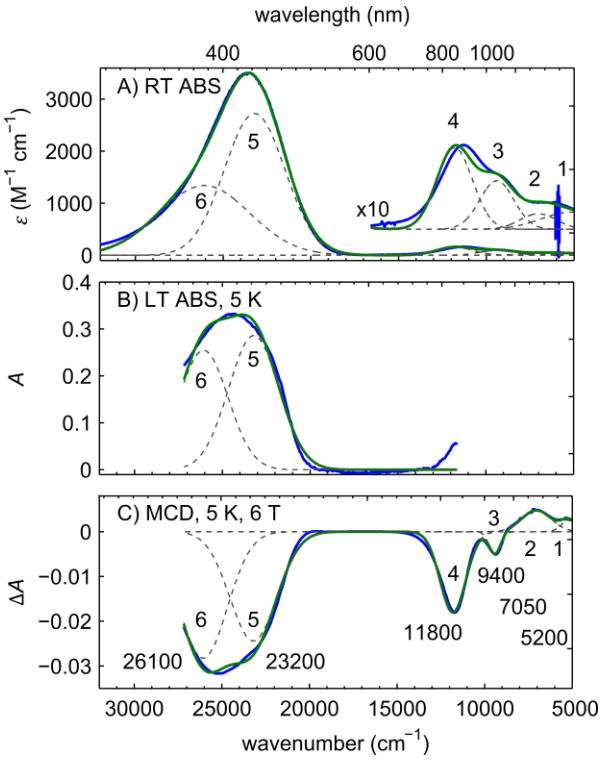

Figure 6.6. Optical spectra resolving six transitions in the near-IR and near-UV; bands 1-4 are copper based d → $d_{x^2-y^2}$ transitions, bands 5-6 are O(TFE) → Cu $d_{x^2-y^2}$ transitions. A) Room temperature UV-Vis and near-IR absorption spectrum of Cu^{II}-O(TFE) in DCM (from ref. 21). B) Electronic absorption of a thin film of Cu^{II}-O(TFE) collected simultaneously with MCD spectrum at 5 K and 0 T. C) MCD spectrum of a thin film of Cu^{II}-O(TFE) acquired at 5 K and 6 T. Individual fitted Gaussian resolved bands are shown as dashed gray lines, the total fit in green, and experimental data in blue. The λ_{max} of transitions 1-6 are labeled in the MCD spectrum.

Finally, the presence of the CT transition in Cu^{II}-O(TFE) but not in the precursor $Tp^{tBu}Cu^{II}(OTf)$ suggests the trifluoroethoxide ligand as the donor primarily responsible for bands 5-6 and the red color of Cu^{II}-O(TFE). Bands 5 and 6 are rationalized as transitions from two lone-pair orbitals O(TFE) p_{π} and O(TFE) $p_{\sim\sigma}$, named for their π and σ bonding orientation relative to the Cu-O bond, respectively. The σ bond to copper is expected to be stabilized in energy relative to the π bond to copper, making O(TFE) $p_{\sim\sigma} \rightarrow$ Cu $d_{x^2-y^2}$ the higher energy transition, band 6. Additionally, we calculate the experimental oscillator strength $f_{\exp} = 4.61 \times 10^{-9} \epsilon_{\max} \nu_{1/2}$ from the RT ABS maximum $\epsilon_{\max}$ and the full width at half maximum $\nu_{1/2}$ using the Gaussian fit parameters for bands 5-6 in Table A6.2. The oscillator strength of these transitions roughly correlates with the overlap of the donor orbitals (O(TFE) p_{π} and O(TFE) $p_{\sim\sigma}$) and acceptor orbital Cu $d_{x^2-y^2}$in the charge transfer transition and is used in the discussion section below.[36]

Bands 1-4 are due to transitions from the four fully occupied copper-based d orbitals to the singly occupied copper based $d_{x^2-y^2}$ orbital. We can assign the identity of each transition based on the literature assignments for Cu^{II} compounds in distorted tetrahedral environments. From lowest to highest energy (bands 1-4) the assignments are usually $d_{z^2} \rightarrow d_{x^2-y^2}$, $d_{xy} \rightarrow d_{x^2-y^2}$, $d_{yz+xz} \rightarrow d_{x^2-y^2}$, and $d_{yz-xz} \rightarrow d_{x^2-y^2}$.[33–35,37] The transitions have a +, +, −, − sign pattern in the MCD spectrum (Figure 6.6C). However, typically these transitions for Cu^{II} compounds in distorted tetrahedral ligand fields show a +, −, +, − sign pattern.

It is possible to fit the MCD spectrum with five Gaussian bands resulting in λ_{max} at 5100, 7100, 9500, 10500, and 11500 cm^{-1} and the sign pattern +, +, −, +, − (Figure A6.11, Table A6.3). In this case the transitions are assigned as $d_{z^2} \rightarrow d_{x^2-y^2}$, N(Pz) $\rightarrow d_{x^2-y^2}$, $d_{xy} \rightarrow d_{x^2-y^2}$, $d_{yz+xz} \rightarrow d_{x^2-y^2}$, and $d_{yz-xz} \rightarrow d_{x^2-y^2}$ with the sign pattern for the ligand field transitions consistent with the literature. The N(Pz) $\rightarrow d_{x^2-y^2}$ transition has been observed before in a similar Cu^{II}-thiolate complex.[33] However, we would expect a dipole allowed N(Pz) $\rightarrow d_{x^2-y^2}$ CT transition to have increased intensity in the RT ABS, which is not observed for Cu^{II}-O(TFE). The discrepancy in the signs of the MCD transitions compared to previous

literature leaves the assignment of the ligand field transitions somewhat ambiguous. The implications of this for the electronic structure analysis are discussed below.

6.2.4 Resonance Raman

To further support the assignment of the LMCT transition, we performed resonance Raman (rR) spectroscopy on Cu^{II}-O(TFE) and the isotopically labeled Cu^{II}-O(TFE)-d_2 (deuteration only on the trifluoroethoxide ligand). Spectra were recorded with an incident wavelength of 426 nm (23474 cm^{-1}). In Cu^{II}-O(TFE), three low-energy peaks at 524, 592, and 690 cm^{-1} and two high energy peaks at 1139 and 1274 cm^{-1} were observed (Figure 6.7A, Table A6.4A). In Cu^{II}-O(TFE)-d_2, the three low energy peaks downshifted to 521, 567, and 678 cm^{-1}, and two high energy peaks at 1008 and 1154 cm^{-1} were observed. In both Cu^{II}-O(TFE) and Cu^{II}-O(TFE)-d_2 low intensity features are also observed at very low energies < 400 cm^{-1} and are not affected by deuteration of O(TFE). The most intense features in the rR spectrum are all affected by deuteration of O(TFE), supporting assignment of the electronic transition at 23200 cm^{-1} as an O(TFE) → Cu $d_{x^2-y^2}$ CT. As such we expect the observed frequencies to correspond to normal modes involving displacement of copper and the trifluoroethoxide ligand.

First, we will assign the three low-energy features from 500 to 700 cm^{-1}. These likely involve the heaviest atoms which indicates that these bands are ν(Cu-O) in character. The peak at 592 cm^{-1} is the most intense indicating it has the most ν(Cu-O) stretch character of the three since these two atoms are involved in the CT. It is also substantially shifted by deuteration (−25 cm^{-1}) indicating movement of the oxygen atom may drag along the Cα-H2 group. The lowest-frequency and least intense peak at 524 cm−1 is also least effected by deuteration, shifting only −3 cm^{-1}. It likely has substantial movement of the heaviest fluorine atoms, furthest from the Cu-O bond, indicating distortions of C_β-F_3. The peak at 690 cm^{-1} involves an intermediate amount of ν(Cu-O) character. However, it is also substantially shifted by deuteration (−12 cm^{-1}), indicating movement of the C_α-H_2 group. The peak at 592 cm^{-1} with the most ν(Cu-O) stretch character constitutes one of the few known Cu^{II}-alkoxide stretch frequencies.

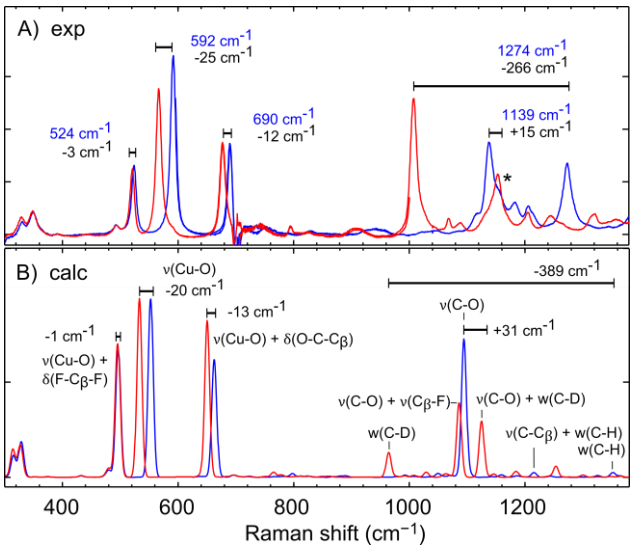

Figure 6.7. A) Room temperature resonance Raman spectra of Cu^{II}-O(TFE) (blue) and Cu^{II}-O(TFE)-d_2 (red) in DCM with an incident wavelength of 426 nm, exciting the O(TFE) → Cu $d_{x^2-y^2}$ transition. Vibrational frequencies of Cu^{II}-O(TFE) are labeled in blue and the shifts upon isotopic labeling are listed in black. The peak in Cu^{II}-O(TFE)-d_2 that lies under a DCM solvent peak is labeled with a star. B) Calculated resonance Raman spectra of the optimized structure of Cu^{II}-O(TFE) (blue) and Cu^{II}-O(TFE)-d_2 (red). The dominant motions associated with each normal mode are labeled. Shifts upon isotopic labeling are listed for normal modes that closely correspond in Cu^{II}-O(TFE) and Cu^{II}-O(TFE)-d_2.

In support of our interpretation, we note Cu^{II} proteins and small molecule complexes in similar distorted tetrahedral environments exhibit similarly complicated Cu-ligand stretching patterns. Plastocyanin, a type 1 blue copper protein, has multiple Cu-S stretching frequencies between 350 and 500 cm^{-1}.[38–40] The five-coordinate thiolate-bound green and red copper sites in nitrite reductase, nitrosocyanin, and BSco exhibit multiple Cu-S frequencies between 340-450 cm^{-1}, 300-350 cm^{-1}, and 310-380 cm^{-1} respectively.[26,28,41] Small molecules with similar pyrazolyl ligand scaffolds typically exhibit slightly simpler resonance Raman patterns. A type 1 blue copper mimetic molecule (HB(3,5-iPr$_2$pz)$_3$)Cu-SC(CH$_3$)$_3$ exhibits three frequencies at 348, 400, and 437 cm^{-1} assigned as δ(C-C-S), δ(C-C-C), and ν(Cu-S), respectively.[42] A Cu^{II}-alkylperoxo complex ((HB(3,5-iPr$_2$pz)$_3$)Cu-OOCMe$_2$Ph) exhibits a similar pattern with Raman shift frequencies at 536, 551, and 645 cm^{-1} assigned as δ(C-C-O), δ(C-C-C), and ν(Cu-O), respectively.[34]

Next, we will assign the features in the high-energy region above 1000 cm^{-1}, where we expect normal modes based on the O(TFE) ligand with little movement of the heavy copper atom. We suggest two interpretations of the data in this region. First, the peaks at 1139 cm^{-1} and 1274 cm^{-1} for Cu^{II}-O(TFE) can

be assigned as dominantly ν(C-O) and w(C-H), respectively, based on the expected frequencies of these modes from IR and Raman spectroscopy (≈ 1090 cm^{-1} for ν(C-O) and 1140-1400 cm^{-1} for w(C-H)).[43] In Cu^{II}-O(TFE)-d_2, a w(C-D) is expected to appear at much lower frequency and is assigned as the peak at 1008 cm^{-1}. Deuteration of the αC-H is expected to slightly raise ν(C-O) (see calculations). We tentatively assign the low intensity peak at 1154 cm^{-1} to ν(C-O); however, a DCM solvent peak appears at this frequency, which obscures the assignment.

In a second possible interpretation, the high-energy peaks in Cu^{II}-O(TFE) may be assigned as a Fermi resonance between a w(C-H) mode and the first overtone of the peak at 592 cm^{-1} (expected to appear at 1184 cm^{-1}). The Fermi resonance red shifts the overtone peak by −45 cm^{-1} so it appears at 1139 cm^{-1}. An equivalent blue shift of the w(C-H) up to 1274 cm^{-1} means the true w(C-H) is expected to appear at ≈1229 cm^{-1}. In Cu^{II}-O(TFE)-d_2, a significant red shift of the w(C-D) would inactivate the Fermi resonance coupling and lead to one w(C-D) at 1008 cm^{-1} with double the intensity of the peaks in Cu^{II}-O(TFE). DFT calculations (see below) support the first interpretation presented, but due to the solvent background, assignments remain uncertain.

Overall, our rR data confirm the assignment of the LMCT as predominantly O(TFE) $p_\pi \rightarrow$ Cu $d_{x^2-y^2}$ in character. The main ν(Cu-O) stretch at 592 cm^{-1} indicates that the Cu-O bond is softer than in a comparable Cu-peroxo compound with ν(Cu-O) of 645 cm^{-1}.

6.2.5 Quantum Chemistry

To support our analysis, we performed DFT and TDDFT calculations. An all-atom geometry optimization of Cu^{II}-O(TFE) was initiated from the geometry determined by X-ray crystallography.[21] The atomic coordinates and most relevant structural features are compared in the supporting information (Section 5b, Figure A6.14). Between the crystal structure and the optimized geometry, the long Cu-N_{axial} bond (2.2270(11) vs. 2.26 (Å)), the Cu-O bond length (1.8324(10) vs. 1.87 (Å)), and the large Cu-O-C angle (135.48(9)° vs. 134°) were maintained, respectively. The optimized geometry was used in all further calculations.

EPR property calculations support the interpretation of the experimental EPR data. Calculated Mulliken spin populations of ≈ 8 % on each of the two basal nitrogen atoms agree with the experimental spin populations derived from ^{14}N ENDOR ($\sigma_{N1,N2}$ ≈ 9 %, 5 %). The hyperfine coupling values of the basal nitrogen atoms are in reasonable agreement with the values determined from simulation of the ^{14}N ENDOR (compare Table A6.1D and A6.1E). However, the calculation predicts about 60 % spin population on copper and 20 % spin population on the trifluoroethoxide oxygen, which is larger than the experimental upper bound for σ_O of ≈ 15 %. Also, DFT predicts hyperfine couplings for the trifluoroethoxide protons that are larger than observed. Overall, this suggests DFT over-delocalizes the spin density and overestimates the radical character on the trifluoroethoxide ligand. The DFT-predicted copper hyperfine coupling and g values are in poor agreement with experiment. Correct modeling of the electron correlation and the covalency of Cu^{II}-ligand bonds is essential for accurate *g* shift predictions. Multiple approaches have been used to improve EPR property calculations in related systems, although these were not pursued here.[44,45]

DFT calculations support the assignment of the experimental rR shifts. Calculations were performed on Cu^{II}-O(TFE) and Cu^{II}-O(TFE)-d_2. Calculation of resonant enhancement of vibrational modes predicts three vibrations enhanced between 400 and 700 cm^{-1} (Figure 6.7B, Table A6.4A). Dominantly, the modes are ν(Cu-O) + δ(F-Cβ-F), ν(Cu-O), and ν(Cu-O) + δ(O-C-Cβ) at 497, 553, and 663 cm^{-1}. In Cu^{II}-O(TFE)-d_2, three peaks with nearly identical normal modes are down shifted by −1, −20, and −13 cm^{-1}, respectively. This is in reasonable agreement with the experimental isotopic shifts of −3, −25, and −12 cm^{-1} allowing more definitive assignment of the rough experimental mode assignments described above.

To higher energy, the rR calculation for Cu^{II}-O(TFE) predicts enhancement of a nearly pure ν(C-O) at 1094 cm^{-1}. The calculation for Cu^{II}-O(TFE)-d_2 predicts enhancement of two vibrational modes involving ν(C-O); ν(C-O) + ν(Cβ-F) at 1086 cm^{-1} and ν(C-O) + w(C-D) at 1125 cm^{-1}. The latter is isotopically shifted +31 cm^{-1} from the calculated ν(C-O) for Cu^{II}-O(TFE). This is in reasonable agreement with the experimental isotopic shift of +15 cm^{-1} for the features at 1139 cm^{-1} and 1154 cm^{-1} in Cu^{II}-O(TFE) and Cu^{II}-O(TFE)-d_2, respectively.

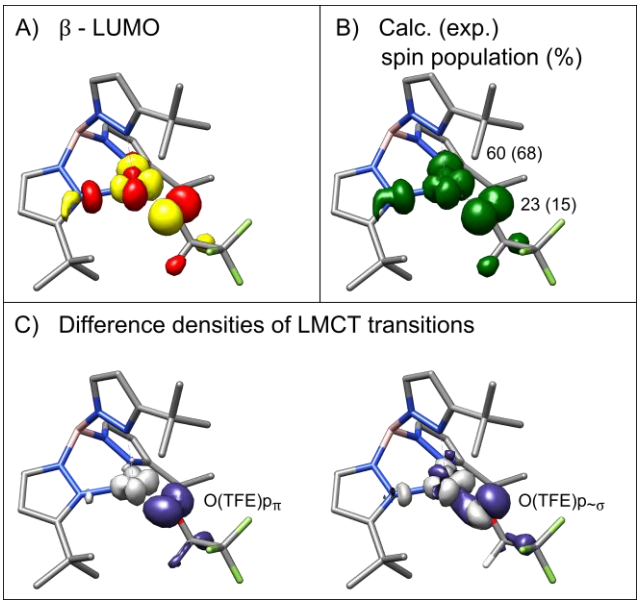

Figure 6.8. DFT-predicted electronic structure. A) Ground state β-LUMO isosurface contoured at ±0.05 $a_0^{-3/2}$. B) The spin population isosurface contoured at ±0.0025 a_0^{-3}. The calculation (UKS/B3LYP/EPR-II) predicts 60 % spin population on copper and 23 % spin population on oxygen in contrast to the experimentally determined spin populations of ≥ 68 % and ≤ 15 %, respectively. C) The isosurfaces of the difference density of the O(TFE) $p_\pi \rightarrow$ Cu $d_{x^2-y^2}$ transition and the O(TFE) $p_{\sim\sigma} \rightarrow$ Cu $d_{x^2-y^2}$ transition contoured at ±0.005 $a_0^{-3/2}$. Purple represents the donor state and gray the acceptor state. The transitions demonstrate the π and σ interactions, respectively, in the Cu-O bond. Note that C) is for illustrative purposes only, as the TDDFT calculation incorrectly predicted the relative order in energy of the two transitions (details in Appendix).

The experimental feature we assign as w(C-H) at 1274 cm^{-1} in Cu^{II}-O(TFE) is not enhanced in the calculation. A numerical Raman calculation for Cu^{II}-O(TFE) (Appendix A6.3.3) predicts that a ν(C-Cβ) + w(C-H) mode at 1217 cm^{-1} and a w(C-H) mode at 1359 cm^{-1} will have Raman activity (appearing unenhanced at 1215 and 1353 cm^{-1} in the analytical rR calculation). However, the calculation for Cu^{II}-O(TFE)-d_2 does predict enhancement of the w(C-D) mode at 964 cm^{-1}, isotopically shifted by −251 cm^{-1} and −389 cm^{-1} from the ν(C-Cβ) + w(C-H) and w(C-H) in Cu^{II}-O(TFE), respectively. The former is in closer agreement with the experimental isotopic shift of −266 cm^{-1} from 1274 to 1008 cm^{-1}. Given this similar isotopic red shift between calculation and experiment, these experimental modes likely involve a w(C-H) and w(C-D), respectively.

Figure 6.8 shows a selection of DFT-calculated molecular orbitals, spin populations and transition difference densities. The β-LUMO (Figure 6.8A) and the spin density distribution (Figure 6.8B) support our selection of nuclei used in the distributed point-dipole approximation. As will be discussed below, the calculated β-LUMO also supports the orientation of the $d_{x^2-y^2}$ orbital such that the lobes are nearly bisected by the Cu-O(TFE) bond. In Figure 6.8C, the TDDFT-predicted transition difference densities are shown for two O(TFE) p $\rightarrow$ Cu $d_{x^2-y^2}$ transitions that make up the intense near-UV absorption band. The calculation incorrectly predicted the energy order of these two transitions so the images are used only to illustrate the orientation of the O(TFE) p orbitals as discussed below (TDDFT discussion in Appendix A6.5.1).

6.3 Discussion

With our spectroscopic results, we characterized the electronic structure of this Cu^{II}-alkoxide complex. Below we examine the ligand field equations for a d^9 transition metal in a $d_{x^2-y^2}$ ground state to ascertain the physical origin of the unique EPR parameters. To understand the spectroscopic features engendered by the trifluoroethoxide ligand, we will compare the Cu^{II}-alkoxide to well-characterized small molecule Cu^{II}-thiolate (Cu^{II}-SR) and Cu^{II}-alkylperoxo (Cu^{II}-OOR) complexes in nearly identical geometries (see Table A6.5 for structural comparison).[46,47] These complexes exhibit similar EPR spectra, in particular the small $^{Cu}A_{zz}$ hyperfine coupling. However, in contrast to the near-UV LMCT transition of Cu^{II}-O(TFE), the LMCT transitions (from thiolate and alkylperoxo ligand donors) in both of these complexes are in the near-IR region, which imparts a blue color to the compounds (see Tables 6.1 and A6.6 for spectroscopic comparison).[33,34,42] We will also compare the Cu^{II}-O(TFE) to the biological type 1 blue copper sites, type 2 red copper sites, and galactose oxidase (GAO). Finally, we will address the implications of the electronic structure of the Cu^{II}-alkoxide on alcohol oxidation.

6.3.1 Comparison of Cu^{II}-O(TFE), Cu^{II}-OOR, and Cu^{II}-SR

Large g_{zz} and NIR MCD transitions. The origins of the unusually large g_{zz} in Cu^{II}-O(TFE) can be rationalized via a ligand field theory argument for a d^9 transition metal in the $d_{x^2-y^2}$ ground state.[29] Assuming the simplified case of an axial g tensor, the $g_{zz} = g_{\parallel}$ value can be approximated as

$$\Delta g_{\parallel} = g_{\parallel} - g_{\mathrm{e}} = 8\zeta_{\mathrm{Cu}} \frac{\alpha^2_{x^2-y^2}\alpha^2_{xy}}{E_{x^2-y^2} - E_{xy}} = \frac{C}{\Delta E_{\perp}}. \qquad \text{Eq. 6.3}$$

Here ζ_{Cu} is the one-electron spin-orbit coupling constant (830 cm^{-1} for the free Cu^{II} ion). The coefficients $\alpha_{x^2-y^2}$ and α_{xy} quantify the $d_{x^2-y^2}$ and d_{xy} character of the ground state and excited state, respectively. Larger α indicates increased d orbital character. $\Delta E_{\perp} = E_{x^2-y^2} - E_{xy}$ is the transition energy for promoting one electron from the doubly occupied d_{xy} Cu-based molecular orbital (MO) to the $d_{x^2-y^2}$ Cu-based singly occupied MO (SOMO).

$\Delta E_{\perp}$ can be estimated from Eq. 6.3 by comparison to the alkylperoxo complex, Cu^{II}-OOR, using

$$\Delta E_{\perp,\mathrm{CuOR}} = \Delta E_{\perp \mathrm{CuOOR}} \frac{C_{\mathrm{CuOR}}}{C_{\mathrm{CuOOR}}} \frac{\Delta g_{\parallel,\mathrm{CuOOR}}}{\Delta g_{\parallel,\mathrm{CuOR}}} \qquad \text{Eq. 6.4}$$

with $\Delta g_{\parallel,\mathrm{CuOOR}}$ = 0.316 and $\Delta E_{\perp,\mathrm{CuOOR}}$ = 8050 cm^{-1} (Table 6.1)[34] and $\Delta g_{\parallel,\mathrm{CuOR}}$ = 0.437. As ground-state DFT (B3LYP) predicts more spin population on copper in Cu^{II}-O(TFE) (60 %) versus Cu^{II}-OOR (52 %),[34] we expect increased copper character in the ground state and necessarily larger $\alpha_{x^2-y^2}$ in the Cu^{II}-alkoxide, and therefore $C_{\mathrm{CuOR}}/C_{\mathrm{CuOOR}} > 1$. With this, Eq. 6.4 yields $\Delta E_{\perp,\mathrm{CuOR}} > 5821$ cm^{-1}, and we can assign the peak at 7050 cm^{-1} (band 2 in Figure 6.6C) to the $d_{xy} \rightarrow d_{x^2-y^2}$ transition. We assign the other three transitions in the near-IR region based on the expected energy order of the d orbitals in a distorted tetrahedral environment. Namely, we support the four-Gaussian model described in the Results section and assign band 1 (5200 cm^{-1}) to $d_{z^2} \rightarrow d_{x^2-y^2}$, band 3 (9400 cm^{-1}) to $d_{yz/xz} \rightarrow d_{x^2-y^2}$, and band 4 (11800 cm^{-1}) to $d_{yz/xz} \rightarrow d_{x^2-y^2}$. As noted above, the signs of the MCD transitions differ from expectations based on the literature, but predicting signs can be challenging.[31,32] The small transition energy $E_{x^2-y^2} - E_{xy}$ is the principal reason for the large g_{zz}.

Table 6.1. Spectroscopic comparison of Cu^{II}-alkoxide, Cu^{II}-alkylperoxo,[34] and Cu^{II}-thiolate[33]

	g_{zz} ($\approx g_{\parallel}$)	$E_{x^2-y^2} - E_{xy}$ (cm^{-1})	spin population (%) [a]	$\lvert {}^{Cu}A_{zz}\rvert$ ($\times 10^4$ cm^{-1})	$f_{\sim\sigma,exp}/f_{\pi,exp}$ (CT donor → Cu $d_{x^2-y^2}$)
Cu-O(TFE)	2.45	7050	68[b] (60)	40	0.735
Cu-OOR[34]	2.316	8050	62[c] (52)	55	0.161
Cu-SR[33]	2.21	9250	36[d] (34)	72	0.003

[a] In parentheses are results from a DFT/B3LYP calculations for Cu-OR, Cu-OOR, and Cu-SR using the Mulliken spin population, spin density and copper character in the ground state, respectively.
[b] Experimental from distributed point dipole approximation using hyperfine coupling of remote nuclei.
[c] Experimental from EPR g values and INDO/S-CI calculations.
[d] Experimental from Cu-L edge XAS results.

Small ${}^{Cu}A_{zz}$. The hyperfine coupling can be derived from ligand field theory assuming a simplified axial hyperfine tensor with ${}^{Cu}A_{zz} = A_{\parallel}$ where

$$A_{\parallel} = P_{\mathrm{d}}\left[-\kappa\alpha^2_{x^2-y^2} - \frac{4}{7}\alpha^2_{x^2-y^2} + \frac{3}{7}(g_{\perp} - g_{\mathrm{e}}) + (g_{\parallel} - g_{\mathrm{e}})\right]. \qquad \text{Eq. 6.5}$$

P_{d} is a quasiatomic parameter that depends on the nucleus and is typically given the value ≈ 400·10–4 cm^{-1} for copper. κ is a unitless parameter which represents the isotropic hyperfine coupling of the copper nucleus with a typical upper bound value of 0.43.[29]

The difference in sign of terms one and two compared to terms three and four in Eq. 6.5 means a small $A_{\parallel}$ can be a result of cancellation of terms. Noting that $g_{\perp}$ ≈ 2.09 in both Cu^{II}-O(TFE) and Cu^{II}-OOR, one can simplify Eq. 6.5 to $A_{\parallel} = P_{\mathrm{d}}(-C + \Delta g_{\parallel})$ and estimate a parameter C_{CuOOR} for Cu^{II}-OOR from the literature $\Delta g_{\parallel}$ value (Table 6.1). Using $C_{CuOR} \approx C_{CuOOR}$, this predicts copper hyperfine coupling for Cu^{II}-O(TFE) of $A_{\parallel,\mathrm{CuOR}} \approx P_{\mathrm{d}}\left(-C_{\mathrm{CuOOR}} + \Delta g_{\parallel,\mathrm{CuOR}}\right) \approx 80{\cdot}10^{-4}$ cm^{-1}, close to the experimental value of $40{\cdot}10^{-4}$ cm^{-1}. This again implies $C_{\mathrm{CuOR}}/C_{\mathrm{CuOOR}} > 1$, which indicates larger $\alpha_{x^2-y^2}$ and increased copper character in the ground state of the alkoxide complex. This analysis depends on the sign of the hyperfine coupling being the same in both cases (here assumed positive). The small ${}^{Cu}A_{zz}$ is a result of the large g_{zz} value (term 4 in Eq. 6.5, driven by the small transition energy $E_{x^2-y^2} - E_{xy}$) and the large spin population on copper (terms 1 and 2 in Eq. 6.5, driven by $\sigma_{Cu} \geq 68$ %) canceling terms in Eq. 6.5.

Nature of the Cu-O(TFE) bond. From single crystal EPR, we found the LMCT acceptor orbital ($d_{x^2-y^2}$) is oriented such that the lobes are in a plane approximately perpendicular to the Cu-N_{axial} bond. From resonance Raman and MCD spectroscopies, we know that the LMCT transition in the room temperature absorption spectrum has two components at 26100 and 23200 cm^{-1} originating from the donor O(TFE) $p_{\sim\sigma}$ and O(TFE) p_π orbitals, respectively. The orientations of the pseudo- σ and π p orbitals relative to the Cu-O bond are illustrated by the transition difference densities in Figure 6.8C.

In the thiolate- and alkylperoxo-ligated Cu^{II} complexes, the LMCT transition is similarly comprised of two transitions from p orbitals. These are termed p_π and $p_{\sim\sigma}$ in Cu^{II}-SR and π^*_v and π^*_σ in Cu^{II}-OOR due to their orientation with respect to the Cu-X(CT donor) bond.[33,34] The transition from the donor orbital with π orientation appears to lower energy and in both cases has a larger experimental oscillator strength than the transition from the donor orbital with σ orientation (see Table A6.6).[33,34] The larger intensity of the π transition relative to the pseudo-σ transition is rationalized as a rotation of the $d_{x^2-y^2}$ acceptor orbital so that its lobes are bisected by the Cu-X bond. This allows for excellent overlap of the LMCT donor orbital with π orientation with the copper $d_{x^2-y^2}$ acceptor orbital.

Similarly, in Cu^{II}-O(TFE), the oscillator strength of the lower-energy O(TFE) $p_\pi \rightarrow$ Cu $d_{x^2-y^2}$ transition is larger ($f_{\pi,exp}$ = 0.051) than for the O(TFE) $p_{\sim\sigma} \rightarrow$ Cu $d_{x^2-y^2}$ transition ($f_{\sim\sigma,exp}$ = 0.038). This is evidence that the $d_{x^2-y^2}$orbital lies such that its lobes are bisected by the Cu-O bond (Figure 6.8A) and indicates a dominantly π bonding interaction. However, the ratios of the oscillator strengths $f_{\sim\sigma,exp}/f_{\pi,exp}$ for Cu^{II}-SR, Cu^{II}-OOR, and Cu^{II}-OR (0.003 < 0.161 < 0.735, respectively, Table 6.1) show an increase in the relative overlap of the $p_{\sim\sigma}$ donor compared to the pπ donor with the Cu $d_{x^2-y^2}$ acceptor. This ratio trend is due predominantly to a larger oscillator strength for the $p_{\sim\sigma} \rightarrow$ Cu $d_{x^2-y^2}$ transition in Cu^{II}-O(TFE) (see Table A6.6).

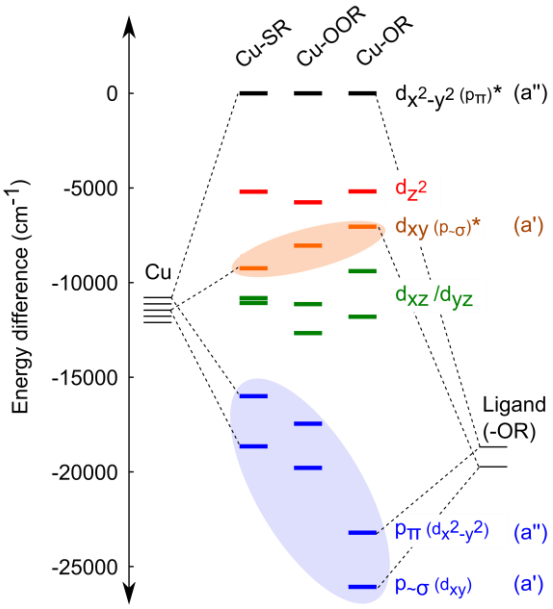

Figure 6.9. An MO diagram based on experimentally determined transition energies for thiolate (Cu-SR), peroxo (Cu-OOR), and alkoxide (Cu-OR) ligated Cu^{II} complexes. Highlighted orbitals indicate major affectors of spectroscopic trends: 1) in orange, an increase in σ character of the Cu-OR bond drives the energy of the dominantly Cu d_{xy} orbital closer to the dominantly Cu $d_{x^2-y^2}$ orbital; this small difference in energy results in a larger shift in g_{zz}, 2) in blue, p orbital donors from the trifluoroethoxide ligand have a large ionization energy resulting in a near-UV LMCT that gives Cu^{II}-O(TFE) its red color; in Cu-SR and Cu-OOR, these donor orbitals are higher in energy (discussed in the text) resulting in the blue color. The singly occupied Cu $d_{x^2-y^2}$ orbitals were set to zero and the vertical placement of each donor orbital reflects its experimental transition energy (data from ref. 33, 34 and this work). The ligand and copper orbital energies before bonding are illustrative only. Orbital symmetry is indicated for the C_s point group.

The increase in relative intensity of the O(TFE) $p_{\sim\sigma}$ → Cu $d_{x^2-y^2}$ transition in Cu^{II}-O(TFE) may indicate increased σ bonding character compared to the Cu^{II}-alkylperoxo and Cu^{II}-thiolate. In a molecular orbital approach, we expect a bonding and antibonding combination of MOs to form between O(TFE) $p_{\sim\sigma}$ and d_{xy}, where the bonding orbital is dominantly O(TFE) $p_{\sim\sigma}$ and the antibonding is dominantly d_{xy}. The π bond results in an analogous set of bonding and antibonding MOs formed between O(TFE) p_{π} and $d_{x^2-y^2}$ (see Figure 6.9). The bonding MO formed by the O(TFE) $p_{\sim\sigma}$ /d_{xy} interaction will have increased metal character as the σ bonding interaction becomes stronger. An increase in metal character of the O(TFE) $p_{\sim\sigma}$ donor orbital will increase overlap with the acceptor $d_{x^2-y^2}$ orbital and result in the large integrated area of the O(TFE) $p_{\sim\sigma}$ → Cu $d_{x^2-y^2}$ transition that we observed in this work.

An increase in the σ bonding interaction would also raise the energy of the d_{xy} antibonding orbital closer to the $d_{x^2-y^2}$ antibonding orbital, as illustrated in Figure 6.9. This is consistent with the small transition energy $E_{x^2-y^2} - E_{xy}$ that drives the large shift in g_{zz} for Cu^{II}-O(TFE) (relative to g_{zz} = 2.21 and 2.316 for Cu^{II}-SR and Cu^{II}-OOR, respectively).

Origin of near-UV charge transfer. The red color (LMCT at 420 nm, 23800 cm^{-1}) of the Cu^{II}-alkoxide is notably different from the blue color of Cu^{II}-alkylperoxo and Cu^{II}-thiolate complexes (LMCT at 600 nm, 16600 cm^{-1}). This is a consequence of the nature of the trifluoroethoxide CT donor. The increased transition energy for an alkoxide donor is expected based on the increase in ionization energy for an alcohol compared to a alkylperoxide or thiol (10.48 > 9.36 > 9.31 eV for ethanol, n-butylperoxide, and ethanethiol, respectively).[48] The increased ionization energy for alcohols compared to peroxides comes in part from the nature of the molecular orbitals formed between the O-Cα bond in an alkoxide versus the O-O bond in a peroxide. The highest occupied MOs in an alkoxide are oxygen non-bonding orbitals, whereas in an alkylperoxo, they are destabilized π* antibonding orbitals.[34] In addition, the trifluoromethyl group is strongly electron withdrawing, further increasing the ionization energy of the trifluoroethoxide ligand (11.49 eV for trifluoroethanol) compared to a non-halogenated alcohol.[49]

6.3.2 Comparison with copper sites in biology.

Cu^{II}-O(TFE) shares a small hyperfine coupling $^{Cu}A_{zz}$ with some members of the family of type 1 blue copper proteins. The type 1 blue copper site in plastocyanin (extensively reviewed by Solomon[25]) is a distorted tetrahedral Cu^{II} site in a $d_{x^2-y^2}$ ground state, which leads to an axial EPR spectrum. Plastocyanin is often described as possessing a uniquely small $^{Cu}A_{zz}$ hyperfine coupling (g_{zz} = 2.23, $^{Cu}A_{zz} = 63 \cdot 10^{-4}\ cm^{-1}$) compared to type 2 or "normal" copper sites such as D_{4h} $[CuCl_4]^{2-}$ (gzz = 2.22, $^{Cu}A_{zz} = 164 \cdot 10^{-4}\ cm^{-1}$). A highly covalent Cu-S(Cys) bond decreases the spin density on the copper nucleus and leads to small $^{Cu}A_{zz}$ hyperfine coupling (decrease of terms 1 and 2 in Eq. 6.5). In contrast, in Cu^{II}-O(TFE) we have found significant spin density on the copper nucleus of ≈ 68 %. The resulting increase in magnitude of the contact and spin-dipolar contributions (terms 1 and 2) to the hyperfine coupling is off-

set by the increased g_{zz}-dependent orbital contribution (term 4) of opposite sign, which is due to the small transition energy $E_{x^2-y^2} - E_{xy}$. Overall, this cancellation of terms in Eq. 6.5 drives the small $^{Cu}A_{zz}$.

Cu^{II}-O(TFE) shares the near-UV transitions of red copper sites such as those in the proteins nitrosocyanin and BSco (a cytochrome c oxidase assembly protein).[26,28] The copper sites in these proteins are five-coordinate and contain thiolate ligands which are the LMCT donors (S(Cys) p_σ and S(Cys) p_π). The increased copper coordination number (relative to type 1 blue copper) raises the energy of the d orbital manifold and shifts the LMCT transitions to the near-UV region, giving the proteins a distinct red color. In addition, the higher energy S(Cys) $p_\sigma \rightarrow Cu^{II}$ $d_{x^2-y^2}$ transition is more intense, indicating that the lobes of the Cu^{II} $d_{x^2-y^2}$ orbital lie along the Cu-S bond and that the bonding interaction is dominantly σ in character.[26,28] These five-coordinate red copper proteins generally have type 2 copper EPR spectra (large $^{Cu}A_{zz} > 100 \cdot 10^{-4}\ \mathrm{cm}^{-1}$ and $g_{zz} \approx 2.2 > g_{yy} \approx g_{xx}$) also indicative of a $d_{x^2-y^2}$ ground state. Although Cu^{II}-O(TFE) shares the red color of nitrosocyanin and BSco, it is four-coordinate and the alkoxide ligand exhibits both π and σ bonding. The red color in Cu^{II}-O(TFE) is dominantly due to a less electron rich LMCT donor (oxygen compared to sulfur) containing a strongly electron withdrawing trifluoromethyl group.

Despite being a rough structural model for the Cu^{II}-alkoxide intermediate suggested in GAO, there are obvious differences in what is known of the electronic structures. The complete electronic structure of GAO when bound to the alkoxide substrate remains elusive due to the difficulty in trapping mechanistic intermediates.[6] A catalytically inactive form of the enzyme (Cu^{II} bound to the reduced 3′-(*S*-cysteinyl)tyrosine residue) shows a type 2 copper EPR spectrum with g_{zz} value of ≈ 2.22 and large $^{Cu}A_{zz}$ hyperfine coupling of ≈ $160 \cdot 10^{-4}\ \mathrm{cm}^{-1}$ and near-UV charge transfer transition9 (indicative of Cu^{II} in a square planar environment, similar to red copper proteins described above). This indicates the open coordination site would support a dominantly sigma bonding interaction. We have shown that despite possessing a type 1 geometry (where covalent π bonding is expected), the alkoxide ligand imparts unique electronic structure with increased σ bonding to Cu^{II}-O(TFE). The nature of the suggested Cu^{II}-alkoxide bond in GAO still remains to be elucidated.

6.3.3 Implications for Alcohol Oxidation.

We observe an increase in copper character in the ground state (≈ 68 % spin density on copper), indicating a more ionic Cu-O bond in Cu^{II}-O(TFE), relative to the comparable Cu^{II}-alkylperoxo (≈ 62 % spin density on copper)[34] and Cu^{II}-thiolate complexes (≈ 40 % spin density on copper).[33,50] The αC-H bond strength of an alcohol is known to depend on the hydroxyl group protonation state. It has been predicted that with ionic counter ions, such as Na^+ and K^+, the αC-H bonds in methanol are weakened from ≈ 91 kcal/mol to ≈ 81 kcal/mol and ≈ 79 kcal/mol, respectively.[8] Similarly, the αC-D stretching frequency (which is roughly proportional to bond strength[51]) in trifluoroethanol-d_2 has been observed to decrease upon deprotonation with NaOH.[52] We expect the ionic interaction between Cu^{II} and the trifluoroethoxide in Cu^{II}-O(TFE) to weaken the αC-H bond strength based on these findings from the literature. However, in a separate reactivity study, it was found that oxidation of the O(TFE) ligand with external oxyl radical hydrogen atom acceptors is not facile, indicating that the activation of the αC-H bond is not significant enough to promote bond cleavage in this system.[21]

6.4 Conclusions and outlook

In this study we have characterized in detail the electronic structure of a Cu^{II}-alkoxide complex as a model structural intermediate in copper catalyzed alcohol oxidation. EPR spectra reveal the orientation of the $d_{x^2-y^2}$ SOMO with lobes bisected by the Cu-O bond. MCD and resonance Raman spectra show the donor in the LMCT transition is dominantly the O(TFE) ligand. The increased contribution from the O(TFE) $p_{\sim\sigma}$ donor in the LMCT transition indicates both σ and π bonding interactions are present, relative to Cu^{II}-thiolate and Cu^{II}-alkylperoxo bonds. This increased ratio of σ/π bonding character reduces the energy of the $d_{xy} \rightarrow d_{x^2-y^2}$ transition. This small transition energy drives a large shift in g_{zz} and, together with small spin delocalization, contributes to the small hyperfine coupling $^{Cu}A_{zz}$. Single-crystal and solution ENDOR spectra, analyzed using a distributed point-dipole model, suggest the unpaired electron is highly localized on the copper atom with $\leq$ 15 % spin density on oxygen of the alkoxide ligand. A ligand field analysis using EPR and MCD data indicates substantial copper character in the ground state SOMO relative to related Cu^{II}-alkylperoxo and Cu^{II}-thiolate systems in nearly identical pyrazolyl ligand scaffolds.

However, this relatively ionic bond does not sufficiently modulate the αC-H bond to promote ligand oxidation.[21] This model complex serves as one of the only Cu^{II}-alkoxide complexes spectroscopically characterized to this extent.

There are a couple outstanding questions remaining concerning the reactivity and electronic structure of Cu^{II}-O(TFE) and related Cu^{II} molecules. First, presented in Appendix A6.11 are the CW EPR spectra of three additional $Tp^{tBu}Cu^{II}$–X compounds where X is a unique fourth ligand. Despite the similar ligand scaffold, the compounds have very different EPR properties dependent on the geometry enforced by the fourth ligand. Understanding the connection between the geometric and electronic structure will lead to deeper insight into Cu^{II} chemistry. Second, an analogue of Cu^{II}-O(TFE) (Me-Cu^{II}-O(TFE) with a ligand scaffold Tp^{tBuMe} = hydro-tris (3-tert-butyl-5-methyl-pyrazol-1-yl) borate) possesses similar spectroscopic characteristics to Cu^{II}-O(TFE) including a nearly identical CW EPR spectrum and UV-Vis spectrum. However, Me-Cu^{II}-O(TFE) displays alternative reactivity to Cu^{II}-O(TFE). This begs the question that if a deeper electronic structure characterization was performed on Me-Cu^{II}-O(TFE), could the electronic structure contributing to the alternative reactivity be measured and understood. Finally, it would be satisfying to have a deeper understanding of the discrepancy in the signs of the d → d transitions of in the MCD spectrum. This may be achieved with further DFT calculations.

6.5 Experimental section

Synthesis and Characterization. $Tp^{tBu}Cu^{II}(OCH_2CF_3)$ and $Tp^{tBu}Cu^{II}(OCD_2CF_3)$ were synthesized as previously described and the structure of $Tp^{tBu}Cu^{II}(OCH_2CF_3)$ was determined previously.[21] $Tp^{tBu}Cu^{II}(OCD_2CF_3)$ was used to assign hyperfine coupling of the αC-H protons of the trifluoroethoxide ligand and to assign vibrational modes in the resonance Raman spectra. $Tp^{tBu}Zn^{II}(OCH_2CF_3)$ was prepared through an analogous synthetic route. $Tp^{tBu}Cu^{II}(OCH_2CF_3)$ and $Tp^{tBu}Zn^{II}(OCH_2CF_3)$ crystalize in the same space group (P21/n) with nearly identical unit cell dimensions (see Appendix A6.6.1). All samples for spectroscopy were prepared in a nitrogen filled glovebox using de-oxygenated and water-free solvents.[53]

Single-Crystal 34 GHz EPR and ENDOR. Single crystals of $Tp^{tBu}Zn^{II}$-OCH_2CF_3 doped with $Tp^{tBu}Cu^{II}$-OCH_2CF_3 were grown from a concentrated pentane solution containing a ≈ 1:99 ratio of Cu/Zn complexes at −30 °C. The exact percentage of Cu incorporation was not determined.

A single crystal was loaded into a 1 mm O.D. quartz capillary EPR sample tube and sealed in place with vacuum grease. A goniometer was mounted on to the sample rod and EPR sample tubes were placed into a Bruker EleXsys E580 X/Q spectrometer such that the long axis of the capillary was perpendicular to the direction of the magnetic field. The sample was rotated around the capillary axis (sample rod axis) in 15° increments from 0° to 180°. The orientation of the crystal relative to this rotation axis was determined by X-ray crystallography after recording EPR and ENDOR data.

At each rotation increment, a pulse field-swept EPR spectrum and a Davies ENDOR spectrum were recorded. All single-crystal measurements were carried out in a Bruker EN 5107D2 resonator at ≈ 34 GHz held at 10 K with an Oxford CF935O liquid helium cryostat and ITC503S temperature controller. Pulse field-swept EPR spectra were FID detected following a 1 μs pulse. The Davies ENDOR spectra were Hahn echo detected ($\pi - T - \pi/2 - \tau - \pi - \tau -$ echo) with pulse lengths and timings given in specific figure captions. During time T, the RF pulse was applied. Microwave frequencies were measured with the built-in frequency counter, and accurate magnetic field values were obtained using a teslameter.

The above was repeated for a second single crystal. Data are shown in Appendix 6.1.

Frozen solution 9.2 and 34 GHz EPR and ENDOR. The continuous-wave (CW) EPR spectrum at 9.2 GHz, reported previously, was recorded on a Bruker EMX spectrometer in an SHQE resonator at 120 K in a frozen glass of ≈ 3 mM $Tp^{tBu}Cu^{II}(OCH_2CF_3)$ in toluene.[21] The field axis was corrected for a 0.5 mT difference between nominal and teslameter-determined field values.

For pulse field-swept 34 GHz EPR spectroscopy, a 1.5 mM solution of $Tp^{tBu}Cu^{II}(OCH_2CF_3)$ in 1:1 DCM:toluene was flash frozen in a 1 mm O.D. quartz EPR sample tube. Pulse field-swept and Davies ENDOR spectra were recorded in the same spectrometer and resonator as described above at 10 K. The field swept spectrum was Hahn echo detected ($\pi/2 - \tau - \pi - \tau -$ echo). Davies ENDOR was echo detect-

ed ($\pi - T - \pi/2 - \tau - \pi - \tau -$ echo) with pulse lengths and timings given in the figure captions. Microwave frequencies were measured with the built-in frequency counter. Magnetic field values were corrected for a 1.5 mT shift between nominal and teslameter-determined field values.

Electronic Absorption and Magnetic Circular Dichroism. The UV-Vis spectrum was acquired previously and recorded with a 2 nm step size.[21] The near-IR/IR spectrum was collected using an Agilent Cary 5000 spectrophotometer with a 1 cm path length.

MCD samples were prepared by saturating a pentane:toluene (9:1) solution with $Tp^{tBu}Cu^{II}(OCH_2CF_3)$. To this, a drop of paratone oil was added to increase the viscosity. The solution was pipetted dropwise onto a quartz disk and the solvent was allowed to evaporate, creating a thin film. Several layers of $Tp^{tBu}Cu^{II}(OCH_2CF_3)$ were deposited in this way and the film then sandwiched with a second quartz disk. The thin film sample was briefly exposed to atmosphere while mounting into the MCD sample rod which was then placed in a liquid helium cooled variable temperature, superconducting magneto-optical cryostat (Cryo-Industries SMC-1659 OVT) with the sample compartment oriented in the Faraday configuration. Absorption and MCD spectra were collected simultaneously using an Aviv 40 DS spectropolarimeter equipped with an additional InGaAs (Teledyne Judson) detector for detection down to 5000 cm^{-1} (2000 nm). Variable temperature, variable field measurements were carried out at 5, 10, 20, and 40 K with the magnetic field varied from 0 to 6 T in 1 T steps at each temperature. Data was collected with a 2 nm step size from 370 to 860 nm and a 5 nm step size from 800 to 2000 nm. At 5 K, the sample was screened for depolarization by matching the CD spectra of a chiral molecule placed before and after the sample. Depolarization was less than 10 %. The differential absorption of the MCD experiment is defined as $\Delta A = A_L - A_R$, where A_L and A_R refer to the absorption of left and right circularly polarized photons in the sign convention of Piepho and Schatz.[54]

Spectra were modeled using a sum of Gaussians defined in the Matlab program. The models were simultaneously fit to the data (using the assumptions presented in the Results section) using the least-

squares fitting algorithms implemented in EasySpin.[55] Further details on data processing and the fitting routine are presented in Appendix A6.8.

Resonance Raman. Resonance Raman samples were prepared by dissolving $Tp^{tBu}Cu^{II}(OCH_2CF_3)$ to an optical density of 2 at 420 nm (1.38 mM) in DCM. The same was done for the deuterated $Tp^{tBu}Cu^{II}$-OCD_2CF_3. These solutions were deposited in 5 mm OD NMR tubes and sealed with electrical tape before removing from the inert atmosphere glovebox.

The 426 nm Raman excitation beam was obtained from the frequency-doubled output of a titanium-sapphire laser (16 ns pulse, 5 μJ/pulse) pumped by a Q-switched (1 kHz), intracavity frequency-doubled Nd:YLF laser (Photonics Industries International). Excitation light was focused through a spherical lens onto the surface of the spinning sample tube, and backscattered (135°) light was collected and collimated with a camera lens and focused with an second lens onto the 0.200 mm entrance slit of a 0.8 m spectrometer (Spex 1401) equipped with a liquid N_2-cooled charge-coupled device detector (Roper Scientific). A 430 nm-cutoff notch filter (angle tuned) was placed at the slit to minimize the spectral contribution of Rayleigh scattering. The samples showed no signs of photodegradation after 15 minutes of continuous laser irradiation. Samples showed decay of rR signal and color after more than 5 hours out of the glove box. Experimental data shown here were collected in less than 3 hours. Additional experimental details are given in Appendix A6.9.

EPR Simulations. All EPR and ENDOR simulations were performed using Easyspin 5.0.[55] For simulation of EPR spectra, the various frames were defined as follows. For P21/n symmetry (space group 14), the crystal frame C (principal axes x_C, y_C, z_C) was defined with y_C along the crystal b axis, z_C along the crystal c axis, and x_C along the a* axis normal to the bc plane of the crystal. The laboratory frame L (x_L, y_L, z_L) was defined as z_L along the static field and y_L along the axis of single crystal rotation (sample tube long axis).

To determine the orientation of the crystal in the EPR spectrometer, X-ray diffraction was recorded for the single crystal within the EPR tube (identical instrument described in Appendix A6.6). Using the previously solved crystal structure, the rotation axis of crystal sample 1 (presented in article) was found to

be along the (0, −3, 4) crystal direction in abc coordinates with 3° accuracy. The rotation axis of crystal sample 2 (presented in Appendix) was found to be along the (−7, −4, 5) direction in abc coordinates with 2° accuracy.

The molecular frame M (principal axes x_M, y_M and z_M) was defined with z_M along the Cu-N_{axial} bond and y_M perpendicular to z_M within the N_{axial}-Cu-O plane such that it points in the direction of the Cu-O bond. The initial *g* tensor frame before least-squares fitting was taken as collinear with the molecular frame. The copper hyperfine frame was assumed to be collinear with the *g* frame in all simulations.

With the above frame definitions, the starting orientation (azimuthal angle φ), of the crystal in the laboratory x_Lz_L plane and the three Euler angles relating the *g* tensor frame to the molecular frame remained unknown, for a total of four variables. These variables were determined by least-squares fitting. In increments of 3°, φ was varied, follow by a simultaneous least squares fit of the Euler angles of all 13 spectra in Figure 6.2C using a grid search algorithm implemented in EasySpin. This same procedure was carried out for crystal 2 and yielded a nearly identical set of Euler angles relating the *g* frame to the molecular frame.

The frequency change of spectra in Figure 6.2C is due to a small repositioning of the sample along the laboratory y_L axis (perpendicular to the field) to optimize sensitivity. This frequency change is negligibly small, but was nevertheless accounted for in the simulations.

Simulations of single-crystal ^{1}H ENDOR spectra used the full hyperfine tensors (calculated using the point dipole approximation) and the full *g* tensor. The hyperfine frames are visualized in Figure A6.7.

Hyperfine frames (x_A, y_A, z_A) for simulation of the ^{14}N and ^{19}F frozen-solution ENDOR spectra were defined using the crystal structure coordinates. For each nucleus, its z_A axis was defined as the unit vector pointing from the nucleus to the copper atom. x_A and y_A were defined in the plane perpendicular to z_A, pointing in arbitrary but perpendicular directions. The frames are visualized in Figure A6.7.

A detailed account of the frame definitions and the fitting procedures are given in Appendix A6.7

Density Functional Theory. Unrestricted Kohn-Sham (UKS) density functional theory (DFT) calculations were performed with Orca 3.0.2 or 3.0.3.[56] Geometry optimization was initiated from the crystal structure coordinates.[21] All atom positions were optimized using the BP86[57,58] functional, the Ahlrichs tzvp[59] basis set, with grid size of 4 and SCF convergence criteria of $1 \cdot 10^{-8}$ Eh. Convergence thresholds for the geometry optimization were as follows: energy change $5 \cdot 10^{-6}$ Eh, maximum gradient $3 \cdot 10^{-4}$ Eh/a_0, RMS gradient $1 \cdot 10^{-4}$ Eh/a_0, maximum displacement $4 \cdot 10^{-3}$ a_0, and RMS displacement $2 \cdot 10^{-3}$ a_0.

EPR property calculations of the optimized geometry used the hybrid B3LYP[60–62] functional and Barone's EPR-II basis set.[63] The copper atom was modeled with a specialized CP(PPP) basis set to model core polarization.[64,65]

In preparation for resonance Raman calculations, time-dependent DFT calculations were carried out with the B3LYP functional, the tzvp basis set and a grid size of 5.[59] The auxiliary basis set tzvp/j was used for the RI approximation for hybrid functionals.[66–68] The first 30 excited states were calculated. As solvent models are not available for the resonance Raman calculations in Orca, no solvent model was used. Separate TDDFT calculations using the COSMO[69] model for dichloromethane showed little difference in the predicted excited states. States 10 and 12 showed O(TFE) $p_\sigma \rightarrow$ Cu $d_{x^2-y^2}$ and O(TFE) $p_\pi \rightarrow$ Cu $d_{x^2-y^2}$ character, respectively, and were used to predict resonance enhancement of Raman modes.

To obtain a Hessian file for resonance Raman calculations, an analytical frequency calculation was performed using an identical level of theory as for the geometry optimization. Additionally the tzvp/j auxiliary basis set was used for the RI approximation. The SCF was converged to an energy change tolerance of $1 \cdot 10^{-8}$ Eh. Resonance enhancements were predicted using the Hessian file from the analytical frequency calculation for excited states 10 and 12 using the same level of theory as for TDDFT calculations. Resonance Raman calculations for the isotopic molecule Cu^{II}-O(TFE)-d_2 were calculated by manually editing the masses of the appropriate hydrogen atoms in the Hessian input file. The new vibrational frequencies for the isotopically labeled molecule were calculated using the standalone orca_vib program. This adjusted Hessian was used in the input block for resonance Raman calculations of Cu^{II}-O(TFE)-d_2. In

both cases, the resonance Raman calculation produced .asa input files which were fed into the orca_asa program to produce resonance Raman spectra.[70] A sample input block is provided in the Appendix A6.3.2 and a detailed account of performing the calculations is given in A6.10.

Normal modes were visualized using Avogadro (version 1.0.3).[71] Molecular orbitals, spin density, and transition difference densities were visualized using UCSF Chimera (version 1.8).[72]

6.6 References

(1) Avigad, G.; Amaral, D.; Asensio, C.; Horecker, B. L. *J. Biol. Chem.* **1962**, *237* (9), 2736.
(2) Whittaker, M. M.; Whittaker, J. W. *J. Biol. Chem.* **1988**, *263* (13), 6074.
(3) Hoover, J. M.; Stahl, S. S. *J. Am. Chem. Soc.* **2011**, *133* (42), 16901.
(4) Hoover, J. M.; Steves, J. E.; Stahl, S. S. *Nat. Protoc.* **2012**, *7* (6), 1161.
(5) Ryland, B. L.; Stahl, S. S. *Angew. Chem. Int. Ed.* **2014**, *53* (34), 8824.
(6) Whittaker, J. W. *Chem. Rev.* **2003**, *103* (6), 2347.
(7) Hoover, J. M.; Ryland, B. L.; Stahl, S. S. *J. Am. Chem. Soc.* **2013**, *135* (6), 2357.
(8) Steigerwald, M. L.; Goddard, W. A.; Evans, D. A. *J. Am. Chem. Soc.* **1979**, *101* (8), 1994.
(9) Whittaker, M. M.; Whittaker, J. W. *J. Biol. Chem.* **2003**, *278* (24), 22090.
(10) Lee, Y.-K.; Whittaker, M. M.; Whittaker, J. W. *Biochemistry* **2008**, *47* (25), 6637.
(11) Whittaker, M. M.; Ballou, D. P.; Whittaker, J. W. *Biochemistry* **1998**, *37* (23), 8426.
(12) Brackman, W.; Gaasbeek, C. J. *Recl. des Trav. Chim. des Pays-Bas* **1966**, *85* (3), 221.
(13) Dijksman, A.; Arends, I. W. C. E.; Sheldon, R. A. *Org. Biomol. Chem.* **2003**, *1* (18), 3232.
(14) Michel, C.; Belanzoni, P.; Gamez, P.; Reedijk, J.; Baerends, E. J. *Inorg. Chem.* **2009**, *48* (24), 11909.
(15) Belanzoni, P.; Michel, C.; Baerends, E. J. *Inorg. Chem.* **2011**, *50* (23), 11896.
(16) Ryland, B. L.; McCann, S. D.; Brunold, T. C.; Stahl, S. S. *J. Am. Chem. Soc.* **2014**, *136* (34), 12166.
(17) Jeffries, P. M.; Wilson, S. R.; Girolami, G. S. *Inorg. Chem.* **1992**, *31* (22), 4503.
(18) Chi, Y.; Hsu, P.-F.; Liu, C.-S.; Ching, W.-L.; Chou, T.-Y.; Carty, A. J.; Peng, S.-M.; Lee, G.-H.; Chuang, S.-H. *J. Mater. Chem.* **2002**, *12* (12), 3541.
(19) Tubbs, K. J.; Fuller, A. L.; Bennett, B.; Arif, A. M.; Berreau, L. M. *Inorg. Chem.* **2003**, *42* (16), 4790.
(20) Gephart, R. T.; McMullin, C. L.; Sapiezynski, N. G.; Jang, E. S.; Aguila, M. J. B.; Cundari, T. R.; Warren, T. H. *J. Am. Chem. Soc.* **2012**, *134* (42), 17350.
(21) Porter, T. R.; Capitao, D.; Kaminsky, W.; Qian, Z.; Mayer, J. M. *Synthesis, Radical Reactivity and Thermochemistry of Monomeric Cu(II) Alkoxide Complexes: Insight Into Cu/Radical Alcohol Oxidation Catalysis*; 2015.
(22) Ruggiero, C. E.; Carrier, S. M.; Antholine, W. E.; Whittaker, J. W.; Cramer, C. J.; Tolman, W. B. *J. Am. Chem. Soc.* **1993**, *115* (24), 11285.
(23) Kumar, M.; Dixon, N. A.; Merkle, A. C.; Zeller, M.; Lehnert, N.; Papish, E. T. *Inorg. Chem.* **2012**, *51* (13), 7004.
(24) Trofimenko, S. *Scorpionates: The Coordination Chemistry of Polypyrazolylborate Ligands*; Imperial College Press, 1999.
(25) Solomon, E. I.; Szilagyi, R. K.; DeBeer George, S.; Basumallick, L. *Chem. Rev.* **2004**, *104* (2), 419.
(26) Basumallick, L.; Sarangi, R.; DeBeer George, S.; Elmore, B.; Hooper, A. B.; Hedman, B.; Hodgson, K. O.; Solomon, E. I. *J. Am. Chem. Soc.* **2005**, *127* (10), 3531.
(27) Andruzzi, L.; Nakano, M.; Nilges, M. J.; Blackburn, N. J. *J. Am. Chem. Soc.* **2005**, *127* (47), 16548.

(28) Siluvai, G. S.; Mayfield, M.; Nilges, M. J.; Debeer George, S.; Blackburn, N. J. *J. Am. Chem. Soc.* **2010**, *132* (14), 5215.
(29) Mabbs, F. E.; Collison, D. *Electron Paramagnetic Resonance of d Transition Metal Compounds*; Elsevier Science: Amsterdam, 1992.
(30) Morton, J. R.; Preston, K. F. *J. Magn. Reson.* **1978**, *30*, 577.
(31) Gerstman, B. S.; Brill, A. S. *J. Chem. Phys.* **1985**, *82* (3), 1212.
(32) Neese, F.; Solomon, E. I. *Inorg. Chem.* **1999**, *38* (8), 1847.
(33) Randall, D. W.; George, S. D.; Hedman, B.; Hodgson, K. O.; Fujisawa, K.; Solomon, E. I. *J. Am. Chem. Soc.* **2000**, *122* (47), 11620.
(34) Chen, P.; Fujisawa, K.; Solomon, E. I. *J. Am. Chem. Soc.* **2000**, *122* (41), 10177.
(35) Gewirth, A. A.; Solomon, E. I. *J. Am. Chem. Soc.* **1988**, *110* (12), 3811.
(36) Solomon, E. I. *Comments Inorg. Chem.* **1984**, *3* (5), 225.
(37) Solomon, E. I.; Hare, J. W.; Gray, H. B. *Proc. Natl. Acad. Sci. U. S. A.* **1976**, *73* (5), 1389.
(38) Nestor, L.; Larrabee, J. A.; Woolery, G.; Reinhammar, B.; Spiro, T. G. *Biochemistry* **1984**, *23* (6), 1084.
(39) Dong, S.; Spiro, T. G. *J. Am. Chem. Soc.* **1998**, *120* (40), 10434.
(40) Woodruff, W. H.; Norton, K. A.; Swanson, B. I.; Fry, H. A. *J. Am. Chem. Soc.* **1983**, *105* (3), 657.
(41) Han, J.; Loehr, T. M.; Lu, Y.; Valentine, J. S.; Averill, B. A.; Sanders-loehr, J. *J. Am. Chem. Soc.* **1993**, *115* (10), 4256.
(42) Qiu, D.; Kilpatrick, L. T.; Kitajima, N.; Spiro, T. G. *J. Am. Chem. Soc.* **1994**, *116* (6), 2585.
(43) Kalasinsky, V. F.; Anjaria, H. V. *J. Phys. Chem.* **1980**, *84* (15), 1940.
(44) Sinnecker, S.; Neese, F. *J. Comput. Chem.* **2006**, *27* (12), 1463.
(45) Vancoillie, S.; Pierloot, K. *J. Phys. Chem. A* **2008**, *112* (17), 4011.
(46) Kitajima, N.; Fujisawa, K.; Tanaka, M.; Moro-oka, Y. *J. Am. Chem. Soc.* **1992**, *114*, 9232.
(47) Kitajima, N.; Katayama, T.; Fujisawa, K.; Iwata, Y.; Moro-oka, Y. *J. Am. Chem. Soc.* **1993**, *115* (17), 7872.
(48) Lias, S. G. In *NIST Chemistry WebBook, NIST Standard Reference Database Number 69*; Linstrom, P. J., Mallard, W. G., Eds.; National Institute of Standards and Technology: Gaithersburg, MD, 2015.
(49) Koppel, I. A.; Molder, U. H.; Pikver, R. J. *Org. React. (Tartu)* **1983**, *20* (1), 45.
(50) George, S. J.; Lowery, M. D.; Solomon, E. I.; Cramer, S. P. *J. Am. Chem. Soc.* **1993**, *115* (7), 2968.
(51) Cioslowski, J.; Liu, G.; Mosquera Castro, R. A. *Chem. Phys. Lett.* **2000**, *331* (5–6), 497.
(52) Gawlita, E.; Lantz, M.; Paneth, P.; Bell, A. F.; Tonge, P. J.; Anderson, V. E. *J. Am. Chem. Soc.* **2000**, *122* (47), 11660.
(53) Armarego, W. L. F.; Chai, C. L. L. *Purification of Laboratory Chemicals*, 6th ed.; Elsevier, 2009.
(54) Piepho, S. B.; Schatz, P. N. *Group Theory in Spectroscopy with Applications to Magnetic Circular Dichroism*; Wiley: New York, U.S.A., 1983.
(55) Stoll, S.; Schweiger, A. *J. Magn. Reson.* **2006**, *178* (1), 42.
(56) Neese, F. *WIREs Comput. Mol. Sci.* **2012**, *2*, 73.
(57) Perdew, J. P. *Phys. Rev. B* **1986**, *33* (12), 8822.
(58) Becke, A. D. *Phys. Rev. A* **1988**, *38* (6), 3098.
(59) Schäfer, A.; Horn, H.; Ahlrichs, R. *J. Chem. Phys.* **1992**, *97* (4), 2571.
(60) Stephens, P. J.; Devlin, F. J.; Chabalowski, C. F.; Frisch, M. J. *J. Phys. Chem.* **1994**, *98* (45), 11623.
(61) Becke, A. D. *J. Chem. Phys.* **1993**, *98* (2), 1372.
(62) Lee, C.; Yang, W.; Parr, R. G. *Phys. Rev. B* **1988**, *37* (2), 785.
(63) Barone, V. In *Recent Advances in Density Functional Methods, Part I*; Chong, D. P., Ed.; World Scientific: Singapore, 1996.
(64) Sinnecker, S.; Slep, L. D.; Bill, E.; Neese, F. *Inorg. Chem.* **2005**, *44* (7), 2245.

(65) Neese, F. *Inorg. Chim. Acta* **2002**, *337*, 181.
(66) Dunlap, B. I.; Connolly, J. W. D.; Sabin, J. R. *J. Chem. Phys.* **1979**, *71* (8), 3396.
(67) Feyereisen, M.; Fitzgerald, G.; Komornicki, A. *Chem. Phys. Lett.* **1993**, *208* (5), 359.
(68) Neese, F.; Wennmohs, F.; Hansen, A.; Becker, U. *Chem. Phys.* **2009**, *356* (1–3), 98.
(69) Klamt, A.; Schuurmann, G. *J. Chem. Soc. Perkin Trans. 2* **1993**, No. 5, 799.
(70) Petrenko, T.; Neese, F. *J. Chem. Phys.* **2007**, *127* (16), 164319.+
(71) Hanwell, M. D.; Curtis, D. E.; Lonie, D. C.; Vandermeersch, T.; Zurek, E.; Hutchison, G. R. *J. Cheminform.* **2012**, *4*, 17.
(72) Pettersen, E. F.; Goddard, T. D.; Huang, C. C.; Couch, G. S.; Greenblatt, D. M.; Meng, E. C.; Ferrin, T. E. *J. Comput. Chem.* **2004**, *25* (13), 1605.

Chapter 6 Appendix

Electronic structure of a Cu^{II}-alkoxide complex modeling intermediates in copper-catalyzed alcohol oxidations

---

A6.1 Simulation parameters for EPR spectra

A6.1.1 Simulation parameters for field swept spectra

Table A6.1a. Simulation parameters for field sweep frozen solution spectra in Figure 6.1A,B

	Principal *g* values (error)[a], gStrain	Principal ^{Cu}A values in MHz (error)[b], AStrain	Gaussian, Lorentzian peak-to-peak broadening in mT
9.22 GHz (X-band)	2.06 (0.01), 0.046 2.09 (0.01), 0.022 2.44 (0.01), 0.012	30 (29), 1 92 (20), 5 120 (10), 6	0, 1.8
34.061 GHz (Q-band)	2.060 (0.006), 0.01 2.093 (0.006), 0.02 2.447 (0.006), 0.01	30 (20), 0 92 (30), 1 118 (15) , 6	0, 1.5

[a] The error was obtained from two sources. First, we assume an error in the magnetic field measurement of 0.5 mT and 1.5 mT at X-band and Q-band, respectively. This results in *g* value errors of ≈ 0.003. Second, the simulation error was estimated by varying the individual simulation parameters until visually unsatisfactory fits of the data were obtained. These two sources of error were summed to obtain the error estimates.

[b] Simulation error is accounted for by varying the parameter until visually unsatisfactory fits were obtained.

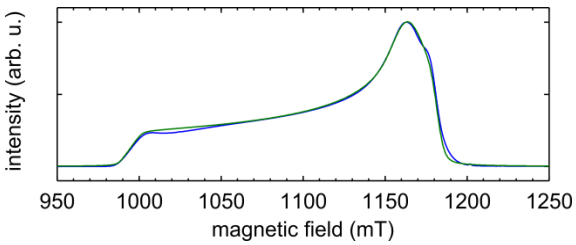

Figure A6.1. Pulse field swept spectrum of Cu^{II}-O(TFE) (blue) shown in Figure 6.2B prior to taking derivative. Simulation (green) uses the parameters from Table A6.1A.

Table A6.1b. Simulation parameters for single-crystal pulse field sweep EPR

	Principal *g* values (error)	Euler angles in degrees Molecular → *g* Frame (error)[a]	Principal ^{Cu}A values in MHz (error)[a]	Gaussian, Lorentzian peak-to-peak broadening in mT
Crystal 1 Figure 6.2C	2.063 (0.006) 2.093 (0.006) 2.453 (0.004)	-69 (5) -10 (3) 91 (15)	60 (30) 60 (30) 118 (10)	2, 1.5
Crystal 2 Figure A6.2	2.063 (0.008) 2.093 (0.02) 2.463 (0.006)	-73 (10) -10 (4) 111 (15)	60 (30) 60 (30) 118 (10)	2, 1.5

[a] Simulation error is accounted for by varying the parameter until visually unsatisfactory fits were obtained.

Table A6.1c. Summary of ENDOR simulation parameters for crystals 1 and 2[a]

	g values (crystal 1)	*g* values (crystal 2)	Hyperfine coupling in MHz for H_S (error)[b]	Hyperfine coupling in MHz for H_R (error)[b]
Isotropic coupling			8 (1)	25.8 (0.5)
Dipolar coupling xx yy zz			 -3.3(0.3) -2.6(0.1) 6.3(0.5)	 -2.5(0.2) -3.1(0.3) 5.5(0.5)
Principal values xx yy zz	 2.06 2.09 2.45	 2.06 2.09 2.46	 4.7 5.4 14.3	 23.3 22.7 31.3
Euler angles (degrees) Molecular → Tensor Frame	-69 -10 91	-73 -10 111	-73 31 65	-123 49 -31

[a] ^{1}H ENDOR simulations used identical parameters for the hyperfine couplings in crystals 1 and 2. However, different *g* values and molecular frame to *g* tensor frame Euler angles were used and the different orientation of each crystal in the EPR spectrometer was determined by X-ray diffraction (see Experimental in main article) and used for simulations.

[b] To estimate simulation error, a range of satisfactory fits was found by simultaneously varying the spin population on oxygen (0.10 ± 0.03) and copper (0.73 ∓ 0.03). Error in the dipolar coupling was taken from the range of hyperfine coupling calculated when the spin population was varied.

A6.1.2 Crystal 2 field swept and ENDOR data, simulations

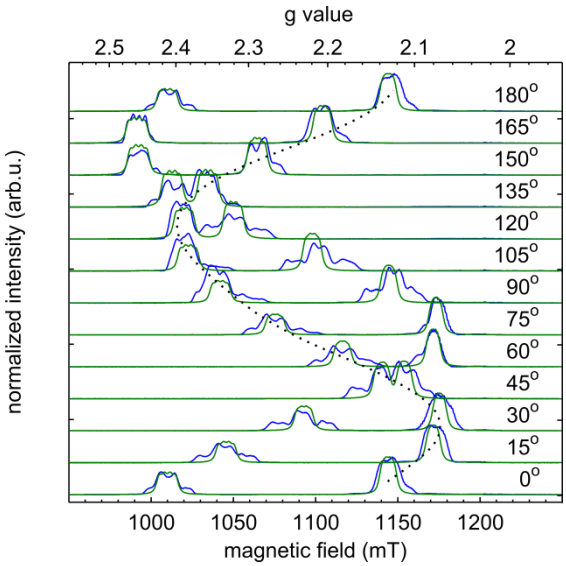

Figure A6.2. FID detected single-crystal spectra acquired at 34.100 GHz. Spectra were acquired at 10 K with a 1 μs π/2 pulse and 2 ms repetition time in 0.1 mT steps. Low-intensity wing features around the central transitions are due to twining of the crystal, which was confirmed by X-ray diffraction. Experimental traces are shown in blue and simulations in green. Simulation parameters are summarized in Tables A6.1A.

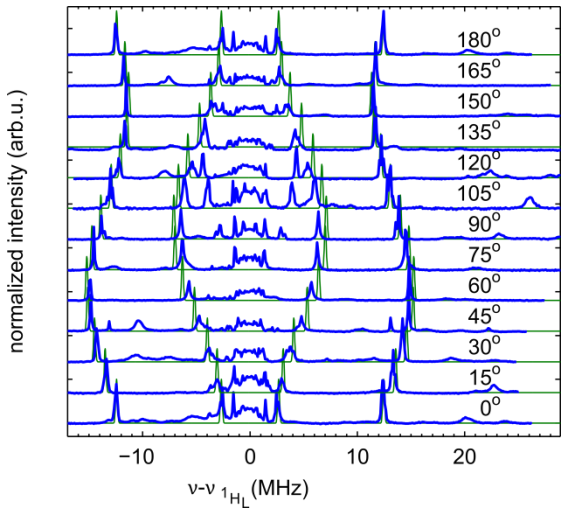

Figure A6.3. 34.100 GHz Davies ENDOR spectra (blue) of a single crystal of Cu^{II}-O(TFE) at 10 K. Spectra were acquired at the *g* values and magnetic fields corresponding to the site marked with a dotted line in Figure A6.2. π/2 and π pulse lengths were 40 ns and 80 ns with a spacing τ = 230 ns. A 13 μs RF pulse was applied. Spectra were acquired with a 3 ms repetition time with a frequency resolution of 0.1 MHz. Simulations are shown in green (simulation parameters in Table A6.1C).

A6.1.3 Supplemental ENDOR spectra

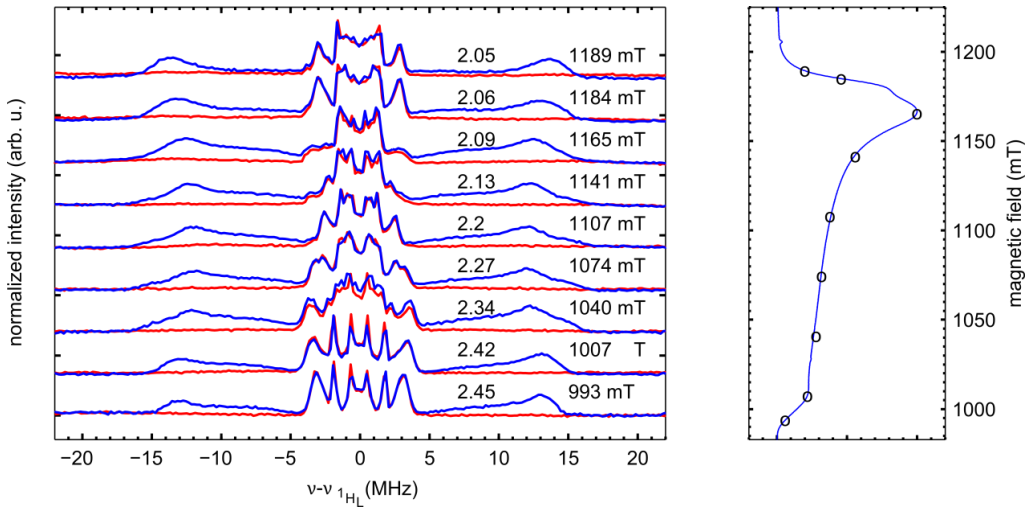

Figure A6.4. Davies ENDOR spectra of a frozen solution of Cu^{II}-O(TFE) at 10 K (blue, 34.118 GHz) and Cu^{II}-O(TFE)-d_2 (red, 34.068 GHz) in 1:1 DCM:toluene. Spectra were acquired at the *g* values and fields listed in the figure for the protiated sample. Due to a frequency shift in the spectrometer with the deuterated sample, the fields where data were recorded were adjusted to correspond to the listed *g* values. Magnetic fields were measured with a Hall probe, the frequency was measured with the internal counter in the Bruker spectrometer. π/2 and π pulse lengths were 40 ns and 80 ns with a spacing τ = 240 ns. A 14.5 μs RF pulse was applied. Spectra were acquired with a 3 ms repetition time with a resolution of 0.2 MHz.

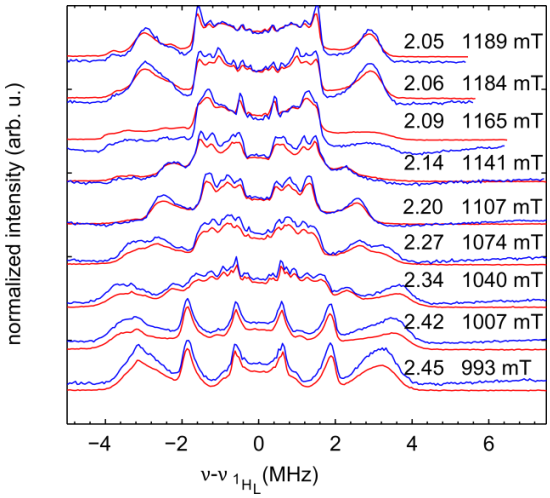

Figure A6.5. Davies ENDOR spectra of a frozen solution of Cu^{II}-O(TFE) (blue, 34.118 GHz) and Cu^{II}-O(TFE)-d_2 (red, 34.068 GHz) at 10 K in 1:1 DCM:toluene. Spectra of Cu^{II}-O(TFE) were acquired at the fields and *g* values listed in the figure. The fields used to calculate the listed *g* values were down shifted by 1.5 mT to account for a known deviation between the field value measured by the spectrometer Hall probe and the actual field at the sample location. Due to a frequency shift in the spectrometer for the Cu^{II}-O(TFE)-d_2 sample, the magnetic field where each spectrum was recorded was adjusted to correspond to the listed *g* values. The frequency was recorded on the internal counter in the Bruker spectrometer. π/2 and π pulse lengths were 40 ns and 80 ns with a spacing τ = 240 ns. A 14.5 μs RF pulse was applied. Spectra were acquired with a 3 ms repetition time with a resolution of 0.2 MHz.

Table A6.1d. Simulation parameters for ^{19}F and ^{14}N ENDOR spectra in Figure 6.5A, B (hyperfine coupling in MHz).

	g	F1[a]	F2[a]	F3[a]	N_{1basal}[b]	N_{2basal}[b]
Isotropic coupling		0	0	0	32.9	31.9
Dipolar coupling						
xx		-1.12(0.07)	-0.65(0.04)	-1.11(0.08)	-4.1	-1.6
yy		-1.44(0.09)	-0.75(0.04)	-1.31(0.02)	-4.1	-1.6
zz		2.37(0.2)	1.35(0.08)	2.24 (0.2)	8.2	3.2
Principal values						
xx	2.06				28.8 (8)	30.3(2)
yy	2.09				28.8 (3)	30.3(2)
zz	2.45				41.1 (1)	35.1(2)
Euler angles	-69	-65	-85	-92	47	141
(degrees)	-10	75	60	83	89	89
Molecular → Tensor	91	-132	56	111	-89	89
Frame						

[a]The range of satisfactory simulations was found by simultaneously varying the spin population on oxygen (0.15 ± 0.03) and copper (0.68 ∓ 0.03). Error in the dipolar coupling was taken from the range of hyperfine coupling calculated when the spin population was varied.

[b]Error was estimated by individually varying the principal values of the hyperfine coupling until fits were visually unsatisfactory.

A6.1.4 Comparison of experimental EPR results to DFT EPR property calculations

Table A6.1e. Results from DFT EPR property calculations[a] (hyperfine and quadrupole coupling in MHz).

g		Cu	H_S	H_R	N_{1basal}	N_{2basal}	F1	F2	F3
	Hyperfine								
2.076	xx	-6.7	38.1	30.3	30.9	31.4	-0.9	0.03	-0.6
2.115	yy	18.1	39.5	31.8	31.9	32.5	1.5	-0.9	1.3
2.237	zz	-688	46.4	38.6	40.3	40.9	-1.7	-1.7	-1.9
	Quadrupole								
	xx				-0.74	-0.75			
	yy				-1.01	-1.00			
	zz				1.76	1.76			

[a] ORCA, unrestricted Kohn-Sham theory, B3LYP functional, EPR-II basis set, specialized CP(PPP) basis set on copper for improved capture of core polarization.

Table A6.1f. Comparison of experimental[a] and calculated[b] spin populations

	Cu	O (error)	H_R	H_S	N_{1basal}	N_{2basal}
Experimental spin population	0.73 (0.03)	0.10 (0.03)	0.018	0.006	0.09	0.05
Mulliken spin population	0.597	0.230	0.02	0.02	0.08	0.08

[a] Spin population determined from single-crystal ^1H ENDOR using the distributed point dipole approximation.

[b] ORCA, unrestricted Kohn-Sham theory, B3LYP functional, EPR-II basis set, specialized CP(PPP) basis set on copper for improved capture of core polarization

A6.1.5 Visualization of laboratory, crystal, molecular and tensor frames

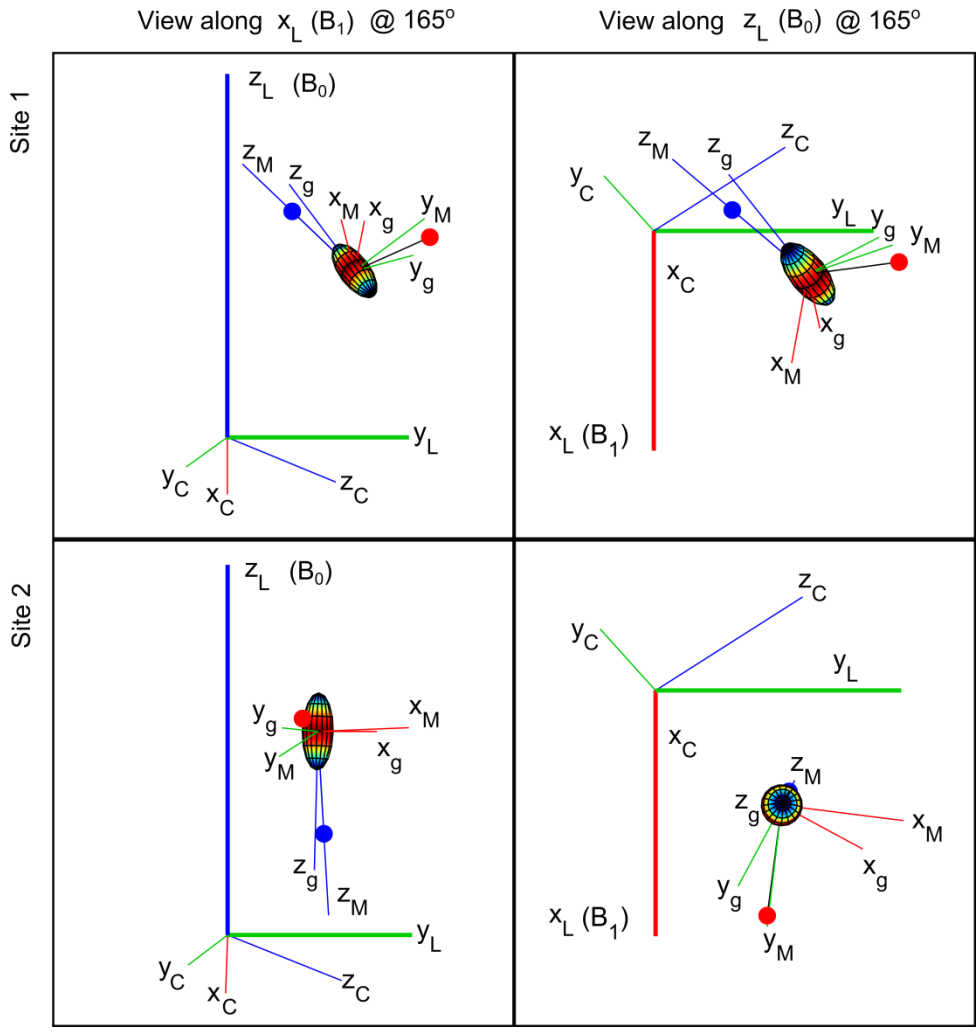

Figure A6.6. The orientation of Cu^{II}-O(TFE) in the laboratory frame for crystal 1 (Figure 6.2C and Figure 6.4) at the 165° rotation increment. There are two EPR active sites in the crystal due to the $P2_1/n$ space group of the crystal. Site 2 is highlighted by a dotted line in Figure 6.2C. The axial nitrogen ligand (blue dot) and the oxygen of the trifluoroethoxide ligand (red dot) are labeled. The ellipsoid represents the g tensor and is centered on the copper nucleus. The subscripts L, C, M, and g stand for laboratory, crystal, molecular and g tensor, respectively. In all cases x axes are shown in red, y axes in green, and z axes in blue. The crystal was rotated around the y_L axis.

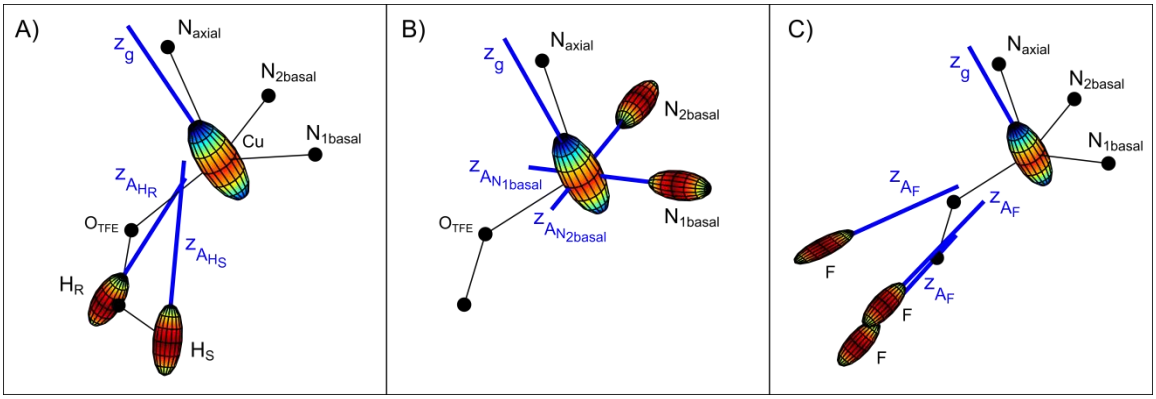

Figure A6.7. Illustrated direction of the principle *z* component (blue, thick line) of the hyperfine tensors and *g* tensor in Cu^{II}-O(TFE). In all cases, an axial *g* tensor ellipsoid is centered on copper and ligand atoms are represented by black dots and the bonds by thin black lines. A) Hyperfine tensor ellipsoids for the hydrogen atoms of the trifluoroethoxide ligand are shown. Frames are generated by extracting the rotation matrix from the diagonalized hyperfine tensor calculated from the point dipole approximation. For these frames, the hyperfine tensor was calculated using an isotropic *g* value to remove contributions from the interaction between the hydrogen nucleus and the spin orbital. B) Hyperfine tensor ellipsoids for basal nitrogen nuclei of the Tp^{tBu} ligand. These frames were defined so that the largest principal value of the hyperfine coupling points towards copper, as described in the Experimental section of the main text. C) Hyperfine tensor ellipsoids for fluorine nuclei of the trifluoroethoxide ligand. These frames were defined so that the largest principal value of the hyperfine coupling points towards copper, as described in the Experimental section of the main text.

A6.1.6 Derivation of nitrogen spin density from ^{14}N ENDOR following Morton and Preston[1]

Isotropic: The isotropic hyperfine coupling can be computed using the equation $\frac{8\pi}{3} g_e \mu_B g_N \mu_N \Psi^2(0)$ where $\Psi^2(0)$ represents the spin population in an s orbital. For nitrogen, the above yields a hyperfine coupling of 1811 MHz when 100% of the spin density is in the 2s orbital. Using the experimental isotropic hyperfine values of 32.9 and 31.8 MHz, we can compute the spin density $\rho(2s)$ using the simple relation

$$N_1 \qquad \rho(2s) = 100 \times \frac{32.9}{1811} = 1.81\ \%$$

$$N_2 \qquad \rho(2s) = 100 \times \frac{31.9}{1811} = 1.76\ \%$$

Anisotropic: The anisotropic component of the hyperfine coupling is a traceless tensor with principle values [2*b* –*b* –*b*] where *b* can be computed from the hyperfine values. For N_{1basal}, $b_{N1} = \frac{1}{3}(a_{\parallel} - a_{\perp}) =$ 4.1 MHz and for N_{2basal}, $b_{N2} = \frac{1}{3}(a_{\parallel} - a_{\perp}) = 1.6$ MHz, assuming the hyperfine values have same sign. The

anisotropic (dipolar) hyperfine coupling in a p, d, or f orbital can be computed using the equation $\alpha g_e \mu_B g_N \mu_N \langle r^{-3} \rangle$. Here, α = $\frac{2}{5}$ for a p orbital and $\langle r^{-3} \rangle$ is obtained from the Hartree-Fock-Slater orbitals. For nitrogen, the resulting hyperfine coupling will be 55.5 MHz when 100% of the spin density is in a 2p orbital. We can compute the spin density $\rho(2p)$ using the simple relation

$$N_1 \qquad \rho(2p) = 100 \times \frac{4.1}{55.52} = 7.38\,\%$$

$$N_2 \qquad \rho(2p) = 100 \times \frac{1.6}{55.52} = 2.88\,\%$$

The final results are ≈ 9 % spin density on N_{1basal} and ≈ 5 % spin density on N_{2basal}.

A6.1.7 Three Pulse ESEEM

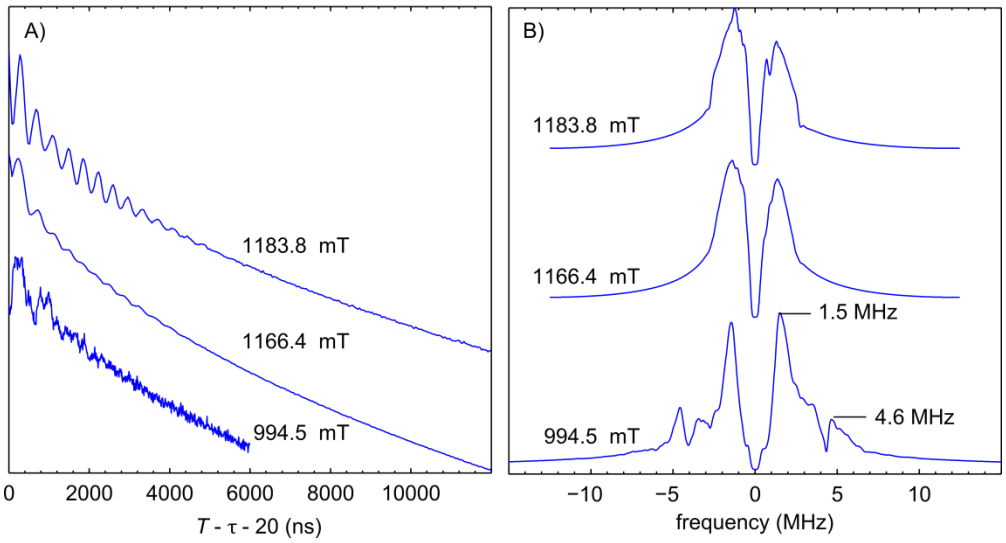

Figure A6.8. Orientation selection in 3 pulse electron spin echo envelope modulation (ESEEM) experiments recorded at field values listed in the figure on ≈ 1.5 mM Cu^{II}-O(TFE) in 1:1 DCM:toluene. A) At 1166.4 mT and 1183.8 mT, spectra were echo-detected [π/2(60 ns) – *τ*(180 ns) – π/2(60 ns) – *T*(200ns + t) – π/2(60 ns) – echo] at 34.081 GHz (10 K, 3 ms repetition time) with an increment in *T* of t = 40 ns. At 994.5 mT, spectra were echo-detected [π/2(60 ns) – *τ*(160 ns) – π/2(60 ns) – *T*(180ns + t) – π/2(60 ns) – echo] at 34.081 GHz (10 K, 3 ms repetition time) with an increment in *T* of t = 10 ns. B) Fourier transforms of the ESEEM spectra in A) show only very small (< 3 MHz) modulation frequencies at 1166.4 mT and 1183.8 mT. At 994.5 mT, frequencies of 1.5 MHz and 4.5 MHz are observed. The expected Larmor frequency of ^{14}N at this field is 3.05 MHz so this may correspond to the A_{zz} component of the axial nitrogen hyperfine coupling. However, isotopic labeling is needed to confirm this assignment.

A6.2 Supplemental electronic absorption and MCD spectra

A6.2.1 Temperature dependence of MCD signal

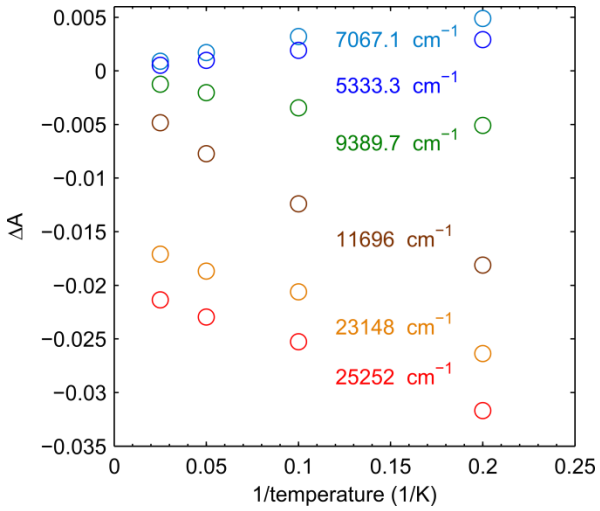

Figure A6.9. Temperature dependence of MCD absorption maxima for positive features and minima for negative features taken at 6 T and varying temperature. There is no significant saturation of the signal at 5 K, meaning the peak maxima of this spectrum can be used in the C_0/D_0 comparison discussed in the main text.

A6.2.2 Full UV-Vis absorption spectrum

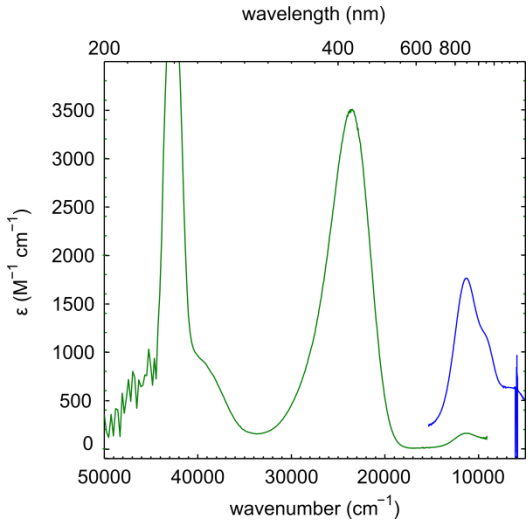

Figure A6.10.: Room temperature UV-Vis and near-IR absorbtion spectra. The high energy transitions near 40000 cm^{-1} prevent the pseudo-σ transition (near 26000 cm^{-1}) from returning to a zero baseline at wavelengths shorter than 360 nm. In addition, the light source for the MCD spectrometer did not go to wavelengths shorter than 380 nm so the full transition could not be included in the Gaussian fit discussed in the main text. As such, the room temperature absorption spectrum was truncated at ~ 310 nm for fitting.

A6.2.3. Electronic absorption and MCD fitting parameters

Table A6.2. Gaussian resolved fitting parameters for MCD, 5 K absorption, and room temperature absorption

Peak	Donor to Cu $d_{x^2-y^2}$	λ_{max} (cm^{-1})	integrated area	Full Width at Half Maximum (cm^{-1})	Maximum (ΔA, ε)	ΔA (MCD) / ε (RT ABS)[a] ($\times 10^3$) ≈ C_0/D_0	f_{exp}[b]
1 MCD	d_{z^2}	5185	3	1033	0.0025	0.076	
LT ABS			N.A.	N.A.	N.A.		
RT ABS			1×10^5	4006	33		6.1×10^{-4}
2 MCD	d_{xy}	7047	10	1967	0.0048	0.16	
LT ABS			N.A.	N.A.	N.A.		
RT ABS			1×10^5	2440	30		3.4×10^{-4}
3 MCD	d_{yz+xz}	9403	-4	787	-0.0049	-0.053	
LT ABS			N.A.	N.A.	N.A.		
RT ABS			2×10^5	2290	93		9.8×10^{-4}
4 MCD	d_{yz-xz}	11807	-33	1726	-0.018	-0.12	
LT ABS			N.A.	N.A.	N.A.		
RT ABS			4×10^5	2400	157		0.0017
5 MCD	O(TFE) p_π	23205	-81	3121	-0.024	-0.0090	
LT ABS			1027	3377	N.A.		
RT ABS			118×10^5	4065	2722		0.0510
6 MCD	O(TFE) $p_{\sim\sigma}$	26066	-97	3210	-0.028	-0.021	
LT ABS			889	3282	N.A.		
RT ABS			87×10^5	6073	1340		0.0375

Fitting parameters are reported here with more significant figures than reported in the main article and are the result of the least-squares fitting described in the main text. Significant figures in the main article are based on the 2 nm step size used to record the MCD near-UV data (equivalent to a < 200 cm^{-1} step size) and the 5 nm step size used to record the MCD near-IR data (equivalent to a < 100 cm^{-1} step size for bands 3 and 4 and < 50 cm^{-1} step size for bands 1 and 2).

[a] $\Delta A/\varepsilon$ is an approximation of the commonly used C_0/D_0 ratio to compare the expected increase in intensity of transitions centered on nuclei with large spin orbit coupling in an MCD spectrum.

[b] The experimental oscillator strength is calculated as $f_{\text{exp}} = 4.61 \times 10^{-9} \epsilon_{\max} \nu_{1/2}$ using the $\epsilon_{\max}$ and the full width at half maximum $\nu_{1/2}$ of the transitions in the RT ABS spectrum.

A6.2.4 Alternative interpretation of near-IR transitions in MCD spectrum

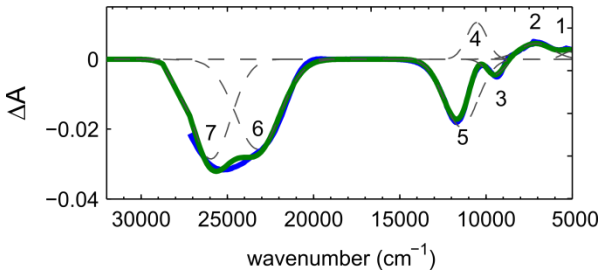

Figure A6.11. MCD spectrum acquired at 5 K and 6 T. Individual Gaussian resolved bands are shown as dashed gray lines, the total fit in green, and experimental data in blue. In the near IR region, 5 Gaussian transitions are used in the fit. Although these d $\rightarrow$ d transitions have the expected sign based on previous literature data, this analysis is not preferred. In this analysis, the $d_{xy} \rightarrow d_{x^2-y^2}$ transition energy is 9534 cm^{-1}. This is much larger than the small transition energy necessary to drive the large g_{zz} shift.

Table A6.3. Gaussian resolved fitting parameters for 5K, 6T MCD spectrum using five peaks in the near-IR region

Peak	Donor to Cu $d_{x^2-y^2}$	λ_{max} (cm^{-1})	integrated area	Full Width at Half Maximum (cm^{-1})	Maximum (ΔA)
1	d_{z^2}	5060	3	1219	0.0022
2	N(Py)	7116	11	2287	0.0045
3	d_{xy}	9534	-6	1280	-0.0044
4	d_{yz+xz}	10538	15	1376	0.0105
5	d_{yz-xz}	11450	-47	2284	-0.0193
6	O(TFE) p_π	23226	84	3059	-0.0257
7	O(TFE) p_σ	25950	81	2674	-0.0286

A6.3 Supplemental results of resonance Raman and Raman calculations

A6.3.1 Tabulated experimental and calculated resonance Raman results

Table A6.4a. Experimental and calculated resonance Raman shifts and their shifts upon isotopic labeling

Mode [a]	Experimental Raman shift [b] (cm^{-1})	Isotopic shift, ^1H-^2H (cm^{-1})	Calculated Raman shift [c] (cm^{-1})	Calculated isotopic shift, ^1H-^2H (cm^{-1})
ν(Cu-O) + δ(F-$C_β$-F)	524	-3	497	-1
	521		496	
ν(Cu-O)	592	-25	553	-20
	567		533	
ν(Cu-O) + δ(O-C-$C_β$)	690	-12	663	-13
	678		650	
ν(C-O)	1139	+15	1094	+30.4
ν(C-O) + w(C-D)	1154[d]		1125	
ν(C-O)	1139	+15	1094	-8
ν(C-O) + ν($C_β$-F)	1154[d]		1086	
w(C-H)	1274	-266	1353	-389
	1008		964	
ν(C-$C_β$) + w(C-H)	1274	-266	1215	-251
w(C-D)	1008		964	

Based on measurement step size, all shifts have an error within ± 1 cm^{-1}, giving an isotopic shift error of ± 2 cm^{-1}.

[a] Experimental modes are assigned based on the DFT calculation after visualizing normal modes in Avogadro. All motions describe the copper atom or the trifluoroethoxide ligand. When not specified, C corresponds to the α carbon. In some cases, modes on the trifluoroethoxide ligand change upon deuteration and the dominant motions are listed for Cu^{II}-O(TFE) (top) and Cu^{II}-O(TFE)-d_2 (bottom) in the split cells.

[b] The split cells for each mode list the resonantly enhanced Raman shift for Cu^{II}-O(TFE) (top) and the Raman shift for Cu^{II}-O(TFE)-d_2 (bottom).

[c] The split cells for each mode list the calculated resonantly enhanced Raman shift for Cu^{II}-O(TFE) (top) and the calculated Raman shift for Cu^{II}-O(TFE)-d_2 (bottom).

[d] This peak lays underneath a DCM solvent peak and cannot be confirmed as peaks due to the sample Cu^{II}-O(TFE)-d_2 as discussed in the main text.

A6.3.2 Sample input file for resonance Raman calculations

```
! UKS B3LYP tzvp tzvp/j RIJCOSX PAL6
! MORead TightSCF NMGrad Grid5
%maxcore 4000
%moinp "Cu_opt.gbw"
%tddft
        MaxDim 52
        nRoots 13
end
%rr    States 10,12
        HessName "Cu_AnFreq.hess"
        ASAInput true
        end
*xyzfile 0 2 Cu_opt.xyz
```

A6.3.3 Raman calculation in Orca 3.0.3

The calculation of ground state vibrational frequencies and normal mode polarizabilities was performed with numerical differentiation with an increment of 0.005 a_0. An identical level of theory as for the geometry optimization was used but included the resolution of the identity (RI) approximation with the auxiliary tzvp/j basis set.[2–4] The SCF was reconverged with the new basis set and a convergence criterion of 1×10^{-8} E_h. Vibrational frequencies for isotope shifts upon deuteration of the trifluoroethoxide ligand were calculated using the standalone orca_vib program. The hessian output file of the ground state frequency calculation was used as input to orca_vib after manually modifying the masses of the appropriate hydrogen atoms. A grid size of 4 correctly modelled the number of electrons for the system as necessary for accurate results for vibrational frequencies. In both frequency calculations, no negative frequencies were observed suggesting the calculations are reliable and run from an energy minimum.

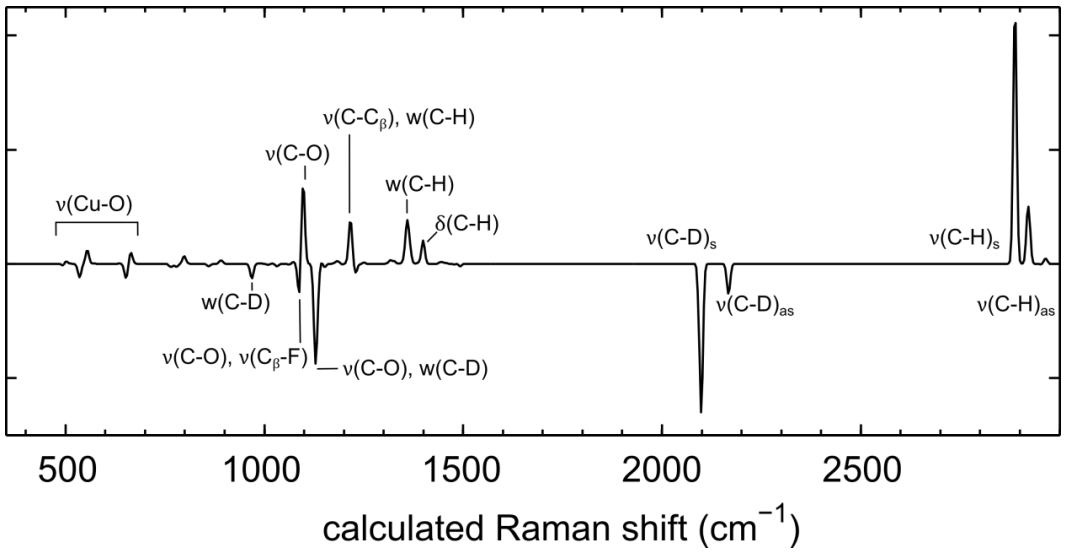

Figure A6.12. Difference spectrum (Cu^{II}-O(TFE) – Cu^{II}-O(TFE)-d_2) of predicted Raman enhancement of vibrational modes. Peaks due to Cu^{II}-O(TFE) appear as positive features, and peaks due to Cu^{II}-O(TFE)-d_2 appear as negative features. Notably, for Cu^{II}-O(TFE), a ν(C-C_β) + w(C-H) mode at 1216.7 cm^{-1} and a w(C-H) mode at 1359.2 cm^{-1} are predicted to have Raman activity. However, neither of these modes are predicted to have resonance enhancement.

Table A6.4b. Calculated Raman shifts and shifts upon isotopic labeling

Normal Mode	Cu^{II}-O(TFE) Raman shift (cm^{-1})	Normal Mode	Cu^{II}-O(TFE)-d_2 Raman shift (cm^{-1})	Isotopic shift (cm^{-1})
ν(Cu-O) + δ(F-C_β-F)	498	ν(Cu-O) + δ(F-C_β-F)	497	-1
ν(Cu-O)	555	ν(Cu-O)	535	-20
ν(Cu-O) + δ(O-C-C_β)	664	ν(Cu-O) + δ(O-C-C_β)	652	-12
ν(C-O)	1097	ν(C-O) + w(C-D)	1128	31
ν(C-O)	1097	ν(C-O) + ν(C_β-F)	1090	-7
w(C-H)	1359	w(C-D)	968	-391
ν(C-C_β) + w(C-H)	1217	w(C-D)	968	-249
δ(C-H)	1400			
ν(C-H)s	2888	ν(C-D)s	2098	-790
ν(C-H)as	2921	ν(C-D)as	2167	-754

A6.4 Structural and spectroscopic properties of Cu^{II} complexes

Table A6.5. Structural comparison of Cu^{II}-alkoxide, Cu^{II}-alkylperoxo,[5] and Cu^{II}-thiolate[6]

Structural feature [a]	Cu-OR	Cu-OOR[b]	Cu-SR[c]	Cu-SR[d]
Cu-N_{axial}	2.227	2.16	2.05	2.119
Cu-LMCT donor	1.832	1.81	2.12	2.176
Cu-N_{1basal}	1.972	1.96	1.97	1.930
Cu-N_{2basal}	1.964	1.98	2.03	2.037
OC,OO,SC	1.359	1.46	--	
Cu-X-X angle	135.48	112.1	--	111.7
Cu-X-X-C dihedral	158.19	179.3	--	
Nax-Cu-X	104.96	--	--	112.7

[a] Units are Ångstroms for bond lengths and degrees for angles.

[b] $Cu(OOCMe_2Ph)(HB(3,5\text{-}iPr_2pz)_3)$

[c] $Cu(SCPh_3)(HB(3,5\text{-}iPr_2pz)_3)$

[d] $Cu(SC_6F_5)(HB(3,5\text{-}iPr_2pz)_3)$

Table A6.6. Spectroscopic comparison of Cu^{II}-alkoxide, Cu^{II}-alkylperoxo,[7] and Cu^{II}-thiolate[8]

	Cu-OR	Cu-OOR[a]	Cu-SR[b]
g_{zz}	2.44	2.316	2.23
$g_{\perp}$ (X-band)	2.079	2.097	2.07
$\lvert {}^{Cu}A_{zz}\rvert$ ($\times 10^4$ cm^{-1})	40	55	74
$E_{x^2-y^2} - E_{xy}$(cm^{-1})	7050	8050	9250
f, oscillator strength $p_{\sim\sigma}$ CT donor → Cu $d_{x^2-y^2}$	0.0375	0.009	0.0002
f, oscillator strength p_{π} CT donor → Cu $d_{x^2-y^2}$	0.0510	0.056	0.0713

[a] $Cu(OOCMe_2Ph)(HB(3,5\text{-}iPr_2pz)_3)$, where $-OOCMe_2Ph$ is the CT donor to Cu $d_{x^2-y^2}$

[b] $Cu(SCPh_3)(HB(3,5\text{-}iPr_2pz)_3)$, where $-SCPh_3$ is the CT donor to Cu $d_{x^2-y^2}$

A6.5 Additional calculation results and details

A6.5.1 Time-dependent DFT

A time-dependent DFT calculation was used to produce the UV-Vis spectrum and the difference density maps of the transitions shown in Figure A6.13. In these figures, the grey surface represents the acceptor state and the purple the donor state. In the near IR region, the first four calculated transitions (1-4)

show substantial copper d orbital character in the donor state and are assigned as dominantly d_{z^2}, $d_{xz/yz}$, d_{xy}, and $d_{xz/yz}$ in character, respectively. The expected order of the transition donors (lowest to highest transition energy) in a distorted tetrahedral environment is d_{z^2}, d_{xy}, $d_{xz/yz}$, and $d_{xz/yz}$.[7,8] These have been assigned based on MCD experiments and typically show a + − + − sign pattern, respectively. Based on the sign of the transitions in this work, transitions 1-4 in the experimental MCD spectrum could be assigned as (+)d_{z^2}, (+)$d_{xz/yz}$, (−)d_{xy}, and (−)$d_{xz/yz}$, respectively, which matches the order of the TDDFT calculation but does not match the order of the d manifold transitions based on the literature. This order also does not support the difference in energy $E_{x^2-y^2} - E_{xy}$ necessary to drive the large g_{zz}.

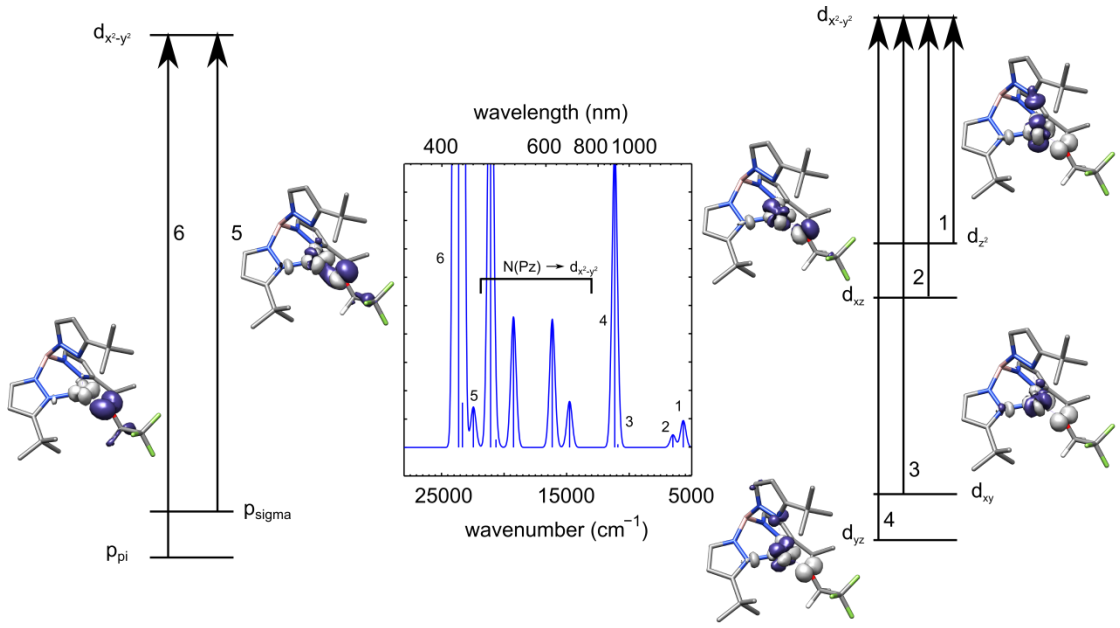

Figure A6.13. Calculated absorption spectrum and difference density plots. Grey represents the acceptor state and purple the donor state.

The charge transfer transitions from the ethoxide ligand are calculated to be in the near-UV region as seen experimentally. In the calculation, the O(TFE) $p_{\sim\sigma}$ transition (labeled 5) is lower in energy and less intense than the O(TFE) p_{π} transition (labeled 6). The lower intensity is due to poor overlap of the O(TFE) $p_{\sim\sigma}$ orbital with the acceptor Cu $d_{x^2-y^2}$. It is unexpected that the O(TFE) $p_{\sim\sigma} \rightarrow$ Cu $d_{x^2-y^2}$

transition is lower in energy in the calculation as this orbital is stabilized (larger transition energy) due to the σ bonding interaction it has with copper.

A6.5.2 Comparison of crystal structure geometry and optimized geometry

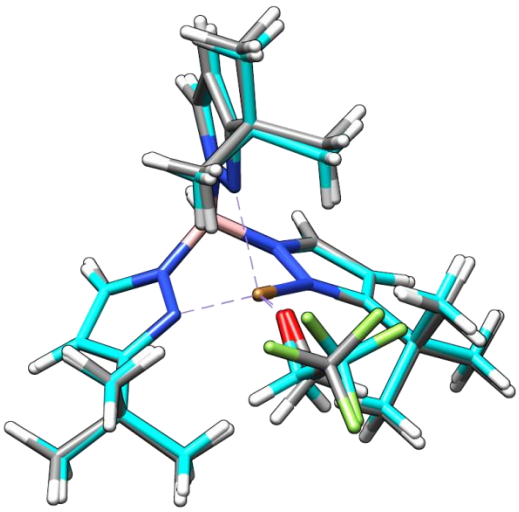

Figure A6.14. Comparison of XYZ coordinates of crystal structure (cyan) and optimized geometry (grey) of Cu^{II}-O(TFE).

Table A6.7. Structural comparison of crystallographic and calculated geometry of Cu^{II}-O(TFE)[9]

Structural feature [a]	Crystal	Calculated
Cu-N_{axial}	2.2270(11)	2.26
Cu-O	1.8324(10)	1.87
Cu-N_{1basal}	1.9717(11)	2.01
Cu-N_{2basal}	1.9638(11)	2.01
O-C	1.3593(18)	1.38
Cu-O-C	135.48(9)	134.006
Nax-Cu-O	104.96(4)	105.307
Cu-O-C-C	158.19	-177.771
Cu-O-C-H_R	-81.06	-57.700
Cu-O-C-H_S	37.43	62.855

[a] Units are Ångstroms for bond lengths and degrees for angles.

Optimized geometry (UKS BP86 TZVP) in *xyz* coordinates

Used for EPR property calculations, frequency, and time-dependent DFT calculations

C -1.29092 3.41700 -3.90409
C -1.17568 0.94198 -3.50157
C -0.75923 2.32666 -2.95423
C 0.780537 2.428944 -2.889226
C 2.002332 -2.543908 -2.875725
C 1.902269 -1.191829 -2.159336
C -1.33992 2.52492 -1.56372
C -2.27253 3.49019 -1.13019
C -2.06995 -3.01677 -1.13184
C -2.46720 3.24476 0.22399
C 3.590114 1.263303 0.189568
C -1.89501 -3.28576 0.37974
C -0.44591 -3.73826 0.66676
C -2.85901 -4.41358 0.79844
C -2.20637 -2.02243 1.16850
C 3.367469 -0.926622 1.443219
C 3.394876 0.613414 1.577575
C 2.089793 1.099865 2.184496
C -3.20815 -1.84534 2.15172
C 4.577313 1.012647 2.480703
C -3.09054 -0.52813 2.56715
C 1.882996 1.757323 3.414894
C 0.515358 1.993563 3.490081
H -0.86127 3.27542 -4.90659
H -0.77198 0.79697 -4.51557
H -2.38571 3.36842 -4.00048
H 1.217227 2.273047 -3.887511
H -2.27090 0.85665 -3.55488
H -1.01594 4.42505 -3.55975
H 1.810332 -0.422295 -2.952385
H -0.80631 0.12625 -2.86469
H 1.097728 3.417018 -2.524609
H 1.196175 1.672204 -2.207509
H 2.883458 -1.028027 -1.669107
H -1.88553 -3.93968 -1.70352
H -2.73913 4.26693 -1.72443
H -1.35828 -2.25767 -1.47968

H -3.09172 -2.67297 -1.35312
H 2.757876 1.013051 -0.484903
H 4.526478 0.910148 -0.268536
H -0.23015 -4.67565 0.13101
H -2.63322 -5.32226 0.22082
H 0.275396 -2.983645 0.328649
H 3.637085 2.359221 0.270525
H -3.90828 -4.14497 0.60305
H -3.09670 3.73783 0.95767
H 2.527260 -1.263806 0.820468
H 4.303124 -1.282178 0.984370
H -0.29756 -3.91571 1.74279
H -2.75669 -4.66082 1.86613
H 5.517987 0.656134 2.035452
H 3.267946 -1.404576 2.428841
H -3.92055 -2.57889 2.51044
H 4.650464 2.104527 2.593669
H -2.20471 2.10463 2.78425
H -3.64811 0.04465 3.30176
H 4.491383 0.564041 3.481382
H 2.632160 2.028837 4.149319
H -0.08775 2.47142 4.25528
B -1.56434 1.49282 1.96397
N -1.00486 1.74233 -0.50824
N -1.69649 2.19287 0.58048
N -1.52075 -0.86561 1.00414
N 0.892735 0.950875 1.565356
N -2.07588 0.04200 1.86964
N -0.06260 1.50492 2.36984
O 0.853543 -1.159658 -1.256910
F 3.056084 -2.523999 -3.752006
F 0.885020 -2.835728 -3.592992
F 2.213090 -3.573094 -2.013744
Cu 0.155360 0.151314 -0.126235

xyz coordinates from crystal structure .cif file

C	-1.19804	3.41553	-3.86799
C	-1.23501	0.93749	-3.50294
C	-0.74824	2.28779	-2.93958
C	0.78459	2.30614	-2.87083
C	2.14904	-2.48764	-2.56264
C	1.67785	-1.08437	-2.30589
C	-1.33505	2.50317	-1.56265
C	-2.27388	3.45856	-1.14895
C	-2.10338	-2.86728	-1.14005
C	-2.47558	3.21905	0.19249
C	3.52894	1.15998	0.19333
C	-1.82030	-3.20578	0.33253
C	-0.34906	-3.61722	0.48644
C	-2.71448	-4.37415	0.76562
C	-2.12169	-1.98916	1.18159
C	3.20224	-1.00418	1.44240
C	3.31369	0.52216	1.57239
C	2.04613	1.07489	2.18087
C	-3.08021	-1.85689	2.19784
C	4.51932	0.87231	2.45184
C	-2.99414	-0.54981	2.61399
C	1.86135	1.74474	3.39207
C	0.51150	2.03343	3.45935
H	-0.76245	3.31432	-4.73987
H	-0.84003	0.79128	-4.38787
H	-2.17064	3.37636	-3.98220
H	1.15360	2.13433	-3.76222
H	-2.21202	0.94851	-3.57900
H	-0.94957	4.27920	-3.47699
H	1.25868	-0.71988	-3.12530
H	-0.96244	0.21468	-2.89994
H	1.08690	3.18336	-2.55551
H	1.09205	1.61234	-2.25078
H	2.45135	-0.51143	-2.07470
H	-1.88505	-3.64068	-1.70080
H	-2.68439	4.12963	-1.68147
H	-1.55438	-2.10197	-1.41064
H	-3.05143	-2.64335	-1.24733
H	2.76634	0.95157	-0.38565

H	4.34965	0.80392	-0.20677
H	-0.15748	-4.37313	-0.10707
H	-2.51459	-5.16001	0.21528
H	0.22813	-2.86152	0.24960
H	3.60854	2.13186	0.29155
H	-3.65548	-4.12547	0.65045
H	-3.06029	3.70781	0.75971
H	2.42849	-1.22881	0.88443
H	4.01717	-1.35696	1.02796
H	-0.17880	-3.87971	1.41509
H	-2.54491	-4.58350	1.70785
H	5.33961	0.54680	2.02598
H	3.08986	-1.40045	2.33149
H	-3.66482	-2.52874	2.52838
H	4.57191	1.84475	2.56169
H	-2.11860	2.03655	2.63080
H	-3.51939	-0.14806	3.29607
H	4.41694	0.44937	3.32979
H	2.52594	1.95803	4.03638
H	0.07657	2.48931	4.17040
B	-1.57424	1.53456	1.95859
N	-1.00113	1.73377	-0.51303
N	-1.71321	2.18551	0.56497
N	-1.48503	-0.81465	1.00171
N	0.85407	0.96774	1.55677
N	-2.03577	0.06675	1.88817
N	-0.08170	1.56149	2.35209
O	0.77771	-1.06769	-1.28749
F	3.03777	-2.50838	-3.57824
F	1.15311	-3.32337	-2.88762
F	2.76174	-3.02755	-1.50780
Cu	0.16109	0.19305	-0.10931

A6.6 Synthesis and crystallographic information for $Tp^{tBu}Zn^{II}(OCH_2CF_3)$

A6.6.1 Unit cell dimensions compared to $Tp^{tBu}Cu^{II}(OCH_2CF_3)$[9]

$Tp^{tBu}Cu^{II}(OCH_2CF_3)$	$Tp^{tBu}Zn^{II}(OCH_2CF_3)$
a = 9.6749(12) Å α = 90°	a = 9.5516(12) Å α = 90°
b = 16.817(2) Å β = 96.881(6)°	b = 17.010(2) Å β = 95.412(7)°
c = 16.646(2) Å γ = 90°	c = 16.615(2) Å γ = 90°

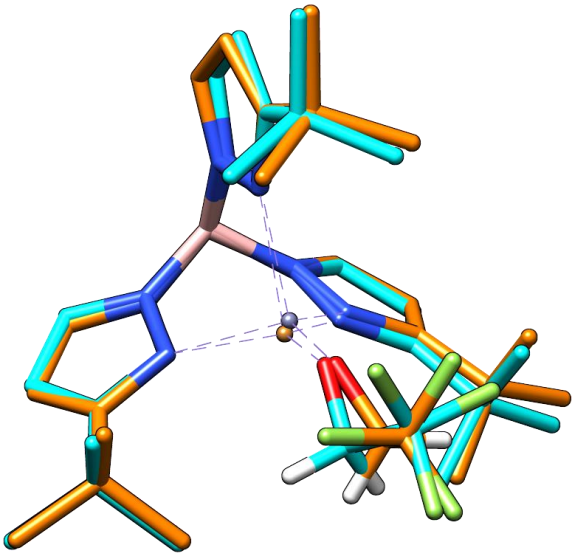

Figure A6.15. Visualization of the xyz coordinates of Cu^{II}-O(TFE) (carbon in cyan, copper in brown, nitrogen in blue, oxygen in red, fluorine in yellow) and Zn^{II}-O(TFE) (carbons in orange, zinc in purple, nitrogen in blue, oxygen in red, fluorine in yellow). Hydrogens are not shown for clarity, except on the trifluoroethoxide ligand (white). The xyz coordinates from the crystal structure files were related by a translation. This image was created using the match function in Chimera where the atoms C5,N3,N4,N1,C12,B1,C19 in Cu^{II}-O(TFE) were matched to the atoms C20, N4, N6, N3, C14, B1, C7 in Zn^{II}-O(TFE).

A6.6.2 Synthesis and structural characterization of $Tp^{tBu}Zn^{II}$-OTf

General Considerations. Unless otherwise noted, all chemicals were purchased from Sigma-Aldrich and used without purification. Solvents were purchased from Fischer and dried using a "Grubbs type" Seca Solvent System installed by GlassContour. 2,2,2-trifluoroethanol was distilled from $CaSO_4$ with a small amount of $NaHCO_3$ and stored over 3Å molecular sieves. All glassware was dried in an oven at 150 °C overnight and pumped into a nitrogen filled glovebox while hot. Celite was dried at 100 °C overnight under vacuum. All reactions were performed in a nitrogen filled glovebox.

Preparation and Characterization hydro-*tris*(3-*tert*-butylpyrazol-1-yl)borate) zinc(II) triflate, $Tp^{tBu}Zn^{II}$-OTf. To a toluene solution of 5 mL $Tp^{tBu}Zn^{II}Cl$ (328 mg, 0.68 mmol, prepared as previously described[10]) was added AgOTf (175 mg, 0.68 mmol) with stirring. A chalky gray-red precipitate formed over 1 hour and was collected by filtration on a Celite plug. Extraction with dichloromethane yielded a colorless solution, which upon removal of the solvent, gave $Tp^{tBu}Zn^{II}$-OTf as a white solid (367 mg, 91%). ^{1}H NMR (500 MHz, CD_2Cl_2): 7.62 (d, $^3J_{H-H}$ = 2.3 Hz, 3H), 6.12 (d, $^3J_{H-H}$ = 2.3 Hz, 3H), 1.37 (s, 27H). The product was crystallized from pentane at -30 °C yielding $Tp^{tBu}Zn^{II}$-OTf and a co-crystallized and disordered pentane molecule. Elemental Analysis was found to be slightly high in C and H which is likely a result of residual co-crystallized pentane. Anal. calcd. for $C_{22}H_{34}BF_3N_6O_3SZn$: C, 44.35; H, 5.75; N, 14.11. Found: C, 44.84; H, 5.91; N, 14.13.

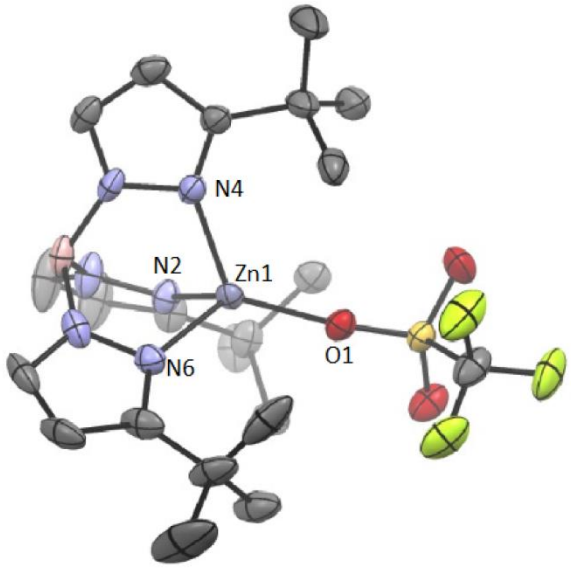

Figure A6.16. ORTEP drawing of $Tp^{tBu}Zn^{II}$-OTf with select atom labels showing 50% probability ellipsoids. Hydrogen atoms and the co-crystallized pentane molecule are omitted for clarity. Selected interatomic distances (Å) and angles (deg) are as follows: N2-Zn1, 2.010(4); N4-Zn1, 2.024(4); N6-Zn1, 2.018(4); O1-Zn1, 1.938(4); N2-Zn1-N4, 97.04(18); N2-Zn1-N6, 94.78(18); N2-Zn1-O1, 126.31(17); N4-Zn1-N6, 95.26(18); N4-Zn1-O1, 119.82(17); N6-Zn1-O1, 116.87(1).

Crystallographic Data for $Tp^{tBu}Zn^{II}$-OTf

General Procedure. A colorless prism, measuring 0.30 × 0.20 × 0.05 mm^3 was mounted on a loop with oil. Data was collected at -173 °C on a Bruker APEX II single crystal X-ray diffractometer, Mo-radiation.

Crystal-to-detector distance was 40 mm and exposure time was 10 seconds per frame for all sets. The scan width was 0.5°. Data collection was 99.1% complete to 25° in ϑ. A total of 93541 reflections were collected covering the indices, h = -12 to 12, k = -24 to 24, l = -18 to 18. 5986 reflections were symmetry independent and the R_{int} = 0.1165 indicated that the data was of slightly less than average quality (0.07). Indexing and unit cell refinement indicated a primitive monoclinic lattice. The space group was found to be P 2_1/n (No. 14).

The data was integrated and scaled using SAINT, SADABS within the APEX2 software package by Bruker.

Solution by direct methods (SHELXS, SIR97) produced a complete heavy atom phasing model consistent with the proposed structure. The structure was completed by difference Fourier synthesis with SHELXL97. Scattering factors are from Waasmair and Kirfel.[11] Hydrogen atoms were placed in geometrically idealized positions and constrained to ride on their parent atoms with C---H distances in the range 0.95-1.00 Å. Isotropic thermal parameters U_{eq} were fixed such that they were 1.2U_{eq} of their parent atom U_{eq} for CH's and 1.5U_{eq} of their parent atom U_{eq} in case of methyl groups. All non-hydrogen atoms were refined anisotropically by full-matrix least-squares.

The Zn complex is accompanied by a 4-fold disordered pentane.

Table A6.8. Crystallographic data for $Tp^{tBu}Zn^{II}$-OTf•Pentane provided.

Empirical formula	$C_{27}H_{46}BF_3N_6O_3SZn$
Formula weight	667.94
Temperature	100(2) K
Wavelength	0.71073 Å
Crystal system	Monoclinic
Space group	P21/n
Unit cell dimensions	a = 10.4203(10) Å α = 90°.
	b = 20.5076(19) Å β = 91.771(5)°.
	c = 15.4032(15) Å γ = 90°.
Volume	3290.0(5) Å3
Z	4
Density (calculated)	1.348 Mg/m3
Absorption coefficient	0.864 mm-1
F(000)	1408
Crystal size	0.30 × 0.20 × 0.05 mm3
Theta range for data collection	1.99 to 25.35°.
Index ranges	$-12 \le h \le 12$, $-24 \le k \le 24$, $-18 \le l \le 18$
Reflections collected	93541
Independent reflections	5986 [R(int) = 0.1165]
Completeness to theta = 25.00°	99.1 %
Max. and min. transmission	0.9581 and 0.7816
Refinement method	Full-matrix least-squares on F2
Data / restraints / parameters	5986 / 11 / 380
Goodness-of-fit on F2	1.140
Final R indices [I>2sigma(I)]	R1 = 0.0690, wR2 = 0.1576
R indices (all data)	R1 = 0.1007, wR2 = 0.1813
Largest diff. peak and hole	1.104 and -1.019 e.Å-3

A6.6.3 Synthesis and characterization of $Tp^{tBu}Zn^{II}$-OCH_2CF_3

Preparation of hydro-*tris*(3-*tert*-butylpyrazol-1-yl)borate) zinc(II) 2,2,2-trifluoroethoxide, $Tp^{tBu}Zn^{II}$-OCH_2CF_3. To a dichloromethane solution of 5 mL $Tp^{tBu}Zn^{II}$-OTf (363 mg, 0.61 mmol) was added a ~2 mL dichloromethane solution containing 1,8-Diazabicyclo[5.4.0]undec-7-ene (DBU; 93 mg, 0.61 mmol) and 2,2,2-trifluoroethanol (180 mg, 1.83 mmol). The reaction mixture was stirred for 30 minutes after which the solvent was removed in vacuo yielding a white solid (282 mg, 85%). ^{1}H NMR (500 MHz, CD_2Cl_2): 7.55 (d, $^3J_{H\text{-}H}$ = 2.3 Hz, 3H), 6.05 (d, $^3J_{H\text{-}H}$ = 2.3 Hz, 3H), 4.50 (q, $^3J_{H\text{-}F}$ = 9.5 Hz, 2H), 1.39 (s, 27H). $Tp^{tBu}Zn^{II}$-OCH_2CF_3 was extracted with ether and crystallized from pentane at -30 °C. Anal. calcd. for $C_{23}H_{36}BF_3N_6OZn$: C, 50.62; H, 6.65; N, 15.40. Found: C, 50.88; H, 6.80; N, 15.49.

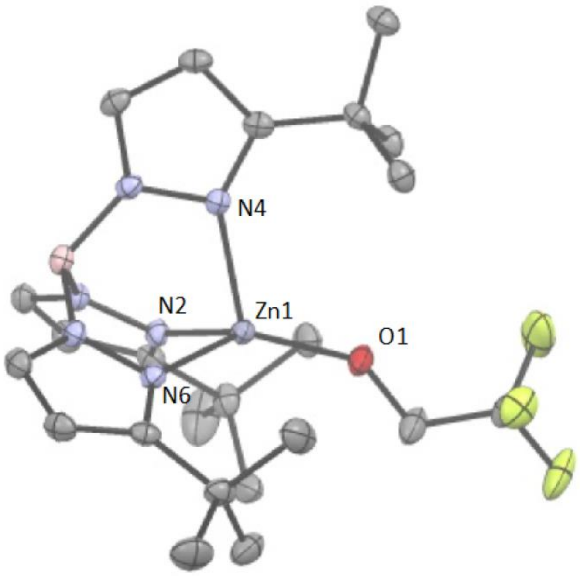

Figure A6.17. ORTEP drawing of $Tp^{tBu}Zn^{II}$-OCH_2CF_3 with select atom labels showing 50% probability ellipsoids. Hydrogen atoms are omitted for clarity. Selected interatomic distances (Å) and angles (deg) are as follows: N2-Zn1, 2.0304(16); N4-Zn1, 2.0586(16); N6-Zn1, 2.0553(16); O1-Zn1, 1.8471(14); N2-Zn1-N4, 92.64(6); N2-Zn1-N6, 94.71(6); N2-Zn1-O1, 129.59(7); N4-Zn1-N6, 93.51(6); N4-Zn1-O1, 113.76(6); N6-Zn1-O1, 123.63(7).

Crystallographic Data for $Tp^{tBu}Zn^{II}$-OCH_2CF_3

General Procedure. A colorless prism, measuring 0.14 x 0.10 x 0.05 mm^3 was mounted on a loop with oil. Data was collected at -173°C on a Bruker APEX II single crystal X-ray diffractometer, Mo-radiation.

Crystal-to-detector distance was 40 mm and exposure time was 10 seconds per frame for all sets. The scan width was 0.5°. Data collection was 100% complete to 25° in ϑ. A total of 117542 reflections were collected covering the indices, h = -12 to 12, k = -22 to 22, l = -22 to 22. 6749 reflections were symmetry independent and the R_{int} = 0.0842 indicated that the data was of slightly less than average quality (0.07). Indexing and unit cell refinement indicated a primitive monoclinic lattice. The space group was found to be P 2_1/n (No.14).

The data was integrated and scaled using SAINT, SADABS within the APEX2 software package by Bruker.

Solution by direct methods (SHELXS, SIR97) produced a complete heavy atom phasing model consistent with the proposed structure. The structure was completed by difference Fourier synthesis with

SHELXL97. Scattering factors are from Waasmair and Kirfel.[11] Hydrogen atoms were placed in geometrically idealised positions and constrained to ride on their parent atoms with C---H distances in the range 0.95-1.00 Å. Isotropic thermal parameters U_{eq} were fixed such that they were 1.2U_{eq} of their parent atom U_{eq} for CH's and 1.5U_{eq} of their parent atom U_{eq} in case of methyl groups. All non-hydrogen atoms were refined anisotropically by full-matrix least-squares.

Table A6.9. Crystallographic data for the structures provided.

Empirical formula	$C_{23}H_{36}BF_3N_6OZn$
Formula weight	545.76
Temperature	100(2) K
Wavelength	0.71073 Å
Crystal system	Monoclinic
Space group	P 2_1/n
Unit cell dimensions	
	a = 9.5516(12) Å α = 90°
	b = 17.010(2) Å β = 95.412(7)°
	c = 16.615(2) Å γ = 90°
Volume	2687.4(6) Å3
Z	4
Density (calculated)	1.349 Mg/m3
Absorption coefficient	0.961 mm-1
F(000)	1144
Crystal size	0.14 × 0.10 × 0.05 mm3
Theta range for data collection	1.72 to 28.55°.
Index ranges	-12 ≤ h ≤ 12, -22 ≤ k ≤ 22, -22 ≤ l ≤ 22
Reflections collected	117542
Independent reflections	6749 [R(int) = 0.0842]
Completeness to theta = 25.00°	100.0 %
Max. and min. transmission	0.9535 and 0.8772
Refinement method	Full-matrix least-squares on F2
Data / restraints / parameters	6749 / 0 / 325
Goodness-of-fit on F2	1.018
Final R indices [I>2sigma(I)]	R1 = 0.0346, wR2 = 0.0673
R indices (all data)	R1 = 0.0631, wR2 = 0.0781
Largest diff. peak and hole	0.325 and -0.397 e.Å-3

A6.7 $Tp^{tBu}Cu^{II}$-OCH_2CF_3 EPR/ENDOR simulations

A6.7.1 Definitions and code used to fit the single crystal data

The Matlab programming language with the Easyspin toolbox was used for spectral simulations. The following definitions were used to transform the single crystal coordinates of $Tp^{tBu}Cu^{II}$-OCH_2CF_3 into an orthogonal frame *a*bc*. (where length_a, length_b, and length_c are the sides of the unit cell in Angstroms):

```
Code (1)
a = [sind(ac);  0 ; cosd(ac)]*length_a;
b = [0; 1; 0]*length_b;
c = [0; 0; 1]*length_c;
```

The following definitions transformed the atomic coordinates into the newly orthogonal crystal frame.

```
Code (2)
Cu1  =  0.31882*a  +  0.22184*b  +  0.78010*c;
O1   =  0.24149*a  +  0.15172*b  +  0.84618*c;
.
.
.
```

These vectors were used to compute distances for the distributed point dipole approximation.

The axis of single crystal rotation was determined by X-ray crystallography to be [-7, -4, 5] in the non-orthogonal *abc* crystal coordinates with 2° accuracy. The following definition was used to determine the axis of single crystal rotation in the orthogonal frame *a*bc*.

```
Code (3)
capillaryAxis_C = -7*a - 4*b + 5*c;
capillaryAxis_C = capillaryAxis_C/norm(capillaryAxis_C);
```

The following definitions were used to create an orthogonal molecular frame in the crystal coordinates.

```
Code (4)
zM_C   =  N6 - Cu1;
zM_C   =  zM_C/norm(zM_C);
CuO_C =  O1 - Cu1;
```

```
CuO_C =  CuO_C/norm(CuO_C);
xM_C  =  cross(CuO_C,zM_C);
xM_C  =  xM_C/norm(xM_C);
yM_C  =  cross(zM_C,xM_C);
```

With the atomic coordinates and molecular frame defined as above and the principle components of the *g* tensor determined by Q-band EPR of a frozen solution of $Tp^{tBu}Cu^{II}$-OCH_2CF_3, four parameters remained unknown for accurate simulation of the single crystal EPR data. First, the starting axis in crystal coordinates parallel to the external magnetic field B_0 (parallel to the laboratory axis, z_L). This starting orientation could be summarized with one parameter using the following code making use of the built in Easyspin function 'rotatecrystal'.

Code (5)

```
% Starting orientation of crystal
% (a) build lab frame around known yL_C
yL_C = capillaryAxis_C; % given by XRD
yL_C = yL_C/norm(yL_C); % normalize
% (b) create arbitrary orthogonal lab frame
xL_C = [yL_C(2); -yL_C(1); 0]; % construct xL perpendicular to yL
xL_C = xL_C/norm(xL_C);
zL_C = cross(xL_C,yL_C);
% (c) get arbitrary C->L transformation
R0_L2C = [xL_C yL_C zL_C];
R0_C2L = R0_L2C.';
ang0_C2L = eulang(R0_C2L);

% Generate crystal orientations
rotaxis_L = [0;1;0]; % crystal rotation axis, in lab coordinates
rho0 = 0; % arbitrary starting rotation angle, degrees
drho = 15; % experimental rotation angle increment, degrees
rho = rho0*pi/180 + (0:drho:180)*pi/180; % rotation angle around yL in radians
nOrientations = numel(rho);
ang_C2L = rotatecrystal(ang0_C2L,rotaxis_L,rho);
```

Above, the only unknown value is *rho0*. The three Euler angles relating the *g* tensor frame to the molecular frame are also unknown. These parameters were simultaneously fit to the set of thirteen

spectra rotated from 0° to 180°, using the following looped least-squares fitting which sampled the possible values for *rho0* in 3° steps and fit the Euler angles:

Code (6)

```
for i=1:61
rho0_fit = 3*i-3; % starting rotation angle, degrees
rho_fit = rho0_fit*pi/180 + (0:drho:165)*pi/180; % rotation angle around that axis
ang_C2L_fit = rotatecrystal(ang0_C2L,rotaxis_L,rho_fit);
        Exp1.CrystalOrientation = ang_C2L_fit;
        % course fitting
        Vary1.gFrame = [pi/8 pi/8 pi/8]*2;
        FitOpt1.Method = 'grid';
        FitOpt1.Scaling = 'maxabs';
        FitOpt1.GridSize = [10 20 10];
[Sys_fit_M spc_fit_M] =  esfit('multifit',spc_con,Sys1,Vary1,Exp1,Opt1,FitOpt1);
        % refined fitting
        FitOpt2.Method='levmar';
        FitOpt2.Scaling='minmax';
        FitOpt2.TolFun=1e-2;
        Vary2.gFrame=[pi/8 pi/8 pi/8];
[Sys_fit_ref{i} spc_fit_ref{i}] = esfit('multifit',spc_con,Sys_fit_M,Vary2,Exp1,Opt1,FitOpt2);
RMSDs(i,1) = sqrt((sum((spc_con - spc_fit_ref{i}).^2)/length(spc_con)));
end
```

It is important to note that all the data (each spectrum at each rotation angle) must be concatenated into a one dimensional vector, above defined as *spc_con*. The fit made use of a home-written function 'multifit' for concatenation of the simulated spectra (concatenation is a common technique for fitting multiple data sets simultaneously).

Code (7)

```
function [bsim_con,sim_con]=multifit(Sys,Exp,Opt);
Exp.nPoints = Exp.nPoints/size(Exp.CrystalOrientation,1);
        [b,sim]=pepper(Sys,Exp,Opt);
sim1=sim.';
sim_con=reshape(sim1,1,size(sim,2)*size(sim,1)); % concatenate simulated spectra
% create field axis for simulated spectra
for k=1:size(sim,1);%number of spectra in sim
        bsim(k,:)=b+max(b)*(k-1);
```

```
end
b1=bsim.';
bsim_con=reshape(b1,1,size(bsim,2)*size(bsim,1));
end
```

The above fitting found a value for *rho0* of 72° for crystal 1 and 86° for crystal 2 which were used in the simulation of the single crystal ENDOR data.

A6.7.2 Definitions and code used to fit the single crystal ^{1}H ENDOR data

The following nested function was used to compute the dipolar component of the hyperfine coupling between the TFE (-OCH_2CF_3) ligand hydrogens and the spin density on copper, oxygen, and basal nitrogens (N2 and N4).

Code (8)

```
% point dipole interaction as a nested function
hfH_C  = @(r) (mu0/4/pi)*bmagn*nmagn*gn*g_C.'*(3*r*r.'/norm(r)^2-E)/(norm(r*1e-10)^3);

% here E= identity matrix, mu0 is the vacuum permeability, bmagn is the Bohr magneton, nmagn is
the nuclear magneton, gn is the nuclear g value of the proton, and g_C is the electron g tensor in the
crystal frame

% dipolar hyperfine coupling between copper and proton 22A
A1_Cu_C = sigmaCu*hfH_C(H22A-Cu1); % joule
A1_O_C  = sigmaO*hfH_C(H22A-O1); % joule
A1_N2_C = sigmaN2*hfH_C(H22A-N2); % joule
A1_N4_C = sigmaN4*hfH_C(H22A-N4); % joule
% sum to create full tensor
A1_C = A1_Cu_C + A1_O_C + A1_N2_C + A1_N4_C;
```

Here the distance vectors, *r = H22A - Cu1, etc…*, were computed from the atomic crystal coordinates described in 'Code (2)'. Each interaction was weighted by a value *sigmaX* which represents the spin population on the atom Cu, O, N2, or N4. The full 3x3 tensor that resulted from the sum of these individual contributions (*A1_C* above) was used in single crystal ENDOR simulations. The same process was used to compute the dipolar hyperfine coupling for the second proton H22B.

Note that using the full g tensor defined in the crystal coordinates (*g _C*) accounts for the spin Hamiltonian term that describes the weak interaction between the nuclear spin and the electron orbital. Therefore, for significant *g* anisotropy, this equation returns a non-symmetric matrix from which an accurate rotation matrix can not be extracted. It is always important to check rotation matrices for the relation $R*R^T=\begin{bmatrix}1 & 0 & 0\\ 0 & 1 & 0\\ 0 & 0 & 1\end{bmatrix}$ when using them in simulations.

However, it has been recently argued that this interaction is not physically relevant, and instead the free electron *g* value should be used in computing the dipole interaction between nuclei and electrons. The paper published on this project utilizes the full *g* matrix for this calculation, however, it was observed that the free *g* value gave more satisfying agreement between the simulation and experimental data and is likely the correct method to use. Overall, this choice is inconsequential for the conclusions made from the study.

A6.7.3 Simulations of frozen solution ^{14}N ENDOR spectra

The following definitions were used to create the hyperfine frame and Euler angles for the basal nitrogen atom, N_2, where the unique A_{zz} axis pointed toward the copper nucleus. These frames were found to give better simulations of the data than the frames extracted from the point dipole approximation.

Code (9)

```
N2_ = Cu1 - N2;
zN2_C = N2_/norm(N2_); % Azz points at the Copper
N2_N4 = N4 - N2;
yN2_C = cross(zN2_C, N2_N4);
yN2_C = yN2_C/norm(yN2_C);
xN2_C = cross(yN2_C, zN2_C); % Axx is the cross product Ayy x Azz
% transformation matrix from crystal frame to H1 hyperfine frame
R_N2toC = [xN2_C yN2_C zN2_C];
R_N2toM = R_C2M*R_N2toC;
R_MtoN2 = R_N2toM.';
N2Frame_estimate = eulang(R_MtoN2);
```

An analogous procedure was carried out for the hyperfine frame of basal nitrogen atom, N4.

Using the orientation of hyperfine frame as defined above, the principle components of the hyperfine tensor were determined. However, instead of using a least squares fitting routine which failed to provide adequate results, the spectra were fit by eye. The hyperfine coupling values were initially estimated from the DFT parameters and defined in the spherical form A_{tot} =[a_{iso}, a_{dip}, $a_{rhombic}$] (see EasySpin documentation for the difference between Sys.A and Sys.A_).

A6.7.4 Frozen solution ^{19}F ENDOR

The nested function for the point dipole approximation (Code(8)) was similarly use to compute the hyperfine coupling between the fluorine atoms and the spin density on copper, oxygen, and basal nitrogen atoms (N2 and N4). The principle components of the tensor were extracted (using the 'eig' function in Matlab) and rotated with copper centric hyperfine frames defined in a similar fashion as the nitrogen hyperfine frames (Code (9)) described above.

A6.8 Analysis of UV-Vis and MCD spectra

Magnetic circular dichroism spectroscopy measures the differential absorption of left and right circularly polarized light by a sample placed in a magnetic field. For paramagnetic molecules, the features in a spectrum are a result of "C-term" transitions which are depicted in Figure A6.18. The photons drive electronic transitions. Because they are circularly polarized, they are in pure angular momentum states that can simultaneously drive EPR transitions. The intensity of C-term features in an MCD spectrum depends on the sample temperature following a Boltzmann population distribution. Below will be described the procedure for background correction and simultaneous fitting of MCD and UV-Vis absorption spectra.

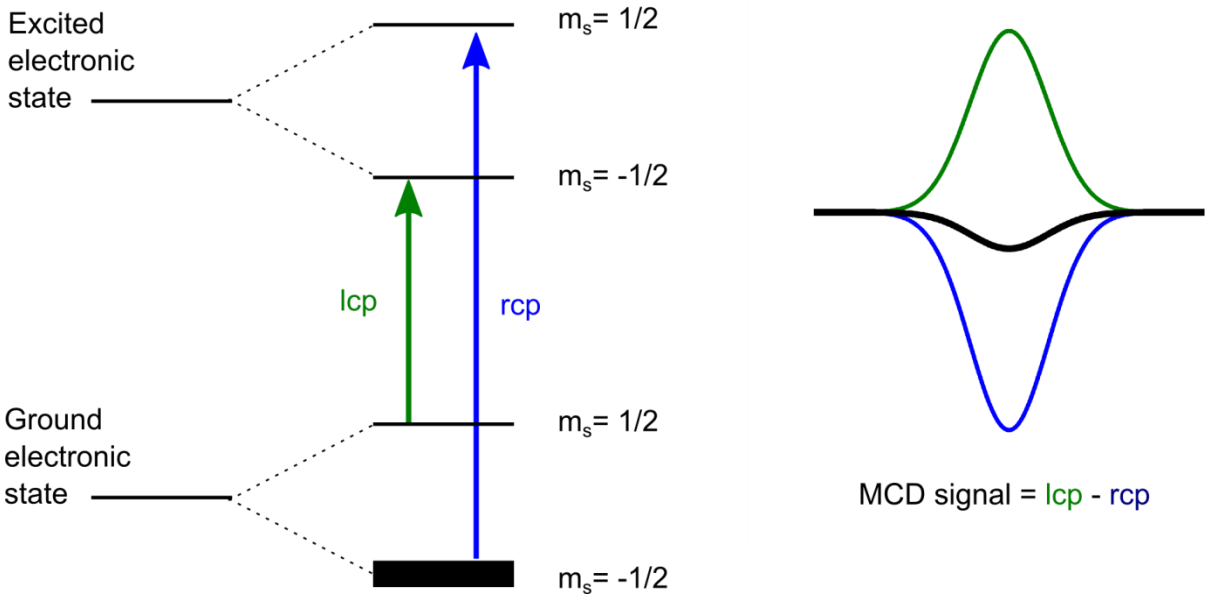

Figure A6.18. *Left*: An energy level diagram depicting the origin of C-term intensity (due to paramagnetism) in MCD spectra. Right circularly polarized light (rcp) drives an electronic transition and the EPR transition (m_s = -1/2 → m_s = 1/2) while left circularly polarized light (lcp) drives an electronic transition and the EPR transition (m_s = 1/2 → m_s = -1/2). *Right*: Because the signal is measured as absorption of lcp – rcp, the transition intensity can be either positive or negative.

A6.8.1 Processing simultaneous MCD, absorption data

Several of the most important considerations to keep in mind when collecting and processing MCD data are described below. To begin, it is important and useful to note all of the information that can be gained from the experiment. The MCD spectrometer simultaneously records a low temperature absorption spectrum on a separate dynode detector. Each data file contains both the MCD spectrum (second column in text file) and the absorption spectrum (dynode, third column in text file). In addition, one may be able to see natural circular dichroism absorption of the sample if there are features in the data collected at 0 Tesla.

It is possible for the sample to depolarize the light as it passes through which can distort the final measured signal. To test for this, two measurements are recorded. First, a chiral molecule is placed between the light source and the sample and data recorded (blue trace in Figure A6.19). Next, the same chiral molecule is placed between the sample and the detector and data recorded (red trace in Figure

A6.19). The extent of depolarization is determined by comparing the two data sets where, if excessive depolarization is present, the second measurement will be distorted.

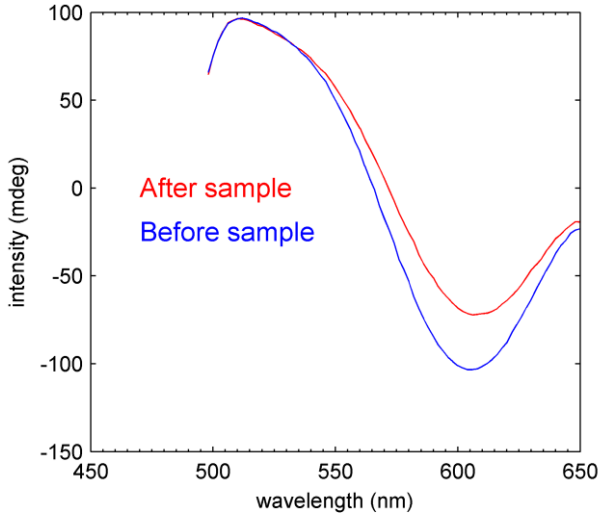

Figure A6.19. The spectra recorded to test for depolarization of the light by the Cu^{II} sample.

Correcting low temperature absorbance spectrum. The low temperature absorption data taken simultaneously with the MCD spectrum (on the dynode) will need to be converted to absorbance units. To convert to absorbance, *A*, in the UV-Vis region, one should use the equation based on Beer's Law $A = 7.4*\log_{10}(I/I_{NS})$, where *I* is the dynode intensity at 0 Tesla and the temperature of interest. I_{NS} is the reference dynode signal with no sample present and can be taken at any temperature and magnetic field because of the absence of a sample. The additional factor 7.4 relates the intensity of the sample and reference beam. In the IR region, one can simply use the relation $A = \log_{10}(I/I_{NS})$ without the additional factor.

The low temperature absorption data will need to be baseline corrected. One should compare the low temperature absorption spectrum taken on the MCD spectrometer to a standard UV-Vis electronic absorption spectrum taken at room temperature when doing these background corrections. First, if a sloping baseline is observed (such as in Figure A6.20, top) in the low temperature absorption spectrum that is not observed in the room temperature spectrum, a simple linear baseline should be subtracted from the spectrum as a correction. In addition, the low temperature absorption spectrum will likely be

offset from a zero baseline (Figure A6.20, top). If so, use the room temperature absorption spectrum to determine where there is zero absorption (in this case at 650 nm), and set the zero baseline to this point.

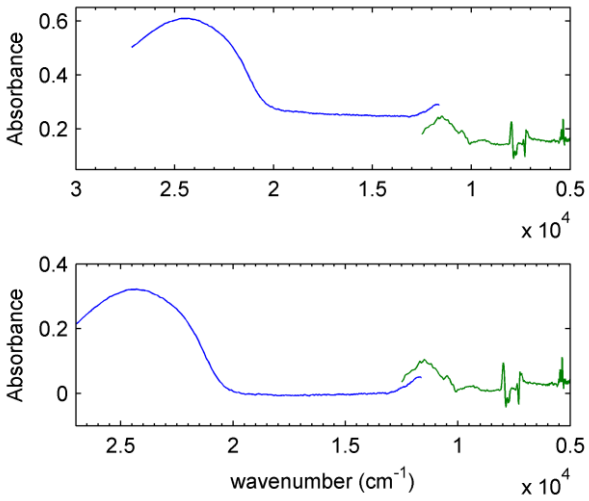

Figure A6.20. *Top*: Low temperature absorption data collected simultaneously with MCD data at 5K and 6T. These traces show the slopping baseline and offset from zero. *Bottom*: Low temperature absorption after baseline correction. Note, the IR detector introduces noise and this data was not used in analysis or published.

Background correcting MCD data. The raw MCD data is recorded in units of millidegrees (mdeg). To convert to units of Δ*A*, the data should be element-wise divided by the constant 32980.

MCD data can suffer from background and baseline issues. There are two common ways to background correct the data which were both employed for the complex $Tp^{tBu}Cu^{II}$-OCH_2CF_3. MCD data was recorded in the UV-Visible region from 360 nm to 860 nm. Using a separate IR detector, data was recorded from 800 nm to 2000 nm. In the UV-Vis region, it was noted that the signal depended strongly on the direction of the current generating the magnetic field (i.e. operating at 6 T vs -6 T). To correct this issue, at every field and temperature measured, both the negative and positive field spectrum was recorded. The final processed data was then the average of these two measurements. For example, for the data at 5 Kelvin and 6 Tesla, the final spectrum equals the average $\Delta A = (\Delta A_{6T,5K} - \Delta A_{-6T,5K})/2$. In the IR region, the spectra recorded with negative and positive magnetic field were found to be equivalent, so spectra

were only recorded with the positive field. In this case, at each corresponding temperature, the MCD spectrum recorded at 0 Tesla was subtracted from the spectrum. For example, in the IR region of the data recorded at 5 Kelvin and 6 Tesla the final spectrum equals $\Delta A = (\Delta A_{6T,5K} - \Delta A_{0T,5K})$. These corrections can remove any features that may be due to natural differential absorption of circularly polarized light (or natural CD). This background correction process is shown in Figure A6.21.

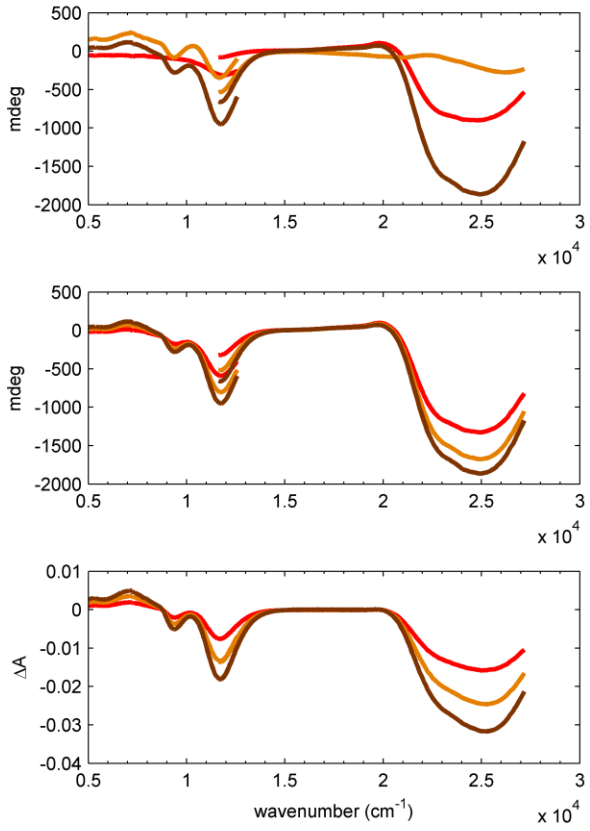

Figure A6.21. MCD spectra at 5 Kelvin through background correction. *Top*: Red, the MCD trace at 0T, 5K. Brown, the MCD trace at 6T, 5K. Tan, the MCD trace at -6T, 5K. Note the IR region does not depend on the direction of the magnetic field, but the UV-Vis does. *Middle*: The MCD spectra at 2 T (red), 4 T (tan), and 6 T (brown) before background subtraction. *Bottom*: The MCD spectra at 2 T (red), 4 T (tan), and 6 T (brown) after background subtraction and converting units to Δ*A*.

A6.8.2 Simultaneous Gaussian fitting of MCD and absorption data

Electronic spectra can be fit as the sum of a series of Gaussian peaks, where each peak represents an electronic transition. For transition metal compounds like the Cu^{II} complex presented here, it is typical for a combination of absorption, circular dichroism, and MCD spectra to be analyzed simultaneously by assuming transitions are expected to appear at the same energy in each different spectrum. Absorption data are always positively signed, however, both CD and MCD spectra can have negative and positive features because the data is plotted as the difference in absorption between left and right circularly polarized light $\Delta A = A_L - A_R$. This signed nature of the data makes it easier to resolve the energy of electronic transitions.

To simultaneously fit multiple spectra, the absorption, low temperature absorption, and MCD spectra were concatenated. Each transition was modeled with the function 'voigt' below which made use of the built in Easyspin functions, 'gaussian' and 'lorentzian' to plot a Gaussian peak which could be optionally combined with Lorentzian character (although ultimately no Lorentzian character was used in the published analysis).

Code (1)

```
function peak = voigt(x, E, I, W, G)
if I == 0
  peak = zeros(size(x));
else
g = gaussian(x,E,W)*I;
l = lorentzian(x,E,W)*I;
peak = g*G + l*(1-G);
end
```

Importantly, *E*, the second term fed into 'voigt', represents the transition energy (the center of the Gaussian) of the peak.

The MCD spectra made it more obvious that two transitions were underlying the broad LMCT feature in the near UV absorption of $Tp^{tBu}Cu^{II}$-OCH_2CF_3. Concatenating the MCD, low temperature absorption, and room temperature absorption spectra meant six Gaussian peaks were generated using the 'voigt'

function (fed into a loop). The two energy values of the LMCT transitions (or peak centers) were constrained to the same value, plus a known, user defined constant (see Figure A6.22). Constraining the energy to the same value allows the user to narrow down the possible solutions to the fit. This series of six peaks generated a starting point for the fitting procedure, *totalfit0*.

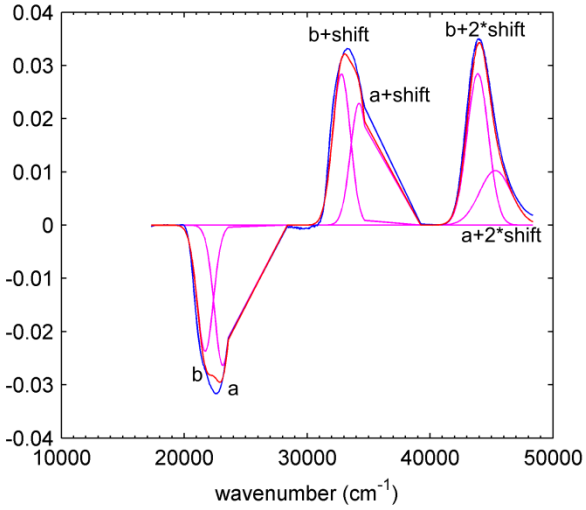

Figure A6.22. In blue is the concatenated electronic absorption data in the near-UV LMCT transition region for $Tp^{tBu}Cu^{II}$-OCH_2CF_3. From left to right, the MCD, low temperature absorption, and room temperature absorption are shown. The peak maxima (labeled *a* and *b* in the MCD spectrum and Code (2)) are constrained to the same value, but shifted by a known constant *shift* and *shift*2*, which can be removed after the fitting. The individual peaks generated in *fit0* are shown in pink and the sum of the Gaussian peak *totalfit0* is shown in red.

Code (2)

```
clf;
a=26266.2;
b=23404.8;
f0.x=x;
f0.max=[a,b,a+shift,b+shift,a+shift*2,b+shift*2];
f0.int=[-90.209 -78.7816 80.0276 102.0179 66.1745 123.0541];
f0.width=[3210.36 3121.04 3282.76 3376.53 6071.3 4064.7];
f0.G2L=[1 1 1 1 1 1];
f0.shiftspec=shift;
%f0.xsep=[numel(MCD_x) numel(MCD_x) numel(MVis_x) numel(MVis_x) numel(Vis_y) numel(Vis_y)]
for i = 1:size(f0.max,2)
   fit0(:,i)= voigt(x,f0.max(i),f0.int(i),...
      f0.width(i),f0.G2L(i));
```

```
    totalfit0 = sum(fit0,2);
end
plot(x,fit0,'m',x,y,'b',x,totalfit0,'r');
```

The concatenated data (*x* and *y*), the initial fitting parameters (*f0*), and the initial simulation (*totalfit0*) were fed into the 'esfit' function

```
esfit('simul_LMCT',y,f0,vary,x);
using a homebuilt function 'simul_LMCT'.
function totalfit = simul_LMCT(fit0,ydata,xdata);
names=fieldnames(fit0);
fit1=fit0.(names{1})
fit2=fit0.(names{2})
fit3=fit0.(names{3})
fit4=fit0.(names{4})
fit5=fit0.(names{5})
fit6=fit0.(names{6})
% for holding parameters the same
fitstart(:,1)= voigt(fit1,fit2(1),fit3(1),fit4(1),fit5(1));
fitstart(:,2)= voigt(fit1,fit2(2),fit3(2),fit4(2),fit5(2));
fitstart(:,3)= voigt(fit1,fit2(1)+fit6,fit3(3),fit4(3),fit5(3));
fitstart(:,4)= voigt(fit1,fit2(2)+fit6,fit3(4),fit4(4),fit5(4));
fitstart(:,5)= voigt(fit1,fit2(1)+fit6*2,fit3(5),fit4(5),fit5(5));
fitstart(:,6)= voigt(fit1,fit2(2)+fit6*2,fit3(6),fit4(6),fit5(6));

totalfit = sum(fitstart,2);
end
```

This function makes use of the esfit function in Easyspin and any of the available algorithms can be used in the fitting. A similar scheme was used to simultaneously fit the near IR region of the various electronic spectra which contained the d$\rightarrow$d transitions.

A6.9 Additional resonance Raman data

Scattered light in the resonance Raman experiment was recorded on a monochromator equipped with a liquid-N_2 cooled charged-coupled device detector. As a result, the data is recorded in units of pixels on the abscissa as shown in Figure A6.23. Different ranges of wavelength are recorded by rotating the

grating of the monochromator (with a built-in motor on the spectrometer). However, the numerical pixel window does not change as the grating is rotated. To calibrate the x-axis, separate standard samples must be measured along with the analyte. Using known Raman scattering values in wavenumbers for the peaks in standard samples, a simple linear relation between pixels and wavenumbers can be used to scale the x-axis for the data of interest. Measuring a standard sample for calibration must be done each time the monochromator grating is rotated to a new window.

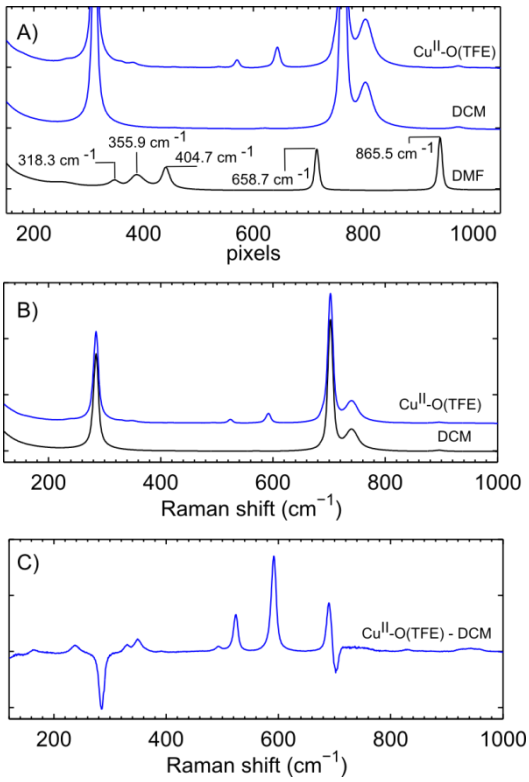

Figure A6.23. A) The known vibrational frequencies in the Raman spectrum of the solvent DMF were used to convert the x axis from pixels to wavenumbers (cm^{-1}). B) rR spectra of the solvent DCM and the analyte Cu^{II}-O(TFE) in DCM. C) The spectrum obtained by subtracting the solvent DCM spectrum in B) from the spectrum of the sample containing Cu^{II}-O(TFE).

In addition to measuring a standard sample to calibrate the x-axis, one must measure a background sample which contains all the materials of a sample except the analyte of interest. A resonance Raman spectrum of a sample in solution at room temperature will contain intense peaks from the Raman scattering of the solvent, as shown in Figure A6.23. It may also be necessary to collect data in multiple solvents because of overlap of analyte and solvent peaks. As shown in Figure A6.23, the ν(Cu-O) peak at

690 cm^{-1} of Cu^{II}-O(TFE) overlaps with a solvent feature in dichloromethane. The position of each peak is confirmed using multiple solvents, as shown by the rR spectrum collected in benzene (Figure A6.24) which shows vibrational frequencies in excellent agreement with those found in DCM (presented in the main text). Using multiple solvents also allows one to monitor the influence of solvent interaction on the normal mode frequencies. In Cu^{II}-O(TFE), no significant solvent interactions were present in going from DCM to benzene.

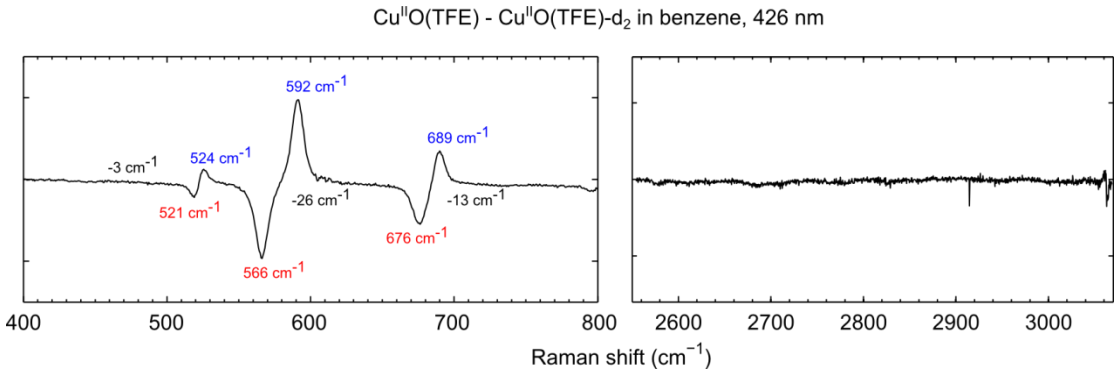

Figure A6.24. rR difference spectra of Cu^{II}-O(TFE)-d_2 subtracted from Cu^{II}-O(TFE) in the ν(Cu-O) stretching frequency region (left) and the ν(C_α-H) stretching frequency region (right).

In our study, we were interested in the modulation of the αC-H bond strength of the alkoxide ligand by the Cu^{II} ion. Indicators of the bond strength are the symmetric and antisymmetric stretching frequencies ν(C_α-H) which are predicted by a Raman calculation to appear at 2888 and 2921 cm^{-1}, respectively. These features are expected to isotopically shift to 2098 and 2167 cm^{-1} in Cu^{II}-O(TFE)-d_2. However, as shown in Figure A6.24, no features due to Cu^{II}-O(TFE) or Cu^{II}-O(TFE)-d_2 were observed at higher frequencies.

Exposure to light may chemically alter the analyte of interest, so it is important to check for photodegradation of the sample. This can be done by recording spectra in time series and monitoring the analyte features as a function of time. Cu^{II}-O(TFE) showed no change in its spectrum during 15 minutes of continual laser irradiation. rR spectra recorded over time with continual laser irradiation are shown in Figure A6.25.

However, over several hours outside of the glove box, the yellow color of the solution faded to clear, indicating loss of the LMCT transition (420 nm) being used for resonance enhancement (incident wavelength of 426 nm). As expected, this resulted in intensity decay of all Raman features due to Cu^{II}-O(TFE) as shown in Figure A6.25

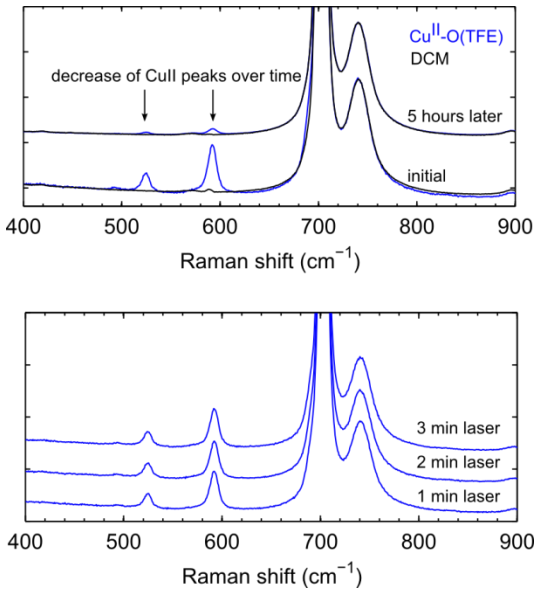

Figure A6.25. *Top*: rR spectra recorded as a function of time outside the glove box showing a decrease in Raman intensity which occurs as the yellow color of the Cu^{II}-O(TFE) solution fades. *Bottom*: rR spectra recorded as a function of time with incident laser irradiation. During the length of time of a typical experiment, there is no appreciable intensity decay.

A6.10 Performing resonance Raman calculations with the Orca software

Here I have compiled a step-by-step procedure for performing resonance Raman calculations using the Orca software. This compiles some information found in the Orca manual, in Orca online tutorials, and from trial and error by the author.

1. First, calculate a Hessian file doing an opt+freq calculation. This can be either an analytical calculation (keyword: AnFreq) or a numerical calculation (keyword: NumFreq).
2. Now you will have an optimized geometry (output file molecule.xyz) and a hessian (output file molecule.hess).
3. Next, run a TDDFT calculation to find the excited states of your molecule that you want to use for the resonance Raman calculation. It saves time to run this calculation beforehand and analyze it, so that you don't do a resonance Raman calculation for all the excited states.

   TDDFT block:

```
! UKS B3LYP tzvp tzvp/j RIJCOSX #RIJCOSX auxiliary basis for hybrid functionals speeds up calculation
! MORead TightSCF Grid5 #reconverge previous MOs with MORead, TightSCF if the basis of functionals are new
! PAL6 # run on 6 processors, check how many your computer has
%maxcore 4000 #limit the amount of RAM the TDDFT calculation uses as these are memory intensive calculations → 4 G per processor
%moinp "Cu_opt.gbw" # take MOs from tightly converged geometry optimization

%tddft
      MaxDim 120 # needs to be a multiple of nRoots. at least 3x larger
      nRoots 30 # run TDDFT for 30 excited states
end
*xyzfile 0 2 Cu_opt.xyz
  .
  .
*
```

Note that although you should always run TDDFT with a solvent model (COSMO), the rR calculation in the current version of Orca (3.0.3) does not accept solvent models, so this preliminary calculation should also not use COSMO.

4. Look at the TDDFT calculation and find which states correspond to the transition you are interested in. For example, you could plot the absorption spectrum to look for strong LMCT transitions that you would excited in rR. Do this using the stand alone orca program orca_mapspc. To generate a text file that you can plot with Matlab or your favorite program do:

```
orca_mapspc molecule.out ABS –x0 –x1
```

*See orca input library for more information

After plotting, you can look in the orca output file for the excited states:

```
TD-DFT/TDA EXCITED STATES

-------------------------

the weight of the individual excitations are printed if larger than 0.01

STATE  1:  E=   0.025845 au      0.703 eV     5672.4 cm**-1
  119b -> 142b  :     0.095249 (c=  0.30862494)
  132b -> 142b  :     0.050123 (c= -0.22388124)
  133b -> 142b  :     0.387430 (c=  0.62243880)
  137b -> 142b  :     0.413783 (c=  0.64325991)
```

Note that this is the first excited state and it involves transitions from four molecular orbitals. To visualize this, you can then plot the difference densities that correspond to the states you are interested in using orca_plot in interactive mode:

```
orca_plot molecule.gbw –i
```

Running this in the terminal will bring up a screen with the option to plot MOs, transition densities, and several other things. In this case you want to plot option 6:

```
6 - Plot CIS/TD-DFT difference densities
```

which you can then look at in a program like Chimera.

5. After choosing you states (this case uses states 10 and 12 for the rR calculation) run another .oif with the rR block.

```
! UKS B3LYP tzvp tzvp/j RIJCOSX PAL6
! MORead TightSCF NMGrad Grid5 # note the NMGrad keyword
%maxcore 4000
%moinp "Cu_opt.gbw"
%tddft
        MaxDim 52
        nRoots 13 # calculate only as many excited states as you need to
end

# this block generates ASA specific input
%rr     States 10, 12 # calculate the rR for the excited states you already chose
        HessName "molecule.hess" # use the hessian you calculated in step 1
        ASAInput true
        end
*xyzfile 0 2 Cu_opt.xyz
```

6. Run this .oif like any other orca input file. In the output you get all the usual output files, plus a .asa.inp file. This must be edited, then used in the orca_asa program to generate rR spectra. The orca_asa program is very fast because no new quantum calculations occur; it just generates text files. Below are the necessary edits you must make:

   Add the excited state energies you want asa to generate spectra for.

```
%sim
      model IMDHO
      method Heller
      AbsRange     21000.0,  25000.0
      NAbsPoints   100
      RRSRange     0.0,    4000.0
      NRRSPoints   4000
      RRSE 17106, 19485 # Add this line, get energies from $el_states below
      RRS_FWHM 10.0
      AbsScaleMode Ext
      RamanOrder  2
      EnInput E0
      CAR   0.800
end
$el_states # use these energies above
2
  1 17105.72   100.00    0.00    -0.0575   0.0694   0.0391
  2 19484.62   100.00    0.00     0.5679  -0.9268  -0.8341
```

Note your excited states energy will not match the energies from the TDDFT calculation, because the rR block computes the vertical excited state energies.

7. Now run

   orca_asa molecule.asa

   and you will get the rR spectra to plot.

8. To do this for an isotopic shift, you must edit the hessian file. For instance to calculate a deuterium spectrum instead of a proton spectrum, go into the .hess file, find the atom you interested in and change its mass and save the file molecule_2H.hess

   H 1.008 becomes H 2.008

9. Recalculate the vibrational frequencies in the hessian with adjusted masses using orca_vib

   orca_vib molecule_2H.hess

   which replaces molecule_2H.hess with new, isotope shifted frequencies.

10. Repeat steps 5-7, but use this new hessian in the %rr block

A6.11. Electronic structure of additional $Tp^{tBu}Cu^{II}$-X compounds

In addition to Cu^{II}-O(TFE), other Cu^{II} compounds were synthesized in the Mayer group in the Tp^{tBu} ligand scaffold with a fourth unique ligand. The EPR spectra of these compounds are shown in Figure A6.26. Despite the similar ligand scaffold, the compounds have very different EPR properties dependent on the fourth uniquely coordinating ligand. The reactivities of the compounds (bottom two) have been reported but will not be described here.[9,12]

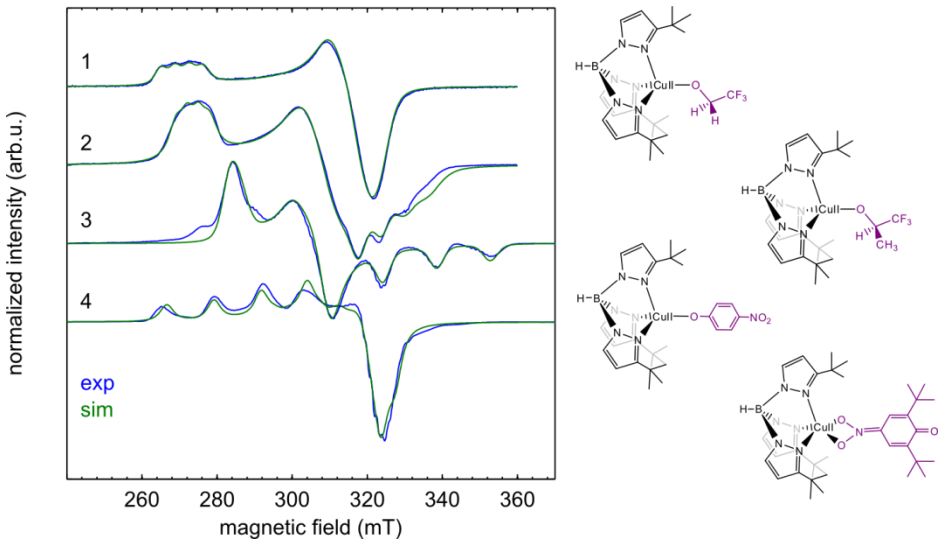

Figure A6.26. CW EPR collected at 9.28 GHz of 2-5 mM copper compounds (structures shown to the right) in DCM:toluene at 120 K. Spectra were collected with 2 mW of microwave power and 1 G modulation amplitude. The top spectrum is the same as that presented in the main text.

The simulation parameters are listed in Table A6.10 and for the top spectrum (Cu^{II}-O(TFE)) they are the same as those reported in the main text. The spectra reveal interesting differences in the ground state electronic structure of the compounds.

Table A6.10. *g* values and Cu hyperfine coupling values for the simulations in Figure A6.26

		g	^{Cu}A (MHz)
1	xx	2.06	60
	yy	2.09	60
	zz	2.44	120
2	xx	2.03	170
	yy	2.15	55
	zz	2.42	100
3	xx	2.32	30
	yy	2.15	40
	zz	2.002	405
4	xx	2.07	20
	yy	2.16	250
	zz	2.32	415

Compound 2 with isopropyloxy ligand shows a rhombic spectrum with g_{zz} = 2.42, g_{yy} = 2.15, and g_{xx} = 2.03. The largest copper hyperfine lies along the g_{xx} axis with a value $^{Cu}A_{zz}$ = 170 MHz. A large gStrain

was applied in the g_{yy} direction to account for the broadening which makes exact quantification of the $^{Cu}A_{yy}$ value difficult. None of the *g* values used in the simulation are close to the *g* free value g_e=2.002, so it is assumed this molecule is in the dx^2-y^2 ground state. This molecule has an unusually large g_{zz} value, like Cu^{II}-O(TFE), but also shows a much larger copper hyperfine in the x direction

Compound 3 shows a rhombic spectrum with g_{zz} = 2.002, g_{yy} = 2.15, and g_{xx} = 2.32. The largest copper hyperfine lies along the g_{zz} axis with a value $^{Cu}A_{zz}$ = 405 MHz. The unique g_{zz} axis is the close to the free *g* value g_e suggesting this molecule is in the dz^2 ground state. Considering the symmetry of the molecule, it is very likely that the molecular frame is rotated so that the z axis of the dz^2 orbital points to the unique 4-nitrophenoxide ligand.

Compound 4, the only five coordinate Cu^{II} complex can be modeled with rhombic *g* values of g_{xx} = 2.07, g_{yy} = 2.16 and g_{zz} = 2.32. The largest hyperfine value is in the g_{zz} direction with a value of $^{Cu}A_{zz}$ = 415 MHz. A large broadening due to *g* value strain was applied along the g_{yy} direction to achieve the broadening seen in the simulation. This makes determining the exact value of the g_{yy} and A_{yy} parameters impossible. No *g* value is close to g_e so this molecule is likely in the dx^2-y^2 ground state.

A6.12 References

(1) Morton, J. R.; Preston, K. F. *J. Magn. Reson.* **1978**, *30*, 577.
(2) Dunlap, B. I.; Connolly, J. W. D.; Sabin, J. R. *J. Chem. Phys.* **1979**, *71* (8), 3396.
(3) Feyereisen, M.; Fitzgerald, G.; Komornicki, A. *Chem. Phys. Lett.* **1993**, *208* (5), 359.
(4) Neese, F.; Wennmohs, F.; Hansen, A.; Becker, U. *Chem. Phys.* **2009**, *356* (1–3), 98.
(5) Kitajima, N.; Katayama, T.; Fujisawa, K.; Iwata, Y.; Moro-oka, Y. *J. Am. Chem. Soc.* **1993**, *115* (17), 7872.
(6) Kitajima, N.; Fujisawa, K.; Tanaka, M.; Moro-oka, Y. *J. Am. Chem. Soc.* **1992**, *114*, 9232.
(7) Chen, P.; Fujisawa, K.; Solomon, E. I. *J. Am. Chem. Soc.* **2000**, *122* (41), 10177.
(8) Randall, D. W.; George, S. D.; Hedman, B.; Hodgson, K. O.; Fujisawa, K.; Solomon, E. I. *J. Am. Chem. Soc.* **2000**, *122* (47), 11620.
(9) Porter, T. R.; Capitao, D.; Kaminsky, W.; Qian, Z.; Mayer, J. M. *Inorg. Chem.* **2016**, *55* (11), 5467.
(10) Gorrell, I. B.; Looney, A.; Parkin, G. *J. Chem. Soc. Chem. Commun.* **1990**, *20* (3), 220.
(11) Waasmaier, D.; Kirfel, A. *Acta Crystallogr. Sect. A* **1995**, *51* (3), 416.
(12) Porter, T. R.; Hayes, E. C.; Kaminsky, W.; Mayer, J. M. *Dalt. Trans.* **2017**, *46*, 2551.

Vita

Ellen C. Hayes was born and raised in Midland, Texas. She attended the University of Texas at Austin from the fall of 2007 until the spring of 2011 when she graduated with her Bachelor of Science in biochemistry. While at UT, she worked in the lab of Dr. Lauren J. Webb probing the influence of electrostatic interactions on the specificity of protein binding using vibrational stark effect spectroscopy. She arrived at the University of Washington in the fall of 2011 and began her doctoral research in the lab of Dr. Stefan Stoll. After completing her Ph.D. at UW in the summer of 2017, she will remain in the Stoll research group as a post-doctoral researcher until winter 2017. She plans to pursue a career in the biotechnology industry.